TESIS DE LA UNIVERSIDAD
DE ZARAGOZA

2018

57

Carlos Laliena Iranzo

Superconducting MgB2 wires and Bi2Sr2CaCu2O8+x monoliths: Precursor influence on their global and local properties and on scale-up processing

Departamento

Ciencia y Tecnología de Materiales y Fluidos

Director/es

Angurel Lamban, Luis Alberto
Martinez Fernandez, Elena

ISSN 2254-7606

Prensas de la Universidad
Universidad Zaragoza

ISSN 2254-7606

Tesis Doctoral

SUPERCONDUCTING MGB2 WIRES AND BI2SR2CACU2O8+X MONOLITHS: PRECURSOR INFLUENCE ON THEIR GLOBAL AND LOCAL PROPERTIES AND ON SCALE-

Autor

Carlos Laliena Iranzo

Director/es

Angurel Lamban, Luis Alberto
Martinez Fernandez, Elena

UNIVERSIDAD DE ZARAGOZA
Ciencia y Tecnología de Materiales y Fluidos

2018

Tesis Doctoral

Superconducting MgB_2 wires and $Bi_2Sr_2CaCu_2O_{8+x}$ monoliths: Precursor influence on their global and local properties and on scale-up processing

Carlos Laliena Iranzo

Instituto de Ciencia de Materiales de Aragón
Departamento de Ciencia y Tecnología de Materiales y Fluidos
CSIC - Universidad de Zaragoza

Abril 2018

icma
Instituto de Ciencia
de Materiales de Aragón

Dª Elena Martínez Fernández, Científico Titular del CSIC, y D. Luis Alberto Angurel Lambán, Catedrático de Universidad, ambos pertenecientes al Instituto de Ciencia de Materiales de Aragón (CSIC- Universidad de Zaragoza)

HACEN CONSTAR

Que esta memoria de tesis doctoral elaborada por D. Carlos Laliena Iranzo y titulada “Superconducting MgB_2 wires and $Bi_2Sr_2CaCu_2O_x$ monoliths: precursor influence on their global and local properties and on scale-up processing” contiene un trabajo original de investigación y ha sido realizada bajo su dirección.

Por ello, en cumplimiento de la legislación vigente, autorizan su tramitación ante la Universidad de Zaragoza para proceder, en su caso, a su posterior defensa.

Zaragoza, 9 de abril de 2018

Elena Martínez

Luis Alberto Angurel

ICMA - Instituto de Ciencia de Materiales de Aragón
Facultad de Ciencias, Universidad de Zaragoza - CSIC
C/ Pedro Cerbuna 12. 50009 Zaragoza. Spain
CSIC
Consejo Superior de Investigaciones Científicas
Universidad Zaragoza
1542

Se apaga el carrousel
¡Deséame suerte!
Vetusta Morla, “Deséame suerte”

Contents

Resumen

En 1911, Kamerlingh Onnes descubrió la superconductividad enfriando mercurio a temperaturas muy bajas. Observó que, por debajo de 4.2 K, la resistencia eléctrica era nula. Desde entonces se han descubierto muchos otros materiales superconductores, algunos con temperaturas de transición superiores al punto de ebullición del nitrógeno líquido (77 K) que se conocen como superconductores de alta temperatura.

El interés en estos materiales es elevado y actualmente se utilizan en muchos campos diferentes. Una de las aplicaciones más relevantes son los imanes superconductores que se emplean, por ejemplo, en física de altas energías (CERN) o para diagnóstico médico en aparatos de imagen por resonancia magnetica (MRI) o espectroscopía de resonancia magnetica nuclear (NMR).

Cada aplicación precisa unos requisitos específicos y, generalmente, los materiales superconductores tienen que ser procesados en forma de hilos o cintas conductoras. Sin embargo, no todos los superconductores son susceptibles de ser procesados y solo unos pocos están disponibles comercialmente: Nb47wt%Ti, $\mathrm{Nb_3Sn}$, $\mathrm{MgB_2}$, $\mathrm{Bi_2Sr_2Ca_{n\text{-}1}Cu_nO_{2n+4+x}}$ o BSCCO (también conocidos como Bi-2212 si $n = 2$ y Bi-2223 si $n = 3$) e $\mathrm{YBa_2Cu_3O_{7\text{-}x}}$ (también YBCO o REBCO si el Y es sustituido por una tierra rara). Además para determinadas aplicaciones se utilizan superconductores en forma masiva, principalmente REBCO y BSCCO. Existen una serie de parámetros asociados a los superconductores, como la temperatura crítica (T_c), el campo crítico superior (H_{c2}), el campo de irreversibilidad (H_{irr}), la anisotropía superconductora (γ) o la densidad de corriente crítica (J_c), que juegan un papel fundamental en su aplicabilidad.

La microestructura de los materiales es esencial para las propiedades su-

perconductoras finales por lo tanto, es fundamental analizar y optimizar las características microestructurales más relevantes (presencia de las fases superconductoras y secundarias, homogeneidad, calidad de la textura, tamaño de grano, etc) que dependen en gran medida del método de procesado y de los polvos utilizados como precursores en su preparación.

Este trabajo se ha centrado en el estudio y optimización de hilos compuestos metal/MgB_2 y de materiales masivos de Bi-2212. El objetivo principal de la tesis es el estudio de la microstructura de estos materiales, que han sido fabricados a partir de diferentes precursores y usando métodos específicos de procesado, y de cómo la microestructura influye en sus propiedades superconductoras. Debido a su diferente naturaleza, propiedades y comportamiento, el manuscrito se ha divido en dos partes, cada una de ellas dedicadas a cada uno de estos materiales.

En la investigación del MgB_2 se analiza el efecto de los parámetros de molienda de los polvos precursores, realizada en un molino de bolas planetario, y de su dopaje con carbono, mediante al adición de ácido oleico, en las propiedades superconductoras de hilos compuestos metal/MgB_2. Para ello hemos fabricado hilos con forro de hierro y núcleo superconductor de MgB_2 usando la reacción *in situ*. El objetivo es encontrar las condiciones óptimas de molienda y dopaje con carbono que permitan alcanzar una microestructura controlada y homogénea con altos valores de $J_c(H)$.

La estructura de esta parte del trabajo se detalla a continuación:

- En el Capítulo 2 se resume el estado actual de los conductores de MgB_2 y se describen los objetivos y la motivación del trabajo desarrollado en la tesis en este campo.

- En el Capítulo 3 se explica el proceso de fabricación de los hilos, desde los polvos precursores hasta la propia fabricación del hilo mediante la técnica *polvo en tubo* (PIT, de sus siglas en inglés) y el tratamiento térmico final necesario para obtener la fase superconductora.

- En el Capítulo 4 se ha estudiado la influencia de los parámetros de molienda en la microestructura y en las propiedades superconductoras, concretamente en los valores de $J_c(H)$ y de temperatura crítica.

- En el Capítulo 5 se ha analizado el efecto combinado de la molienda y el dopaje con ácido oleico.

- El Capítulo 6 se centra en el uso de técnicas magneto-ópticas (MO) para analizar la distribución espacial del flujo magnético en el interior de las muestras. Usando la técnica MO junto con la microscopía electrónica de barrido de emisión de campo (FESEM), se han correlacionado las propiedades superconductoras locales con las observaciones microestructurales. Además, se ha demostrado que las imágenes MO obtenidas son muy útiles para analizar la homogeneidad de los conductores y para comprender los valores de J_c globales obtenidos mediante medidas magnéticas o de transporte.

- Finalmente, en el Capítulo 7 se presentan las principales conclusiones obtenidas en esta primera parte de la tesis.

El objetivo principal del estudio realizado sobre materiales masivos de Bi-2212 es el desarrollo de un proceso industrialmente escalable basado en el uso de hornos en continuo que puede ser utilizado para procesar piezas de este material de grandes dimensiones. El proceso comprende todas las etapas: la preparación de los precursores, el texturado por fusión zonal láser (LZM) y el tratamiento térmico final necesario para obtener la fase superconductora. También se analizan los parámetros más relevantes y su efecto en la microestructura y propiedades superconductoras de las muestras.

A continuación, se describe la estructura de esta segunda parte de la tesis:

- En el Capítulo 8 se resumen los principales resultados obtenidos para el texturado de barras y monolitos de Bi-2212 con las técnicas LZM y fusión zonal láser asistida con corriente (EALZM). También se recogen algunas de las modificaciones introducidas en los sistemas de procesado láser para desarrollar procesos continuos. Finalmente, se describe la motivación y los objetivos de esta segunda parte.

- En el Capítulo 9 se ha analizado la posibilidad de preparar polvos de Bi-2212 utilizando un proceso continuo de síntesis de estado sólido. Esta técnica se realiza en un horno de rodillos y permite superar ciertas limitaciones con respecto a la cantidad de polvo a preparar y su uniformidad. Se han analizado las características de los polvos fabricados con esta técnica, comparándolas con otros polvos comerciales y otros fabricados con técnicas estándar de estado sólido. Teniendo en cuenta las características del horno utilizado se ha determinado cuántas veces debe repetirse el tratamiento térmico para obtener un grado mínimo de prestaciones en el polvo.

- En el Capítulo 10 se ha descrito un método para texturar materiales masivos de Bi-2212 en geometría plana, utilizando métodos de fusión zonal inducida con láser (LZM) que son industrialmente escalables. Se ha validado la técnica de texturado utilizando precursores fabricados con polvos comerciales y posteriormente se ha analizado la posibilidad de utilizar precursores fabricados con el método de estado sólido en continuo.

- En el Capítulo 11 se ha analizado el efecto de aplicar una corriente eléctrica durante el procesado de fusión zonal de muestras planas masivas de Bi-2212, analizando sus propiedades microestructurales y superconductoras. Se ha demostrado que un porcentaje importante de la corriente aplicada no pasa a través de la zona fundida.

- Finalmente, las principales conclusiones de esta parte se recogen en el Capítulo 12.

Chapter 1

Introduction

1.1 Superconductivity: materials and relevant parameters

In 1911, Kamerlingh Onnes discovered superconductivity by cooling mercury to extremely low temperatures, and observing that the metal exhibits zero resistance to electric current at $T < 4.2\,\mathrm{K}$. During the first half of the the twentieth century many other metals and alloys were found to be superconductors, known as low temperature superconductors (LTS). These materials present a transtition temperature from superconductor-to-normal state, T_c, typically below 20 K, being 23.3 K the highest for Nb_3Ge [1]. Probably the most widely used superconductors discovered during this period were Nb47wt.%Ti and Nb_3Sn, with T_c values of 9.8 K [2] and 18.1 K [3] respectively.

In 1986, Bednorz and Müller discovered oxide based ceramic materials with T_c of 35 K [4], inaugurating the high temperature superconductors (HTS) research field. Since then, extensive research has raised T_c up to 138 K in Tl-doped $HgBa_2Ca_2Cu_3O_{8+x}$ (Hg-1223) [5, 6], and even up to 164 K in undoped Hg-1223 under 31 GPa [7]. Most important cuprate superconductors are $YBa_2Cu_3O_{7-x}$ (known as YBCO or Y-123) and $Bi_2Sr_2Ca_{n-1}Cu_nO_{2n+4+x}$ where n ranges from 1 to 3 (BSCCO) [8]. YBCO was the first discovered superconductor above the boiling point of liquid nitrogen (77 K), specifically at 93 K [9]. T_c in BSCCO materials ranges from $\sim 90\,\mathrm{K}$ for $Bi_2Sr_2CaCu_2O_{8+x}$ (Bi-2212) to 110 K for $Bi_2Sr_2Ca_2Cu_3O_{10+x}$ (Bi-2223).

Thereafter, superconductivity has been found in other materials, such as MgB_2 (with $T_c \sim 39\,K$) and iron-based family, which awakened great interest, both for their unconventional mechanism that governs superconductivity and their potential applications. The first superconductor discovered of this Fe-based family was LaFePO in 2006 with a T_c of $\sim 4\,K$ [10]. The T_c has been increased up to 109 K in 2014 for FeSe films grown over Nb-doped $SrTiO_3$ surfaces [11]. One year later, in 2015, superconductivity was observed in the hydrogen sulfide system (most probably H_3S) under 155 GPa of pressure at $\sim 203\,K$ [12], setting the record of highest T_c up to date.

In addition to the temperature constraint ($T < T_c$), there exist other parameters that limit the superconducting state, such as the critical magnetic field, H_c, and the critical current, I_c. All practical superconductors are type II superconductors, presenting two critical fields: the lower critical field, H_{c1}, and the upper critical field, H_{c2}. When the superconductor is exposed to field values in the range $H_{c1} < H < H_{c2}$, it is penetrated by magnetic flux forming an ordered lattice of quantized line vortices of fluxons. This state is known as the mixed state and the vortices are normal state cylinders of radius equal to the coherence length, ξ. Associated to the core of these vortices, there are superconducting screening currents whose density decreases exponentially over a length equal to the London penetration length, λ_L. When increasing the applied field, more vortices penetrate the sample increasing the flux density in the superconductor. This process progresses until $H = H_{c2}$, where the cores of the vortices begin to overlap and the whole superconductor ends up transitioning into the normal state.

When a current density J flows through a type II superconductor subjected to an applied magnetic field such as $H_{c1} < H < H_{c2}$, a Lorentz force F_L (perpendicular to J and H) will act on the vortices inducing a flux flow that will cause energy dissipation. In order to avoid magnetic flux motion, vortices must be pinned (flux pinning) by nanostructural or microstructural defects, depending on the material. The overall force at which these vortices are pinned is known as pinning force $F_p(T, H)$. The critical current density, $J_c(T, H)$, which is defined by the balance of the pinning and Lorentz forces, $F_p = F_L$, constitutes then the upper limit of transport current density in practical applications.

Furthermore, J_c will decrease when increasing H until it becomes zero. That characteristic field is known as the irreversibility field, H_{irr}, which is always lower than H_{c2} and plays a crucial role in the development of applications because it determines the highest magnetic field at which the superconductor can be put in service. Figure 1.1 shows both the H_{irr} and H_{c2} fields of some type II superconductors.

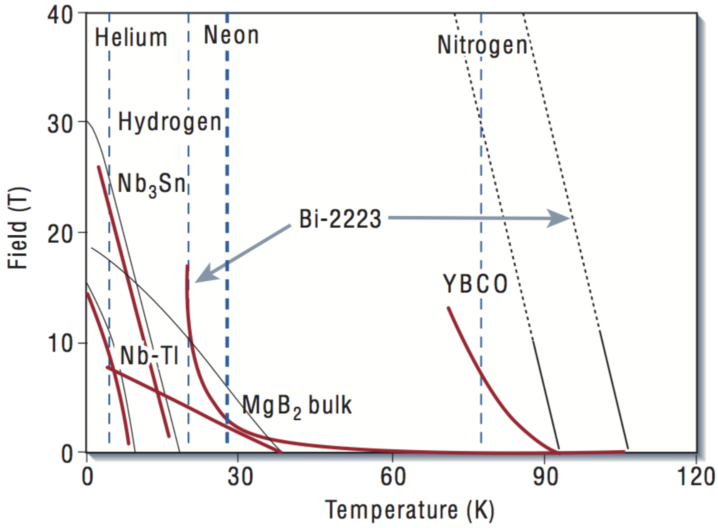

Figure 1.1: Magnetic field-temperature diagram for Nb47wt.%Ti, Nb_3Sn, MgB_2, Bi-2223 and YBCO [13]. H_{c2} is indicated in black and H_{irr} in red.

1.2 Applications of superconductivity

In terms of applications of superconductors, these can be divided in two main categories: superconducting electronics, based on their quantum properties (such as the Josephson effect), and electric power applications, which take advantage of their high current transport properties.

Superconducting quantum interference devices, SQUID, are without doubt the most widely recognised application in the field of superconducting electronics. They are currently used as the main component of magnetometers because they are the most sensitive devices for detecting magnetic flux.

Electric power applications include among others, superconducting magnetic energy storage (SMES), flywheel electrical energy storage (FEES) devices, superconducting cables for power transmission and distribution, superconducting fault current limiters (SFCL) to protect the grid against shot-circuits, superconductor-based transformers and also superconducting rotating machines, rotors and generators, which provide important mass and size reductions.

Other major field of superconductivity applications is in high-field superconducting magnets. Superconductors are the only possibility for building the high field magnets needed in high energy physics, as in CERN, and nuclear energy applications, such as ITER. However, the largest and most commercially successful applications of superconducting magnets are magnetic resonance imaging (MRI) devices for medical diagnosis, and in nuclear magnetic resonance (NMR) spectroscopy, widely used in chemical, biological, biochemical and pharmaceutical research and development.

For the majority of these applications, superconductors must be fabricated into composite wires or tapes, and only a few are suitable and commercially available: NbTi, Nb_3Sn, MgB_2, Bi-2212, Bi-2223 and YBCO (or REBCO where Y is substituted by a rare earth). However, other applications demand bulk superconductors, mainly REBCO and BSCCO [14].

Each application presents an specific set of requirements making certain commercial superconductors more adequate than others. In addition to the previously mentioned T_c, H_{c2} and H_{irr}, the superconducting anisotropy γ, defined as the ratio $H_{c2}^{\parallel ab}/H_{c2}^{\perp ab}$, plays a crucial role, especially in HTS. Another crucial parameter is the engineering current density, J_e, defined as the ratio between I_c and the cross-sectional area of the overall conductor (including metal sheaths and matrix), which gives the "effective" current density that the superconducting wire is able to carry. With all this in mind, the design of superconducting applications has to pay special attention to the operating requirements (T, direction and intensity of H, J) in order to choose the most appropriate superconducting material.

1.3 Objective and structure of the thesis

The intrinsic properties of each superconductor impose specific requirements in their fabrication process in order to be practical from the technological point of view [13]. For example, in HTS, J_c decreases exponentially as a function of the misorientation angle between neighbour grains. Thus, these superconductors require specific fabrication methods to induce texture, i.e. to reduce as much as possible the grain misorientation. However, grain boundaries can contribute to flux pinning in LTS and MgB_2, which do not need texture.

In the process of developing practical superconducting materials, it is fundamental to analyse and optimize their microstructure, due to its essential role in their final superconducting properties. Relevant microstructural characteristics, which include superconducting and secondary phases present in the material, homogeneity, texture quality, grain size, etc, depend strongly on the processing method and powders used as precursor.

The study of the microstructure of superconducting materials processed from different precursors and their influence in their superconducting properties is the main objective of this thesis. It has been focused on the analysis of two different superconductors, MgB_2 and Bi-2212, for their interest from the point of view of the applications. Due to their different nature, properties and behaviour, the manuscript has been divided in two different parts:

- The first part is devoted to the analysis and improvement of monocore Fe-sheathed MgB_2 wires and tapes manufactured by the powder-in-tube (PIT) technique, using drawing and rolling deformation methods and *in situ* reaction. The effects of the precursor milling energy and carbon doping on the microstructural homogeneity and critical currents of these conductors have been investigated. Combined magneto-optical, microstructural and magnetization measurements in tapes made from differently milled precursors have been performed in order to correlate their local and global critical current densities with microstructural observations.

- The second part explores the development of an industrially scalable process to texture $Bi_2Sr_2CaCu_2O_{8+x}$monoliths. This scale-up covers from the synthesis of the precursor powders, the laser texturing method to the final heat treatment required to obtain the superconducting phase.

Bibliography

[1] Gavaler, J. R., "Superconductivity in Nb–Ge films above 22 K", *Appl. Phys. Lett.* **23**, 480 (1973).

[2] Berlincourt, T. G., Hake, R. R., "Pulsed-magnetic-field studies of superconducting transition metal alloys at high and low current densities", *Bull. Am. Phys. Soc.* **7**, 408 (1962).

[3] Matthias, B. T., Geballe, T. H., Geller, S., Corenzwit, E., "Superconductivity of Nb_3Sn", *Phys. Rev.* **95**, 1435 (1954).

[4] Bednorz, J. G., Müller, K. A., "Possible high T_c superconductivity in the Ba-La-Cu-O system" *Z. Phys. B* **64**, 189 (1986).

[5] Sun, G. F., Wong, K. W., Xu, B. R., Xin, Y., Lu, D. F., "T_c enhancement of $HgBa_2Ca_2Cu_3O_{8+\delta}$", *Phys. Lett. A* **192**, 122 (1994).

[6] Dai, P., Chakoumakos, B. C., Sun, G. F., Wong, K. W., Xin, Y., Lu, D. F., "Synthesis and neutron powder diffraction study of the superconductor $HgBa_2Ca_2Cu_3O_{8+\delta}$ by Tl substitution", *Physica C* **243**, 201 (1995).

[7] Gao, L., Xue, Y. Y., Chen, F., Xiong, Q., Meng, R. L., Ramirez, D., Chu, C. W., Eggert, J. H., Mao, H. K., "Superconductivity up to 164 K in $HgBa_2Ca_{m-1}Cu_mO_{2m+2+\delta}$ ($m = 1$, 2, and 3) under quasihydrostatic pressures", *Phys. Rev. B* **50**, 4260 (1994).

[8] Maeda, H., Tanaka, Y., Fukutomi, M., Asanao, T., "A new high-T_c oxide superconductor without a rare earth element", *Jpn. J. Appl. Phys.* **27**, L209 (1988).

[9] Wu, M. K., Ashburn, J. R., Torng, C. J., Hor, P. H., Meng, R. L., Gao, L., Huang, Z. J., Wang, Y. Q., Chu, C. W., "Supercon-

ductivity at 93 K in a new mixed-phase Y-Ba-Cu-O compound system at ambient pressure", *Phys. Rev. Lett.* **58**, 908 (1987).

[10] Kamihara, Y., Hiramatsu, H., Hirano, M., Kawamura, R., Yanagi, H., Kamiya, T., Hosono, H., "Iron-based layered superconductor: LaOFeP", *J. Am. Chem. Soc.* **128**, 10012 (2006).

[11] Ge, J. F., Liu, Z. L., Liu, C., Gao, C. L., Qian, D., Xue, Q. K., Liu, Y., Jia, J. F., "Superconductivity above 100 K in single-layer FeSe films on doped $SrTiO_3$", *Nat. Mat.* **14**, 285 (2014).

[12] Drozdov, A. P., Eremets, M. I., Troyan, I. A., Ksenofontov, V., Shylin, S. I., "Conventional superconductivity at 203 kelvin at high pressures in the sulfur hydride system", *Nature* **525**, 73 (2015).

[13] Larbalestier, D. C., Gurevich, A., Feldmann, D. M., Polyanskii, A., "High-T_c superconducting materials for electric power applications", *Nature* **414**, 368 (2001).

[14] Hull, J. R., Murakami, M., "Applications of bulk high-temperature superconductors", *Proc. IEEE* **92**, 1705 (2004).

Part I

Study of global and local superconducting properties of MgB_2 wires enhanced by milled and doped precursors

Chapter 2

Introduction and motivation

2.1 Current status of MgB_2 conductors

The discovery of superconductivity in MgB_2 by Nagamatsu *et al.* in 2001 [1], evoked great interest in the superconducting community. Its critical temperature of ~39 K, simple crystal structure and high critical current densities made soon this material very promising for technological applications.

Compared to LTS, the main advantage of MgB_2 is its higher T_c because it allows operation temperatures around 20 K, which implies lower operating cost than LTS devices, usually working at temperatures below 5 K, and enhanced thermal stability. Therefore, no liquid helium (with a boiling temperature of 4.2 K at atmospheric pressure) is required, making systems safer, easier to design, more compact and less expensive, both in production and maintenance. Liquid neon could be interesting for MgB_2 cooling due to its boiling temperature, 27 K, but it is quite rare and expensive (more than 50 times of liquid helium) and therefore is not suitable for its extensive use in commercial applications. Liquid hydrogen, with boiling temperature of 20 K at 1 bar, has been proposed as a promising cooling alternative in future. Although safety precaution requirements complicate a wide-spread use in certain laboratory and industry environments and leave closed circuit refrigerators (cryocoolers) as the preferred cooling option for MgB_2 devices at present.

Compared to HTS, the starting materials of MgB_2 are cheap and abundant and the manufacturing methods significantly cheaper. This is because MgB_2 has a low anisotropy γ and thus expensive texturing methods to achieve bulks and wires with good superconducting properties are not required as for HTS. Moreover, critical currents in MgB_2 are not limited by weak-links as in HTS, and clean grain boundaries are possible. Nonetheless, it must be remarked that the presence of secondary phases at the grain boundaries, like magnesium or boron oxides, could reduce the $J_c(H)$ values significantly and should be avoided. The cost of HTS conductors is still very high and therefore MgB_2 would be preferable for certain applications despite the penalty of lower operating temperatures imposed by its lower T_c. Moreover, superconducting joints between MgB_2 wires have been successfully developed [2], which is a significant advantage with respect to HTS conductors.

MgB_2 wires and HTS coated conductors require some technological advances for their commercial use, such as reliable long length manufacturing, improved J_c values and enhanced conductor homogeneity. Moreover, a significant decrease of the conductors cost, which is usually measured in terms of cost/performance ratio (in €/kAm) is compulsory. Important efforts are being made nowadays to achieve these objectives.

Many ways to optimise the superconducting properties of MgB_2 materials have been searched. Up to now, doping and grain size reduction have been proven to be the most successful ways to increase H_{irr}, H_{c2} and $J_c(H)$ at high magnetic fields, as it will be reviewed in more detail in sections 2.2 and 2.3.

In terms of superconducting performance, MgB_2 can challenge commercial LTS, i.e. NbTi and Nb_3Sn, in the temperature operation range of 15-30 K. Most applications require a flexible conductor architecture and MgB_2 can be manufactured with different shapes such as round or squared wires and tapes. It can be a competitive conductor for low field applications, such as superconducting transformers [3], motors [4] and generators [5]. There are also moderate field applications in which MgB_2 conductors can be potentially used, for example, adiabatic demagnetization refrigerators, superconducting magnetic separators and magnetic energy storage (SMES) devices [6] and even in magnetic levitation [7]. Also high energy applications, such as high current busbars to feed the high-field magnets, currently in developement at CERN [8], are target applications for MgB_2 conductors. Tomsic *et al.* [9] present a general overview of possible applications.

MgB_2 offers an interesting perspective for new magnetic resonance imaging (MRI) systems, specifically toward the development of liquid-helium-free MRI. Although NbTi is well-established and still remains the MRI manufacturer's choice, due to the continuous rising cost and supply difficulties of helium, growing interest has been shown in MgB_2-based systems. A model of cryogen-free MgB_2-based MRI is already commercialized by Paramed Srl with 0.5 T central field magnet operating at 18 K [10].

In particular, superconducting MgB_2 conductors must fulfill some requirements for their use in applications. The need to ensure good thermal and electrical stability for quench protection, usually requires multifilamentary conductors made of a certain number of metallic sheathed monocore MgB_2 wires embedded in a metal matrix encompassing different architectures. Both metallic sheath and matrix need to provide an adequate thermal stability and good mechanical properties to the conductor. Copper is usually used as metal matrix to achieve the required thermal stability due to its high thermal and electrical conductivity. On the other hand, the outer sheath is usually made of nickel, monel or another alloys in order to increase the mechanical strength. Finally, to act as diffusion barrier, the metal sheath surrounding the MgB_2 cores has to be inert, i.e. not reactive with Mg, B or MgB_2. Both Mg and MgB_2 tend to react with many metals such as Al, Cu, Ag [11], etc. There are some elements that are inert or less reactive, for example Fe, Nb [12, 13], Ti [14], Mo, Nb, V, Ta, Hf and W. Among these, the refractory metals (Mo, Nb, V, Ta, Hf, W) have inferior ductility and higher price compared to Fe, and consequently Fe is among the most appropriate sheath material for MgB_2 wire and tape fabrication. Nb and Ti have also been widely used as diffusion barriers. Some multifilamentary MgB_2 wires and tapes commercialized by Columbus Superconductors and Hyper Tech Research are displayed in Figure 2.1.

Another important fulfilled requirement of MgB_2 for practical applications is that MgB_2 conductors can be available in long lengths (of few kilometres) [15], which is industrially achievable by several methods. Among those, the powder-in-tube (PIT) technique was primerly used by Glowacki *et al.* [16] and has been widely used since then. More recently the internal Mg diffusion

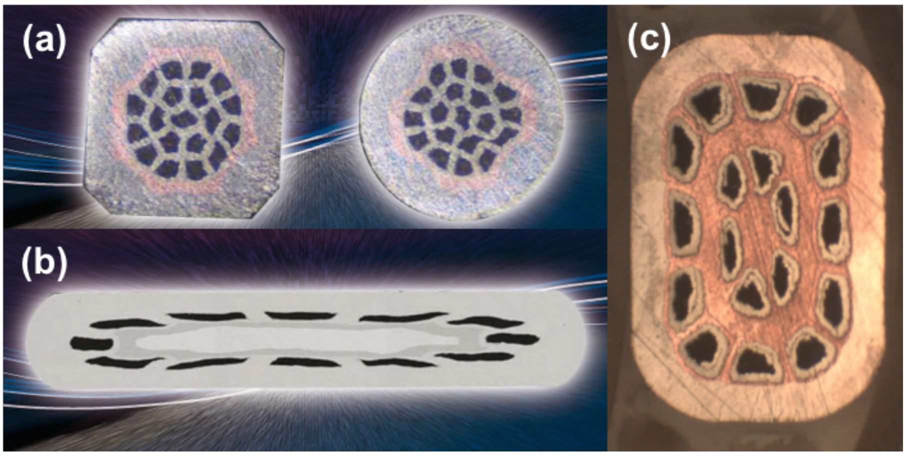

Figure 2.1: Cross-sections of commercial MgB_2 multifilamentary conductors with diverse architectures: (a) 19-MgB_2-filaments inside a Cu ring with monel external sheath and (b) 12-filaments surrounding a Fe+Cu core with Ni external matrix, are commercialized by Columbus Superconductors. (c) 18-filaments surrounded by Nb barrier, with Cu matrix for stabilization and monel outer sheath, from Hyper Tech Research.

(IMD) process, originally proposed by Giunchi *et al.* [17], has also generated great interest.

A diagram of the PIT method is displayed in Figure 2.2. In this technique, a metallic tube is filled with either reacted MgB_2 powders, so called *ex situ* route, or a mixture of raw Mg and B powders that will eventually form the superconducting phase, known as *in situ* route. After filling the metal tube with those precursor powders, it is sealed and deformed to a thinner wire by means of different mechanical deformation processes such as swaging, drawing or groove rolling. Once obtained the monocore wires, these are inserted into another metallic tube and then deformed again to the desired final shape and dimensions to form a multifilamentary wire or tape, which is finally heat treated to form the MgB_2 phase (*in situ* route) or to sinter the prereacted MgB_2 grains (*ex situ* route) [18].

A scheme of the IMD process [19] is displayed in Figure 2.3. A pure Mg rod is embedded axially in a B-powder filled metal tube prior to mechanical deformation. Then, some wires are bundled together as with the PIT method to form multifilamentary wires. The superconducting MgB_2 phase is formed

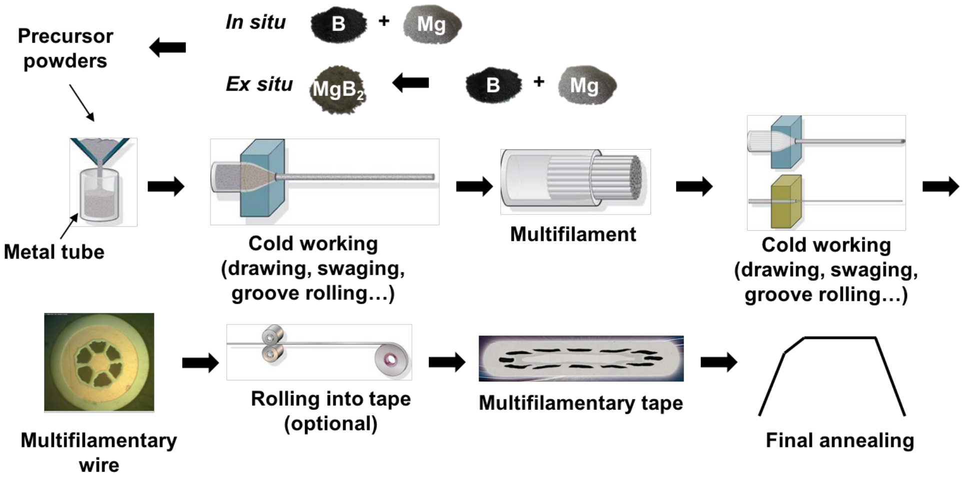

Figure 2.2: Draft of the different steps used in the PIT technique to produce mulfilamentary MgB_2 wires or tapes for both *in situ* and *ex situ* routes.

during an annealing process in which the Mg diffuses into the B powders to form a very dense layer of superconducting phase, typically <100 µm thick, leaving a hole at the centre of each filament where the Mg rod was located before the reaction. This resultant MgB_2 layer has a very high density close to 100 %, much higher than that of wires fabricated using the PIT technique because the porosity associated with the Mg powder sites produced during the annealing is eliminated [20,21]. Thus, this dense MgB_2 layer presents excellent $J_c(H)$ values, higher than for wires fabricated with other techniques. It must be noted, that due to the central hole in IMD-processed wires, there is a large difference between J_c and J_e, which is the relevant parameter for the device designer. Despite this drawback, high J_e values have already been obtained by this method and intense research is under way by several research groups to optimise the process [19]. The scale-up from laboratory to industrial implementation in order to achieve wires of several km length is challenging, since the Mg rod should be in the centre with a very uniform B powder distribution around it. Small misalignments of the Mg rod in the initial composite wire way produce significant J_e inhomogeneities along the final wire.

Regarding the PIT technique, both *in situ* and *ex situ* routes present various advantages and drawbacks, as Braccini *et al.* [22] discuss. The *ex situ* route is suitable for long multifilamentary wires and tapes as it allows a better

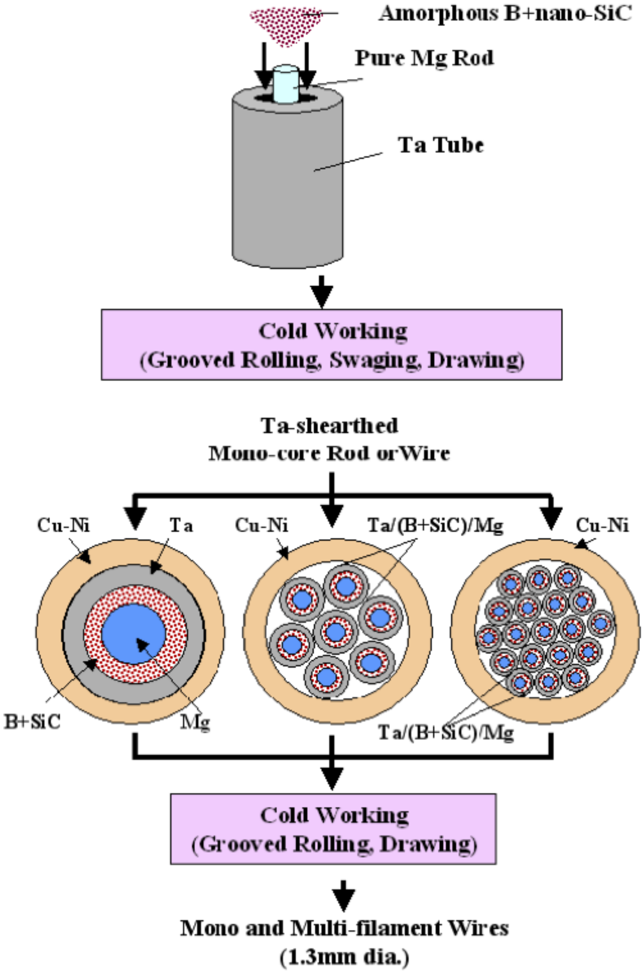

Figure 2.3: A scheme of the IMD process followed by Togano *et al.* [19] to obtain single-, 7- and 19-filament wires.

control of the powder granulometry and purity degree of the MgB_2, making easier to maintain homogeneity over very long lengths and thus resulting more attractive for the industrial applications. But *ex situ* samples require a heat treatment for sintering in order to improve the grain connectivity and $J_c(H)$, which induces a recrystallization that decreases H_{c2}. On the other hand, *in situ* route seems to be more promising due to its lower cost, high speed processing, lower reaction temperatures and greater ease of doping. However, the main concern of this route is to obtain homogeneous and dense samples. The final density of *in situ* wires has been estimated to be about 50 % of the theoretical value [23], compared to the 70-80 % of *ex situ* wires [24]. It must be noted that the B and Mg precursors individually have a higher density than MgB_2, and thus the formation of the superconducting phase theoretically leave a ∼23 % of empty space with respect to the initial volume occupied by the precursors [25]. Another problem for industrial manufacture of MgB_2 wires or tapes using the PIT technique comes from the hardness and brittleness of used precursors and metallic sheaths, making drawing or rolling processes with very fine filaments difficult [26].

Some techniques have been developed to increase the mass density and grain connectivity of MgB_2 wires improving both the $J_c(H)$ and $J_e(H)$ performance, being the most relevant the Cold High Pressure Densification (CHPD) technique developed by Flükiger *et al.* in 2009 [24] which allows an increase of the *in situ* PIT mass density from 43 % to 73 % of MgB_2 theoretical one. It is based in the room temperature (RT) application of pressures up to 6.5 GPa using solid anvils acting simultaneously on all the sides of a squared wire, followed by a preassure release that allow a recovery of the wire without damage, and prior to the heat treatment. This method achieved a considerable enhancement of both $J_c(H)$ and H_{irr} values [24, 27].

2.2 Doping of MgB_2

Doping MgB_2 process has been widely searched to optimise $J_c(H)$ values for technological applications. There are three main doping strategies:

- By introducing elements or compounds that partially substitute the B or Mg atoms inducing both strain and defects in the crystalographic lattice, as well as changes in the densities of the electronic conduction bands. This may produce an enhancement of the flux pinning reflected on the $H_{irr}(T)$ improvement, an increase of the $H_{c2}(0)$ value [28] but also results in a lower T_c.
- By introducing nanoparticles that act as pinning centers and therefore increase flux pinning and $J_c(H)$.
- By introducing elements or compounds that reduce the oxygen content in MgB_2 thus reducing the insulating MgO phase that tends to reduce grain

connectivity and $J_c(H)$. As a consequence, a purer superconducting MgB_2 is obtained. Another related possibility is to introduce elements or compounds that reduce grain boundary contamination and improve connectivity.

Many substitutions of Mg and B by other element and the adittion of different compounds have been tried as reviewed by Eisterer [23] and Collings *et al.* [29].

When using metallic elements as dopants, those who are magnetic (Mn, Fe, Co, Ni, etc) tend to decrease pinning or even supress superconductivity. However, other metallic elements such as Ti, Zr [30], Ag [31], Si [32] and La [33] seem to form nano-sized compounds, either with B or Mg, which favour pinning. For example Shekhar *et al.* [31] have reported an improvement of $J_c(H)$ when a 10 % atomic Ag addition is performed in MgB_2 bulk samples.

Another attempt to create nano-pinning centres has been followed using metal oxides as dopants. Typically these materials are decomposed during the heat treatments required to form the MgB_2 phase and recombine either producing nano-sized B-compounds and MgO (for Y_2O_3 [34], Dy_2O_3 [35], HoO_2 [36] and Pr_6O_{11} [37]), or substituting Mg in the lattice (for Al_2O_3 [38] and SiO_2 [39]), or remaining as nanoparticles (for example TiO_2 [40]). It seems that the presence of nano-sized MgO grains in low quantities can improve pinning [41]. These nano-MgO are formed when oxygen is released due to decomposition of the added nano-oxide particles during annealing. Therefore, there are serious limitations on the amount of metal-oxide dopants that can be added without decreasing T_c and $J_c(H)$.

Also inorganic compounds from nitrides, such as Si_3N_4 [42], silicides, such as WSi_2 and $ZrSi_2$ [43], and borides, such as ZrB_2, TiB_2, NbB_2 [44] and WB [45], families have been used for doping MgB_2. Best results to increase $J_c(H)$ have been obtained when these compounds are in the nano-size range [41]. However, further research in the pinning mechanisms and chemistry involved is required.

Carbon doping of MgB_2

In order to increase the amount of strain in the lattice, pure carbon allotropes and C-rich compounds have been extensively used for doping MgB_2 [46] . C randomly substitutes B in the graphite-like honeycomb sub-lattice formed by B atoms, thus introducing defects that act as pinning centres. In addition, $Mg(B_{1\text{-}x}C_x)_2$ compounds are isostructural in a wide range of compositions therefore C atoms increase lattice disorder and tend to decrease grain size [47]. The overall result is an increase of J_c values, mainly at high fields.

Carbon doping has been obtained by addition of many different C rich sources: solid and liquid, pure carbon and compounds (either organic or inorganic), powders and nano-particles. The most relevant are detailed next.

As a figure-of-merit to compare the effect of the different types of doping, the value of the magnetic field at which $J_c = 1 \times 10^4\,\mathrm{A\,cm^{-2}}$ at 4.2 K has normally been used.

Addition of pure carbon allotropes

Different pure carbon allotropes have been used for doping MgB_2, most notably graphite [48–51], nanodiamonds [52–54], C-nanoparticles [55, 56], C-nanotubes [57–60], fullerene [61] and graphene [62]. No matter in which form, pinning is enhanced and consequently $J_c(H)$ performance is improved. However, this does not occur only by C-substitution but also due to the formation of nano-sized inclusions, coming from the non-reacted dopant introduced. Typically, the amount of C introduced in the lattice depends both on the sample annealing temperature and on the reactivity of the dopant (higher for nanoparticles and nanotubes, lower for nanodiamonds and graphite powders).

Best results achieved so far are for nano-sized fullerene (C_{60}, $\sim$0.71 nm) doping with $J_c(H)$ value at 4.2 K of $1 \times 10^4\,\mathrm{A\,cm^{-2}}$ at 14 T [61]. Good results have also been obtained by Xu *et al.* using graphene, although with lower $J_c(H)$ value of $1 \times 10^4\,\mathrm{A\,cm^{-2}}$ at 5 K and 9.2 T [62].

Addition of carbon rich inorganic compounds

The addition of nano-SiC particles was firstly proposed by Dou *et al.* [63] to improve the pinning force and $J_c(H)$ values of MgB_2 bulk and wires, reaching high $J_c(H)$ values of $1 \times 10^4\,\mathrm{A\,cm^{-2}}$ at 12 T and 4.2 K. Later on, many research groups confirmed this improvement in the performance of these materials [64–70]. To understand the mechanisms for such enhancement, Dou *et al.* proposed a model in which fresh and highly reactive C is released from SiC at low temperatures, 600 °C, when reacting with Mg to form Mg_2Si and Mg_2SiO_4, thus introducing C-atoms in the B-sites and increasing H_{c2} [71]. Besides, the resultant products, including the mentioned Mg_2Si and the excess of nano-sized C particles, can be embedded into the MgB_2 matrix and act as pinning centres.

The addition of submicron-sized inorganic compounds, such as carbides and carbonates: TiC or Mo_2C [72], NbC [73], Na_2CO_3 [74] or B_4C [75, 76] have also been found to influence the MgB_2 microstructure, either by decreasing grain size or by increasing densification.

It must be remarked that nano-sized dopants are required in order to increase flux pinning [77].

Addition of carbohydrates

Another used solid source of fresh C have been inexpensive carbohydrates, such as sugar [78, 79], glucose ($C_6H_{12}O_6$) and sucrose ($C_{12}H_{22}O_{11}$) [80]. In both cases, B is coated with the carbohydrate via wet route and then gathered with Mg prior sample fabrication. It has been found to increase MgO and C impurities content but also a substantial enhancement of $J_c(H)$ at high fields, with J_c value of $1 \times 10^4\,\mathrm{A\,cm^{-2}}$ at 5 K and 10 T for sugar addition [79], figure-of-merit similar to those accomplished with C-nanotubes and C-nanoparticles.

Addition of aromatic hydrocarbons, ketones and alcohols

The addition of aromatic hydrocarbons, ketones and alcohols were initially used as liquid media for wet ball milling processes in order to introduce C in the MgB_2 lattice. Rather scarce success was obtained for acetone (C_3H_6O), ethanol (C_2H_6O) and glycerine ($C_3H_8O_3$), which results in a decrease of $J_c(H)$ values, probably due to the presence of oxygen in the compound that increases the presence of MgO and B_2O_3 impurities.

However, the aromatic hydrocarbon toluene (C_7H_8) was proven to be a useful media for wet ball milling and produced an increase in $J_c(H)$ values due to grain refinement in comparison with pure samples [81]. Good results have been obtained for other aromatic hydrocarbons used for wet ball milling such as benzene (C_6H_6), naphthalene ($C_{10}H_8$), thiophene (C_4H_4S), ethyltholuene (C_9H_{12}) and xylene (C_8H_{10}), achieving $J_c(H)$ value of $1 \times 10^4\,\mathrm{A\,cm^{-2}}$ at 4.2 K and 10.5 T [82, 83].

For other solid at RT polycyclic aromatic hydrocarbons, such as coronene ($C_{24}H_{12}$) and pyrene ($C_{16}H_{10}$), similar results in terms of $J_c(H)$ performance have been obtained with values of $1 \times 10^4\,\mathrm{A\,cm^{-2}}$ at 4.2 K and 11.5 T [84–86]. It is believed that their greater C content, in terms of atomic weight, and their decomposition temperatures in the range of MgB_2 formation favour C doping, and thus enhance flux pinning. Excellent results were obtained by Yamada *et al.* [87] using ethyltholuene in combination with SiC (10 mol% each) and wet ball milling of the precursor powders. Thus, the C content in MgB_2 was increased in comparison with SiC doping alone and also the grain size was slightly reduced as a consequence of ball milling, improving flux pinning and $J_c(H)$ dramatically up to $1 \times 10^4\,\mathrm{A\,cm^{-2}}$ at 4.2 K and 13.5 T although T_c decreased down to 32.5 K. Main concern about aromatic hydrocarbons is their inherent toxicity. Besides mutagenic and carcinogen effects they can also produce pulmonar, gastrointestinal, renal and dermatological issues, so they have to be carefully handled and specific safety precautions are required when manipulating them.

Addition of carboxylic acids

The addition of different carboxylic acids with MgB_2 has been proposed not only for doping purposes but also for MgO removal. One example of the latter is acetic acid ($C_2H_4O_2$), which was used for washing *ex situ* MgB_2 powder with good results, as MgO content diminished, but no appreciable

C doping was observed [88]. Many other carboxylic acids have been used as a source of fresh C, such as citric ($C_6H_8O_7$), oxalic ($C_2H_6O_5$) [89], malic ($C_4H_6O_5$) [90–92], glycolic ($C_2H_4O_3$) [93], tartaric ($C_4H_6O_6$) [94], and stearic acids ($C_{18}H_{36}O_2$) [95–97] as well as maleic anhydride ($C_4H_2O_3$) [98]. Typically the doped precursor powders are subjected to different degrees of milling to homogenize them and the substitution of B lattice sites by C atoms is estimated to be at least one order of magnitude lower than the total amount of carbon added to the precursor powders. Kim *et al.* [90] point out that C doping occurs via nano-width coating of B grains when the fresh C is released during the decomposition of carboxylic acids. In particular, good results have been found when doping with stearic acid and maleic anhydride achieving $J_c(H)$ values at 4.2 K of $1 \times 10^4\,\mathrm{A\,cm^{-2}}$ at 12 T and 12.3 T respectively [95,98], comparable to those obtained by nano-C and nano-SiC additions.

From the previously mentioned alternatives, a compilation of the most effective C dopants, to increase J_c at high fields and low temperatures (4.2 K), is presented in Table 2.1. From there, one can conclude that the best results so far have been obtained when doping with pure carbon alone, in particular with nano-sized fullerene, obtaining a value of $J_c = 1 \times 10^4\,\mathrm{A\,cm^{-2}}$ at 14 T and 4.2 K.

Dopant	*Magnetic Field*	*Reference*
Nano-C_{60}	14 T	[61]
Nano-SiC	12 T	[63]
Ethyltholuene and nano-SiC	13.5 T	[87]
Stearic acid	12 T	[95]
Maleic anhydride	12.3 T	[98]

Table 2.1: Comparison of the magnetic field values at which $J_c = 1 \times 10^4\,\mathrm{A\,cm^{-2}}$ at 4.2 K, obtained for some of the most effective dopant additions.

Main drawbacks of many C-doped MgB_2 materials are related to the impurities formation that can act as pinning centres but can also deteriorate $J_c(H)$ values at low fields (i.e. grain connectivity) and decrease T_c. The essential concern about nano-dopants is the possible formation of dopant agglomerations and inhomogeneities within the sample. The core advantages of using liquid C sources is that they can be combined with milling in order to avoid agglomerations and obtain a good homogenization of the dopant in the MgB_2 matrix.

2.3 Ball milling of MgB_2 precursors

Another possible way for improving flux pinning and consequently $J_c(H)$ in MgB_2 is by grain refinement through ball milling [22, 99]. The inversely proportional relation between grain size and flux pinning has been well stablished in the literature [100–102]. This is because lower grain sizes imply larger boundary surface and, hence, higher $J_c(H)$ values. MgB_2 grain size is heavily influenced by precursor powder grain size, particularly B one. Ball milling of the precursors reduces the grain size and enhance $J_c(H)$.

In particular, high energy ball milling, which is a solid-state powder processing technique also known as mechanical alloying [103], produces a very fine grain with a fraction of the precursor powders already reacted to form MgB_2 [104]. Also excellent $J_c(H)$ values were found (as high as $1 \times 10^4\,\mathrm{A\,cm^{-2}}$ at 4.2 K and 12.1 T and 16.4 T for non-doped and nano-sized C doped *in situ* PIT samples, respectively) as a result of boundary pinning [105, 106] and relatively low sensitivity against oxidation in air [107]. These values are not only comparable but greater than those obtained by simply doping, thus proving the utility of this method to reduce grain size increasing flux pinning and $J_c(H)$, and even to introduce dopants in the MgB_2 matrix.

Ball milling may present some technical issues that should be taken into account, such as difficulties during wire drawing, or mechanical conformation problems (shear bands, narrowing and even wire fracture) that can make hard to obtain long wires.

Ball milling of the precursor powders may be applied both to *in situ* and *ex situ* routes. For the latter, good results have been obtained in bulk samples, processed by hot isostatic pressed (HIP) pellets [108–110], and PIT wires [26, 99, 111–114]. In particular, using ball milled C-doped HIP bulks Senkowicz *et al.* [115] found that flux pinning is more influenced by grain refinement than by grain connectivity, which is a weak function of milling time, while T_c typically decreases when increasing ball milling time. They also found that despite of full C introduction achieved within short milling times (30-60 min), further increase of milling time reduces grain size down to ∼20 nm enhancing J_c up to 1×10^4 A cm^{-2} at 4.2 K and 14 T [116]. Very similar results have been obtained for C-doped *ex situ* PIT tapes with $J_c(H)$ values of 1×10^4 A cm^{-2} at 4.2 K and 13 T [22].

Regarding the *in situ* route, bulk samples made from ball milled powders have been obtained from HIP [104, 117–119] and cold isostatic press (CIP) [120–122]. Best results has been reported by Perner *et al.* for ball milled SiO_2 and MgO doped HIP bulk samples with a J_c of 1×10^4 A cm^{-2} at 10.3 T and 7.5 K [123]. Some authors have also studied the influence of Mg stoichiometry in the superconducting properties of ball milled HIP bulks and found better behaviour for those samples with an excess of Mg [124]. Experiments on trapped magnetic field by bulk samples have been performed on ball milled HIP [125] and CIP pellets [126], with good results, specifically in the latter with J_c value of 1×10^4 A cm^{-2} at 5 K and 9.5 T.

PIT wires made from ball milled *in situ* precursors have been investigated by several groups [105, 106, 127–129]. It is worth mentioning that J_c values of 1×10^4 A cm^{-2} at 4.2 K and $9.5 - 10$ T have been reported by different groups [130, 131].

At greater (industrial) scales, issues related to ball milling precursor powders can appear and some authors have studied the possible implications [132].

In conclusion, the ball milling technique is a powerful instrument to increase flux pinning by decreasing grain size, specially when used in combination with somekind of doping. The best results obtained so far have been compiled in Table 2.2. In particular, Herrmann *et al.* obtained excellent results for ball milled nano-sized C-doped *in situ* PIT samples with $J_c > 1 \times 10^4$ A cm^{-2} in magnetic fields < 16.4 T at 4.2 K [106]. This value broadly exceeds the best result obtained with C doping alone (see Table 2.1), thus confirming the crucial role of ball milling in the enhancement of $J_c(H)$.

Method	*Magnetic Field*	*Temperature*	*Ref.*
C-doped *ex situ* PIT	13 T	4.2 K	[22]
Non-doped *in situ* PIT	12.1 T	4.2 K	[105]
C-doped *in situ* PIT	16.4 T	4.2 K	[106]
C-doped *ex situ* HIP	14 T	4.2 K	[116]
Oxides-doped *in situ* HIP	10.3 T	7.5 K	[123]

Table 2.2: Compilation of the magnetic field value when $J_c = 1 \times 10^4\,\mathrm{A\,cm^{-2}}$ for different ball milling treatments of the precursor powders.

2.4 Objectives and motivation

As previously mentioned, C doping is unambiguously the most effective way of improving the superconducting properties of MgB_2. Best results have been obtained when doping *in situ* powders, since this route facilitates the C incorporation into the MgB_2 lattice during the superconducting phase formation. With potential industrial applications in mind, non-toxic nor harmful C dopants are preferred as they are easier to handle and more practical to use. Liquid C sources would be advantageous in order to avoid particle agglomerations and to achieve a better distribution of the dopant within the precursor powders for a more efficient doping.

In this regard, Devener *et al.* showed that oleic acid ($C_{18}H_{34}O_2$) binds efficiently to fresh unoxidized boron surfaces via B-O-C bond formation thus providing an effective barrier to air oxidation [133]. Also, oleic acid surfactant coatings provide chemical stability to magnetic nanoparticles which easily oxidize such as Co, Ni, Fe and FePt [134]. Since oleic acid (Figure 2.4) is a fatty acid present in animal and vegetable fats and oils, also present in human diet, it is completely safe. Moreover, it is liquid at RT and has high C vs O ratio ($r_{CO} = 9$), which can be advantageous in order to avoid the formation of secondary phases. Thus, the addition of oleic acid as C source fulfills the advantages of best inorganic liquids for carbon substitution of boron in MgB_2 conductors [135, 136].

On the other hand, ball milling would be an extraordinary efficient tool for controlling the MgB_2 microstructure, for achieving a better homogeneity of both the precursor powders and the different dopants, but also for reducing

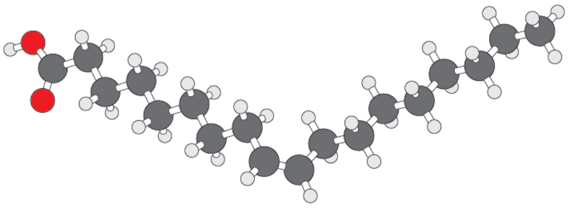

Figure 2.4: Representation of the oleic acid molecule. C atoms are pictured in black, H atoms in white and O atoms in red.

grain size to enhance flux pinning and $J_c(H)$ performance at higher magnetic fields. Still, it must be carefully applied in order to avoid damaging $J_c(H)$ values at low magnetic fields.

The objective of this work is to analyse the effect of ball milling parameters and the addition of oleic acid addition on the properties of superconducting wires made by PIT method. The ultimate intention is to find the optimum conditions for milling and C doping to achieve homogeneous wires with controlled microstructure and high $J_c(H)$ values. This work has been focused on monocore Fe-sheathed MgB_2 wires made by the *in situ* route.

The chapters in which this part is structured are detailed below:

- Chapter 3 covers the whole wire manufacture process, from the starting precursor powder preparation to the wire manufacture by PIT technique and the final thermal treatment to obtain the superconducting phase.
- Chapter 4 studies and compares the influence of ball milling parameters on the microstructure and the superconducting properties of the wires: $J_c(H)$ and T_c.
- Chapter 5 analyses the combined effect of ball milling and oleic acid addition on the microstructure and superconducting properties of MgB_2 wires.
- Chapter 6 focuses on magneto-optical (MO) imaging experiments used to analyse the spatial distribution of magnetic flux inside the samples. Using MO imaging and field-emission scanning electron microscopy (FE-

SEM), the local superconducting properties have been correlated with the microstructural observations. Besides, MO images are a very powerful tool to analyse the homogeneity of the wires and understand J_c global values obtained with magnetic and transport measurements.

- Finally the main conclusions drawn from this part are presented in Chapter 7.

Chapter 3

Manufacture of MgB_2 wires and tapes

In this chapter the full wire manufacturing process of Fe-MgB_2 monocore wires is detailed. Beginning with the *in situ* precursor powder preparation, through the PIT and wire drawing to the final annealing.

3.1 Precursor powder preparation

The precursor powders used as starting materials were commercial Mg powders (99.8 %, Goodfellow, maximum particle size of 250 µm) and amorphous B powders (99 %, New Metal & Chemicals Ltd., mean particle size lower than 1 µm). In most cases the stoichiometry proportion Mg:B 1:2 was used. In some wires a slight Mg excess (1.05:2) was used in order to compare with stoichiometric wires.

A scheme of the three different precursor powder preparation routes used in this work is displayed in Figure 3.1. Oleic acid (99 %, Alfa Aesar, $C_{18}H_{34}O_2$) was used as a C source. The initial addition of oleic acid was always 10 wt.% of the total Mg+2B mass. Three different routes were used. Route 0 was used to prepare non-doped precursors for the wires, while routes 1 and 2 are used as precursor preparation to obtain C-doped wires, using two different procedures as described next.

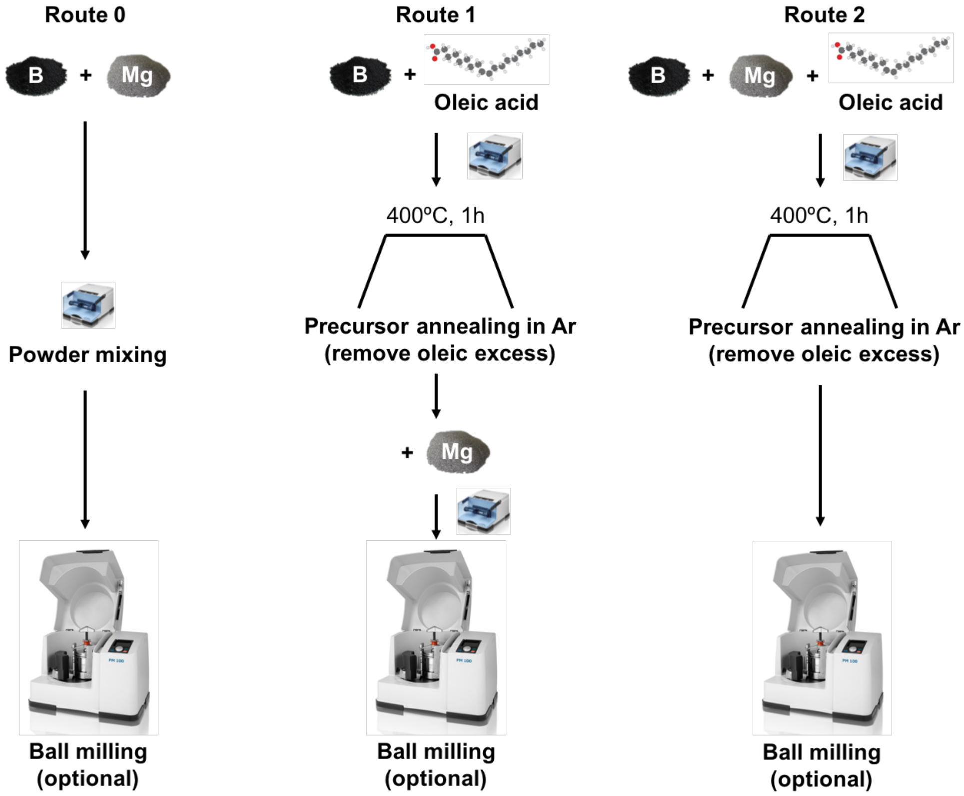

Figure 3.1: Scheme of the three different routes of precursor powder preparation used in this work.

- **Route 0** - This is the non-doped route in which the Mg and B precursors are mixed together in a Retsch MM2000 mixer mill. Subsequently, these powders are ball milled.

- **Route 1** - In this route B powders are mixed with oleic acid in a Retsch mixer. Afterwards, this initial mixture is placed in a folded iron foil (99.5 %, Goodfellow, 0.038 mm of thickness) inside a tubular furnace and preheated at 400 °C for 1 h for oleic acid pyrolysis. This is done in an underpressured Ar atmosphere (∼500 mbar at RT, to avoid oxidation and possible overpressure when heating the Ar). The resulting powders are then mixed with Mg powders in the Retsch mixer. Finally the precursors are ball milled.

- **Route 2** - An initial mixture of Mg and B is mixed in a Retsch mixer. After that, the oleic acid is added to the mixture and mixed again in the same mixer. Then, the pryolysis of the oleic excess is carried out by heating the mixture at 400 °C during 1 h, as in Route 1. Finally, the precursor powders are ball milled.

In all cases, when using the Retsch mixer, a treatment of 30 minutes in air in three steps of 10 min was used.

Three precursor batches were prepared with routes 0, 1 and 2, but without the final ball milling process, to manufacture the corresponding reference wires with non-milled precursor powders.

The precursor powders were ball milled using a planetary ball mill Retsch PM 100, which has a sun disk of radius $r_p = 7\,\text{cm}$. The tungsten carbide (WC) jar, of inner radius $r_v = 5.25\,\text{cm}$, was designed to be able to perform the milling in a controlled atmosphere. Specifically, 1.5 bar pressure of Ar inside the jar was used to avoid any possible air filtration during milling and thus to minimize the oxidation of the precursor powders. The WC ball-to-powder mass ratio, β, was always kept at ~ 36. Typically we prepared $\sim 3\,\text{g}$ of Mg and B mixture for each wire, so that we used 14 WC balls with a radius $r_b = 5\,\text{mm}$.

The energy per unit mass transferred to the powder by ball milling, E_t/m, is a useful parameter to analyse the milling effects. There are different approaches to determine E_t/m. In this work we have used the formula developed in [137], which depends explicitly on the milling parameters as:

$$\frac{E_t}{m} = c\beta\frac{(\omega_p r_p)^3}{r_v}t, \tag{3.1}$$

where ω_p is the angular frequency, c is a dimensionless constant of the order of magnitude of 0.1, m is the powder mass and t is the milling time. Thus, considering only the parameters that are not part of the milling device, E_t/m is directly proportional to β, t, and to the cube of ω_p.

In order to avoid mechanical alloying, in most cases, the powders were milled changing the rotation sense every 3 min with 1 min of pause in between. With this protocol we avoid creating local heating that may lead to MgB_2 formation. Some tests were carried out following the same procedure but without the 1 min pause. For the manufactured wires, different milling conditions were used. They are collected in Table 3.1. The effective ball milling times range from 1.5 h up to 16.5 h, and ω_p values range from 200 rpm to 400 rpm, giving E_t/m values from $1.2 \times 10^6\,\mathrm{J\,kg^{-1}}$ to $1 \times 10^8\,\mathrm{J\,kg^{-1}}$.

Milling Condition	t(h)	ω_p(rpm)	$E_t/m(\mathrm{J\,kg^{-1}})$
M1	1.5	200	1.2×10^6
M1	4	200	3×10^6
M3	3	400	2×10^7
M4	16.5	400	1×10^8

Table 3.1: Different milling conditions of precursor for the manufactured wires. E_t/m values have been estimated using Eq. (3.1) and the parametres given in the text.

3.2 PIT and wire drawing

3.2.1 PIT process

After doping and/or ball milling processes, the precursor powders were introduced into commercial 25-30 cm long Fe tubes (99.5 %, Goodfellow, outer diameter of 5 mm and 0.25 mm of wall thickness) using a piston and a hammer to obtain good compacted powders. Both the initial and final part of the Fe tubes were sealed with lead, thus avoiding powder loss during wire drawing. Then, the wire was drawn through several dies in steps of 0.1 mm from the initial diameter down to a final 1.1 mm diameter, obtaining final wire lengths of ~ 2 m.

An intermediate annealing is required when the wire diameter reaches about 3 mm for favouring the stress relief of the Fe sheath, thus allowing us to continue the drawing process. Heating the wire to a sufficiently high temperature provokes a reduction of its strength and then the residual stress by plastic deformation can be relieved. Figure 3.2 shows the effect of stress relief (in %) for Fe after a 1 h treatment as a function of the annealing temperature. Hence, an intermediate annealing at 550 °C during 1 h was always performed during the wire drawing process in order to remove at least a 70 % of the initial stress. Higher temperatures, which would allow a greater stress relief, were deliberately avoided to prevent the MgB_2 formation.

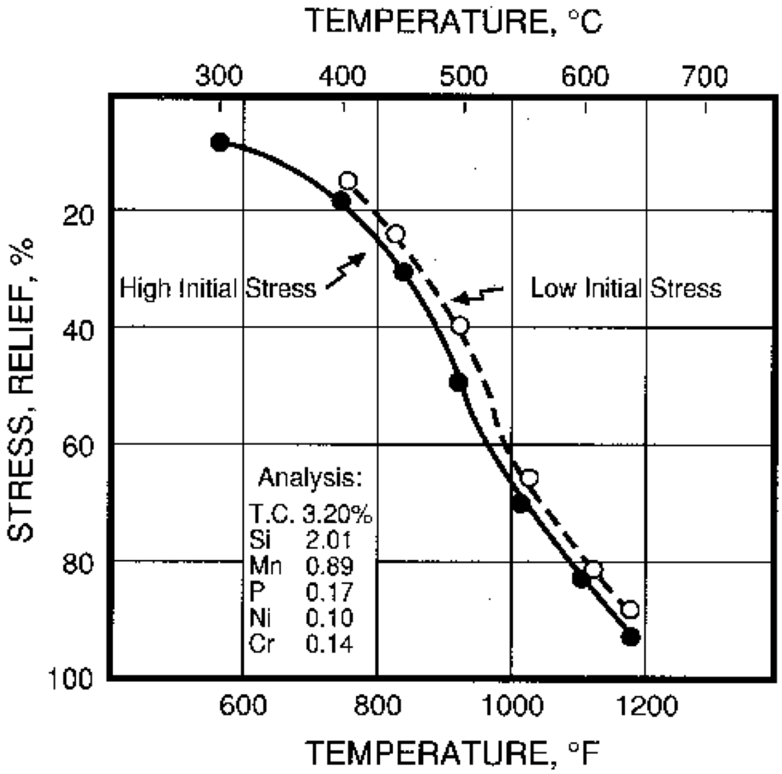

Figure 3.2: Effect of the annealing temperature during 1 h on the stress relief of Fe (data extracted from the Ductile Iron Society [138])

3.2.2 Tape rolling for MO analysis

The MO imaging technique requires flat samples as it will be detailed in Chapter 6. Therefore, in order to study our samples with this technique, tapes were prepared by rolling pieces of MgB_2 wires. Rolling parameters have been defined to obtain flat samples of ~ 2 mm width and 0.3 mm to 0.4 mm thickness. The length of the final tape was ~ 30 cm long. Before rolling, another annealing at 550 °C, 1 h in Ar was performed to relieve the iron stress.

3.3 Final heat treatment

A final heat treatment of the wires or tapes is required in order to form the MgB_2 phase. The performed annealing of all the samples analysed in this work (unless otherwise specified) is displayed in Figure 3.3. It comprises an initial ramp from RT to 630 °C in 6 h (1.7 °C min^{-1}), a slow approach to the annealing temperature (670 °C in this case) at 0.6 °C min^{-1} to avoid temperature overshoot, the proper annealing at 670 °C during 5 h and finally a slow free cooling down to RT.

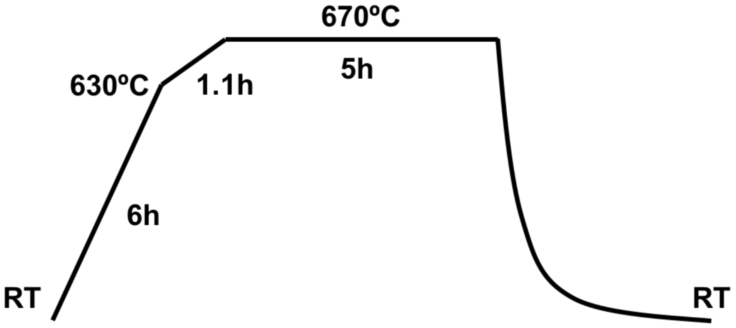

Figure 3.3: Scheme of the final heat treatment of the wires and tapes to form the MgB_2 phase. Neither the time nor the temperatures are at scale for clarifying purposes.

A tubular furnace is used for this purpose. This furnace is sealed at both ends to allow the required controlled atmosphere during the annealing. Either vacuum or Ar flow have been used. To minimize any possible oxidation of the wire during heat treatment, it is placed inside an alumina tube with some iron foils at both ends that act as oxygen trap. In this work the heat treatment has been usually performed in 10 cm long pieces, with both ends sealed, and in vacuum (0.01 − 0.1 mbar).

3.4 Samples nomenclature

The samples we have analysed in this work are named as follows: first letter W or T refers to wires and tapes, respectively; second letter indicates the powder preparation route (0, 1 or 2) as shown in Figure 3.1; and third and fourth characters designate the ball milling condition. For example, sample W2-M1, would correspond to a wire made from C-doped precursor prepared with route 2 and milled with milling conditions M1. Sample T0-M2 would refer to a tape made from non-doped precursor milled with milling conditions M2.

Chapter 4

Influence of ball milling

In this chapter, we analyse the influence of the energy transferred to the precursor powders during ball milling on the microstructure and superconducting properties of the resulting Fe/MgB_2 wires. The aim of this work is to improve the microstructural homogeneity and superconducting properties of the manufactured *in situ* wires.

The experimental techniques used to characterize the phase and microstructure of the samples (FESEM and X-ray diffraction) and their superconducting properties (SQUID-magnetometer and PPMS) are also described.

The manufacturing characteristics of the wires analysed in this chapter are collected in 4.1. All the wires are made from non-doped precursor powders and milled with different conditions. The results of the reference wire W0, made with non-milled precursor powders, are also shown for comparison.

4.1 Phase composition analysis

The microstructural and phase composition of the samples were analysed by field-emission scanning electron microscopy (FESEM, Carl Zeiss MERLIN), using secondary electrons (SE), angle-selective backscattered electrons (AsB) and energy-dispersive X-ray spectroscopy (EDX). SE detector allows topographical analysis of the sample, AsB gives crystal orientation and compositional contrast, and EDX allows the determination of the concentrations

Sample	*Ball Milling*			*O-cont.* (at.%)
	t(h)	ω_p(rpm)	E_t/m(J kg^{-1})	
W0	0	0	0	3.5 (0.6)
W0-M1	1.5	200	$1.2 \cdot 10^6$	8.1 (0.9)
W0-M2	4	200	$3 \cdot 10^6$	9.2 (0.9)
W0-M3	3	400	$2 \cdot 10^7$	8.2 (1.5)
W0-M4	16.5	400	$1 \cdot 10^8$	6.4 (0.7)

Table 4.1: Manufacturing characteristics and properties of the MgB_2 wires analysed in this chapter. The ball milling parameters are t, the effective ball milling time, and ω_p, the mill rotation speed. The milling energy per unit mass transferred to the powder E_t/m was estimated using Eq. (3.1). The oxygen content (O-cont.) values and standard deviations were deduced from FESEM images and EDX analysis. All the wires were annealed at 670 °C for 5 h.

of the different elements present in the sample. All MgB_2 wires FESEM images have been recorded with a 15 kV accelerating voltage and a probe current of 600 pA.

It must be remarked that due to the presence of very light elements, such as O and particularly B, the quantification of the elements by EDX can only be semi-quantitative. In order to minimize these limitations and to facilitate the comparison among the analysed samples, identical experimental conditions were used in all cases. The oxygen content, in at.%, has been collected in Table 4.1 for all the analysed wires. Different regions of the samples were analysed, and the mean values and standard deviations are shown. As a general trend, it is observed that O-content is higher for the wires made from milled precursor, which varies from $\sim$ 6.4 to 9.2 at.%, than for the reference wire W0, which has 3.5 at.%. Due to greater affinity of finer Mg powders to form MgO and to larger reactivity of smaller grains, any small leak in the mill jar would lead to an increase in the oxygen content. Therefore, it would be expected that the oxygen gathered by the precursor during ball milling would increase either with milling time or with milling energy. Nevertheless, we did not observe a clear correspondence between milling conditions and the oxygen content estimated by EDX analysis.

The phase composition was analysed using the X-ray diffraction (XRD) patterns collected at room temperature on a RIGAKU D-max/2500 X-ray diffractometer using Cu Kα radiation.

In Figure 4.1 the XRD patterns of some precursor powders are displayed. For the non-milled precursor powders, M0, Mg peaks are clearly identified but as long as B is amorphous it cannot be detected using this technique.

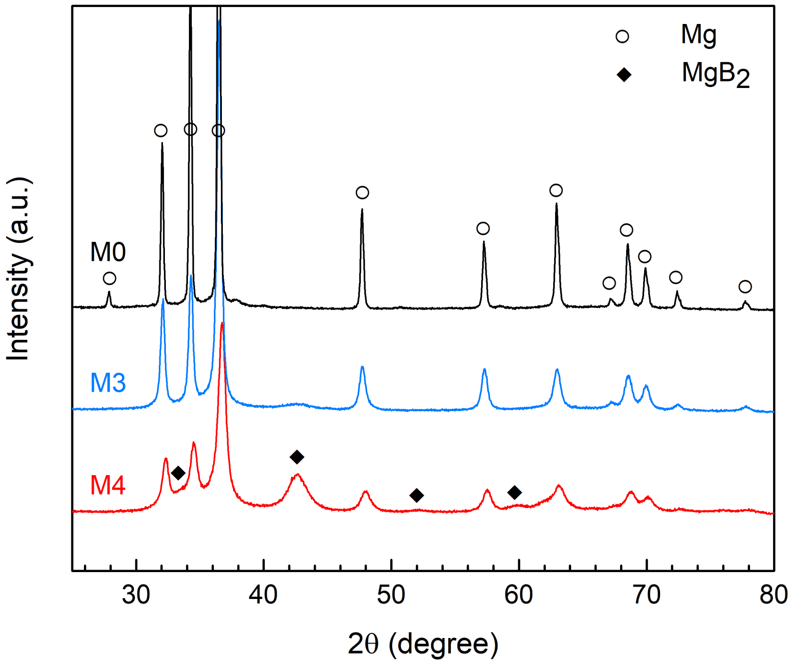

Figure 4.1: XRD patterns of precursor powders after mechanical milling for different milling conditions: M0 (non-milled), M3 and M4. Peaks corresponding to Mg and MgB2 phases are identified.

The XRD patterns of the most extensively milled precursor powders, that is, those corresponding to milling conditions M3 and M4, show a broadening of the Mg peaks due to a reduction of the grain size, which increases with E_t/m. It must be remarked that the MgB_2 phase is clearly visible in the XRD of powders milled with milling conditions M4. This is in agreement with the limit for mechanical alloying at E_t/m of $1 \times 10^8\,\mathrm{J\,kg^{-1}}$ reported in [137]. In order to quantify the amount of MgB_2 formed during milling M4, we have used PDXL2 software of RIGAKU, which allows qualitative and quantitative analysis of the XRD patterns. The estimated phase composition of milled powder M4 was 60.4 wt.%, 36.2 wt.% and 3.4 wt.% of Mg, MgB2 and MgO, respectively.

After annealing, the wires were polished to remove the Fe sheath and to have access to the superconducting core. XRD patterns of those polished surfaces are shown in Figure 4.2. As expected, in all cases MgB_2 appears as the main phase of the core's wires, but also MgO is present as secondary phase. Besides, other residual phases were also identified, such as WC, which is due to contamination from the milling jar and balls during milling process, and it is especially visible in sample W0-M1. Finally, small peaks, identified as Fe_2B phase, are also present, which would be formed during thermal treatment due to the reaction of the Fe sheath and B in the core.

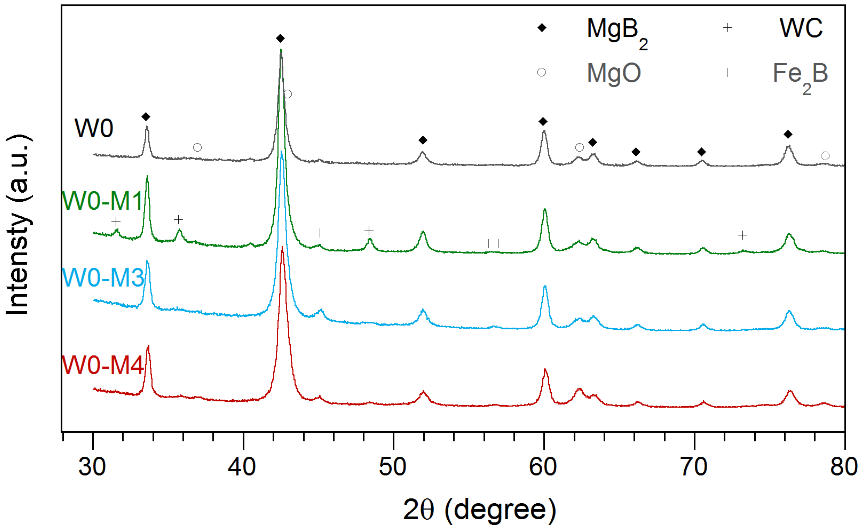

Figure 4.2: XRD patterns of polished wire's cores W0, W0-M1, W0-M3 and W0-M4. Peaks of MgB_2, MgO, WC and Fe_2B are identified.

A semi-quantitative phase composition analysis was performed from these XRD patterns using the reference intensity ratio (RIR) of each phase. RIR is a parameter that can be found in XRD databases [139]. It is defined by the ratio i/i_{cor}, where i is the intensity of the strongest line of the pattern of the given phase and i_{cor} is the intensity of the strongest peak of a reference phase, taken by convention to be α-Al_2O_3, corundum, in a 50/50 weight mixture. Once identified the different phases present in the analysed material, and knowing from the database their XRD patterns and their RIR values, a semi-quantitative phase proportion can be derived by scaling the intensity of the peaks of each phase by the corresponding RIR values. The obtained results in our samples are collected in Table 4.2. The amount of tungsten carbide is very small in all wires, < 1 wt.%, even for wire W0-M1. It must be remarked that WC has a considerably higher RIR value (14.58) than MgO (1.0) [139], therefore the presence of very small amount of this phase is clearly seen by XRD. Also note that the estimated wt.% of MgO slightly increases with milling energy.

Sample	MgB_2 (%)	MgO (%)	WC (%)
W0	95.4	4.6	-
W0-M1	93.5	5.8	0.7
W0-M3	91.3	8.5	0.2
W0-M4	91.2	8.6	0.2

Table 4.2: Phase composition of the annealed wires analysed with a semi-quantitative analysis using the RIR of each phase. % are in weight.

A more accurate estimation of oxygen content in MgB_2 materials would require XRD analysis of grounded cores and Rietveld fitting. Even so, the determination of the oxygen content in these samples presents some challenges. Rosová *et al.* [140] found that superconducting core in PIT samples made from non-milled *in situ* precursor is composed of MgB_2 grains with crystalline MgO in form of thin oriented layers distributed between MgB_2 grains in oriented clusters and also amorphous MgO distributed along MgB_2 cluster boundaries. The presence of amorphous MgO causes differences in oxygen content estimations by different methods (EDX or XRD).

4.2 Effects of milling energy on the wire microstructure

Figure 4.3 shows the FESEM images of the cross-section of longitudinally polished wires, using the SE detector. The images are ordered with increasing E_t/m values from top to bottom.

Thus, Figure 4.3 (a) corresponds to the wire made from non-milled precursor powders, W0, which is used as reference. Its core presents characteristic irregular voids of different shapes and sizes (up to 300-400 µm), left by Mg

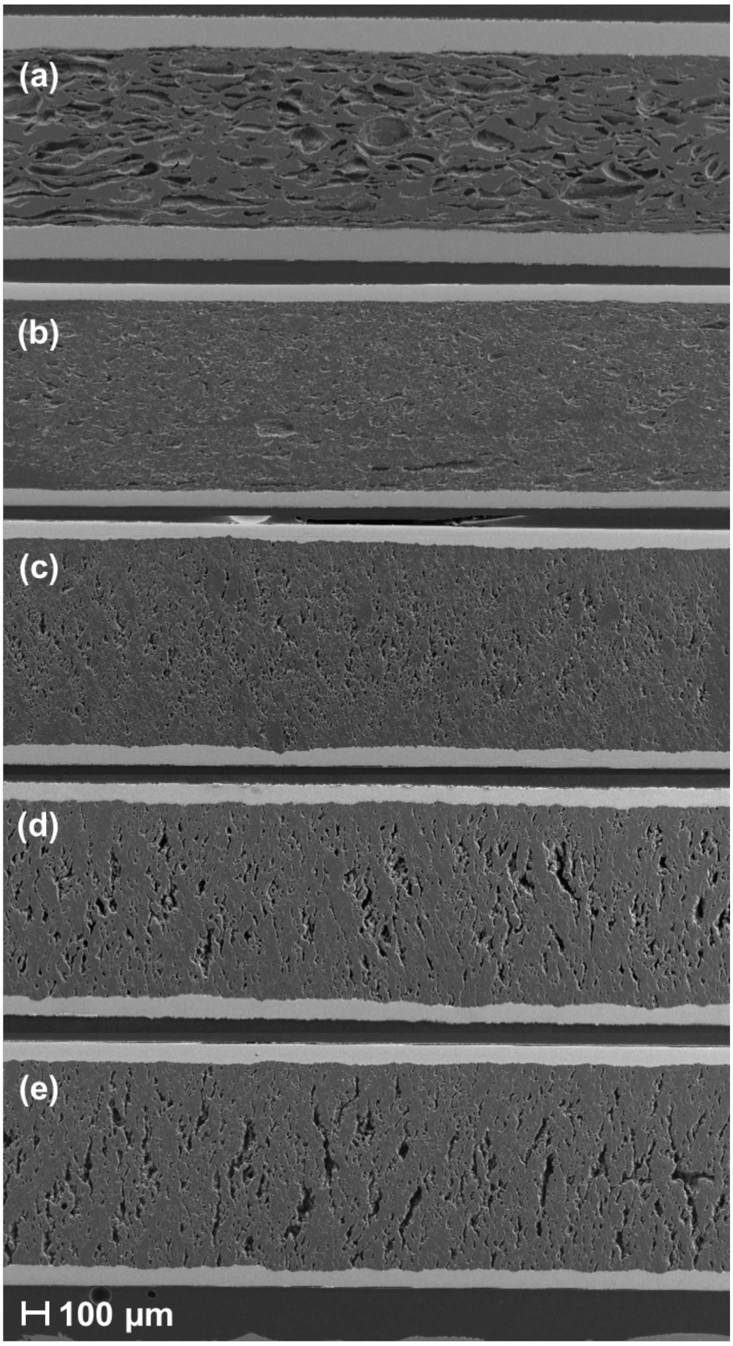

Figure 4.3: FESEM images using SE detector of polished wires from lower (top) to higher (bottom) E_t/m values. Images correspond to (a) W0, (b) W0-M1, (c) W0-M2, (d) W0-M3 and (e) W0-M4.

when reacting with B to form the superconducting phase. Voids closer to the Fe sheath are more elongated and parallel to wire axis, whereas those at the center tend to be more isotropic because the decreasing shear stress transmission from the sheath to the core center during drawing. The core represents about a 75 % of the wire cross-section.

A more homogeneous microstructure is displayed for sample W0-M1 in Fig. 4.3 (b), where smaller and axially oriented voids left by Mg can be seen, especially in regions closer to the Fe sheath. It shows a more dense core than W0 due to grain refinement. W0-M1 core represents a 85 % of wire's total cross-section.

Sample W0-M2, Fig. 4.3 (c), also presents a homogeneous microstructure as W0-M1. However, the voids left by Mg are no longer elongated nor oriented in the axial direction. Also, these voids seem to concentrate in the central part of the core, which represents a 84 % of the total cross-section.

The increase in E_t/m of the precursor used for wire W0-M3, shown in Fig. 4.3 (d), is translated to its microstructure in form of radially oriented voids located in the central part of the core. In the case of wire W0-M4, shown in Figure 4.3 (e), this characteristic orientation of voids in the radial direction is even more severe, as larger voids are formed. Both wires W0-M3 and W0-M4 were difficult to draw. This is because the core becomes less plastic upon increasing milling energy due to the decrease of grain size and to the previously mentioned formation of MgB_2 in the latter. It must be noted that the presence of shear bands, narrowing and wire fracture during deformation of wires made from ball milled precursor has been reported by other groups [137]. The core section of wires W0-M3 and W0-M4 is 85 % of the total wire cross-section.

Further insight into the samples microstructure can be seen in Fig. 4.4, where the images of the four wires whose precursor powders were ball milled are presented at higher magnification using the AsB detector.

The different orientation of the voids in the sample made with the lowest energy milled powders, W0-M1 (Figure 4.4 (a)), compared to the rest of the milled wires (Figures 4.4 (b)-(d)) is clearly observed. The composition is rather homogeneous in all the samples, indicating uniform MgB_2 formation during

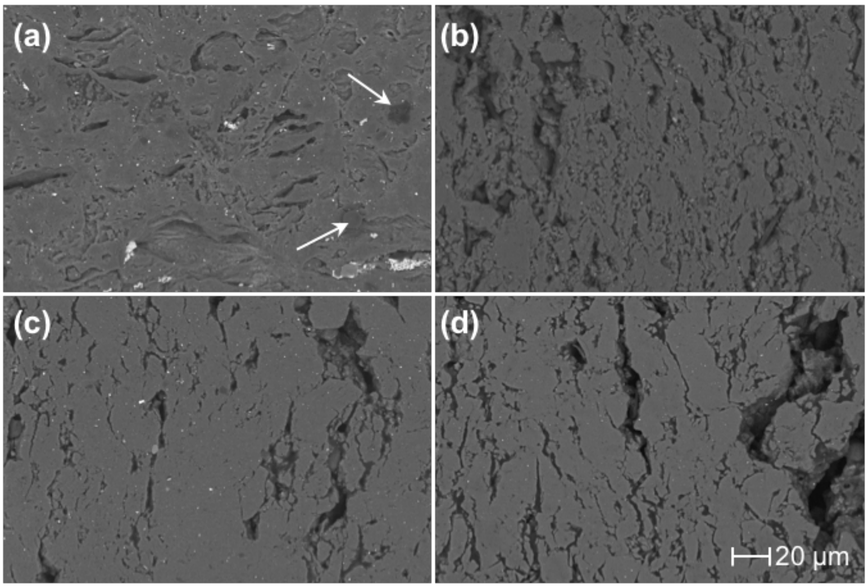

Figure 4.4: FESEM images using AsB detector and the same orientation as in Figure 4.3 of samples (a) W0-M1, (b) W0-M2, (c) W0-M3 and (d) W0-M4. The same magnification has been used in all images.

annealing in agreement with XRD patterns. Nevertheless, there are some areas of darker grey contrast (marked by arrows in Fig. 4.4 (a)), which correspond to boron richer phases, as derived by EDX analysis. In all the samples some small brilliant dots of size $< 100\,\text{nm}$ are also observed. Tungsten element is clearly detected by EDX in these areas, indicating that these particles would correspond to tungsten carbide contamination from the ball milling jar, also in agreement with XRD experiments.

It must be noted that in Figure 4.4 (a) there are also some impurities inside the voids (light grey phase) that correspond to Fe, which are thought to be impurities dragged from the sheath to the core during polishing. Wire W0-M2, Fig. 4.4 (b), shows a very granular microstructure that would lead to poorer intergrain connectivity, which is probably related to the higher oxygen content observed in this wire by EDX analysis, as explained previously (see Table 4.2).

For a better understanding of the effects of the energy transferred to the precursor powder during milling on the microstructure of the final wires, it is also interesting to analyse the FESEM micrographs of the non-annealed wires.

Figure 4.5 shows the images taken on polished longitudinal cross-sections using the AsB detector for some of the analysed wires before (images on the left) and after annealing (images on the right).

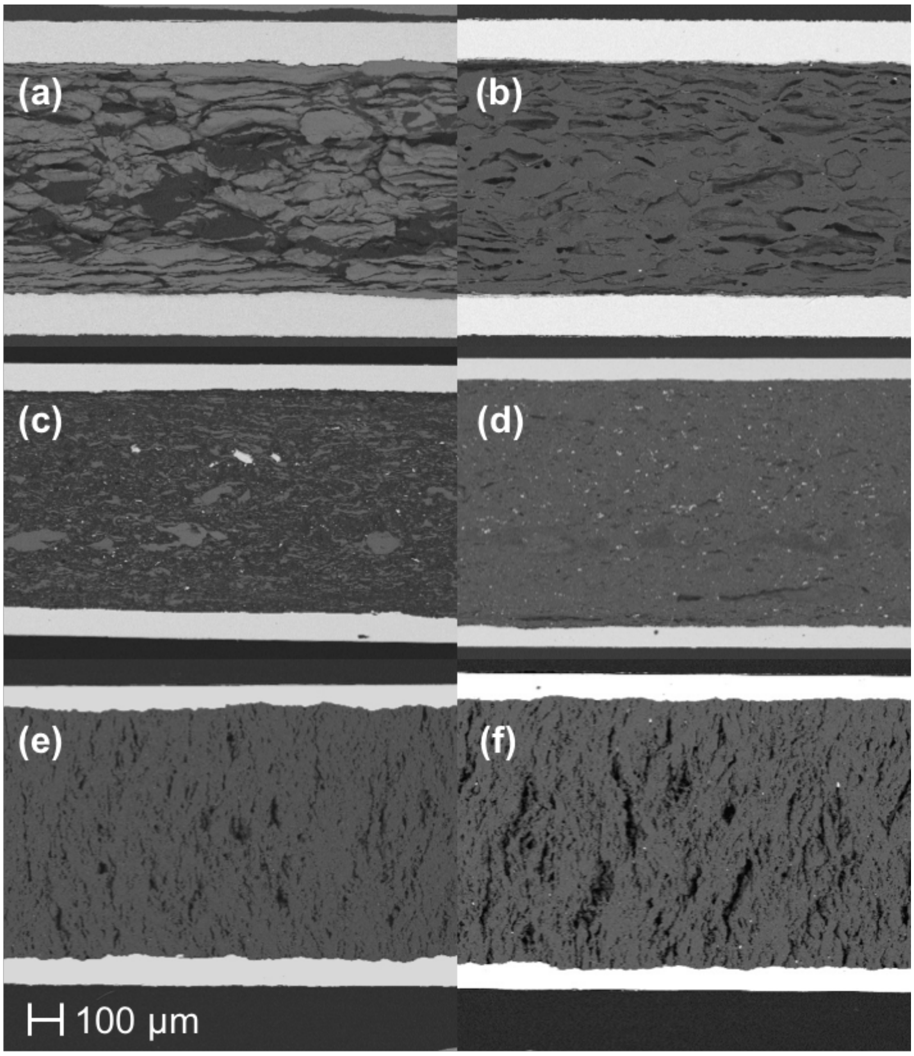

Figure 4.5: FESEM images using AsB detector of polished longitudinal cross-sections before (left) and after (right) annealing. Sample W0 (a) and (b), W0-M1 (c) and (d), W0-M4 (e) and (f) are displayed. The small differences observed in the diameter among the samples are due to different heights at which the cross-section is polished in each sample.

Grain size of Mg particles decreases when increasing E_t/m from the non-milled reference sample W0 (Fig. 4.5 (a) and (b)) to the milled sample W0-M1

(Fig. 4.5 (c) and (d)). A longitudinal texture is observed in the Mg grains of the less milled and non-annealed samples W0 and W0-M1 (Fig. 4.5 (a) and (c)), where majority of Mg grains are elongated and disposed in the axial direction. However, these Mg particles tend to be more spherically-shaped towards the central part of the core. Also, some Fe impurities dragged from the sheath during sample preparation can be seen in sample W0-M1 (Fig. 4.5 (c) and (d)).

In sample W0-M4, both non-annealed and annealed (Fig. 4.5 (e) and (f) respectively), Mg grains are not visible because the high energy milling reduced their size and also because the partial formation of MgB_2, as seen in XRD analysis (section 4.1). Also note that the radially oriented void structure mentioned above already appears in the non-annealed sample. These voids or cracks not only cannot be restored by the final heat treatment, but became larger.

Porosity increases after the annealing in all samples as expected due to the formation of MgB_2, which has higher density than the precursors. It is observed that the voids seen in the annealed samples take the shape and size of the Mg grains observed in the non-annealed samples (except for samples W0-M3 and W0-M4 as previously mentioned).

4.3 Effects of milling on the superconducting properties

The magnetic characterization of the wires was done on 5 mm long samples of radius $r \sim 0.4\,\mathrm{mm}$ obtained after removing the Fe sheath by mechanical polishing. This Fe sheath removal was necessary because its strong ferromagnetic signal hinders the superconductor's contribution.

Vibrating sample magnetometers (VSM, Quantum Design PPMS-9T and PPMS-14T) were employed to measure isothermal magnetic hysteresis loop $M(H)$. A SQUID-based Quantum Design MPMS-5T was used to measure the AC magnetic susceptibility as a function of the temperature, $\chi_{ac}(T)$. From these measurements we estimated the T_c value, defined from the in-phase component of χ_{ac}, $\chi'(T)$, as the onset of diamagnetism, i.e. the temperature at which the magnitude of diamagnetic signal increases above the noise level. The error in this estimation is in our case approximately $\pm 0.3\,\mathrm{K}$. Also, the transition width ΔT_w , defined as the temperature interval at which the χ' varies from 10 % to 90 % of $\chi'(5\,\mathrm{K})$, is obtained.

AC measurements were performed at a frequency of 120 Hz and with a magnetic field amplitude of 0.1 mT. Figure 4.6 displays $\chi'/|\chi'(5\,\mathrm{K})|$, as a function of temperature for all the analysed wires. It is clear that T_c decreases as E_t/m increases, as seen in Table 4.3, but the transition is narrow in all cases, $\Delta T_w = 0.5 - 1\,\mathrm{K}$.

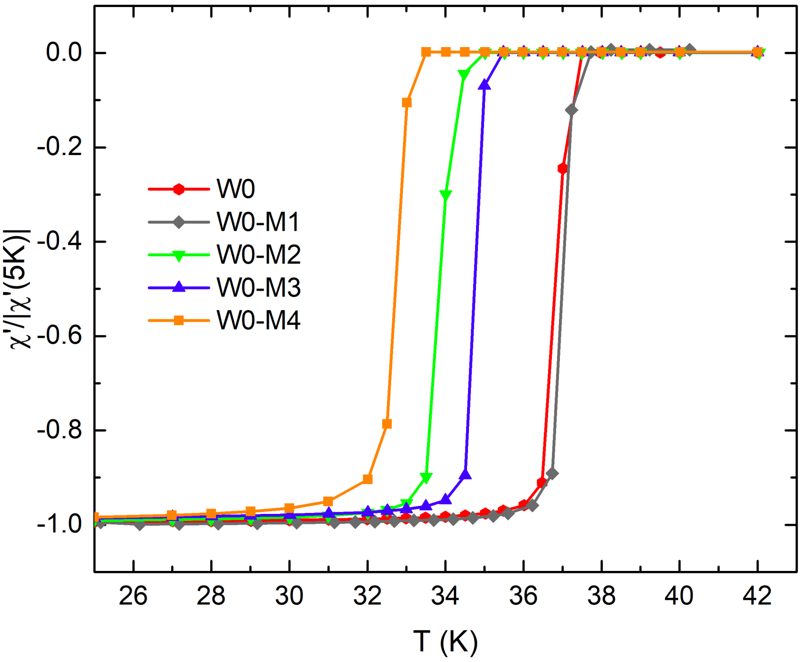

Figure 4.6: Temperature dependence of the in-phase component of the AC susceptibility, $\chi'(T)$, divided by $|\chi'(5\,\mathrm{K})|$, for all analysed wires W0, W0-M1, W0-M2, W0-M3 and W0-M4.

Regarding the estimated T_c values, a correlation between this value and E_t/m is established in Fig. 4.7. T_c decreases as E_t/m increases to an approximate rate of 2 K per order or magnitude of transferred energy to the precursor powders, in the studied range. The exception of this behaviour is observed for W0-M2 wire, which shows lower T_c than expected. This can be explained taking into account that the oxygen content is higher in this wire as it is presented in Table 4.1.

Sample	T_c(K)	ΔT_w(K)
W0	37.7	0.7
W0-M1	37.5	0.6
W0-M2	34.7	0.9
W0-M3	35.2	0.5
W0-M4	33.3	1.0

Table 4.3: T_c and ΔT_w as derived from $\chi_{ac}(T)$ measurements of the milled MgB_2 wires.

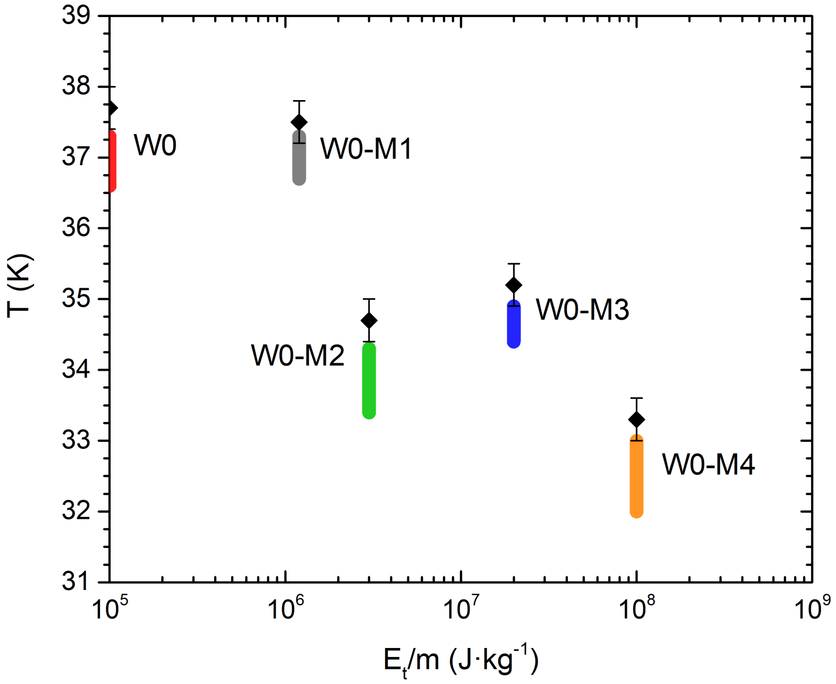

Figure 4.7: T_c values for the ball milled samples (black solid symbols) as a function of the milling energy E_t/m. Coloured bars correspond to the temperature intervals at which χ' varies from 10 % to 90 % of $\chi'(5\,\mathrm{K})$ for each sample. The non-milled sample W0, with $E_t/m = 0\,\mathrm{J\,kg^{-1}}$, is presented on the left edge of the figure for clarity purposes.

In all measurements the magnetic field was applied perpendicular to the wire axis so that the induced superconducting currents would be mostly flowing along the wire axis. From the width of the magnetic hysteresis loops, $\Delta M(H)$, the inductive critical current densities were derived using Bean's critical state model [141]:

$$J_c(H) = \frac{3\pi}{8}\frac{\Delta M(H)}{r}, \tag{4.1}$$

where $\Delta M(H)$ is in $\mathrm{A\,m^{-1}}$, r in m and $J_c(H)$ in $\mathrm{A\,m^{-2}}$. This equation is valid for wires of length L when $L \gg r$. An example of a $M(H)$ measurement at 5 and 20 K corresponding to wire W0-M1 is shown in Figure 4.8. For these experiments the sample is zero-field-cooled from a temperature above T_c to the measurement temperature. Once the temperature is stabilized, the magnetic field amplitude is increased in steps of 1 T to maximum field of 9 T (initial branch), then it is decreased down to zero in steps of -0.2 T, a finally increased again in the opposite direction with the same steps of -0.2 T up to -9 T.

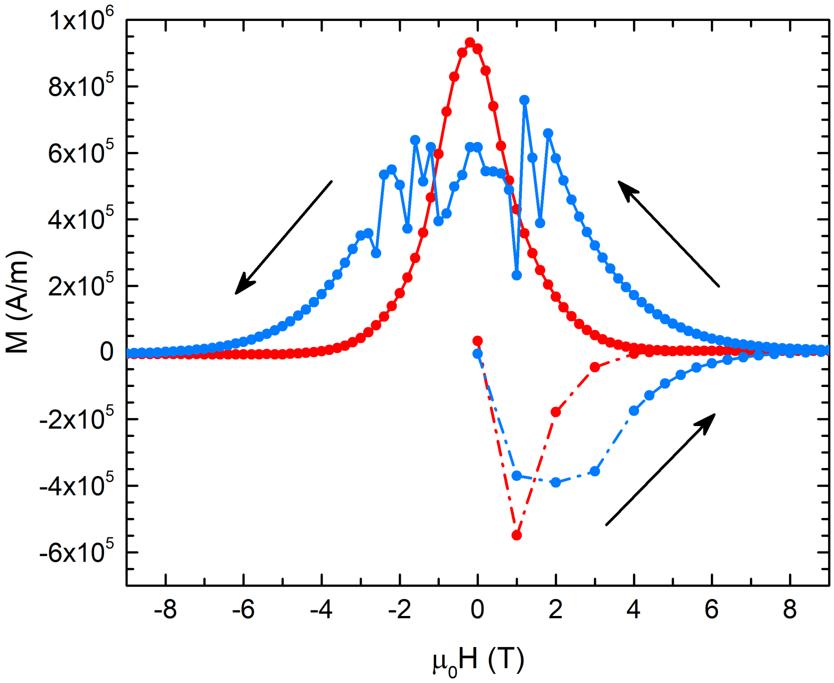

Figure 4.8: Magnetization, M, as a function of magnetic field, $\mu_0 H$, applied perpendicular to the wire's axis, for sample W0-M1 at 5 K (blue) and 20 K (red). For this wire, flux jumps are visible at 5 K upon decreasing the field in the range between 1.8 T and -3 T. Lines are just an eye guide.

The flux jumps observed in the $M(H)$ curve at 5 K are caused by thermomagnetic instabilities [142, 143]. These are originated by avalanches of pinned magnetic vortices triggered by changes in the applied magnetic. The motion of a vortex dissipates heats and, if it is not removed quickly enough, will provide energy to surrounding vortices and unpin them, so they will also move into the sample and dissipate even more heat, and so on. These thermomagnetic instabilities result in flux avalanches at low temperatures and applied magnetic fields.

A comparison of $J_c(H)$ curves of ball milled samples is presented in Fig. 4.9 at 5 K. Magnetic flux jumps (see Fig. 4.8) limit the magnetization values at low magnetic fields, typically below 1 T to 2.5 T at 5 K depending on the sample. Thus $J_c(H)$ values are underestimated in that field range and have been eliminated in the figure in order to gain clarity. W0 is presented as a reference.

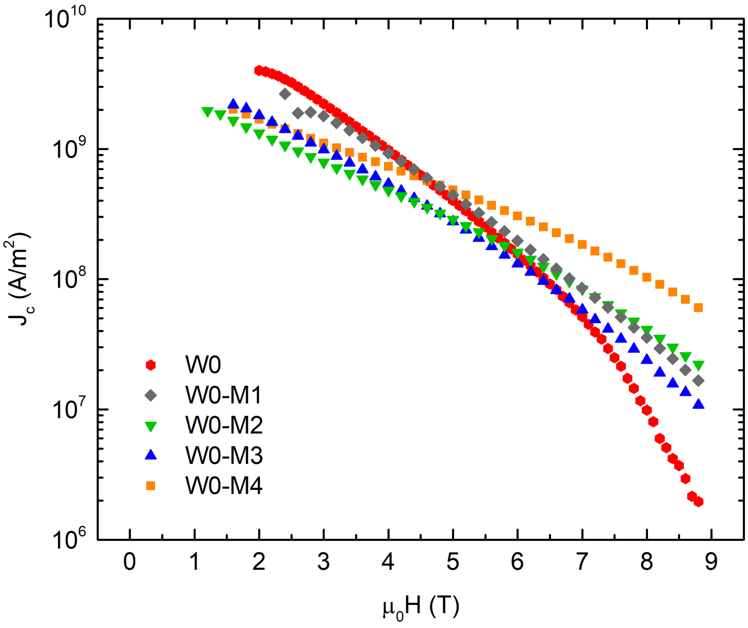

Figure 4.9: $J_c(H)$ values at 5 K for non-milled, W0, and milled samples, W0-M1, W0-M2, W0-M3 and W0-M4.

At 5 K, the two opposite effects of ball milling on J_c are clearly seen in Figure 4.9. As mentioned before, on one hand, higher energy milling enhances vortex pinning at high fields, so that the highest J_c's at 5 K and $\mu_0 H > 5$ T correspond to wire made from the highest energy milled precursor, W0-M4. On the other hand, at low fields ($\mu_0 H < 5$ T), the highest J_c values correspond to the non-milled and low-energy milled samples W0 and W0-M1, respectively, which indicates better grain connectivity and/or smaller amounts of microstructural defects in these samples compared to wires made from higher energy milling conditions M2, M3 and M4. Larger oxygen content in some ball milled wires, with the presence of electrically insulating MgO precipitates, would decrease supercurrent paths between neighbouring MgB_2 grains and therefore would result in worse connectivity.

Regarding W0-M2 and W0-M3 wires, it is observed that $J_c(H)$ curves of both wires are similar. Nevertheless, at high magnetic fields J_c values of the former are higher than the latter, unexpectedly since W0-M3 is made from higher energy milled precursor. This is probably due to a larger amount of defects in wire W0-M2, in agreement with its higher oxygen content (Table 4.1) and its lower T_c value (see Figure 4.7). As a consequence, J_c values of W0-M3 are lower than those of W0-M2. Finally, sample W0-M1, which shows a homogeneous microstructure and a lack of transversal porosity, exhibits $J_c(H)$ values similar to those measured for W0 at low fields, but higher in the high field range (above $\sim 6\,\mathrm{T}$). The transport critical current values have been measured in selected wires, and the results will be discussed in Chapter 5.

The $J_c(H)$ values at 20 K of the samples are displayed in Fig. 4.10. The lower connectivity in W0-M3 and W0-M4 and the proximity of T_c limit the $J_c(H)$ values of these wires in all magnetic fields at this temperature. Note that these wires have the lowest T_c (35.2 K and 33.3 K respectively). On the other hand, $J_c(H)$ values of the non-milled sample W0 and W0-M1 are almost the same for the whole magnetic field range.

Our results show good agreement with those reported by Häßler *et al.* [137]. For E_t/m of the order of $1 \times 10^8\,\mathrm{J\,kg^{-1}}$, they measured $J_c \sim 1 \times 10^4\,\mathrm{A\,cm^{-2}}$ at $\sim 7\,\mathrm{T}$ and 5 K, which is slightly lower field than for wire W0-M4 ($\sim 8\,\mathrm{T}$) for similar J_c. Furthermore, sample W0-M3 with $E_t/m \sim 1 \times 10^7\,\mathrm{J\,kg^{-1}}$ has J_c of $1 \times 10^4\,\mathrm{A\,cm^{-2}}$ at $\sim 7\,\mathrm{T}$, also slightly better than results presented in [137] ($\sim 6\,\mathrm{T}$) for similar milling energy values.

However, as mentioned previously, both wires made with M3 and M4 milling conditions were difficult to draw and presented some unwanted microstructural features. This indicates that drawing is not the best method for wire deformation when using high energy milled precursors. Recently, Saito *et*

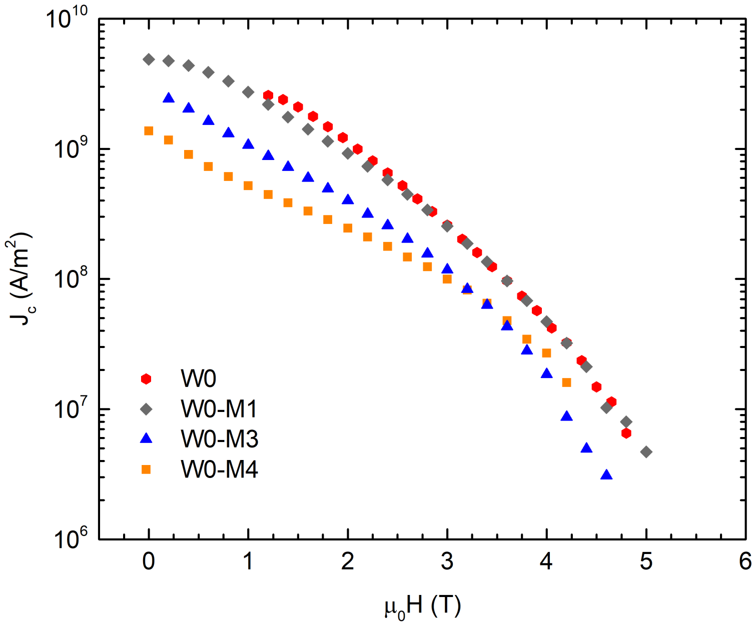

Figure 4.10: $J_c(H)$ values at 20 K for non-milled, W0, and milled samples, W0-M1, W0-M2, W0-M3 and W0-M4.

al. [144] have studied the properties of *in situ* monocore PIT wires manufactured by different mechanical deformation methods (specifically only swaging, groove rolling + roller drawing, and groove rolling + conventional drawing) and concluded that the best superconducting performance is found for wires manufactured by swaging until the final diameter. This method produces optimum radial compressional stress in the core during deformation, which increases both the MgB_2 core density and the homogeneity along the wire's core. Therefore it is envisaged as a good manufacturing method for wires made from high energy milled powders.

From our results, we have demonstrated that the best combination of homogeneous, less-porous microstructure and $J_c(H)$ performance is found for the milling condition M1 with a E_t/m of 1.2×10^6 J kg^{-1}. This is in good agreement with recent results obtained by Kodama *et al.*, who observed optimum performance for milling energies in the range of 1×10^6 J kg^{-1} [145].

4.4 Effect of different annealing temperatures on the superconducting properties

The final heat treatment of all the above analysed samples was 670 °C × 5 h (see Fig. 3.3). The influence of the heat treatment temperature on J_c values was studied for some selected samples. The results of wire W0-M3 for annealing temperatures ranging from 630 °C to 720 °C are shown in Figure 4.11. At 5 K the $J_c(H)$ curves do not present any significant difference in the measured field range. At 20 K and $\mu_0 H < 3$ T, J_c values increase slightly when increasing the annealing temperature, but become similar upon increasing the magnetic field.

Besides, the value of T_c for the samples annealed at 630 °C and 720 °C differs only in 0.5 K below and above respectively the obtained value of the sample W0-M3, annealed at 670 °C, that is 35.2 K. This is in agreement with the measured $J_c(H)$ curves, previously discussed. Also, ΔT_w is the same for

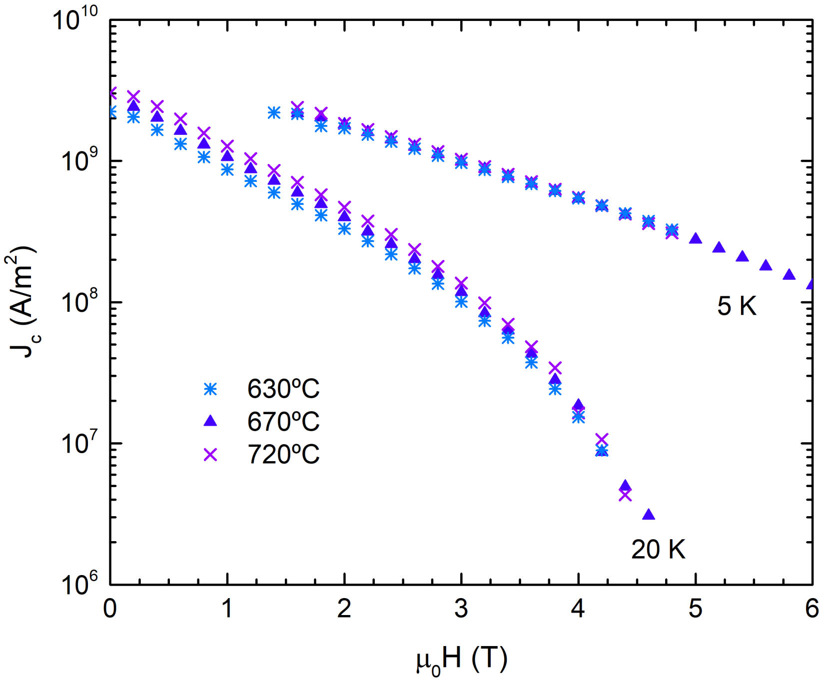

Figure 4.11: $J_c(H)$ values of wire W0-M3 at 5 and 20 K for three different annealing temperatures. Annealing time was 5 h in all cases.

all the three samples, 0.9 K, indicating that the superconducting transition remains the same despite the annealing temperature.

The low melting temperature of Mg at 650 °C facilitates the Mg and B reaction to form the superconducting MgB_2 phase when using the *in situ* reaction method. The effect of the heat treatment temperature on the superconducting properties of the wires has already been reported in the literature for a wide range of temperatures, typically from 600 °C to 900 °C [146–148].

In general, it is well known that cristallinity improves when raising the reacting temperature, leading to higher T_c and a better grain connectivity. On the other hand, low temperature sintering leads to small grain size and grain distortion, which creates more grain boundaries and defects enhancing flux pinning and J_c at high fields. This makes temperatures close to the melting point of Mg as the preferred option for *in situ* reaction method. We have used annealing temperatures just above this temperature to ensure full reaction of the precursor, as when using annealing temperatures below 650 °C, some wire regions may remain unreacted depending on the precursor's grain size and heat treatment time.

Chapter 5

Co-effect of ball milling and carbon doping

Grain refinement and carbon doping are two processes used to improve the $J_c(H)$ performance of metal composite MgB_2 wires and tapes. As it has been shown in the previous chapter, precursor ball milling significantly affects the wire microstructure of the final wires, as very fine and well mixed precursors with higher reactivity can be obtained with this method. On the other hand, the addition of oleic acid to the precursor powders can be successfully used as a carbon source to improve $J_c(H)$ of the wires. Nevertheless this doping process also produces some unwanted inhomogeneity issues, both across and along the wires, which are necessary to solve [135].

In order to enhance $J_c(H)$ performance and the homogeneity of MgB_2 wires, in this chapter the combined effect of carbon doping with oleic acid and ball milling of the precursor powders is presented. With this aim, a characterization of the microstructure, phase composition and superconducting properties of the wires made from precursors with different milling parameters and with oleic acid addition has been done. The results have been compared with those of non-doped or non-milled reference wires.

The main characteristics of the wires analysed in this chapter are collected in Table 5.1. These Fe-sheathed mono-core MgB_2 wires were manufactured by the PIT technique and *in situ* reaction with the manufacturing process explained in detail in Chapter 3 (Fig. 3.1). The wires W1-M1, W2-M1 and

W1-M3 were made from doped and ball milled precursors. Wires W1 and W2 were made from doped but non-milled precursor. Finally, W0, W0-M1 and W0-M3 wires, which were fabricated from non-doped and milled precursor (already analysed in Chapter 4), are included here as references for a better comparison.

Sample	*C Doping*	*Ball Milling*	*O-cont.* (at.%)	T_c(K)	ΔT_w(K)
W0	-	-	3.5 (0.6)	37.7	0.7
W1	Route 1	-	7.4 (0.9)	36.0	1.5
W2	Route 2	-	5.4 (0.4)	35.3	0.7
W0-M1	-	M1 (200 rpm × 1.5 h)	8.1 (0.9)	37.5	0.6
W1-M1	Route 1	M1	10.2 (0.9)	36.0	0.6
W2-M1	Route 2	M1	11.5 (0.8)	36.0	0.6
W0-M3	-	M3 (400 rpm × 3 h)	8.2 (1.5)	35.2	0.5
W1-M3	Route 1	M3	13.7 (0.5)	32.8	1.1

Table 5.1: Manufacturing characteristics of the MgB_2 wires analysed in this chapter. The oxygen content (O-cont.) values and standard deviations have been deduced from FESEM images and EDX analysis. T_c and ΔT_w are derived from $\chi_{ac}(T)$.

5.1 Co-effect of ball milling and C doping on microstructure

The microstructural properties of the analysed wires have been analysed using FESEM. The oxygen content has been deduced from EDX analysis, as explained in Chapter 4, and the results are given in Table 5.1. It is observed that O-content of carbon doped wires is higher than for similarly processed wires made with non-doped precursors. In the case of samples W1 and W2, non-milled but C-doped, this is 7.4 and 5.4 at.% respectively, which is higher than the obtained value in W0 (3.5 at.%). In principle, it seems that doping the precursor powders with Route 1 introduces slightly more oxygen than with Route 2. However, any significant difference vanishes with the ball milling process of the precursor powders, as similar oxygen content values are obtained for samples W1-M1 and W2-M1. These values, ∼ 10 at.%, are also slightly higher than for W0-M1, 8.1 at.%. Moreover, for similar carbon doping conditions, the estimated O-content increases with the milling energy, from 10.2

at.% in wire W1-M1 up to 13.7 at.% in wire W1-M3. In summary, the increase of O-content in the samples caused by C doping can be attributed to the introduction of additional oxygen by the carboxylic groups (-COOH) of the oleic acid.

Figure 5.1 shows the FESEM images of the cross-section of longitudinally polished wires using the AsB detector. The slight differences in diameters between the samples are again only due to differences during the polishing process. The images on the left side of the figure correspond to non-milled samples, while the corresponding images on the right side are for wires of similar characteristics, but from precursor milled with condition M1. The two wires displayed on the top of the figure are the non-doped W0 (Fig. 5.1 (a)) and W0-M1 (Fig. 5.1 (b)), which are used as reference samples. There are large differences among wires made with non-milled powders and those fabricated with milled precursors using conditions M1. It must be remarked that the holes are reduced significantly upon milling for all samples, as explained in Chapter 4.

Moreover, the non-milled and C-doped wire using route 1, W1, Fig. 5.1 (c), shows a very inhomogeneous microstructure, with areas of large porosity (upper part) and other denser areas (lower part of the image). A similar trend is also observed in sample W2 (Figure 5.1 (e)). The contrast differences in the images indicates differences in the composition in both regions. A semi-quantitative analysis of the elements using EDX revealed that denser and darker areas are Mg-B phases with higher boron contents while those surrounded by pores (light grey) correspond to the superconducting MgB_2 phase. The observed phase inhomogeneity in these non-milled wires is thought to be caused by the poorly mixed precursor due to the agglomeration of B powders soaked in the oleic acid. This phenomenon is especially drastic for wires made from precursor doped using Route 1, Figure 5.1 (c). Since the extension of these boron rich areas across and along the wire is very irregular, this would lead to very inhomogeneous critical current values for wire W1, or even to resistive portions. As a consequence, W1 is a wire that cannot be used in technological applications. Wire W2 also presents some non-superconducting zones, Figure 5.1 (e), but these are of less extension and also more homogeneously distributed along the wire.

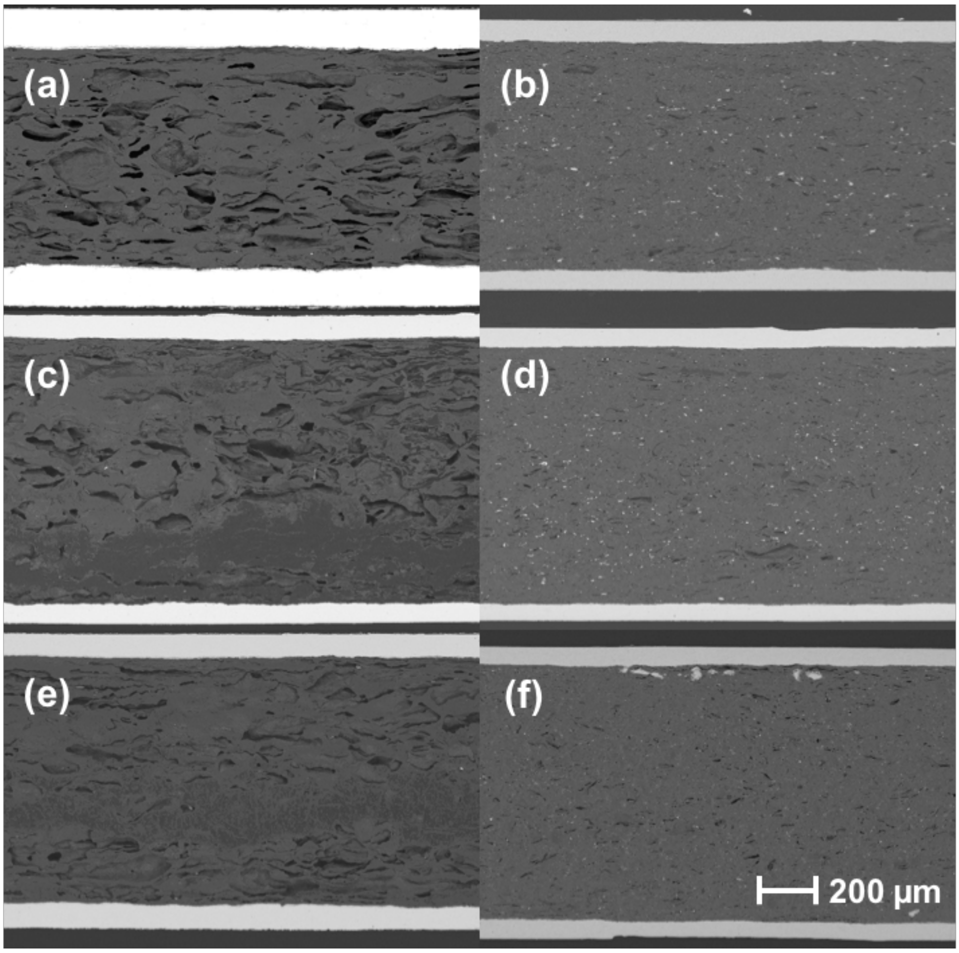

Figure 5.1: FESEM images using the AsB detector of polished non-milled (left) and milled (right) wires. Images correspond to (a) W0, (b) W0-M1, (c) W1, (d) W1-M1, (e) W2 and (f) W2-M1. Wires W0 and W0-M1 are used here as references.

It is worth noting that the low-energy milling (M1) prevents this problem and results in a remarkable improvement of the microstructure and phase homogeneity of the cores when milling the C-doped precursor with milling conditions M1, as shown in Figure 5.1 (d) and 5.1 (f). With this magnification, no substantial differences are seen between these wires and the corresponding non-doped one shown in Figure 5.1 (b).

A more detailed study can be done by analysing FESEM images at higher magnification, which are displayed in Figure 5.2 for the same samples and orientation as in Figure 5.1. Thus, sample W0, shown in Fig. 5.2 (a), presents a very homogeneous and well connected MgB_2 regions. The inherent porosity of this wire is also present.

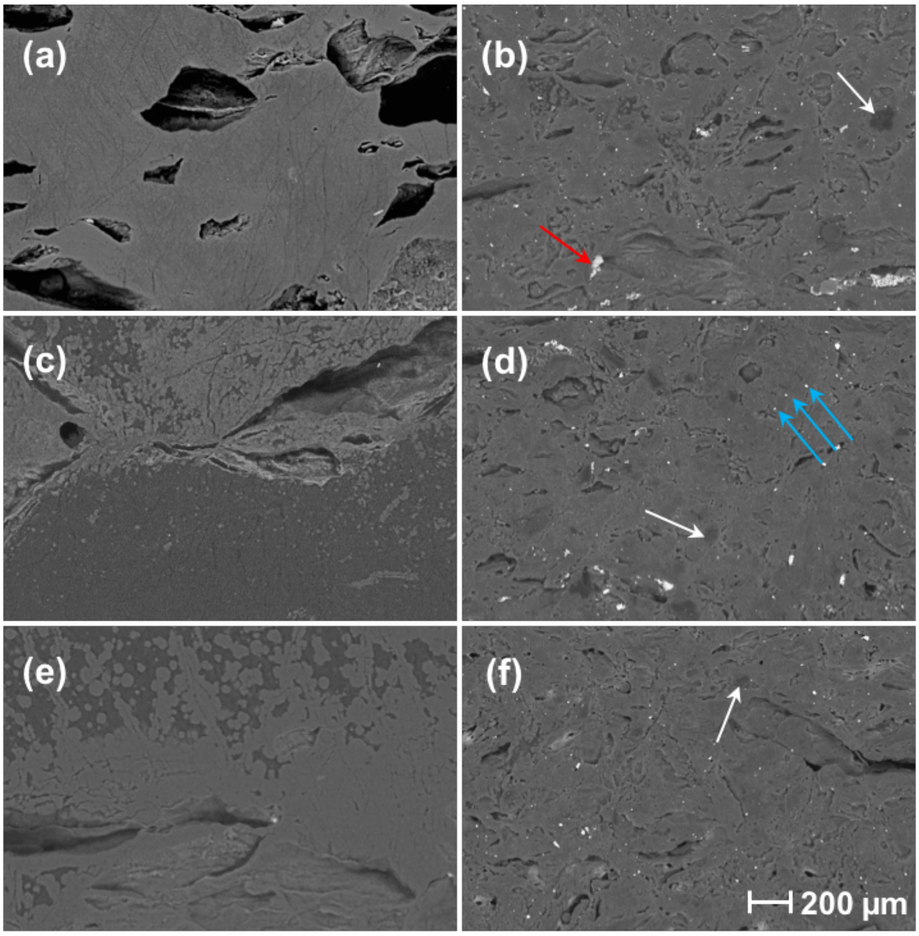

Figure 5.2: FESEM images using the AsB detector and the same orientation as in Figure 5.1 of samples W0 (a), W0-M1 (b), W1 (c), W1-M1 (d), W2 (e) and W2-M1 (f). All images are with the same magnification.

Samples W1, Fig. 5.2 (c), and W2, Fig. 5.2 (e), show inhomogeneous phase microstructure, with pure dense MgB_2 regions (light grey) combined with B rich regions (dark grey). However, a very similar microstructure is shown among all milled samples, whether C-doped, like W1-M1, Fig. 5.2 (d), and W2-M1, Fig. 5.2 (f), or non-doped, like W0-M1, Fig. 5.2 (b). Samples W0-M1, W1-M1 and W2-M1, present small B rich regions in their cores (marked with white arrows). Besides, in these three samples, the sizes of the voids are similar. As already mentioned in Chapter 4, WC particles are present in the milled samples (marked with blue arrows). Metallic impurities within the voids correspond to Fe from the sheath, which were introduced during the preparation of the sample (marked with a red arrow).

Figure 5.3 shows the co-effect of ball milling and C doping on the microstructure of the wires, similarly to the comparison in Figure 5.2 but using a higher milling energy (M3). Both wires, W0-M3 and W1-M3, present similar microstructural features in terms of phase homogeneity and porosity. Despite the observed granularity in both samples, the doped sample, Fig. 5.3 (b), seems to present worse intergrain connectivity than the non-doped one, Fig. 5.3 (a), which is probably related to its higher oxygen content. Similar difficulties were found during mechanical deformation of both wires by drawing, as previously mentioned in Chapter 4.

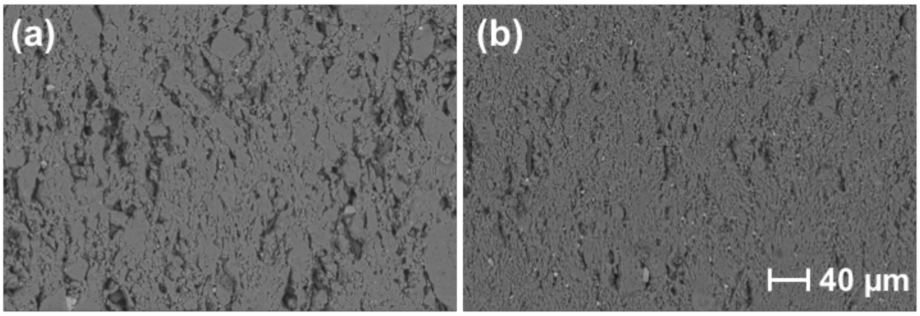

Figure 5.3: FESEM images using the AsB detector of samples W0-M3 (a) and W1-M3 (b). Both images are with the same magnification.

5.2 Co-effect of ball milling and C doping on the superconducting properties

The magnetic characterization of the samples was performed using SQUID and PPMS systems as explained in Chapter 4. The T_c and ΔT_w value (as derived from $\chi_{ac}(T)$ magnetic measurements) of the analysed wires are collected in Table 5.1.

Besides, electrical DC transport measurements in perpendicular DC magnetic fields were performed on 6 cm long wires, with the samples immersed in liquid helium. The $J_c(H)$ values were determined by the standard four-probe method using the $1\,\mu\mathrm{V\,cm^{-1}}$ criterion.

T_c values obtained for the C-doped wires show a decrease of 1.5 K to 2.5 K when compared to their corresponding reference wires, that is, non-doped wires with the same milling conditions. This would mean that the average C doping in milled and non-milled samples is similar. The average doping amount, x, of the $\mathrm{Mg(B_{1\text{-}x}C_x)_2}$ grains in the wire core was estimated in the range of 1 % to 1.5 % for wires W1 and W2 [135].

Moreover, it must be remarked that both T_c and ΔT_w values are similar for doped samples with different doping routes and the same milling condition (W1-M1 and W2-M1). This would indicate that both doping routes are similarly effective in introducing C in the MgB_2 phase when used in combination with the ball milling.

Before addressing the analysis of the co-effect of C doping and ball milling on the $J_c(H)$ behaviour of the wires, it is necessary to study the effect of oleic acid addition in non-milled precursors. With this aim, Figure 5.4 compares critical current densities of C-doped wires W1 and W2 with non-doped wire W0. Symbols without lines correspond to the inductively estimated $J_c(H)$ values derived from the M-H measurements using Eq. 4.1. Note that as explained in Chapter 4, J_c values at 5 K and low fields ($< 2.5\,\mathrm{T}$) are not shown due to the presence of flux jumps in $M(H)$. Solid symbols with lines are for transport values measured with the sample immersed in liquid helium (4.2 K).

The benefits of carbon doping can be seen in the improvement of inductive $J_c(H)$ values of wires W1 and W2 compared to W0, at medium and high fields, especially at 5 K. Nevertheless, there are important differences between wires W1 and W2 at 5 K. This is because using route 1 for C doping of non-milled samples produces large phase inhomogeneities, as seen in Fig. 5.1, which also results in significant differences in the derived J_c values in different pieces of the same wire.

Transport J_c values of wires W0 and W2 are higher than the corresponding induced values. The increase of voltage in the transport $I-V$ curves ($V \propto I^n$) is sharper in sample W2 than in sample W0. For example, at $\mu_0 H \sim 8\,\mathrm{T}$, the estimated n-values are $\sim 20-24$ and $\sim 30-33$ for wire W0 and W2,

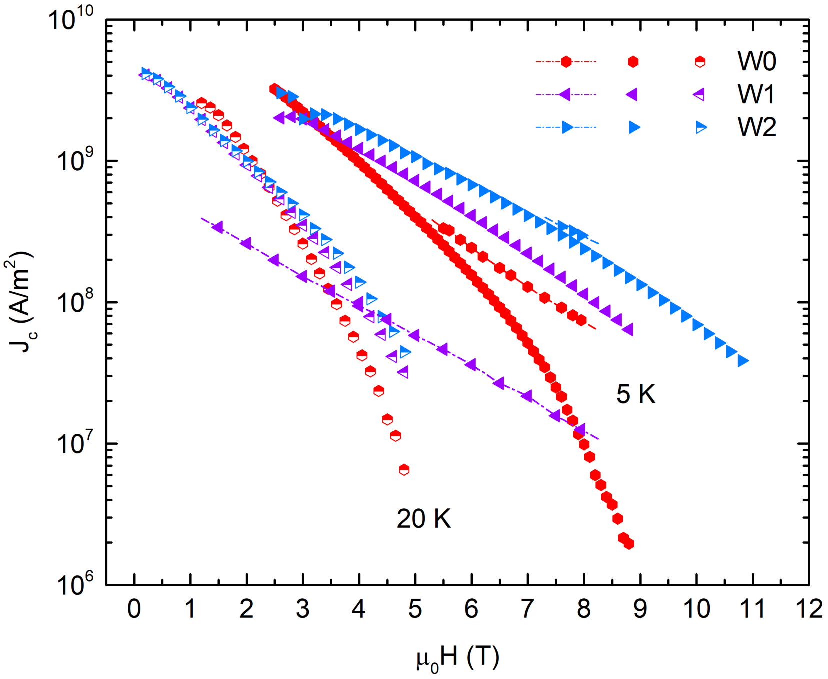

Figure 5.4: $J_c(H)$ values at 5 K (solid symbols) and 20 K (semi-solid symbols) for non-milled wires: non-doped (W0) and doped samples (W1 and W2). Symbols without lines correspond to inductive J_c values and symbols with lines are for transport values at 4.2 K.

respectively. It is very remarkable how the transport critical currents of wire W1 are approximately one order of magnitude lower than their corresponding inductive values. Moreover, the $I - V$ curve measured in this wire is smooth and shows a resistive tail, in clear agreement with microstructural observations showing very inhomogeneous phase formation in wire W1, with large areas of non-superconducting phase (Fig. 5.1 (c)).

Although the absence of weak links in MgB_2 [149] allows in general good agreement between transport and magnetic J_c values, several factors can result in significant differences between values derived by both experiments. It is important to keep in mind that J_c is affected by the selected electric field criterion due to flux creep effects, which are more relevant at high fields and low critical currents ($< 10^8\,\mathrm{A\,m^{-2}}$) [150, 151]. The electric field criteria for determination of J_c from magnetic measurements, which are influenced by the applied field sweep rate, are more restrictive than those of transport.

Therefore, for homogeneous and isotropic samples, transport J_c values should be close but higher than inductively derived J_c's, as it is seen in Fig. 5.4 for wire W2.

For wire W0, the differences between induced and transport values (Figure 5.4) increase with the field strength since inductive values drop off more rapidly in field than those of transport. This behaviour, which has also been reported by different groups in similar processed wires [150–152], has been attributed to the anisotropic connectivity in some PIT wires [151]. The magnetization of a cylinder in perpendicular fields is controlled by the smaller of two quantities: $J_{cL} \cdot d$ or $J_{cT} \cdot L$, where d is the diameter of the superconductor, L is the length, J_{cL} is the critical current density along the wire's axis and J_{cT} along the radial direction. In high fields, it is believed that the 'rooftop' critical state profiles would be dominated by the return currents at both ends of the wire. Since J_{cT} is lower than J_{cL}, magnetic J_c falls below the transport value in this field range. These effects have been attributed to the fibrous microstructure of these wires, with elongated pores produced by the fabrication process and the MgB_2 formation reaction. It must be remarked that other authors [153] have demonstrated the existence of superconducting currents circulating on different length scales in some MgB_2 samples. In consequence, calculating J_c by simply applying the critical state model to the measured ΔM would cause in these cases some errors in the estimations of the induced J_c, mainly at low and very high fields [153].

Next, we analyse the co-effect of C doping and milling, which has the purpose of overcoming the aforementioned problems. Milling conditions M3 and M1 were used in this study and the results are shown in Figures 5.5 and 5.6, respectively.

It is seen that C doping produces in all cases an improvement of J_c at high magnetic fields and a decrease at low magnetic fields compared to the corresponding non-doped wires using the same milling conditions. In the case of the samples with the milling condition M3 the J_c reduction at low fields is more pronounced than for those of M1. Thus, better overall superconducting performance is achieved for the millling condition M1. Also it is remarkable the rather good agreement between induced and transport J_c values (Fig. 5.6) unlike the observed behaviour for non-milled samples. Besides, C-doped

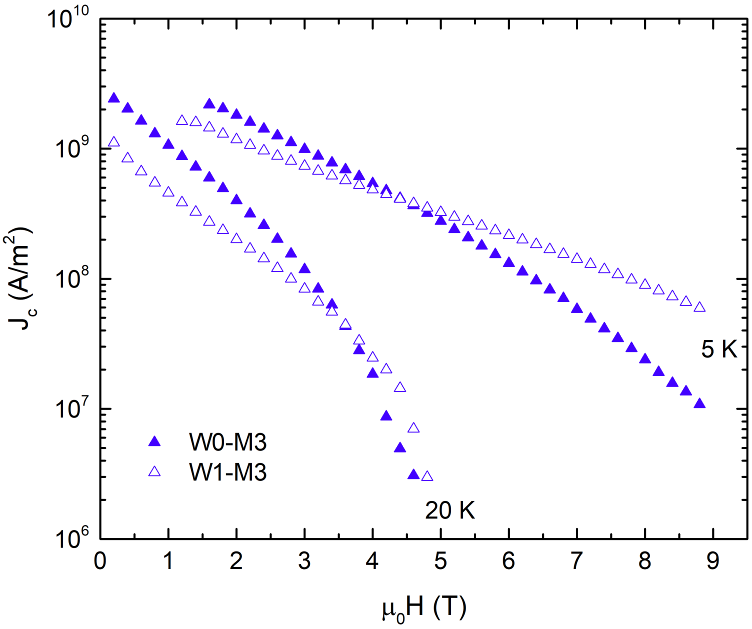

Figure 5.5: Inductive $J_c(H)$ values at 5 K and 20 K for high energy milled samples, non-doped (W0-M3) and C-doped (W1-M3).

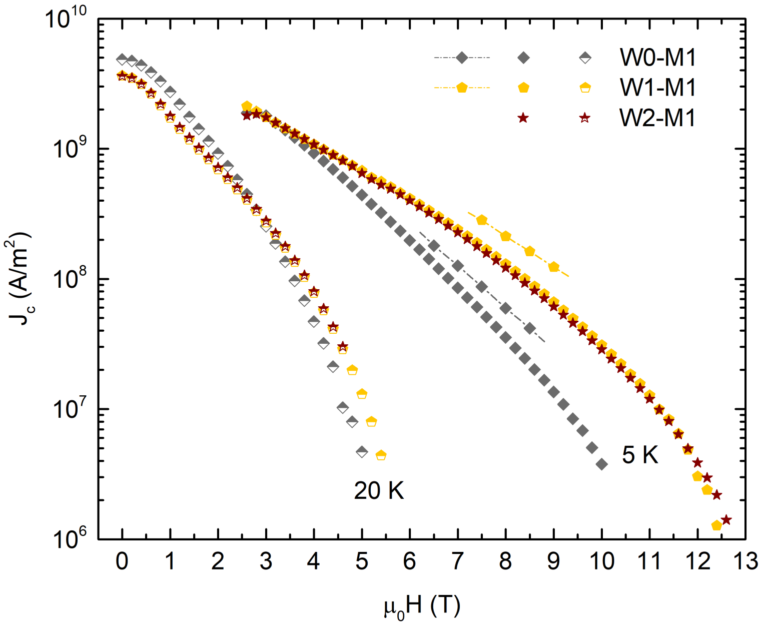

Figure 5.6: Magnetic field dependence of inductive J_c values (symbols without lines) at 5 K (solid symbols) and 20 K (semi-solid symbols) for non-doped, W0-M1, and doped samples, W1-M1 and W2-M1. Transport $J_c(H)$ values at 4.2 K are displayed with solid symbols with lines.

M1 samples still retain the microstructural benefits previously discussed in Chapter 4, but enhancing the $J_c(H)$ in high magnetic fields (up to 4 times at 8.5 T). Note that different pieces of the same wire were measured in the PPMS system, observing very similar J_c values in all of them (with differences smaller than 10 % among samples).

In conclusion, we have obtained a very uniform microstructure and superconducting reproducibility in wires made from precursor powders with oleic acid addition when using low energy milling conditions (M1). Unlike the case of non-milled powders, both used C doping routes result in wires with very similar superconducting properties when using this milling process. In terms of transport J_c's, we observe an increase of J_c with doping from $\sim 3 \times 10^7\,\mathrm{A\,m^{-2}}$ in W0-M1 to $\sim 1.3 \times 10^8\,\mathrm{A\,m^{-2}}$ in W1-M1, at 4.2 K and 9 T, similarly to the behaviour obtained by other authors using other carboxylic acids as C source [95, 96, 130, 131]. Further optimization of the wires would require a better control of the precursor packing process, from the planetary ball mill to the iron tube, which should be done in argon atmosphere to minimize the amount of oxygen content in the precursor powders.

Chapter 6

Magneto-optical imaging of MgB_2 tapes

In order to further analyse the superconducting behaviour and homogeneity of the conductors made from ball milled precursor, and to explore the reasons for the previously seen J_c decrease at low magnetic fields, in this chapter the local magnetic flux distribution inside MgB_2 tapes made from the wires have been analysed using MO imaging. This technique, which is based on the rotation of the polarization plane of light passing through a magnetized ferrimagnetic garnet film (Faraday effect), has been previously used to visualize the magnetic flux distribution in HTS [154–158] and MgB_2 [159,160] superconductors.

Local superconducting properties obtained by MO imaging have been correlated with magnetization measurements and microstructural observations by FESEM for these MgB_2 samples.

6.1 MO imaging set-up and sample preparation

Magnetic flux distribution was visualised using MO imaging technique. As field sensor we used in-plane magnetized bismuth-substituted iron garnet sensor films, as described in [154,155,158,161], which provide strong rotation in a weak magnetic field and give a desirable sensitivity and spatial resolution for monitoring the local magnetic field on the surface of the films. A scheme of the MO microscope used in these experiments can be seen in Figure 6.1. The MO indicator film is placed directly on top of the polished surface of the sample and the light is reflected from the mirror on the bottom of the film before going into the analyser of the optical system set above the sample holder. The brightness of the images obtained with crossed polarizers represents the absolute value of the magnitude of the z-component of the local magnetic field in the sample.

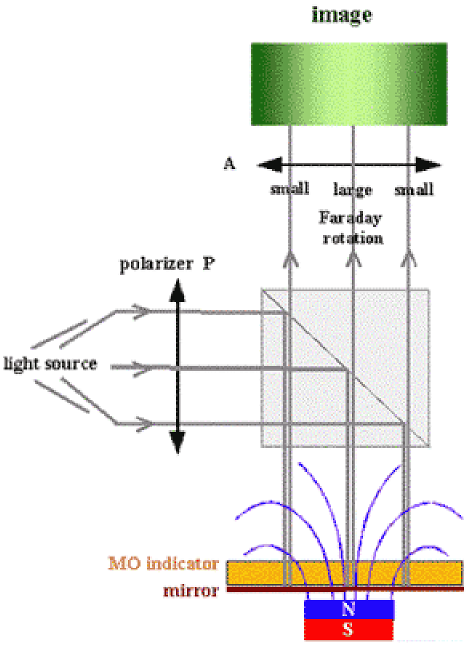

Figure 6.1: Schematic set-up of the MO polarization microscope used for the experiments.

A polarized-light microscope and a charge coupled device (CCD) is used to capture and process the digital images obtained in the experiments. The microscope consists of a stabilized light source, a polariser, an analyser and optical components to project the image plane into the CCD camera with various magnifications. All optical components, especially the objective lenses, have small Verdet constants [157] in order to avoid the depolarization of the light beam. The MO measurements were carried out in reflective mode and the sensitivity is determined by the thickness of the magneto-optical layer crossed by the light. These measurements were performed in collaboration with the

Superconductivity Group at the University of Oslo (Norway) during my stay.

The main advantage of MO imaging technique is that it allows the analysis of the local superconducting properties, whereas other techniques, such as AC susceptibility, DC magnetization and transport critical current, give average values of the overall measured sample. On the other hand, MO imaging technique also has some limitations, since the applied magnetic fields, which are typically produced by an electromagnet, are rather low. Moreover, the sample has to be as flat as possible in order to obtain good contact between its surface and the MO indicator. Therefore a complementary analysis of the superconducting sample by using the aforementioned techniques together with microstructural observations would be very useful.

Originally, the samples proceed from the wires manufactured as explained in Chapter 3. In order to obtain flat samples, some pieces of these wires were cold rolled to tapes in consecutive steps until reaching $\sim 2\,\mathrm{mm}$ width and $\sim 0.4\,\mathrm{mm}$ thickness, before the final annealing. Then, pieces of length $\sim 10-13\,\mathrm{cm}$ were sealed to prevent oxidation, and were heat treated at 670 °C for 5 h in vacuum (0.1 mbar) to form the superconducting MgB_2 phase.

The analysed tapes T0-M1, T0-M3 and T0-M4 were made from the milled wires W0-M1, W0-M3 and W0-M4, respectively. Besides, a tape, T0, was made from the non-milled wire W0 to be used as a reference.

6.2 Correlation between MO images and microstructure

Magneto-optical imaging was performed to evaluate the homogeneity of the superconducting properties across and along the tapes. One of the tapes' faces was polished to remove the Fe sheath, so that there is not magnetic shielding by the ferromagnetic Fe sheath under perpendicular fields and gives direct access to the superconducting core both in MO experiments and microstructural FESEM analysis.

Figure 6.2 shows FESEM and MO images of tapes made from powders with increasing milling energies from top to bottom. FESEM and MO images correspond to the same area of the sample, except in Fig. 6.2 (d) where different areas of the same tape were analysed due to technical reasons. FESEM images were taken with the SE detector to analyse the topographical differences among the samples. MO images were taken after zero-field cooling (ZFC) the sample from a temperature above T_c down to 20 K, then applying a field of 85 mT perpendicular to the sample surface and finally reducing the field to zero, to show the remnant flux density. It should be noted that the length of the tapes analysed by MO imaging is about five times larger than the core width ($\sim$ 10 and $\sim$ 2 mm, respectively) in all samples. MO images shown in Fig. 6.2 reveal that the maximum applied field of 85 mT is below the field of full penetration, H_p, at 20 K in all samples. For example, $M(H)$ curves measured in different pieces of the same tapes, gave estimations of $\mu_0 H_p \sim 800\,\mathrm{mT}$ and $\sim 400\,\mathrm{mT}$ for T0-M1 and T0-M3, respectively.

As previously mentioned in Chapter 4, upon increasing the milling energy, the microstructure of the superconducting cores changes gradually, forming smaller grains and voids, but also producing variations on the voids orientation [136,162]. The FESEM images of the tapes shown in Fig. 6.2 follow the same trend. In the specimen made from non-milled powders (Fig. 6.2 (a)-left), elongated voids parallel to the tape axis, with size of several hundred microns, are observed. The shape of the magnetic flux front obtained by MO imaging, Fig. 6.2 (a)-right, follows this porous structure. It must be remarked that the orientation and shape of the voids in this sample facilitates the magnetic flux penetration from both left and right ends towards the centre, compared to the other analysed samples. Note that the upper and the lower bright horizontal lines observed along the edges of tapes in MO images correspond to the MO contrast from the edges of Fe-sheath where a concentration of the magnetic flux take place.

The FESEM images shown in Fig. 6.2 indicate that the use of precursors with increasing milling energy decreases gradually the porosity of the final tape, as it happens with the wires. The MO image of the tape made with low-energy milled precursors, T0-M1, Fig. 6.2 (b)-right, shows good and homogeneous superconducting properties. Note that during polishing of this tape, some Fe particles from the tape's sheath were dragged towards the superconducting core surface (light grey particles in FESEM, Fig. 6.2 (b)-left). This also occurred during the wire's polishing, see Figs. 4.4 and 5.2.

(a) T0 (non-milled)

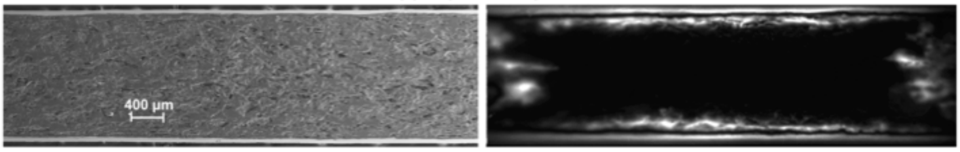

(b) T0-M1 (200 rpm, 1.5 h)

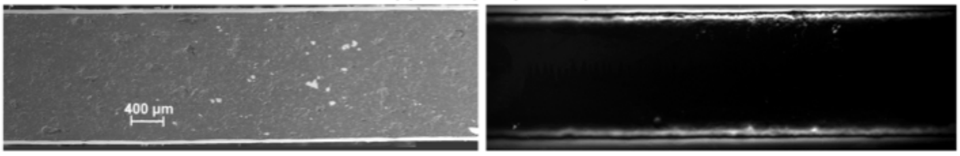

(c) T0-M3 (400 rpm, 3 h)

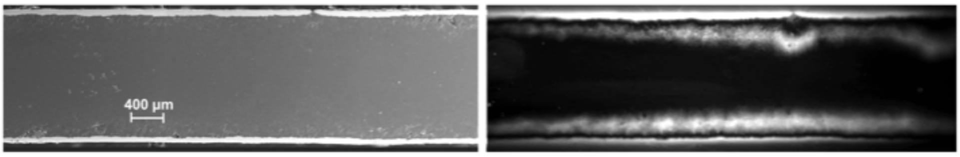

(d) T0-M4 (400 rpm, 16.5 h)

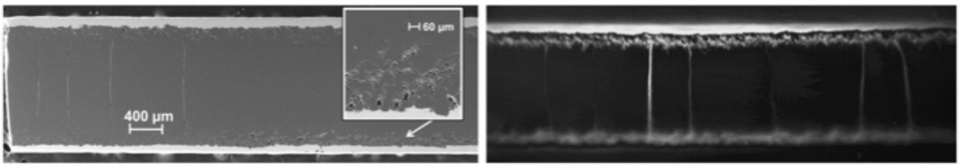

Figure 6.2: FESEM (left) and corresponding MO images (right) of different tapes made from powder with increasing milling energies from top to bottom. FESEM images were taken with the SE detector. MO images were taken after ZFC to 20 K, then applying a field of 85 mT perpendicular to the tape and finally removing the field. FESEM and MO images correspond to the same area, except in (d) where images of different areas of the same tape were analysed. The inset in (d) shows a magnified image of the core near the sheath edge. The same magnification was used for both FESEM and MO images.

Tape T0-M3, Fig. 6.2 (c)-left, has a dense core but also some microstructural defects, such as pores in the Fe sheath (seen in the upper-side of the image), which affect significantly the superconducting properties of the core around, as it is seen in Fig. 6.2 (c)- right. This sample also has a region with lower local J_c (deeper penetration of the magnetic flux) in the upper-right part of the image, which, again, coincides with a microstructural defect.

Finally, the tape made from the highest energy milled precursor (T0-M4) has cracks perpendicular to the long direction of the tape, as clearly seen in Fig. 6.2 (d)-left. MO image (Fig. 6.2 (d)-right) also shows a deep magnetic flux penetration along these cracks that cross the superconducting core and strongly decrease J_c in this tape. During mechanical deformation, the fine-milled precursor forms highly dense blocks separated by less-denser packed powders or even cracks that cross the tape from side to side perpendicular to it. This forms the brick-like structures that cannot be restored by the final heat treatment. Moreover, FESEM images show that the core is very dense in the centre of this tape, while at the edges (upper and lower areas in Fig. 6.2 (d)-left), microstructural defects such as cracks and voids are present, which produce magnetic flux patterns with a ripple-like shape, as shown in Fig. 6.2 (d)-right.

Since the reasons of the observed deterioration of superconducting properties in the sample T0-M3 were unknown, further MO experiments and FESEM analysis were performed, comparing it with tape T0-M1, which shows the best behaviour among the analysed tapes. With this purpose, MO images were recorded with the following thermal and magnetic history: the tape was field-cooled (FC) from $T > T_c$ in a perpendicular field of 17 mT down to 20 K. Next, after stabilizing the temperature, the field was decreased to zero. Subsequently, the field amplitude was increased again but in the opposite direction to -85 mT, and finally returned back to zero. The results for tapes T0-M3 and T0-M1 are shown in Figs. 6.3, 6.4 and 6.5. Figs. 6.3 and 6.4 show MO images of the sample T0-M3 with similar field and temperature histories at 20 K and 5 K, respectively. The corresponding $M(H)$ curves but measured in different pieces of the same tapes, are also included in these figures. MO images taken in a field-cooled sample following this specific magnetic field protocol highlights the distortions in the magnetic pattern so that it is helpful to reveal inhomogeneities in the superconductor.

Figure 6.3 shows MO images of tape T0-M3 taken at different magnetic fields during this measurement. The image (not shown) taken just after field cooling the sample to 20 K in 17 mT, displays a uniform grey background. Upon decreasing the field to zero (b) a magnetic flux inhomogeneity (area marked by an arrow) becomes visible in the MO image, and gets clearer when further increasing the field amplitude in the opposite direction, as shown in images (c) and (d). Note that at the magnetic field of -85 mT, shown in (d), the shape of the penetration front is similar to that in Fig. 6.2 (c).

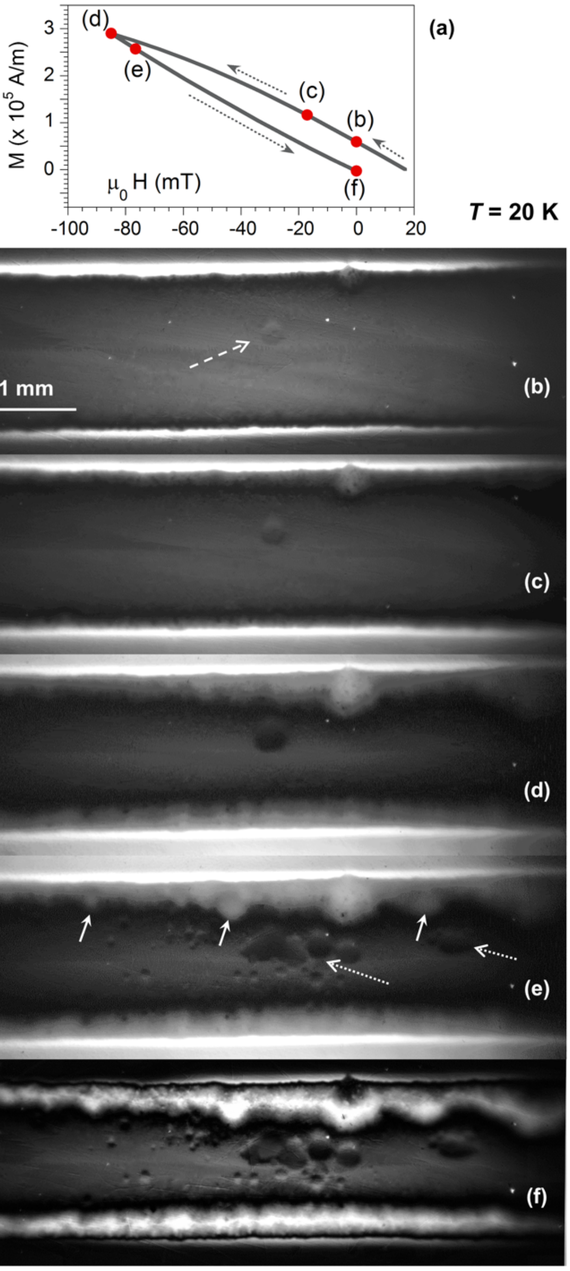

Figure 6.3: (a) Magnetization values, $M(H)$, and (b)-(f) MO images of the tape T0-M3 at different fields after FC in 17 mT down to 20 K, then changing the field to −85 mT and finally removing the field. The images correspond to: (b) 0 mT, (c) −17 mT, (d) −85 mT, (e) −76.5 mT and (f) 0 mT, as marked in (a). The magnetic field is applied perpendicular to the tape. The MO images correspond to the same sample used in measurements of Fig. 6.2 (c), while $M(H)$ was measured in a different piece.

When slightly decreasing the amplitude of the field again to $-76.5\,\mathrm{mT}$, image (e), some new features in the penetration field front appear suddenly in the upper part of the image (at positions marked with continuous arrows), and also some “bubble like shape” magnetic inhomogeneities are formed in the central part of the sample (marked by dotted arrows). Finally, MO image (f) shows the trapped field, which has similar pattern as in (e) but with the expected dark-bright-dark profile revealing the existence of flux-antiflux areas due to hysteresis and the performed thermal-magnetic history. It must be remarked that the left part of this sample shows good homogeneity and better superconducting properties than the centre and right part of the sample.

Note that the initial round inhomogeneity is observed in the same position in all measurement runs performed both at 5 and 20 K. While the bubble-like feature that suddenly forms in the same place have not always the same structure. This can be seen in Figure 6.4, which shows MO images with similar features as at 20 K. Note that “bubble like” structure is also suddenly formed in the same area, but it is not exactly the same as in Figure 6.3. In this particular measurement these “bubbles” were formed in the upper branch, when increasing the magnetic field amplitude from $\sim 68\,\mathrm{mT}$ to $\sim 76\,\mathrm{mT}$. This behaviour suggests the existence of poor superconducting connectivity between regions in this part of the sample.

For comparison, Fig. 6.5 shows the MO images of T0-M1 tape under thermal and magnetic histories similar to those in Fig. 6.3. It must be emphasised that the values of $M(H)$ in the upper and lower branches are very similar, indicating small penetration of the magnetic field and therefore higher J_c values in sample T0-M1 compared to T0-M3. That is also in agreement with observations in ZFC measurements shown in Fig. 6.2. This tape presents indeed a very homogeneous magnetic flux profile and therefore only both images taken in zero-field are shown: in the decreasing (b) and increasing (c) field branch. Note that the Fe particles present in the surface of the core (Fig. 6.2 (b)-left) are well visible in MO images after field-cooling the sample, but do not have any influence in the superconducting behaviour of this tape, as expected.

The magnetic inhomogeneities observed in FC MO images of tape T0-M3 in Figs. 6.3 and 6.4 could be due to the presence of cavities or holes, or to the existence of poor superconducting links between regions within this

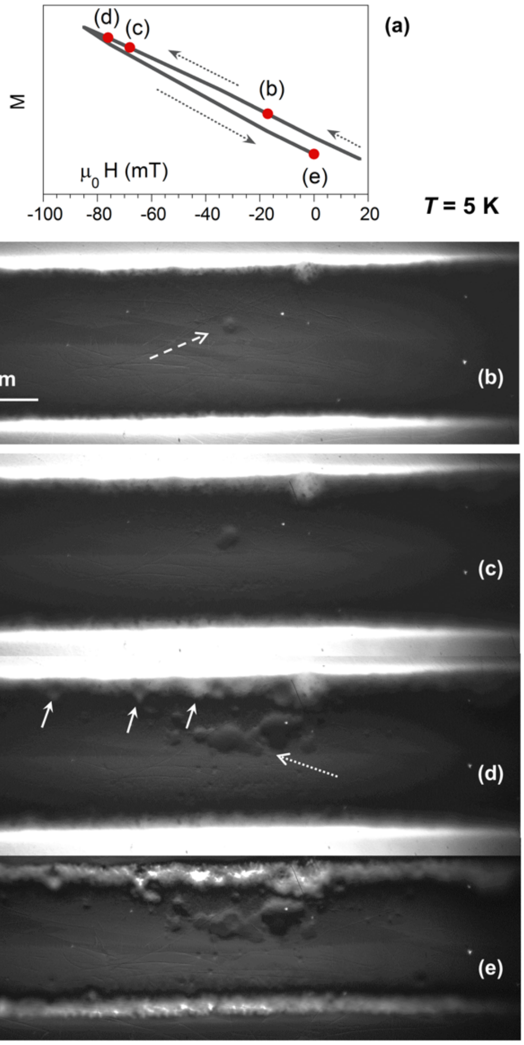

Figure 6.4: MO images of the tape T0-M3 at different fields after FC in 17 mT down to 5 K, then changing the field to −85 mT and finally removing the field. The images correspond to: (b) −17 mT, (c) −68 mT, (d) −76 mT and (e) 0 mT, as marked schematically in (a). The magnetic field is applied perpendicular to the tape. $M(H)$ at 5 K was not measured so a scheme, (a), is shown for clarity purposes.

sample. A further analysis by FESEM of this tape discards the existence of cavities, and confirms the formation of aggregates of MgB_2 poorly connected with each other, which are observed in this part of the sample, as shown in Fig. 6.6 (b). The observed grain structure resembles the microstructure of some *ex situ* MgB_2 materials [163]. By contrast, other areas of this tape,

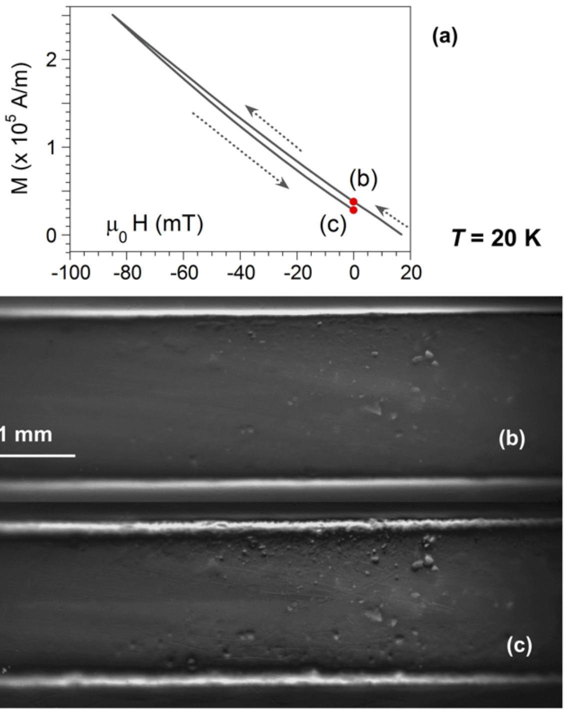

Figure 6.5: (a) Magnetization values, $M(H)$, and (b)-(c) MO images of the tape T0-M1 in zero-field of the upper and lower branch, respectively, as marked in (a). Similar thermal and magnetic history as in Fig. 6.3 was performed: the sample was FC in 17 mT down to 20 K, the field was then changed to −85 mT and finally returned back to zero. The sample of MO images is the same as in Fig. 6.2 (b), while $M(H)$ was measured in a different piece.

with higher J_c and good homogeneity according to MO images (left area in Fig. 6.3), show well connected grains as it is seen in Fig. 6.6 (a). It must be remarked that the FESEM images of tapes made with non-milled, Fig. 6.6 (c), and milled precursors with milling conditions M1, Fig. 6.6 (d), show well-connected superconducting grains.

6.3 Comparison of J_c for wires and tapes

In order to explore deeper the similarities and differences among wires and tapes, a comparison of the $J_c(H)$ values of the wire and tape prepared with the optimum milling condition M1 was carried out. In Figure 6.7, W0-M1 and

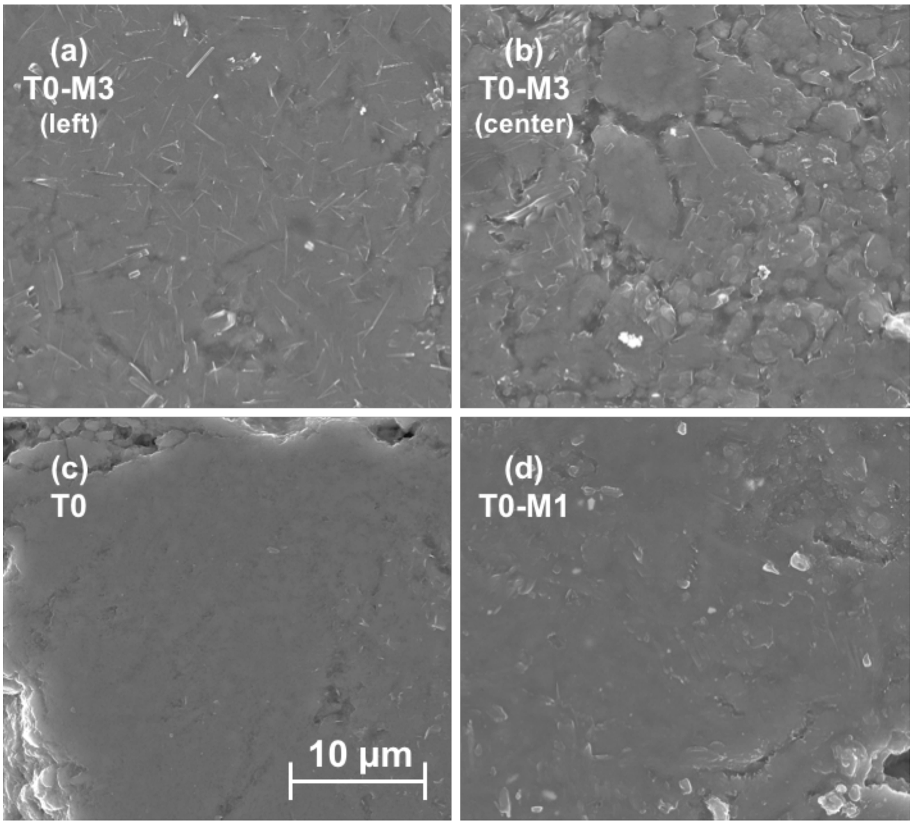

Figure 6.6: FESEM images (SE detector) of the tape T0-M3 in the left region (a), where J_c is higher, and in the central area (b) where"bubble like shape" magnetic inhomogeneities are seen in Figs. 6.3 and 6.4. Image (c) is of the tape with non-milled precursor and (d) of T0-M1. The same magnification has been used in all images.

T0-M1's inductive J_c values at 5 K and 20 K are shown. Wire W0-M1 was chosen due to the favourable balance between its $J_c(H)$ dependence and its desirable microstructural properties, such as good phase homogeneity and the absence of big voids or/and cracks.

As for the wires, to avoid magnetic field shielding by the wire Fe-sheath during magnetic measurements, a gentle mechanical polishing until obtaining samples of an approximately size of $2 \times 4 \times 0.3$ mm. The $J_c(H)$ values of the tapes were estimated from the width of the isothermal hysteresis loop, $\Delta M(H)$, measured with magnetic field applied perpendicular to the tape surface, using the equation [164]:

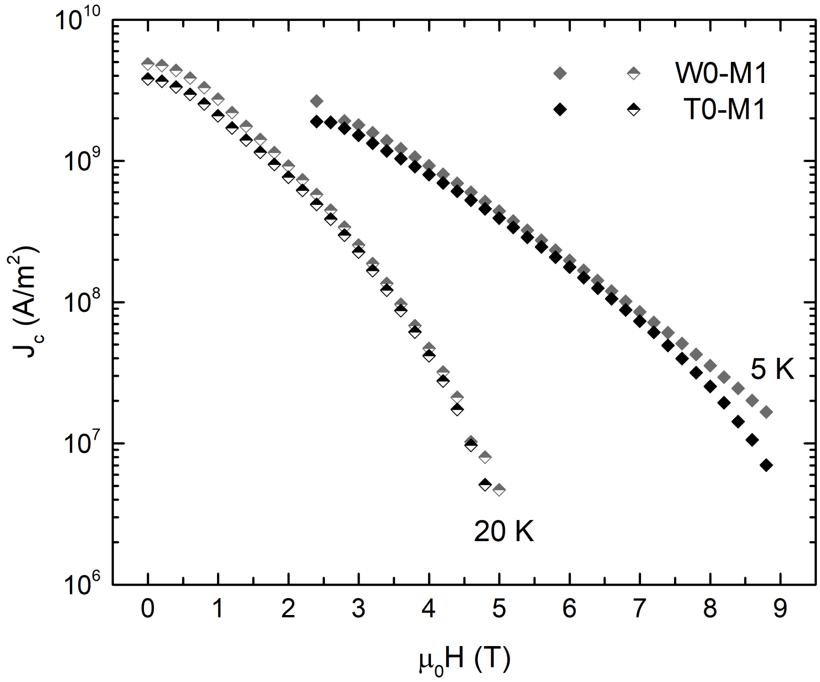

Figure 6.7: Magnetic field dependence of inductive J_c at 5 K and 20 K of non-doped ball milled wire W0-M1 and tape T0-M1. Note that tapes T0-M1 for $M(H)$ and MO imaging are different pieces of the same tape.

$$J_c(H) = \frac{\Delta M(H)}{a \cdot \left(1 - \frac{a}{3c}\right)}. \tag{6.1}$$

Here $2a$ and $2c$ ($a \leq c$) are the dimensions of the samples perpendicular to the applied field. It can be seen that the obtained $J_c(H)$ values for wires and tapes are similar in a wide range of fields both at 5 and 20 K. The only exception is at 5 K and $\mu_0 H > 7.5 - 8.0$ T, where J_c decreases more abruptly in the tape than in the corresponding wire, probably due to their different geometries.

Further insight into the flux front profile behaviour of this T0-M1 tape is presented in Figure 6.8. This corresponds to the same tape as in Figs 6.2 (b) and 6.5. The MO images show the remnant-trapped field at different temperatures below T_c (5 K, 20 K, 30 K or 34 K) after ZFC, applying a maximum perpendicular field of 85 mT and finally reducing the field to zero. Therefore the distance of the maximum brightness to the tape's edges would be roughly half of the penetration depth reached at this maximum applied field. At 5, 20 and 30 K, the magnetic flux front penetrates homogeneously into the tape from the edges. Field penetration through the ends is seen in the images taken at 30 K and above. At 34 K, the proximity to $T_c \approx 37.5\,\mathrm{K}$ enhances inhomogeneities along the tape, as displayed in Figure 6.8 (d). There is almost full magnetic flux penetration at some positions, indicating an induction penetration field, $\mu_0 H_p$, slightly higher than 85 mT at 34 K. Note that the Fe particles observed by FESEM (Fig. 6.2 (b)-left) are also seen by MO imaging in Figure 6.8 (d).

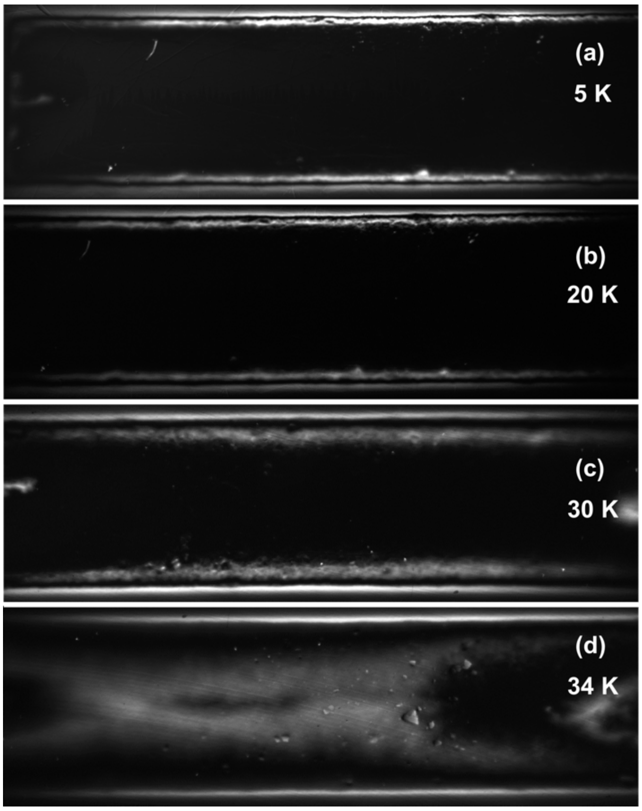

Figure 6.8: MO images of tape T0-M1. The tape was zero-field cooled down to (a) 5 K, (b) 20 K, (c) 30 K and (d) 34 K. Then the field was increased to 85 mT and finally set to zero.

Brandt [165] gives numerical calculations of the perpendicular flux density profiles for long conductors of different thickness to width ratio ($2b/2a$) in perpendicular fields and as a function of the applied field, H/H_p, where H_p depends on J_c, a and b. By comparing the flux front penetration observed in MO images of Figure 6.8 with those given by Brandt's simulations for $b/a \sim 0.1$ (as in this sample), it is possible to get rough estimations for J_c of $\sim 4 \times 10^9\,\mathrm{A\,m^{-2}}$ and $\sim 1.5 \times 10^9\,\mathrm{A\,m^{-2}}$ at 20 K and 30 K, respectively, at applied field of 85 mT, which shows good correspondence with J_c estimations given by $M(H)$ measurements (see Fig. 6.7).

Figure 6.9 shows the $M(H)$ hysteresis loop measurement of sample T0-M1 at 34 K after having removed most of the Fe-sheath. The value of penetration field $\mu_0 H_p$ at that temperature can be estimated to be $\sim 85 \pm 5\,\mathrm{mT}$, which is in good agreement with MO image observed in Fig. 6.8 (d). The remnant Fe-sheath adds a ferromagnetic signal to the superconducting one in the whole $M(H)$ loop.

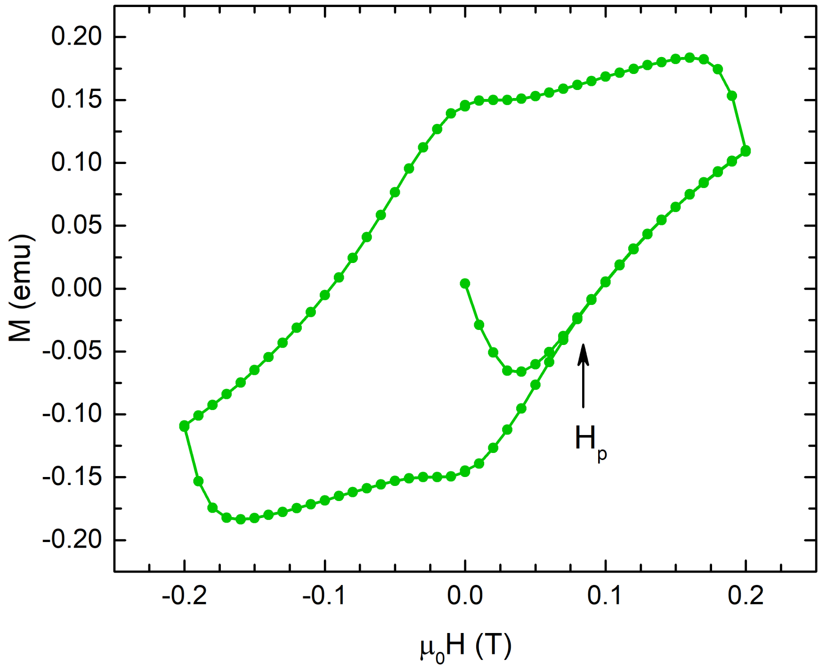

Figure 6.9: Magnetization, M, as a function of the perpendicularly applied magnetic field, $\mu_0 H$, of tape T0-M1 at 34 K. Induction penetration field, $\mu_0 H_p$, is $\sim 85 \pm 5\,\mathrm{mT}$. Note that there are some remnants of the Fe sheath in the sample, which add a ferromagnetic signal to the superconducting signal.

6.4 Dendritic avalanches in MgB_2 tapes

During this thesis work, six MgB_2 tapes were synthesized and characterized by MOI. In one of them, T2-M1, of approximately 50 µm thick after having polished the Fe sheath in one of the sides, dendritic avalanches were unexpectedly observed. It is also worth pointing out that the other five tapes, with a thickness in the range 150-250 µm, which did not show dendritic avalanches in MO imaging, displayed flux jumps registered by magnetometry at higher fields. However, this field range is above the saturation field of the ferrite garnet films used in the present work. This can be seen in Figure 6.10, which shows the field profile after ZFC the tape down to 5 K and then the magnetic field is increased in several steps up to the maximum applied field (85 mT) perpendicular to the tape. MO images were taken during this field ramp, and images in the figure corresponds to applied magnetic fields of (a) 17 mT, (b) 34 mT, (c) 51 mT, (d) 68 mT and (e) 85 mT. The tape is dark and the area outside of its boundaries is brighter, which shows that the tape expels magnetic field. The bright horizontal lines at the upper and lower edges of the tape are from the ferromagnetic contribution of the remaining iron sheath at the edges. Bright flux front propagating into the sample when increasing the field shows advancement of magnetic flux.

In addition to smooth flux penetration, Figure 6.10 clearly shows that specific dendritic avalanches are formed, which were not observed in the other five tapes characterized by MO imaging. The observed dendrites have a branch-like structure that resembles lightning and appear suddenly. The first dendrites are small and as the applied magnetic field increases, new larger dendrites appear. Besides, the small dendrites at lower fields do not have as many branches as those appearing at higher fields.

A systematic study of the observed dendritic avalanches in this tape was carried out in order to understand their nature and behaviour [166]. The spatial structure of the thermomagnetic avalanche events was resolved, and the reproducibility and nucleation thresholds were determined. This study was done in collaboration with the group of the University of Oslo and it is part of the PhD thesis of T. Qureishy. Here we just summarize the main conclusions of this study.

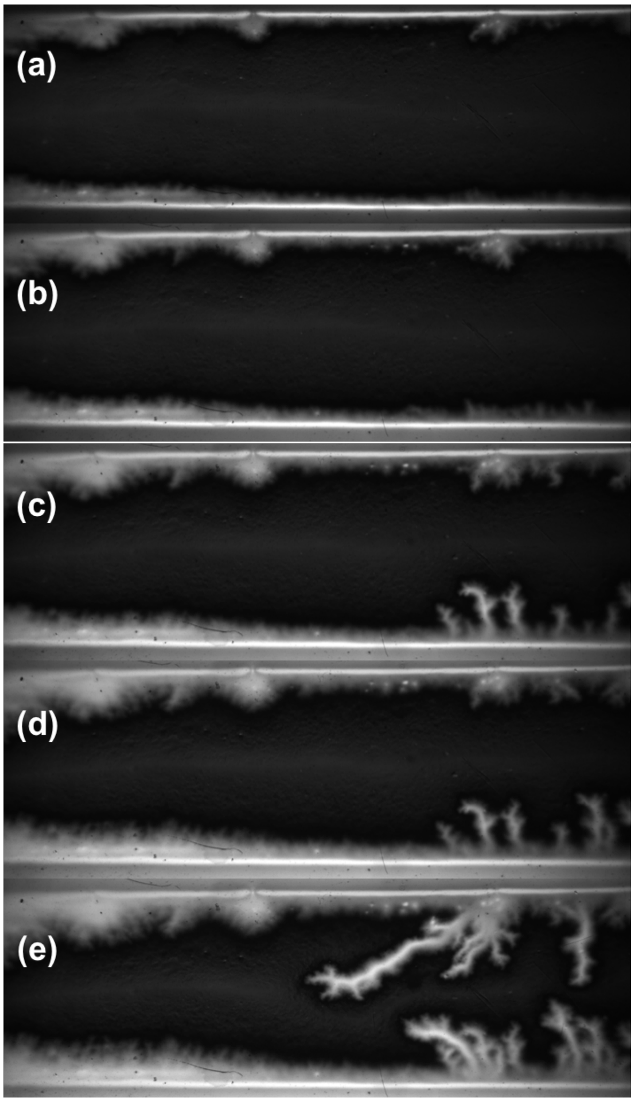

Figure 6.10: MO images of the tape T2-M1 (made from wire W2-M1) at different fields. For this measurement the sample was cooled down to 5 K in zero field. Once the temperature is stable, the magnetic field is increased up to 85 mT. Images are taken during this field ramp at different fields: (a) 17 mT, (b) 34 mT, (c) 51 mT, (d) 68 mT and (e) 85 mT. The magnetic field is applied perpendicular to the tape surface.

The dendritic avalanches in the tape have similar properties to those appearing in thin films, but have relatively few branches. Their patterns are in most cases non-reproducible. The few cases of reproducibility of dendritic formations in this sample were attributed to the presence of defects, probably cracks, near the edges. The average size of new dendritic avalanches, as well as their branching, increases with the increase of applied magnetic field. Upon increasing the temperature, the number of avalanches decreases. The lower threshold magnetic field for their appearance first increases slowly with increasing temperature and then increases rapidly above 8 K. The analysis of the threshold field indicated that the onset may be dictated by the edge properties of the tape.

Dendritic avalanches have also been observed by MO imaging in different superconductors, such as cold-rolled 0.42 mm thick $Nb_{52}Zr_{48}$ and 0.06 mm thick $Nb_{75}Zr_{25}$ foils [167]. The spatial structure of a dendritic avalanche and the exact applied field and temperature at which it occurs are usually unpredictable, and they propagate at a speed of around $5\,\mathrm{km\,s^{-1}}$ [168, 169] and up to $180\,\mathrm{km\,s^{-1}}$ [170]. They have upper and lower threshold fields for increasing and decreasing applied magnetic fields [171]. Dendritic avalanches have a threshold temperature as well, which in MgB_2 films is about 10 K when applying a field from zero and about 13 K when decreasing the field [172].

Chapter 7

Conclusions

We have analysed the effect of precursor ball milling on the properties of monocore Fe-sheathed $\mathrm{MgB_2}$ wires and tapes prepared by the *in situ* powder-in-tube (PIT) method by using drawing and rolling techniques. The effect of milling energies per unit mass in the range between 1.2×10^6 and $1 \times 10^8\,\mathrm{J\,kg^{-1}}$ (above the mechanical alloying limit) on the superconducting properties of these conductors have been analysed.

Ball milling the precursor influences heavily the conductor's microstructure, enhancing vortex pinning at high magnetic fields. Thus, the highest J_c's at 5 K and $\mu_0 H > 5\,\mathrm{T}$ correspond to the conductor made from the highest energy milled precursor. Nevertheless, the use of the precursor with milling energies above a certain limit produces microstructural defects during mechanical deformation, resulting in the formation of large transversal cracks, which indicates that using just drawing to deform the wire is not appropriate to fabricate conductors from high energy milled precursor powders. Other types of mechanical deformation could be more suitable for our experimental conditions, such as swaging because it produces larger radial compressional stress in the core than drawing during wire deformation.

The wire and tape fabricated from the precursor with the lowest milling energy shows good homogeneity with very reproducible J_c values. Thus this solves the phase inhomogeneity problems found in non-milled and C-doped wires. Besides, the combination of this milling energy and C doping enhances J_c at high magnetic fields and retains homogeneous microstructures.

Further optimization of the wires and tapes made from milled precursor (doped and non-doped) would require a better control of the precursor packing process, from the planetary ball mill to the iron tube, which should be done in argon atmosphere to minimize the amount of oxygen content in the precursor powders.

Magneto-optical (MO) imaging analysis has been performed in order to investigate magnetic flux penetration in these samples, revealing local J_c variations in some of these superconductors and allowing further understanding of the reasons of the observed J_c deterioration at low magnetic fields frequently observed when the milling energy of the precursor powders is increased. It was found that microstructural characteristics affect significantly the magnetic flux front propagation observed by MO imaging at zero-field-cooled and field-cooled conditions. MO imaging performed in field-cooled samples, following a specific magnetic field sequence, highlights the distortions in the magnetic pattern so that it has been found very helpful to reveal inhomogeneities in the superconductor. The MO images have been correlated with microstructural features observed with field-emission scanning electron microscopy (FESEM), such as small cracks, sheath pores or weakly-linked aggregates of MgB_2 grains present in some of the analysed tapes.

Bibliography

[1] Nagamatsu, J., Nakagawa, N., Muranaka, T., Zenitani, Y., Akimitsu, J., “Superconductivity at 39 K in magnesium diboride”, *Nature* **410**, 63 (2001).

[2] Penco, R., Grasso, G., “Recent developement of MgB_2-based large scale applications”, *IEEE Trans. Appl. Supercond.* **17**, 2291 (2007).

[3] Hascicek, Y. S., Akin, Y., Baldwin, T. W., Rindfleisch, R. R., Yue, J., Sumption, M. D., Tomsic, M., “A MgB_2 12.5 kV A superconductor transformer”, *Supercond. Sci. Technol.* **22**, 065002 (2009).

[4] Kajikawa, K., Nakamura, T., “Proposal of a fully superconducting motor for liquid hydrogen pump with MgB_2 wire”, *IEEE Trans. Appl. Supercond.* **19**, 1669 (2009).

[5] Terao, Y., Sekino, M., Ohsaki, H., “Electromagnetic design of 10 MW class fully superconducting wind turbine generators”, *IEEE Trans. Appl. Supercond.* **22**, 5201904 (2012).

[6] Sander, M., Gehring, R., Neumann, H., “LIQHYSMES - A 48 GJ toroidal MgB_2 -SMES for buffering minute and second fluctuations”, *IEEE Trans. Appl. Supercond.* **23**, 5700505 (2013).

[7] Patel, A., Giunchi, G., Figini Albisetti, A., Shi, Y., Hopkins, S. C., Palka, R., Cardwell, D. A., Glowacki, B. A., “High force magnetic levitation using magnetized superconducting bulks as a field source for bearing applications”, *Phys. Procedia* **36**, 937 (2012).

[8] Sugano, M., Ballarino, A., Bartova, B., Bjoerstad, R., Scheuerlein, C., Grasso, G., “Characterization of mechanical prop-

erties of MgB_2 conductor for the superconducting link project at CERN", *IEEE Trans. Appl. Supercond.* **25**, 4801004 (2015).

[9] Tomsic, M., Rindfleisch, M., Yue, J., McFadden, K., Phillips, J., "Overview of MgB_2 superconductor applications", *Int. J. Appl. Ceram. Technol.* **4**, 250 (2007).

[10] Paramed OpenSky MRI scanner, `http://www.paramed.it/medical-systems/open-sky-0000111.html`.

[11] Martínez, E., Angurel, L. A., Navarro, R., "Study of Ag and Cu/MgB_2 powder-in-tube composite wires fabricated by *in situ* reaction at low temperatures", *Supercond. Sci. Technol.* **15**, 1043 (2002).

[12] Zhou, S., Pan, A. V., Ionescu, M., Liu, H., Dou, S. X., "Influence of Ag, Cu and Fe sheaths onMgB_2 superconducting tapes", *Supercond. Sci. Technol.* **15**, 236 (2002).

[13] Grovenor, C. R. M., Goodsir, L., Salter, C. J., Kováč, P., Hušek, I., "Interfacial reactions and oxygen distribution in MgB_2 wires in Fe, stainless steel and Nb sheaths", *Supercond. Sci. Technol.* **17**, 479 (2004).

[14] Kováč, P., Hušek, I., Kopera, L., Melišek, T., Rosová, R., Dobročka, E., "Properties of *in situ* made MgB_2 in Nb or Ti sheath", *Supercond. Sci. Technol.* **26**, 025007 (2013).

[15] Braccini, V., Nardelli, D., Penco, R., Grasso, G., "Development of *ex situ* processed MgB_2 wires and their applications to magnets", *Physica C* **456**, 209 (2007).

[16] Glowacki, B. A., Majoros, M., Vickers, M., Evetts, J. E., Shi, Y., McDougall, I., "Superconductivity of powder-in-tube MgB_2 wires", *Supercond. Sci. Technol.* **14**, 193 (2001).

[17] Giunchi, G., Ceresara, S., Ripamonti, G., Di Zenobio, A., Rossi, S., Chiarelli, S., Spadoni, M., Wesche, R., Bruzzone, P. L., "High performance new MgB_2 superconducting hollow wires", *Supercond. Sci. Technol.* **16**, 285 (2003).

[18] Suo, H., Beneduce, C., Dhallé, M., Musolino, N., Genoud, J.-Y., Flükiger, R., "Large transport critical currents in dense Fe-

and Ni-clad MgB_2 superconducting tapes", *Appl. Phys. Lett.* **79**, 3116 (2001).

[19] Togano, K., Hur, J. M., Matsumoto, A., Kumakura, H., "Microstructures and critical currents of single- and multi-filamentary MgB_2 superconducting wires fabricated by an internal Mg diffusion process", *Supercond. Sci. Technol.* **23**, 085002 (2010).

[20] Hur, J. M., Togano, K., Matsumoto, A., Kumakura, H., Wada, H., Kimura, K., "Fabrication of high-performance MgB_2 wires by an internal Mg diffusion process", *Supercond. Sci. Technol.* **21**, 032001 (2008).

[21] Li, G. Z., Sumption, M. D., Susner, M. A., Yang, Y., Reddy, K. M., Rindfleisch, M. A., Tomsic, M. J., Thong, C. J., Collings, E. W., "The critical current density of advanced internal Mg diffusion processed MgB_2 wires", *Supercond. Sci. Technol.* **25**, 115023 (2012).

[22] Braccini, V., Malagoli, A., Tumino, A., Vignolo, M., Bernini, C., Fanciulli, C., Romano, G., Tropeano, M., Siri, A. S., Grasso, G., "Improvements of magnetic field behavior of *ex situ* processed magnesium diboride tapes", *IEEE Trans. Appl. Supercond.* **17**, 2766 (2007).

[23] Eisterer, M., "Magnetic properties and critical currents of MgB_2", *Supercond. Sci. Technol.* **20**, R47 (2007).

[24] Flükiger, R., Hossain, M. S. A., Senatore, C., "Strong enhancement of J_c and B_{irr} in binary *in situ* MgB_2 wires after cold high pressure densification", *Supercond. Sci. Technol.* **22**, 085002 (2009).

[25] Nardelli, D., Matera, D., Vignolo, M., Bovone, G., Palenzona, A., Siri, A. S., Grasso, G., "Large critical current density in MgB_2 wire using MgB_4 as precursor", *Supercond. Sci. Technol.* **26**, 075010 (2013).

[26] Flükiger, R., Suo, H. L., Musolino, N., Beneduce, C., Toulemonde, P., Lezza, P., "Superconducting properties of MgB_2 tapes and wires", *Physica C* **385**, 286 (2003).

[27] Flükiger, R., Hossain, M. S. A., Senatore, C., Buta, F., Rindfleisch, M., "A new generation of *in situ* MgB_2 wires with improved J_c

and B_{irr} values obtained by Cold Densification (CHPD)", *IEEE Trans. Appl. Supercond.* **21**, 2649 (2011).

[28] Wilke, R. H. T., Bud'ko, S. L., Canfield, P. C., Finnemore, D. K., Suplinskas, R. J., Hannahs, S. T., "Systematic effects of carbon doping on the superconducting properties of $Mg(B_{1-x}C_x)_2$", *Phys. Rev. Lett.* **092**, 217003 (2004).

[29] Collings, E. W., Sumption, M. D., Bhatia, M., Susner, M. A., Bohnenstiehl, S. D., "Prospects for improving the intrinsic and extrinsic properties of magnesium diboride superconducting strands", *Supercond. Sci. Technol.* **21**, 103001 (2008).

[30] Hörhager, N., Eisterer, M., Weber, H. W., Prikhna, T., Tajima, T., Nesterenko, V. F., "Ti and Zr doped MgB_2 bulk superconductors", *J. Phys.: Conf. Ser.* **43**, 500 (2006).

[31] Shekhar, C., Giri, R., Tiwari, R. S., Srivastava, O. N., Malik, S. K., "High critical current density and improved flux pinning in bulk MgB_2 synthesized by Ag addition", *J. Appl. Phys.* **101**, 043906 (2007).

[32] Kuševic, I., Babić, E., Husnjak, O., Soltanian, S., Wang, X. L., Dou, S. X., "Correlated vortex pinning in Si-nanoparticle doped MgB_2", *Solid State Commun.* **132**, 761 (2004).

[33] Shekhar, C., Giri, R., Tiwari, R. S., Rana, D. S., Malik, S. K., Srivastava, O. N., "Effect of La doping on microstructure and critical current density of MgB_2", *Supercond. Sci. Technol.* **18**, 1210 (2005).

[34] Wang, J., Bugoslavsky, Y., Berenov, A., Cowey, L., Caplin, A. D., Cohen, L. F., MacManus-Driscoll, J. L., Cooley, L. D., Song, X., Larbalestier, D. C., "High critical current density and improved irreversibility field in bulk MgB_2 made by a scaleable, nanoparticle addition route", *Appl. Phys. Lett.* **81**, 2026 (2002).

[35] Chen, S. K., Wei, M., MacManus-Driscoll, J. L., "Strong pinning enhancement in MgB_2 using very small Dy_2O_3 additions", *Appl. Phys. Lett.* **88**, 192512 (2006).

[36] Cheng, C., Zhao, Y., "Significant improvement of flux pinning and irreversibility field of nano-Ho_2O_3 doped MgB_2", *Physica C* **463**, 220 (2007).

[37] Pan, X. F., Shen, T. M., Li, G., Cheng, C. H., Zhao, Y., "Doping effect of Pr_6O_{11} on superconductivity and flux pinning of MgB_2 bulk", *Phys. Stat. Sol. (a)* **204**, 1555 (2007).

[38] Ansari, I. A., Shahabuddin, M., Ziq, K. A., Salem, A. F., Awana, V. P. S., Husain, M., Kishan, H., "The effect of nano alumina on structural and magnetic properties of MgB_2 superconductors", *Supercond. Sci. Technol.* **20**, 827 (2007).

[39] Rui, X. F., Zhao, Y., Xu, Y. Y., Zhang, L., Sun, X. F., Wang, Y. Z., Zhang, H., "Improved flux pinning behaviour in bulk MgB_2 achieved by nano-SiO_2 addition", *Supercond. Sci. Technol.* **17**, 689 (2004).

[40] Xu, G. J., Grivel, J.-C., Abrahamsen, A. B., Andersen, N. H., "Enhancement of the irreversibility field in bulk MgB_2 by TiO_2 nanoparticle addition", *Physica C* **406**, 95 (2004).

[41] Jiang, C. H., Hatakeyama, H., Kumakura, H., "Effect of nanometer MgO addition on the in situ PIT processed MgB_2/Fe tapes", *Physica C* **423**, 45 (2005).

[42] Jiang, C. H., Nakane, T., Kumakura, H., "Enhanced J_c-B performance in MgB_2/Fe tapes with nanometre Si_3N_4 addition", *Supercond. Sci. Technol.* **18**, 902 (2005).

[43] Ma, Y., Kumakura, H., Matsumoto, A., Hatakeyama, H., Togano, K., "Improvement of critical current density in Fe-sheathed MgB_2 tapes by $ZrSi_2$, ZrB_2 and WSi_2 doping", *Supercond. Sci. Technol.* **16**, 852 (2003).

[44] Bhatia, M., Sumption, M. D., Collings, E. W., "Effect of various additions on upper critical field and irreversibility field of *in situ* MgB_2 superconducting bulk material", *IEEE Trans. Appl. Supercond.* **15**, 3204 (2005).

[45] Fujii, H., Togano, K., Kamakura, H., "Enhacement of critical current density of *in situ* processed MgB_2 tapes by WB additon", *Supercond. Sci. Technol.* **16**, 432 (2003).

[46] Gao, Z., Ma, Y., Wang, D., Zhang, X., "Developement of doped MgB_2 wires and tapes for practical applications", *IEEE Trans. Appl. Supercond.* **20**, 1515 (2010).

[47] Takenobu, T., Ito, T., Chi., D. H., Prassides, K., Iwasa, Y., "Intralayer carbon substitution in the MgB_2 superconductor", *Phys. Rev. B* **64**, 134513 (2001).

[48] Xu, H.-L., Feng, Y., Xu, Z., Yan, G., Cao, L.-Z., Li, X.-G., "Enhacement of critical current density in graphite doped MgB_2 wires", *Chin. Phys. Lett.* **21**, 2511 (2004).

[49] Shimura, S., Machi, T., Nakao, K., Koshizuka, N., Tanaka, S., Mochizuki, K., Shibata, N., Ushio, K., "Graphite coating effects on the critical current characteristics of MgB_2/Cu wires fabricated by an *in situ* PIT method", *Physica C* **426**, 1254 (2005).

[50] Kováč, P., Hušek, I., Skákalova, V., Meyer, J., Dobročka, E., Hirscher, M., Roth, S., "Transport current improvements of *in situ* MgB_2 tapes by the additon of carbon nanotubes, silicon carbide or graphite", *Supercond. Sci. Technol.* **20**, 105 (2007).

[51] Shekhar, C., Giri, R., Tiwari, R. S., Srivastava, O. N., "Enhacement of flux pinning and high critical current density in graphite doped MgB_2 superconductor", *J. Appl. Phys.* **102**, 093910 (2007).

[52] Cheng, C. H., Zhang, H., Zhao, Y., Feng, Y., Rui, X. F., Munroe, P., Zeng, H. M., Koshizuka, N., Murakami, M., "Doping effect of nano-diamond on superconductivity and flux pinning in MgB_2", *Supercond. Sci. Technol.* **16**, 1182 (2003).

[53] Zhao, Y., Cheng, Z. H., Rui, X. F., Zhang, H., Munroe, P., Zheng, H. M., Koshizuka, N., Murakami, M., "Improved irreversibilty behavior and critical current density in MgB_2 -diamond nanocomposites", *Appl. Phys. Lett.* **83**, 2916 (2003).

[54] Cheng, C. H., Yang, Y., Munroe, P., Zhao, Y., "Comparison between nano-diamond and carbon nanotube doping effects on critical current density and flux pinning in MgB_2", *Supercond. Sci. Technol.* **20**, 296 (2007).

[55] Soltanian, S., Horvat, J., Wang, X. L., Munroe, P., Dou, S. X., "Effect of nano-carbon particle doping on the flux pinning properties of MgB_2 superconductor", *Physica C* **390**, 185 (2003).

[56] Ma, Y., Zhang, X., Awaji, S., Wang, D., Gao, Z., Nishijima, G., Watanabe, K., "Large irreversibility field in nanoscale C-doped MgB_2/Fe tape conductors", *Supercond. Sci. Technol.* **20**, L5 (2007).

[57] Yeoh, W. K., Horvat, J., Dou, S. X., Keast, V., "Strong pinning and high critical current density in carbon nanotube doped MgB_2", *Supercond. Sci. Technol.* **17**, S572 (2004).

[58] Chen, S. K., Tan, K. S., Glowacki, B. A., Yeoh, W. K., Soltanian, S., Horvat, J., Dou, S. X., "Effect of heating rates on superconducting properties of MgB_2, carbon nanotube- and nano-SiC-doped *in situ*MgB_2/Fe wires", *Appl. Phys. Lett.* **87**, 182504 (2005).

[59] Kim, J. H., Yeoh, W. K., Qin, M. J., Xu, X., Dou, S. X., "The doping effect of multiwall carbon nanotube on MgB_2/Fe superconductor wire", *J. Appl. Phys.* **100**, 013908 (2006).

[60] Kim, J. H., Yeoh, W. K., Qin, M. J., Xu, X., Dou, S. X., Munroe, P., Kumakura, H., Nakane, T., Jiang, C. H., "Enhacement of in-field J_c in MgB_2/Fe wire using single- and multiwalled carbon nanotubes", *Appl. Phys. Lett.* **89**, 122510 (2006).

[61] Zhang, X., Ma, Y., Gao, Z., Wang, D., Wang, L., Liu, W., Wang, C., "Strongly enhanced current-carrying performance in MgB_2 tape conductors by C_{60} doping", *J. Appl. Phys.* **103**, 103915 (2008).

[62] Xu, X., Dou, S. X., Wang, X. L., Kim, J. H., Stride, J. A., Choucair, M., Yeoh, W. K., Zheng, R. K., Ringer, S. P., "Graphene doping to enhance the flux pinning and supercurrent carrying ability of a magnesium diboride superconductor", *Supercond. Sci. Technol.* **23**, 085003 (2010).

[63] Dou, S. X., Pan, A. V., Zhou, S., Ionescu, M., Liu, H. K., Munroe, P. R., "Substitution-induced pinning in MgB_2 superconductor doped with SiC nano-particles", *Supercond. Sci. Technol.* **15**, 1587 (2002).

[64] Matsumoto, A., Kumakura, H., Kitaguchi, H., Hatakeyama, H., “Effect of SiO_2 and SiC doping on the powder-in-tube processed MgB_2 tapes”, *Supercond. Sci. Technol.* **16**, 926 (2003).

[65] Soltanian, S., Wang, X. L., Horvat, J., Dou, S. X., Sumption, M. D., Bhatia, M., Collings, E. W., Munroe, P., Tomsic, M., “High transport critical current density and large H_{c2} and H_{irr} in nanoscale SiC doped MgB_2 wires sintered at low temperature”, *Supercond. Sci. Technol.* **18**, 658 (2005).

[66] Sumption, M. D., Bhatia, M., Rindfleisch, M., Tomsic, M., Soltanian, S., Dou, S. X., Collings, E. W., “Lager upper critical field and irreversibility field in MgB_2 wires with SiC additions”, *Appl. Phys. Lett.* **86**, 092507 (2005).

[67] Hata, S., Yoshidome, T., Sosiati, H., Tomokiyo, Y., Kuwano, N., Matsumoto, A., Kitaguchi, H., Kumakura, H., “Microstructures of MgB_2/Fe tapes fabricated by an *in situ* powder-in-tube method using MgH_2 as a precursor powder”, *Supercond. Sci. Technol.* **19**, 161 (2006).

[68] Ma, Y., Zhang, X., Xu, A., Li, X., Xiao, L., Nishijima, G., Awaji, S., Watanabe, K., Jiao, Y., Xiao, L., Bai, X., Wu, K., Wen, H., “The effect of $ZrSi_2$ and SiC doping on the microstructure and J_c–B properties of PIT processed MgB_2 tapes”, *Supercond. Sci. Technol.* **19**, 133 (2006).

[69] Matsumoto, A., Kumakura, H., Kitaguchi, H., Senkowicz, B. J., Jewell, M. C., Hellstrom, E. E., Zhu, Y., Voyles, P. M., Larbalestier, D. C., “Evaluation of conectivity, flux pinning, and upper critical field contributions to the critical current density of bulk pure SiC-alloyed MgB_2”, *Appl. Phys. Lett.* **89**, 132508 (2006).

[70] Tomsic, M., Rindfleisch, M., Yue, J., McFadden, K., Doll, D., Phillips, J., Sumption, M. D., Bhatia, M., Bohnenstiehl, S., Collings, E. W., “Development of magnesium diboride (MgB_2) wires and magnets using in situ strand fabrication method”, *Physica C* **456**, 203 (2007).

[71] Dou, S. X., Shcherbakova, O., Yeoh, W. K., Kim, J. H., Soltanian, S., Wang, X. L., Senatore, C., Flükiger, R., Dhalle, M.,

HUSNJAK, O., BABIĆ, E., "Mechanisms of enhacement in electromagnetic properties of MgB_2 by nano SiC doping", *Phys. Rev. Lett.* **98**, 097002 (2007).

[72] YAMAMOTO, A., SHIMOYAMA, J., UEDA, S., HORII, S., KISHIO, K., "Doping effects of TiC and Mo_2C on critical current properties of MgB_2 tapes", *IEEE Trans. Appl. Supercond.* **16**, 1411 (2006).

[73] GAO, Z., ZHANG, X., WANG, D., LIU, X., LI, X., MA, Y., MOSSANG, E., "Effects of NbC addition on the critical current density of MgB_2 tapes", *Supercond. Sci. Technol.* **20**, 57 (2007).

[74] UEDA, S., SHIMOYAMA, J., YAMAMOTO, A., HORII, S., KISHIO, K., "Enhaced critical current properties observed in Na_2CO_3-doped MgB_2", *Supercond. Sci. Technol.* **17**, 926 (2004).

[75] YAMAMOTO, A., SHIMOYAMA, J., UEDA, S., IWAYAMA, I., HORII, S., KISHIO, K., "Effects of B_4C doping on critical current properties of MgB_2 superconductor", *Supercond. Sci. Technol.* **18**, 1323 (2005).

[76] LEZZA, P., SENATORE, C., FLÜKIGER, R., "Improved critical current densities in B_4C doped MgB_2 based wires", *Supercond. Sci. Technol.* **19**, 1030 (2006).

[77] YAMAMOTO A., SHIMOYAMA, J., IWAYAMA, I., KATSURA, Y., HORII, S., KISHIO, K., "Influence of dopant particle size on the critical current properties and microstructures of MgB_2 bulks doped with TiC and SiC", *Physica C* **463**, 807 (2007).

[78] ZHOU, S., PAN, A. V., WEXLER, D., DOU, S. X., "Sugar coating of boron powder for efficient carbon doping of MgB_2 with enhaced current-carrying performance", *Adv. Mater.* **19**, 1373 (2007).

[79] SHCHERBAKOVA, O. V., PAN, A. V., WANG, J. L., SHCHERBAKOV, A. V., DOU, S. X., WEXLER, D., BABIĆ, E., JERČINOVIĆ, M., HUSNJAK, O., "Sugar as an optimal carbon source for the enhaced performance of MgB_2 superconductors at high magnetic fields", *Supercond. Sci. Technol.* **21**, 015025 (2007).

[80] ZHANG, Y., ZHOU, S. H., LU, C., KONSTANTINOV, K., DOU, S. X., "The effect of carbon doping on the upper critical field (H_{c2}) and

resistivity of MgB_2 by using sucrose ($C_{12}H_{22}O_{11}$) as the carbon source", *Supercond. Sci. Technol.* **22**, 015025 (2009).

[81] Xu, X., Kim, J. H., Yeoh, W. K., Zhong, Y., Dou, S. X., "Improved $J_c(H)$ of MgB_2 superconductor by ball milling using different media", *Supercond. Sci. Technol.* **19**, L47 (2006).

[82] Yamada, H., Hirakawa, M., Kumakura, H., Kitaguchi, H., "Effect of aromatic hydrocarbon addition on *in situ* powder-in-tube processed MgB_2 tapes", *Supercond. Sci. Technol.* **19**, 175 (2006).

[83] Yamada, H., Uchiyama, N., Kumakura, H., Kitaguchi, H., Matsumoto, A., "Superconducting properties of aromatic hydrocarbon added powder-in-tube MgB_2/Fe tapes", *IEEE Trans. Appl. Supercond.* **17**, 2850 (2007).

[84] Ye, S. H., Matsumoto, A., Zhang, Y. C., Kumakura, H., "Strong enhancement of high-field critical current properties and irreversibility field of MgB_2 superconducting wires by coronene active carbon source addition via the new B powder carbon-coating method", *Supercond. Sci. Technol.* **27**, 085012 (2014).

[85] Kim, J. H., Xu, X., Hossain, M. S. A., Shi, D. Q., Zhao, Y., Wang, X. L., Dou, S. X., Choi, S., Kiyoshi, T., "Influence of disorder on the in-field J_c of MgB_2 wires using highly active pyrene", *Appl. Phys. Lett.* **92**, 042506 (2008).

[86] Maeda, M., Kim, J. H., Heo, Y.-U., Kwon, S. K., Kumakura, H., Choi, S., Nakayama, Y., Takano, Y., Dou, S. X., "Superior MgB_2 superconducting wire performance through oxygen-free pyrene additive", *Appl. Phys. Express* **5**, 01301 (2012).

[87] Yamada, H., Uchiyama, N., Matsumoto, A., Kitaguchi, H., Kumakura, H., "The excellent superconducting properties of *in situ* powder-in-tube processed MgB_2 tapes with both ethyltoluene and SiC powder added", *Supercond. Sci. Technol.* **20**, L30 (2007).

[88] Fujii, H., Togano, K., Kumakura, H., Ozawa, K., "Improved critical current densities in ex-situ processed $MgB_{2\text{-}x}C_x$ tapes using powders treated in chemical solutions", *IEEE Trans. Appl. Supercond.* **19**, 2698 (2009).

[89] Ojha, N., Malik, V. K., Singla, R., Bernhard, C., Varma, G. D., "The effect of citric and oxalic acid doping on the superconducting properties of MgB_2", *Supercond. Sci. Technol.* **22**, 125014 (2009).

[90] Kim, J. H., Zhou, S., Hossain, M. S. A., Pan, A. V., Dou, S. X., "Carbohydrate doping to enhance electromagnetic properties of MgB_2 superconductors", *Appl. Phys. Lett.* **89**, 142505 (2006).

[91] Kim, J. H., Dou, S. X., Hossain, M. S. A., Xu, X., Wang, J. L., Shi, D. Q., Nakane, T., Kumakura, H., "Systematic study of MgB_2 + $C_4H_6O_5$ superconductor prepared by the chemical solution route", *Supercond. Sci. Technol.* **20**, 715 (2007).

[92] Hossain, M. S. A., Kim, J. H., Xu, X., Wang, X. L., Rindfleisch, M., Tomic, M., Sumption, M. D., Collings, E. W., Dou, S. X., "Significant enhacement of H_{c2} and H_{irr} in $MgB_2 + C_4H_6O_5$ bulks at a low sintering temperature of 600 °C", *Supercond. Sci. Technol.* **20**, L51 (2007).

[93] Wang, C., Ma, Y., Zhang, X., Wang, D., Gao, Z., Yao, C., Awaji, S., Watanabe, K., "Enhanced superconducting properties of MgB_2 tapes achieved by treating B powder with glycolic acid", *Supercond. Sci. Technol.* **24**, 105005 (2011).

[94] Hossain, M. S. A., Kim, J. H., Wang, X. L., Xu, X., Peleckis, G., Dou, S. X., "Enhacement of flux pinning in a MgB_2 superconductor doped with tartaric acid", *Supercond. Sci. Technol.* **20**, 112 (2007).

[95] Ma, Y., Gao, Z., Zhang, X., Wang, D., Yu, Z., Watanabe, K., Wen, H., Mossang, E., "Enhaced high-field performance in Fe-sheathed MgB_2 tapes using inexpensive stearic acid additives", *J. Mater. Res.* **22**, 2987 (2007).

[96] Gao, Z., Ma, Y., Zhang, X., Wang, D., Yu, Z., Watanabe, K., Yang, H., Wen, H., "Strongly enhaced critical current density in MgB_2/Fe tapes by stearic acid and stearate doping", *Supercond. Sci. Technol.* **20**, 485 (2007).

[97] Da Silva, L. S. B., Vianna, A. A., Manesco, A. L. R., Hellstrom, E. E., Rodrigues, D. Jr., "The influcence of stearic acid ad-

dition on the superconducting properties of MgB_2", *IEEE Trans. Appl. Supercond.* **26**, 7100204 (2016).

[98] Gao, Z., Ma, Y. Zhang, X., Wang, D., Yu, Z., Yang, H., Wen, H., Mossang, E., "Enhacement of the critical current density and the irreversibility field in maleic anhydride doped MgB_2 based tapes", *J. Appl. Phys.* **102**, 013914 (2007).

[99] Malagoli, A., Braccini, V., Tropeano, M., Vignolo, M., Bernini, C., Fanciulli, C., Romano, G., Putti, M., Ferdeghini, C., Mossang, E., Polyanskii, A., Larbalestier, D. C., "Effect of grain refinement on enhancing critical current density and upper critical field in undoped MgB_2 *ex situ* tapes", *J. Appl. Phys.* **104**, 103908 (2008).

[100] Wang, S.-F., Liu, Z., Zhou, Y.-L., Zhu, Y.-B., Chen, Z.-H., Lu, H.-B., Cheng, B.-L., Yang, G.-Z., "Correlation between film thickness and critical current density of MgB_2 films", *Supercond. Sci. Technol.* **17**, 1126 (2004).

[101] Martínez, E., Mikheenko, P., Martínez-López, M., Millán, A., Bevan, A., Abell, J. S., "Flux pinning force in bulk MgB_2 with variable grain size", *Phys. Rev. B* **75**, 134515 (2007).

[102] Mikheenko, P., Martínez, E., Bevan, A., Abell, J. S., MacManus Driscoll, J. L., "Grain boundaries and pinning in bulk MgB_2", *Supercond. Sci. Technol.* **20**, S264 (2007).

[103] Suryanarayana, C., "Mechanical alloying and milling", *Prog. Mater. Sci.* **46**, 1 (2001).

[104] Gümbel, A., Eckert, J., Fuchs, G., Nenkov, K., Müller, K.-H., Schultz, L., "Improved superconducting properties in nanocrystalline bulk MgB_2", *Appl. Phys. Lett.* **80**, 2725 (2002).

[105] Hässler, W., Herrmann, M., Rodig, C., Schubert, M., Nenkov, K., Holzapfel, B., "Further increase of the critical current density of MgB_2 tapes with nanocarbon-doped mechanically alloyed precursor", *Supercond. Sci. Technol.* **21**, 062001 (2008).

[106] Herrmann, M., Hässler, W., Rodig, C., Gruner, W., Holzapfel, B., Schultz, L., "Touching the properties of NbTi carbon doped

tapes with mechanically alloyed MgB_2", *Appl. Phys. Lett.* **91**. 082507 (2007).

[107] Kováč, P., Kulich, M., Hässler, W., Hermann, M., Melišek, T., Reissner, M., "Properties of MgB_2 wires made of oxidized powders", *Physica C* **477**, 20 (2012).

[108] Chen, S. K., Glowacki, B. A., MacManus-Driscoll, J. L., Vickers, M. E., Majoros, M., "Influence of *in situ* and *ex situ* ZrO_2 addition on the properties of MgB_2", *Supercond. Sci. Technol.* **17**, 243 (2004).

[109] Kario, A., Nast, R., Hässler, W., Rodig, C., Mickel, C., Goldacker, W., Holzapfel, B., Schultz, L., "Critical current density enhancement in strongly reactive *ex situ* MgB_2 bulk and tapes prepared by high energy milling", *Supercond. Sci. Technol.* **24**, 075011 (2011).

[110] Da Silva, L. B. S., Hellstrom, E. E., Rodrigues, D. Jr., "The influence of milling time and ZrB_2 addition on the superconducting properties of MgB_2", *IEEE Trans. Appl. Supercond.* **25**, 6800404 (2015).

[111] Flükiger, R., Lezza, P., Beneduce, C., Musolino, N., Suo, H. L., "Improved transport critical current and irreversibility fields in mono- and multifilamentary Fe/MgB_2 tapes and wires using fine powders", *Supercond. Sci. Technol.* **16**, 264 (2003).

[112] Suo, H. L., Lezza, P., Uglietti, D., Beneduce, C., Abächerli, V., Flükiger, R., "Transport critical current densities and n factors in mono- and multifilamentary MgB_2/Fe tapes and wires using fine powders", *IEEE Trans. Appl. Supercond.* **13**, 3265 (2003).

[113] Lezza, P., Abächerli, V., Clayton, N., Senatore, C., Uglietti, D., Suo, H. L., Flükiger, R., "Transport properties and exponential n-values of Fe/MgB_2 tapes with various MgB_2 particle sizes", *Physica C* **401**, 305 (2004).

[114] Romano, G., Vignolo, M., Braccini, V., Malagoli, A., Bernini, C., Tropeano, M., Fanciulli, C., Putti, M., Ferdeghini, C., "High-energy ball milling and synthesis temperature study to improve

superconducting properties of MgB_2 *ex situ* tapes and wires", *IEEE Trans. Appl. Supercond.* **19**, 2706 (2009).

[115] Senkowicz, B. J., Giencke, J. E., Patnaik, S., Eom, C. B., Hellstrom, E. E., Larbalestier, D. C., "Improved upper critical field in bulk-form magnesium diboride by mechanical alloying with carbon", *Appl. Phys. Lett.* **86**, 202502 (2005).

[116] Senkowicz, B. J., Mungal, R. J., Zhu, Y., Jiang, J., Voyles, P. M., Hellstrom, E. E., Larbalestier, D. C., "Nanoscale grains, high irreversibility field and large critical current density as a function of high-energy ball milling time in C-doped magnesium diboride", *Supercond. Sci. Technol.* **21**, 035009 (2008).

[117] Perner, O., Eckert, J., Hässler, W., Fisher, C., Müller, K.-H., Fuchs, G., Holzapfel, B., Schultz, L., "Microstructure and impurity dependence in mechanically alloyed nanocrystalline MgB_2 superconductors", *Supercond. Sci. Technol.* **17**, 1148 (2004).

[118] Lorenz, B., Perner, O., Eckert, J., Chu, C. W., "Superconducting properties of nanocrystalline MgB_2", *Supercond. Sci. Technol.* **19**, 912 (2006).

[119] Gruner, W., Herrmann, M., Nilsson, A., Hermann, H., Hässler, W., Holzapfel, B., "Reactive nanostructured carbon as an efective doping agent for MgB_2", *Supercond. Sci. Technol.* **20**, 601 (2007).

[120] Wu, Y. F., Lu, Y. F., Yan, G., Li, J. S., Feng, Y., Tang, H. P., Chen, S. K., Xu, H. L., Li, C. S., Zhang, P. X., "Improved superconducting properties in bulk MgB_2 prepared by high-energy milling of Mg and B powders", *Supercond. Sci. Technol.* **19**, 1215 (2006).

[121] Parakkandy, J. M., Shahabuddin, M., Shah, M. S., Alzayed, N. S., Madhar, N. A., "Effect of ball milling time on critical current density of glucose-doped MgB_2 superconductors", *J. Supercond. Nov. Magn.* **28**, 475 (2015).

[122] Yang, F., Li, S. Q., Yan, G., Feng, J. Q., Xiong, X. M., Zhang, S. N., Wang, Q. Y., Liu, C. Q., Pang, Y. C., Zou, H. F., Li, C. S., Feng, Y., "Improved superconducting properties in Ti-doped MgB_2

prepared by two-step reaction method and high-energy ball milling", *J. Alloys Compd.* **622**, 714 (2015).

[123] Perner, O., Hässler, W., Eckert, J., Fisher, C., Mickel, C., Fuchs, G., Holzapfel, B., Schultz, L., "Effects of oxide particle addition on superconductivity in nanocrystalline MgB_2 bulk samples", *Physica C* **432**, 15 (2005).

[124] Perner, O., Eckert, J., Hässler, W., Fisher, C., Acker, J., Gemming, T., Fuchs, G., Holzapfel, B., Schultz, L., "Stoichiometry dependance of superconductivity and microstructure in mechanically alloyed MgB_2", *J. Appl. Phys.* **97**, 056105 (2005).

[125] Fuchs, G., Hässler, W., Nenkov, K., Scheiter, J., Perner, O., Handstein, A., Kanai, T., Schultz, L., Holzapfel, B., "High trapped fields in bulk MgB_2 prepared by hot-pressing of ball-milled precursor powder", *Supercond. Sci. Technol.* **26**, 122002 (2013).

[126] Sugino, S., Yamamoto, A., Shimoyama, J., Kishio, K., "Enhanced trapped field in MgB_2 bulk magnets by tunning grain boundary pinning through milling", *Supercond. Sci. Technol.* **28**, 055016 (2015).

[127] Fisher, C., Rodig, C., Hässler, W., Perner, O., Eckert, J., Nenkov, K., Fuchs, G., Wendrock, H., Holzapfel, B., Schultz, L., "Preparation of MgB_2 tapes using a nanocrystalline partially reacted precursor", *Appl. Phys. Lett.* **83**, 1803 (2003).

[128] Hässler, W., Rodig, C., Fisher, C., Holzapfel, B., Perner, O., Eckert, J., Nenkov, K., Fuchs, G., "Low temperature preparation of MgB_2 tapes using mechanically alloyed powder", *Supercond. Sci. Technol.* **16**, 281 (2003).

[129] Strickland, N. M., Buckley, R. G., Otto, A., "High critical current densities in Cu-sheathed MgB_2 formed from a mechanically-alloyed precursor", *Appl. Phys. Lett.* **83**, 323 (2003).

[130] Fisher, C., Hässler, W., Rodig, C., Perner, O., Behr, G., Schubert, M., Nenkov, K., Eckert, J., Holzapfel, B., Schultz, L., "Critical current densities of superconducting MgB_2 tapes prepared on the base of mechanically alloyed precursors", *Physica C* **406**, 121 (2004).

[131] Hässler, W., Birajdar, B., Gruner, W., Herrmann, M., Perner, O., Rodig, C., Schubert, M., Holzapfel, B., Eibl, O., Schultz, L., "MgB_2 bulk and tapes prepared by mechanically alloying: influence of the boron precursor powder", *Supercond. Sci. Technol.* **19**, 512 (2006).

[132] Mio, H., Kano, J., Saito, F., "Scale-up method for planetary ball mill", *Chem. Eng. Sci.* **59**, 5909 (2004).

[133] Devener, B. V., Perez, J. P. L., Anderson, S. L., "Air-stable, unoxidized, hydrocarbon-dispersible boron nanoparticles", *J. Mater. Res.* **24**, 3462 (2009).

[134] Pérez-Dieste, V., Castellini, O. M., Crain, J. N., Eriksson, M. A., Kirakosian, A., Lin, J.-L., McChesney, J. L., Himpsel, F. J., Black, C. T., Murray, C. B., "Thermal decomposition of surfactant coatings on Co and Ni nanocrystals", *Appl. Phys. Lett.* **83**, 5053 (2003).

[135] Martínez, E., Navarro, R., Andrés, J. M., "Improvement of the critical current density on *in situ* PIT processed Fe/MgB_2 wires by oleic acid addition", *Supercond. Sci. Technol.* **26**, 125017 (2013).

[136] Laliena, C., Martínez, E., Angurel, L. A., Navarro, R., "Effect of ball milling and fatty acid addition on the properties of MgB_2 wires", *IEEE Trans. Appl. Supercond.* **25**, 6200204 (2015).

[137] Hässler, W., Hermann, H., Herrmann, M., Rodig, C., Aubele, A., Schmolinga, L., Sailer, B., Holzapfel, B., "Influence of the milling energy transferred to the precursor powder on the microstructure and the superconducting properties of MgB_2 wires", *Supercond. Sci. Technol.* **26**, 025005 (2013).

[138] `http://www.ductile.org/didata/Section7/7intro.htm`.

[139] 2000 JCPDS - International Centre for Diffraction Data.

[140] Rosová, A., Kováč, P., Hušek, I., Brunner, B., Dobročka, E., "Microstructure of MgB_2 superconducting wire prepared by internal magnesium diffusion and *in situ* powder-in-tube processes – Secondary phase intergrain nanolayers as an oxygen content indicator", *Physica C* **516**, 1 (2015).

[141] Wilson, M. N., *Superconducting Magnets* (Clarendon Press, 1983).

[142] Mints, R. G., Rakhmanov, A. L., “Critical state stability in type-II superconductors and superconducting-normal-metal composites”, *Rev. Mod. Phys.* **53**, 551 (1981).

[143] Wipf, S. L., “Review of stability in high temperature superconductors with emphasis on flux jumping”, *Cryogenics* **31**, 936 (1991).

[144] Saito, Y., Murakami, M., Matsumoto, A., Kumakura, H., “Improvement in microstructure and superconducting properties of single-filament powder-in-tube MgB_2 wires by cold working with a swaging machine”, *Supercond. Sci. Technol.* **30**, 065005 (2017).

[145] Kodama, M., Suzuki, T., Tanaka, H., Okishiro, K., Okamoto, K., Nishijima, G., Matsumoto, A., Yamamoto, A., Shimoyama, J., Kishio, K., “High-performance dense MgB_2 superconducting wire fabricated from mechanically milled powder”, *Supercond. Sci. Technol.* **30**, 044006 (2017).

[146] Kim, J. H., Dou, S. X., Wang, J. L., Shi, D. Q., Xu, X., Hossain, M. S. A., Yeoh, W. K., Choi, S., Kiyoshi, T., “The effects of sintering temperature on superconductivity in MgB_2/Fe wires”, *Supercond. Sci. Technol.* **20**, 448 (2007).

[147] Kumakura, H., Matsumoto, A., Nakane, T., Kitaguchi, H., “Fabrication and properties of powder-in-tube-processed MgB_2 tape conductors”, *Physica C* **456**, 196 (2007).

[148] Zeng, R., Lu, L., Li, W., Wang, J., Shi, D., Horvat, J., Dou, S. X., Bhatia, M., Sumption, M., Collings, E., Yoo, J., Tomsic, M., Rindfleisch, M., “Excess of Mg addition MgB_2/Fe wires with enhanced critical current density”, *J. Appl. Phys.* **103**, 083911 (2008).

[149] Kováč, P., Reissner, M., Melišek, T., Hušek, I., Mohammad, S., “Current densities of MgB_2 wires by combined *ex situ*/*in situ* process”, *J. Appl. Phys.* **106**, 013910 (2009).

[150] Martínez, E., Angurel, L. A., Schlachter, S. I., Kováč, P., “Transport and magnetic critical currents of Cu-stabilized monofilamentary MgB_2 conductors”, *Supercond. Sci. Technol.* **22**, 015014 (2009).

[151] Shi, Z. X., Susner, M. A., Sumption, M. D., Peng, X., Rindfleisch, M., Tomsic, M. J., Collings, E. W., "Anisotropic connectivity and its influence on critical current densities, irreversibility fields, and flux creep in *in situ* processed MgB_2 strands", *Supercond. Sci. Technol.* **23**, 045018 (2010).

[152] Brunner, B., Kováč, P., Reissner, M., Hušek, I., Melišek, T., Pardo, E., "Critical current density and pinning behaviour of mono-core MgB_2 wires prepared by internal magneisum diffusion and *in situ* powder-in-tube method", *Physica C* **505**, 39 (2014).

[153] Horvat, J., Soltanian, S., Pan, A. V., Wang, X. L., "Superconducting screening on different length scales in high-quality bulk MgB_2 superconductor", *J. Appl. Phys.* **96**, 4342 (2004).

[154] Polyanskii, A. A., Indenbom, M. V., Ossip'yan, Yu. A., Vlasko-Vlasov, V. K., Nikitenko, V. I., "Visualization of magnetization processes in HTSCs", *IEEE Trans. Magn.* **26**, 1445 (1990).

[155] Dorosinskii, L. A., Indembom, M. V., Nikitenko, V. I., Ossip'yan, Yu. A., Polyanskii, A. A., Vlasko-Vlasov, V. K., "Studies of HTSC crystal magnetization features using indicator magneto-optic films with in-plane anisotropy", *Physica C* **203**, 149 (1992).

[156] Koblischka, M. R., Johansen, T. H., Bratsberg, H., "Bending of silver-sheathed (Bi,Pb)-2223 tapes investigated by magneto-optical flux visualization", *Supercond. Sci. Technol.* **10**, 693 (1997).

[157] Jooss, Ch., Albrecht, J., Kuhn, H., Leonhardt, S., Kronmüller, H., "Magneto-optical studies of current distributions in high-T_c superconductors", *Rep. Prog. Phys.* **65**, 651 (2002).

[158] Polyanskii, A. A., Feldmann, D. M., Larbalestier, D. C.; Cardwell D. A., Ginley, D. S. (Eds.), "Magneto-optical characterization techniques", Chapter D3.4 of *Handbook of Superconducting Materials* (IOP publishing Ltd, 2003), pp. 1551-1567.

[159] Larbalestier, D. C., Gurevich, A., Feldmann, D. M., Polyanskii, A., "High-T_c superconducting materials for electric power applications", *Nature* **414**, 368 (2001).

[160] Polyanskii, A. A., Beilin, V., Felner, I., Tsindlekht, M. I., Yashchin, E., Dul'kin, E., Galstyan, E., Roth, M., Senkowicz, B., Hellstrom, E., "Magneto-optical and electromagnetic studies of core connectivity and weak-link behaviour in Cu/MgB_2 and Ni/MgB_2 wires and tapes", *Supercond. Sci. Technol.* **17**, 363 (2003).

[161] Helseth, L. E., Hansen, W., Il'yashenko, E. I., Baziljevich, M., Johansen, T. H., "Faraday rotation spectra of bismuth-substituted ferrite garnet films with in-plane magnetization", *Phys. Rev. B* **64**, 174406 (2001).

[162] Laliena, C., Qureishy, T., Martínez, E., Navarro, R., Mikheenko, P., Johansen, T. H., Kováč, P., "Effect of ball milling on the local magnetic flux distribution and microstructure of *in situ* Fe/MgB_2 conductors", *J. Alloys Compd.* **717**, 164 (2017).

[163] Shimada, Y., Hata, S., Ikeda, K., Nakashima, H., Matsumura, S., Tanaka, H., Yamamoto, A., Shimoyama, J., Kishio, K., "Microstructural connectivity in sintered *ex situ* MgB_2 bulk superconductors", *J. Alloys Compd.* **656**, 172 (2016).

[164] Brandt, E. H., "Electric field in superconductors with rectangular cross section", *Phys. Rev. B* **52**, 15442 (1995).

[165] Brandt, E. H., "Superconductors of finite thickness in a perpendicular magnetic field: Strips and slabs", *Phys. Rev. B* **54**, 4246 (1996).

[166] Qureishy, T., Laliena, C., Martínez, E., Qviller, A. J., Vestgården, J. I., Johansen, T. H., Navarro, R., Mikheenko, P., "Dendritic avalanches in a superconducting MgB_2 tape", *Supercond. Sci. Technol.* **30**, 125005 (2017).

[167] Wertheimer, M. R., Gilchrist, J. le G., "Flux jumps in type-II superconductors", *J. Phys. Chem. Solids* **28**, 2509 (1967).

[168] Leiderer, P., Boneberg, J., Brüll, P., Bujok, V., Herminghaus, S., "Nucleation and growth of a flux instability in superconducting $YBa_2Cu_3O_{7\text{-x}}$ films", *Phys. Rev. Lett.* **71**, 2646 (1993).

[169] Mikheenko, P., Qviller, A. J., Vestgården, J. I., Chaudhuri, S., Maasilta, I. J., Galperin, Y. M., Johansen, T. H., "Nanosec-

ond voltage pulses from dendritic flux avalanches in superconducting NbN films", *Appl. Phys. Lett.* **102**, 022601 (2013).

[170] Bolz, U., Biehler, B., Schmidt, D., Runge, B.-U., Leiderer, P., "Dynamics of the dendritic flux instability in $YBa_2Cu_3O_{7-\delta}$ films", *Europhys. Lett.* **64**, 517 (2003).

[171] Qviller, A. J., Yurchenko, V. V., Eliassen, K., Vestgården, J. I., Johansen, T. H., Nevala, M. R., Maasilta, I. J., Senapati, K., Budhani, R. C., "Irreversibility of the threshold field for dendritic flux avalanches in superconductors", *Physica C* **470**, 897 (2010).

[172] Johansen, T. H., Baziljevich, M., Shantsev, D. V., Goa, P. E., Galperin, Y. M., Kang, W. N., Kim, H. J., Choi, E. M., Kim, M.-S., Lee, S. I., "Dendritic flux patterns in MgB_2 films", *Supercond. Sci. Technol.* **14**, 726 (2001).

Part II

Exploring scale-up laser process texturing of $Bi_2Sr_2CaCu_2O_{8+x}$ monoliths

Chapter 8

Introduction and motivation

8.1 Laser floating zone techniques to induce texture in Bi-2212 rods

The superconducting $Bi_2Sr_2CaCu_2O_{8+x}$ (Bi-2212) phase is a member of the HTS family of BSCCO materials. The general chemical formula of this family is $Bi_2Sr_2Ca_{n-1}Cu_nO_{2n+4+x}$, where n ranges from 1 to 3. Bi-2212 and Bi-2223, which correspond to $n = 2$ and $n = 3$ respectively, are the most studied superconductors of this family due to their higher critical temperatures. T_c ranges from 80 K to 95 K for Bi-2212, depending on the oxygen content and cation intersubstitution, and it is close to 110 K for Bi-2223, whereas for Bi-2201 it is just about 10 K [1].

They all present complex tetragonal crystalline structures, and like other HTS cuprates such as YBCO, are layered perovskites. The crystalline structure of the Bi-2212 phase is shown in Figure 8.1. The Cooper pairs are generated in the CuO_2 planes and they move along them conferring the Bi-2212 phase a very high anisotropy: supercurrents along the a-b planes are up to three orders of magnitude higher than in the c-direction, and the coherence lenght along the c-axis, ξ_c, ~ 0.5 Å, is much lower than the in-plane value ξ_{ab}, ~ 19 Å [1]. This high anisotropy and layered structure is the main cause of the strong deterioration of current-carrying capability of these materials with increasing temperature in presence of high magnetic fields. The influence of grain boundaries is also critical in these materials, as they act as barriers to current flow and therefore reduce J_c values in polycrystalline materials [2].

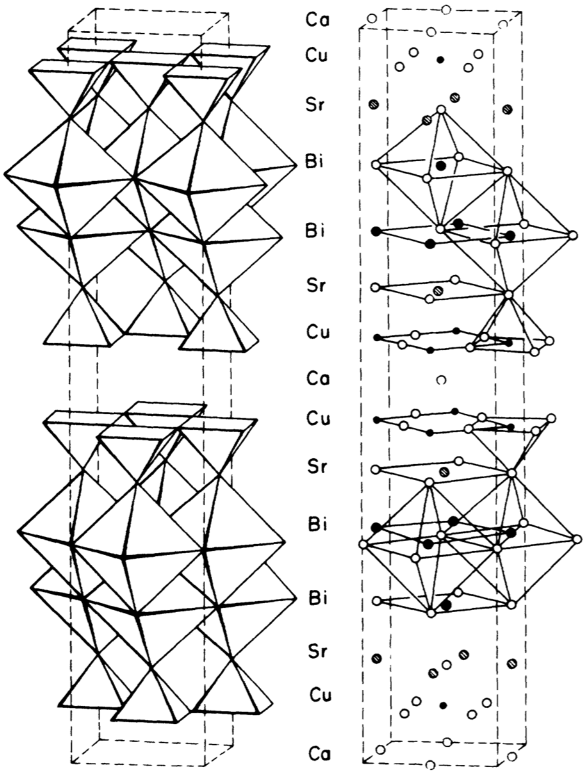

Figure 8.1: Crystal structure of Bi - 2212 high temperature superconductor [3].

The weak-link problem is common to all HTS and has severe effects in the intergranular critical current, decreasing it exponentially with the misorientation angle between grains [4]. Due to this effect, practical HTS (BSCCO superconductors among them) usually require adequate processing to induce texture and align their grains. In the case of Bi-2212 materials, to achieve high J_c values, a microstructure with low misorientation angles between the *a*-*b* planes of neighbouring grains and *c*-axis texture is desirable. In Bi-2212/Ag multifilamentary wires, the grain alignment is obtained by controlling the melt-solidification [5]. However, Bi-2212 monoliths demand texturing methods used both to grow grains with the *a*-*b* planes parallel to the current flow direction and to improve the contacts between them.

Methods that have been introduced to control the microstructure of the Bi-based HTS superconductors include molten-zone techniques. In these cases, a region of the samples is melted using a high energy source and this molten zone is moved in a controlled way along the sample. This technique is adecuate to induce texture in Bi-based HTS materials due to their highly anisotropic crystal growth. One of the most interesting molten zone methods is the floating zone because it does not require holders nor crucibles, thus avoiding potential contamination sources. Due to the surface tension in the molten zone, by controlling the processing parameters it is possible to obtain a stable liquid volume and to control the solidification of the textured material at the solid-liquid interfase. In particular, the laser floating zone method (LFZ) allows texturing with high growth velocities, up to $100\,\mathrm{mm\,h^{-1}}$ [6].

BSCCO superconductors are suitable to be processed with the LFZ technique because they possess a high fusion stability and a lower evaporation tension [7]. The LFZ method was proved to be particularly useful to develop Bi-2212 superconducting fibers or rods very soon after its discovery [8–12]. This is due to the high anisotropy during the solidification process leading to a microstructure in which the superconducting phase has the c-axis normal to the growth direction and their Cu-O planes are oriented along the rod axis [13], thus making possible to obtain attractive transport properties as a consequence of the well-aligned grain orientation that was induced [14]. A scheme of a LFZ device used to grow Bi-2212 fibers is displayed in Figure 8.2. Significant efforts were also carried out to texture Bi-2223 fibers, but it is more difficult to obtain a good microstructure with good superconducting properties due to its characteristic narrow phase stability [15].

Typical J_c values obtained in LFZ textured Bi-2212 thin rods at $77\,\mathrm{K}$ and self-field are about $4000\,\mathrm{A\,cm^{-2}}$ [15], with best results to date of $5500\,\mathrm{A\,cm^{-2}}$ for rods textured at a rate of $15\,\mathrm{mm\,h^{-1}}$ [14].

The main relevant parameters in the LFZ processing of bulk Bi-2212 rods are detailed by Díez *et al.* [15]. It was observed that I_c at $77\,\mathrm{K}$ increases linearly with the rod's radius. Thus, the self-field generated at the surface of the sample could be a limiting factor of the J_c at high temperatures.

Different starting materials and processing methods have been used to study the influence of the precursor powder characteristics on the critical current values of Bi-2212 LFZ processed fibers by Miao *et al.* [16]. They found that the characteristics of the precursors modify the microstructure of the Bi-2212 textured rods but do not affect significantly the superconducting

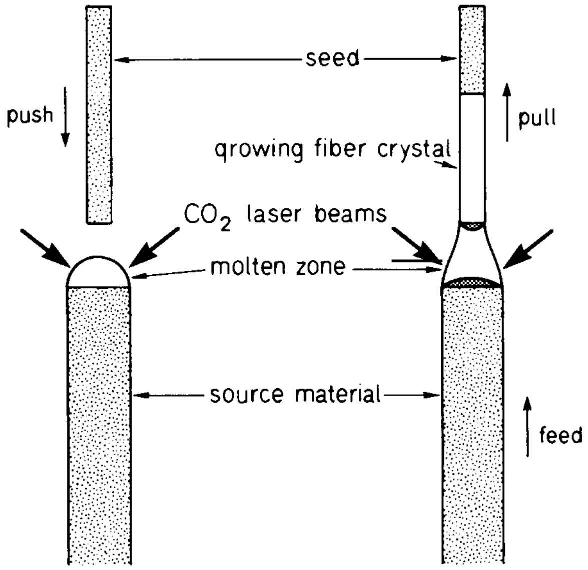

Figure 8.2: Scheme of the laser-heated pedestal growth method used by Gazit *et al.* [9].

properties. Even using the mixture of commercial oxides and carbonates, the differences observed in the transport critical currents were lower than a 20 %. The main differences are induced in the radial distribution of the superconducting phases, in principle, in the inner part of the samples while the supercurrents are confined to the region close to the rods surface, where the best microstructure is obtained. Taking into account the different powders studied, the best results were reported for fibers obtained using precursor powders fabricated by the polymer matrix and by the solid-state reaction methods.

The growth speed, also referred to as pulling rate, plays a crucial role in the LFZ method as well, since lower growth speeds increase grain size and allows a better grain alignment. Thus, the texture is definitely improved and higher J_c values are obtained. However, there exists an optimum range of processing velocities, which is between 15 and 30 mm h^{-1}, because at lower speeds, grains are very large and thermal stresses induce cracks that propagates easily between them [14], reducing J_c values.

Further relevant requirements include the attainment of very low electric resistive joints between the superconducting bulk material and the current leads, not only for the characterization of the samples but also for their applications. Otherwise, the resistive electric contacts will concentrate great amount of heat while operating under high currents and could provoke hot spots that end up melting the sample. Reproducible contact resistivity values, ρ_c, lower than $1 \times 10^{-9}\,\Omega\,\mathrm{cm}^2$ ($\rho_c = R_c \cdot S$ where R_c is the contact resistance and S is the contact area) have been obtained using an electrodeposition process of silver in non-aqueous media on the as-grown samples before the required heat treatment to obtain the superconducting phase [17].

A very interesting modification of the LFZ technique was developed at the University of Aveiro (Portugal) and applied to Bi-2223 superconducting fibre rods [18, 19]. In this technique an electrical current is applied during the texturing process through the crystallization interface to modify the phase composition and texture of the rods. Very few years later it was also applied to Bi-2212 [20,21]. It was demonstrated that the current application during the growth process induces a selective and intense ionic migration along the rod axis, resulting in an increase in the superconducting phase fraction and better grain alignment. Thus, higher J_c values at 77 K have been reached, exceeding the values obtained for LFZ processed fiber rods with the same experimental conditions [20]. This method is known as electrically assisted laser floating zone (EALFZ) growth and it has also been applied to non-superconducting ceramics, such as thermoelectric ceramics [22]. A scheme of a typical EALFZ setup system is displayed in Figure 8.3.

In the frame of the EALFZ technique, the influence of the current polarity in the superconducting properties of the BSCCO fibers has also been studied. It was found that when the DC current is applied from the crystallization interface to the melt, a globular structure is developed instead of a preferential grain alignment, which leads to an absence of superconducting phase solidification. However, reversing the polarization induces an improvement of the grain alignment resulting in excellent textured materials [23, 24].

The influence of the velocity at which the sample is textured has also been studied for EALFZ processed Bi-2223 rods. It was found that low ($< 25\,\mathrm{mm\,h^{-1}}$) and high velocities ($> 100\,\mathrm{mm\,h^{-1}}$) severely damage the J_c performance of these rods processed under direct currents of 200 mA [21].

In particular, best J_c values obtained for EALFZ processed Bi-2212/2.9 wt.% Ag rods are $\sim 5800\,\mathrm{A\,cm^{-2}}$ at 77 K in self-field when applying a current

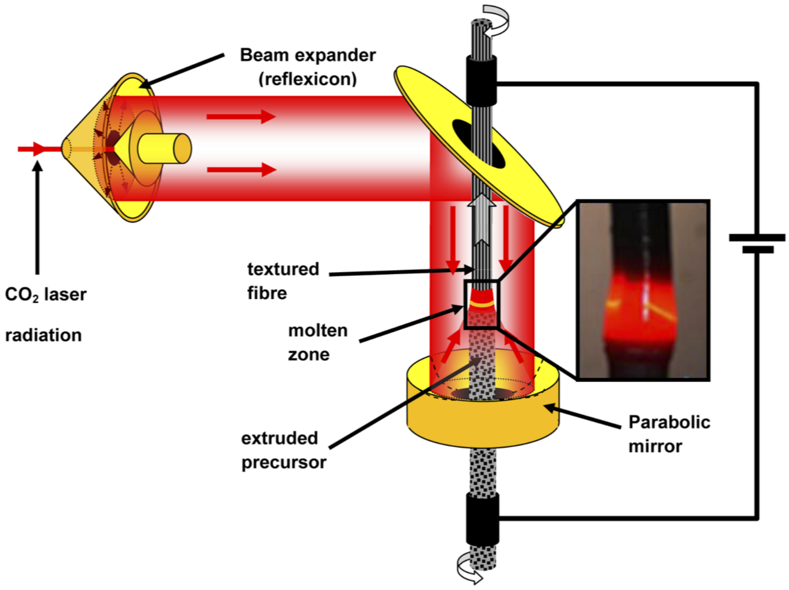

Figure 8.3: Scheme of the electrically assisted laser floating zone system used by Costa *et al.* [25] to grow vertically textured Bi-2212/Ag rods.

of 300 mA during processing [25]. These values are the highest reported to date in massive bulk Bi-2212 superconducting samples.

8.2 Laser assisted zone melting to induce texture in Bi-2212 monoliths

As previously mentioned, for the Bi-2212 rods I_c increases linearly with the radius and so does the microstructural inhomogeneities. In addition, considering high power applications, such as current limiters, controlled and well textured superconducting samples of long length and capable of supporting high critical current density values are required. These facts limit the applicability of these materials and new geometries have been explored. Planar Bi-2212 bulk materials could be used for resistive fault current limiters because long length current-path materials can be obtained in meander geometry. Additionally, controlling the thickness of planar samples, the thermal stability can be improved since problems associated with hot spot generation are reduced. This is a critical limitation in the case of bulk HTSs for high power applications.

In-plane laser zone melting (LZM) method was first applied to process planar oxide eutectis as reported by Larrea *et al.* [26], and was shortly after successfully applied by Mora *et al.* to texture Bi-2212 planar bulk samples of dimensions 100 mm × 10 mm × 1 mm [27]. Figure 8.4 displays a scheme of the LZM used experimental setup [27].

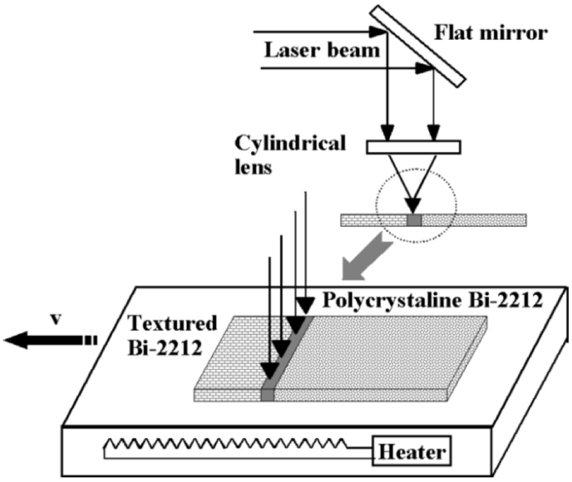

Figure 8.4: Scheme of the LZM experimental setup used by Mora *et al.* [27] to texture planar Bi-2212 bulk materials.

During the LZM processing of planar Bi-2212 bulk samples, the energy dissipation is not the same at the center of the sample and in the borders. This produces a characteristic semi-ellipsoidal shape of the molten zone. The solid-liquid interface separates an amorphous region from the textured region, in which the well-crystallized elongated grains of secondary Bi-free phases tend to grow perpendicular to that solid-liquid interface.

Typically, these Bi-free phases present two out-of-equilibrium compositions: $(Sr_{1-x}Ca_x)CuO_2$ (known as 1:1) and $(Sr_{1-x}Ca_x)_2CuO_3$ (known as 2:1), firstly identified in Bi-2212 samples by Oka *et al.* [28,29]. Also, an equilibrium composition, $(Sr_{1-x}Ca_x)_{14}Cu_{24}O_{41}$ (known as 14:24), was observed for the first time by Roth *et al.* [30]. A scheme of a typical longitudinal cross-section of a planar sample during the laser zone melting process is shown in Figure 8.5.

Mora *et al.* [27] showed how the shape of the solidification profile deter-

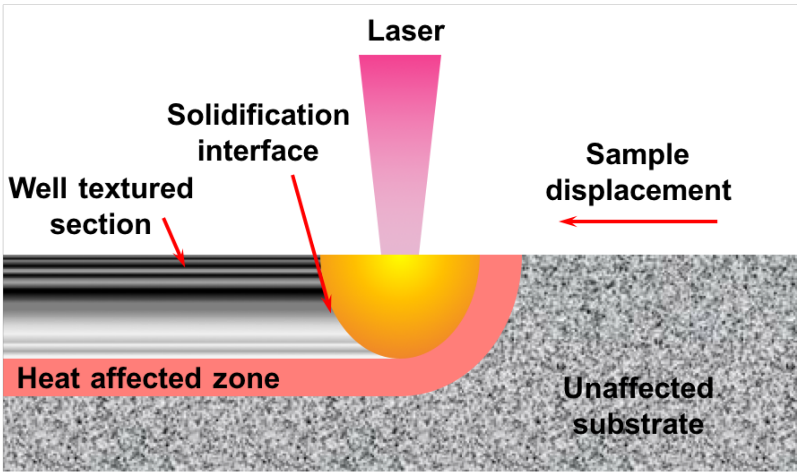

Figure 8.5: Scheme of the typical solidification interface that occurs during laser zone melting of planar samples, as shown by Lennikov *et al.* [32]. Here the longitudinal cross-section of the sample is displayed.

mines the grain orientation within the processed sample. In the region closer to the sample surface, the solidification profile is perpendicular to that surface. Thus, the elongated grains of Bi-free phases are well-aligned parallel to the surface. However, the solidification profile tends to curve as the melt pool advances across the sample thickness, ending up being parallel to the sample's surface. This produces a microstructure of misaligned grains in the lower parts of the laser affected regions, which can be up to 1 mm depth.

An example of these features can be seen in Figure 8.6. The right-hand side image shows the frozen molten pool where both the solidification profile and the different textured regions are displayed. The elongated Bi-free phase grains (darker gray) grown from the molten pool can also be seen. In the left-hand side image, which was taken with a higher magnification, the upper well-aligned region is clearly distinguishable. Also, in the lower part of laser affected zone, Bi-free phase grains are aligned at $\sim 45^\circ$ with respect to the surface.

Morever, Mora *et al.* [27] also found that most of the current flows through the upper well-textured zone, with thickness of $\sim 200\,\mu\text{m}$. The depth of this well-textured region can be enlarged by increasing the laser power or by decreasing the processing speed, which enhances the transport properties. Thus,

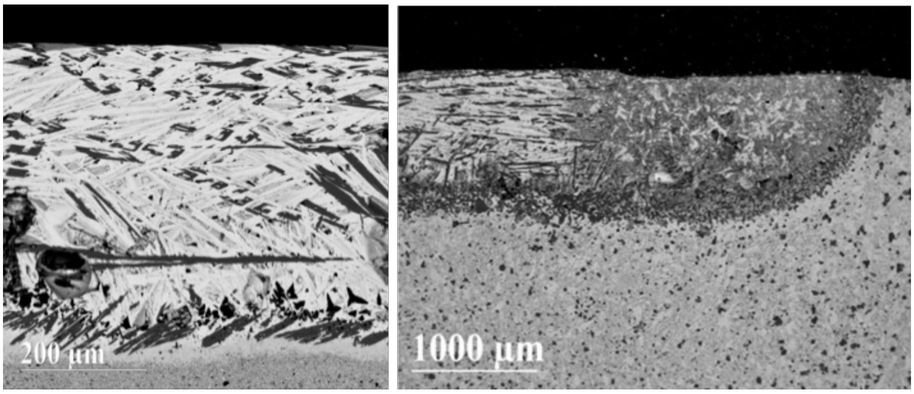

Figure 8.6: FESEM images using AsB detector of longitudinal cross-sections of two planar Bi-2212 LZM textured samples as shown by Mora *et al.* [27,31] respectively.

J_c values of 3000 A cm^{-2} were obtained for optimum processing conditions [27].

Experimentally, a support material able to remove and redistribute the heat during the LZM process is required to reduce the thermal shock. This thermal shock is a consequence of the excessive thermal gradients during the sample processing and may lead to sample bending and crack generation. Therefore, it is desirable to heat the support material from below to reduce this mentioned thermal shock. Mora *et al.* [31] found that when heating the support material up to 600 °C, the thickness of the well-textured region increases from $\sim$ 200 µm to $\sim$ 850 µm, and consequently I_c is enhanced too.

However, there are some critical limitations in the described LZM experimental setup. The used furnace allows processing samples with a maximum width of 10 mm. Besides, since the laser apparatus requires the furnace to be open sky, only temperatures up to $\sim$ 700 °C can be achieved. This open sky furnace configuration, where the sample is heated from below, also induces undesired thermal gradients across the sample thickness.

8.3 Modification of laser processing systems to develop a technological continuous process

In order to overcome the above mentioned limitations, Lennikov *et al.* [32] demonstrated the possibility of processing Bi-2212 by the LZM technique with very wide laser melt lines (up to 250 mm) that allow texturing large areas. In samples textured at low velocities, such as 15 mm h^{-1}, they obtained I_c values of 71 A at 77 K. They also proved that mid-IR radiation was useful for Bi-2212 texturing, using a 350 W and 20 kHz pulsed CO_2 laser emitting at a wavelenght of $\lambda = 10.6\,\mu$m.

The use of these lasers provide some advantages as it allows very high temperature processing (up to 3000 °C, depending on the material), a precise control of processing parameters and the synthesis of materials with controlled properties. But it also has some disadvantages as these conditions provoke high thermal stresses in the ceramic samples that lead to the formation of cracks. This is a critical issue regarding superconductors since these defects end up deteriorating their transport properties. A solution to minimise crack generation was developed by Estepa *et al.* [33], who patented a laser furnace apparatus that allows focusing a laser beam on the surface of a sample which moves inside the furnace at high enough temperatures. A scheme of this device is displayed in Figure 8.7.

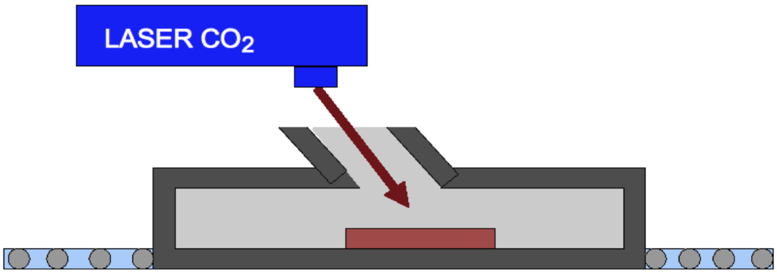

Figure 8.7: Scheme of the patented laser furnace apparatus as presented in [36].

This patented laser furnace apparatus allows obtaining a precise control of the initial temperature of the sample (at $T > 500\,°C$ crack formation is strongly reduced in many ceramic materials) but also a continuous processing, which represents a great advantage in terms of industrial processes. The maximum temperature of the furnace is limited to 1200 °C and it allows processing up to 60 cm wide pieces.

This laser furnace has been proved to be useful in several processes, such as the synthesis of rare-earth aluminate coatings [34], to eliminate defects of eutectic ceramic surfaces [35] and to process planar waveguides [36]. Among these processes, the processing of superconducting samples [37] is included as it will be detailed later.

8.4 Objectives and motivation

The main objective of this work is to develop an industrially scalable process of textured Bi-2212 monoliths regardless of their size. This process comprises all the stages from the precursor powder preparation to the final heat treatment required to obtain the superconducting phase, including the LZM texturing stage, and the analysis of relevant parameters and their effect on the microstructure and superconducting properties of the bulk samples.

The chapters in which this part is structured are detailed below:

- Chapter 9 presents the characterization of precursor powders prepared by different synthesis routes, with a special focus on a continuous solid-state processing method, which is aimed to overcome present precursor limitations regarding price, volume and uniformity. The characteristics of these powders at different process stages are analysed and compared with powders fabricated with the standard solid-state process and those commercially available.

- Chapter 10 describes the method developed for processing large and planar Bi-2212 bulk materials, using industrial scale methods, including a new laser line scanning configuration for LZM texturing. We analyse the effect of the different precursor powders (prepared as described in Chapter 9), laser texturing conditions and different heat-treatment methods, on the material microstructure, which has been correlated with the superconducting properties of the final processed material.

- Chapter 11 analyses the effect of applying an electric current during laser processing of Bi-2212 planar bulk samples (EALZM method) and their microstructural and superconducting properties.

- Finally the main conclusions that can be extracted from this part are presented in Chapter 12.

Chapter 9

Continuous processing of precursor powders

As the price of commercial Bi-2212 powders has increased in recent years, reaching levels above 2 k€/kg, it is convenient to explore alternative routes of synthesis of Bi-2212 powders, which can be industrially scalable and at lower cost than those currently available from commercial suppliers. Different synthesis routes have been proposed to prepare Bi-2212 powders [38]. One of the most frequently used among them is the conventional solid-state reaction, which, at the laboratory scale, is limited to small quantities of the order of 250-500 g. This is very low for a continuous process and requires processing the powder in several batches. The aim of this work is to overcome the above mentioned problems by developing a novel continuous powder processing method based on the use of a continuous furnace. This methodology, which is used routinely by the ceramic industry, can be applied to prepare Bi-2212 precursor powders for melt texture processes without limitation regarding production volume and uniformity.

In this chapter we describe this procedure, that we have called continuous solid-state process. The characteristics of the powders processed with this method are compared to those fabricated with the standard solid-state process and the commercial ones.

9.1 Description of the powders preparation method

Three different types of Bi-2212 precursor powders have been compared: commercial powders, standard solid-state and continuous solid-state. Their synthesis is described as follows:

Commercial powders (C)

Pure commercial precursor powders, named C, from Nexans SuperConductors GmbH, with stoichiometry $Bi_{2.18}Sr_{1.98}Ca_{0.87}Cu_{1.97}O_x$ were analysed. The grain size distribution, provided by the manufacturer, is characterized by $d_{10} = 0.10\,\mu m$, $d_{50} = 1.18\,\mu m$ and $d_{90} = 2.18\,\mu m$.

Standard solid-state powders (SSS)

Precursor powders, named SSS, were made from a mixture of raw oxides and carbonate powders with a Bi-Sr-Ca-Cu stoichiometry of 2.1:2:1:2, using the standard solid-state reaction method. The Bi-2212 powders were prepared from: Bi_2O_3 (99.9 % metal basis, Sigma Aldrich, mean particle size lower than 10 µm), $SrCO_3$ (99.9 % metal basis, Sigma Aldrich), $CaCO_3$ (99.5 % metal basis, Alfa Aesar) and CuO (99.7 % metal basis, Alfa Aesar, maximum particle size lower than 74 µm).

Initially, the precursor powders were dried at 350 °C during 6 h. Subsequently, the required quantities of components (Table 9.1) were mixed with 100 ml of heptane (C_7H_{16}) for 1 h at 300 rpm in a Retsch PM100 planetary ball mill. Typically, a quantity of $\sim$ 115 g of precursor mixture is required to obtain 100 g of $Bi_{2.1}Sr_2CaCu_2O_x$ (see Table 9.1). The used mill has a sun disk radius of $r_p = 7$ cm. The milling was performed in an agate jar of inner radius $r_v = 38$ mm, with 50 agate balls of radius $r_b = 5$ mm and 1.4 g mass each. Thus, the agate ball-to-powder mass ratio, β, was always kept at ~ 0.7. In this setup, the amount of milled powder for each run is limited to about 100 g. After having finished the milling process, the residual heptane was eliminated by slow drying at 120 °C for 24 h in a stove.

The mixed and milled powder is thermally calcined in a muffle furnace, in

Precursor	M_W ($\mathrm{g\,mol^{-1}}$)	n (mol)	*mass* (g)
Bi-2212	909.28	0.11	100
Bi_2O_3	456.96	1.05	53.81
$SrCO_3$	147.63	2.00	32.47
$CaCO_3$	100.09	1.00	11.01
CuO	79.55	2.00	17.50

Table 9.1: Quantities of raw oxide and carbonate precursors used to obtain 100 g of Bi-2212 in the 2.1:2:1:2 proportion.

air atmosphere, at 760 °C for 16 h in order to partially decompose the alkaline earth carbonates. Two additional sintering processes at 830 °C for 16 h were carried out to form the Bi-2212 phase. After each heat treatment, it is essential to mill again the powder in order to avoid the formation of hard and bulky aggregates.

Typically, the maximum amount of precursors that can be processed by this method at the same time is $\sim$ 100 g, depending on the type of furnace used. This is limited by the maximum temperature differences allowed in the powder batch during heat treatment associated to the inherent temperature gradients inside the muffle furnace. This fact constitutes the most restrictive point of the sintering process, since the maximum amount of powders that can be milled in each step can be increased with an adequate milling system.

Continuous solid-state powders (CSS)

The continuous solid-state (CSS) powders are produced from the same raw oxide and carbonate powder mixture as in the standard solid-state reactions.

In this process, the heat treatment in a muffle furnace has been substituted by a heat treatment in a continuous furnace, which is presented in Figure 9.1. It is 4 m long and has three zones in which the temperature can be controlled in an independent way. This allows creating a temperature profile inside the furnace with an initial preheating region, a central zone at the maximum required temperature and a final cooling zone. Temperatures up to 1200 °C can be reached inside the furnace. The movement of the sample inside the furnace is made by means of ceramic cylinders that rotate at a given velocity.

Sample velocities in the range from $0.5\,\mathrm{m\,h^{-1}}$ to $4\,\mathrm{m\,h^{-1}}$ can be used.

Figure 9.1: Photograph of the 4 m long continuous furnace Nannetti ER 20.

Typically, 500 g of oxide and carbonate precursors were processed at the same time (see Figure 9.2) in four ceramic crucibles that contained ~ 125 g each. The temperature of the preheating and cooling zones of the furnace was fixed at 650 °C, and at the central zone it was 800 °C. The displacement velocity of the powders were $1.5\,\mathrm{m\,h^{-1}}$, thus the duration of the heat treatment was 2.5 h, with ~ 45 min soaking at the highest temperature. A rough draft of the temperature profile followed by the precursor powders is displayed in Figure 9.3. In this work, this continuous heat treatment of the raw mixture of the precursor powders was repeated up to seven times. The precursor powders obtained after each heat treatment are named as CSSX with X being the number of repetitions of the heat treatment.

It is important to optimise the velocity at which the sample is moving inside the furnace. If is it too high the sample cannot reach a thermal equilibrium and the maximum temperature reached in the sample is lower than the maximum temperature reached in the furnace. For this reason, this velocity is strongly determined by the length of the furnace. In this work we have chosen an speed that it is low enough to reach this thermal equilibrium during a giving time inside this furnace but high enough to keep the processing time in a period that allows to prepare the powders for performing a new process every day.

Right after every heat treatment, the precursor powders mixture of each ceramic crucible (~ 125 g) were individually ball milled for 15 min at 300 rpm with 80 ml of heptane with the same jar and balls used for SSS powder to break the agglomerates and to decrease the particle size to facilitate the chemical

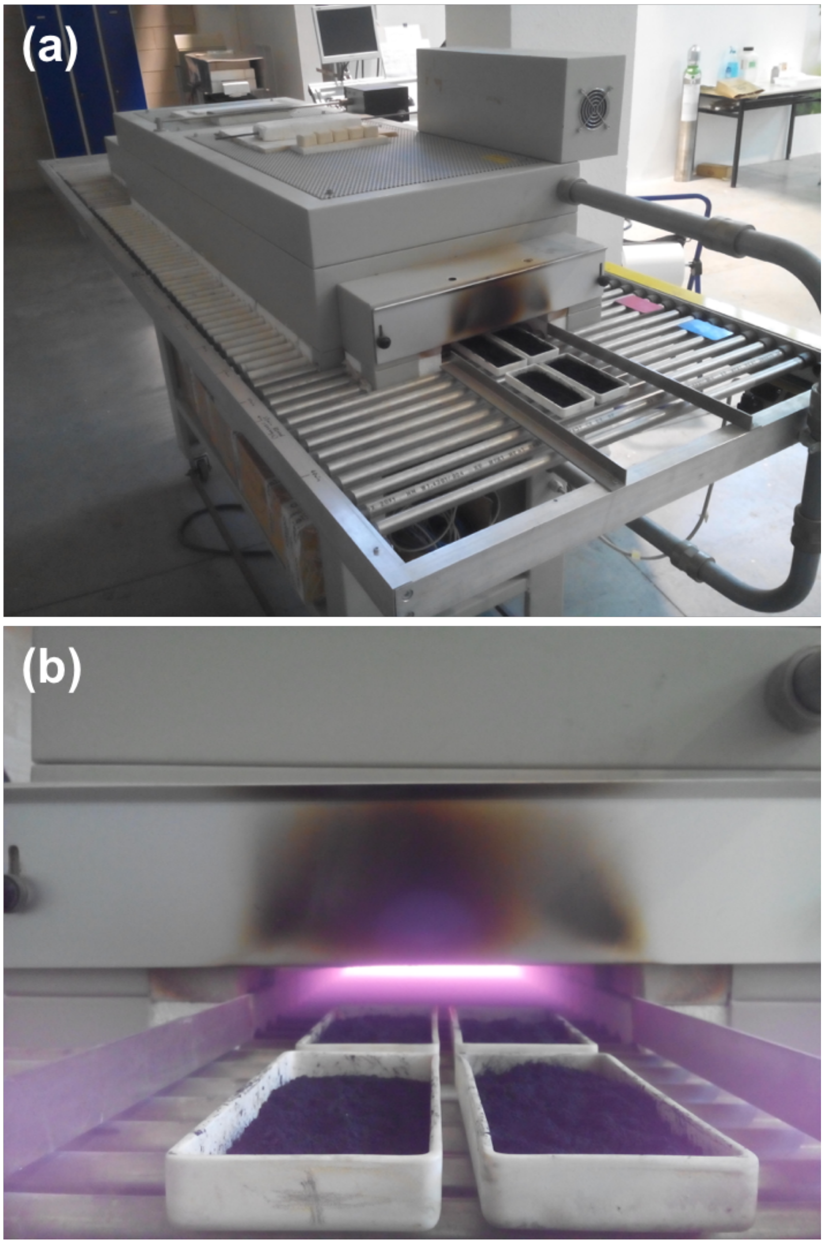

Figure 9.2: Picture (a) shows the four ceramic crucibles that contain approximately 500 g of precursor powders entering the 4 m continuous furnace. Picture (b) shows a closer look of the ceramic crucibles with the precursor powders prior the heat treatment. The pinkish ligth inside the furnace is originated by red-hot resistances.

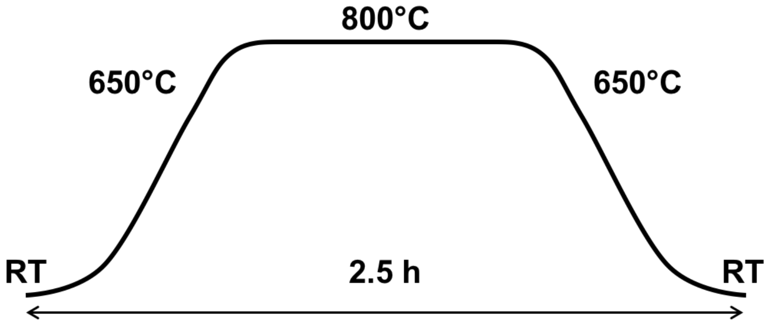

Figure 9.3: Scheme of the temperature profile of the heat treatment at which the precursor powders are subjected to in the continuous furnace. Neither the time nor the temperatures are at scale for clarifying purposes.

reaction in the subsequent heat treatment. This is particularly critical in the first two or three repetitions of the heat treatment, where most agglomerates appear. Then, the residual heptane was evaporated at 120 °C for 24 h.

9.2 Characterization of the precursor powders

The phase composition of the different precursor powders at the different processing steps was analysed using the measured XRD patterns. The particle size distribution was obtained with a laser diffraction analyzer and with FESEM. Besides, a thermal characterization was performed with thermogravimetric analysis (TGA) and differential scanning calorimetry (DSC). Finally, the superconducting properties of the powders were studied using AC magnetic susceptibility measurements as a function of the temperature, $\chi_{ac}(T)$.

9.2.1 Evolution of the phase composition

The evolution of the phase composition during the different steps of the continuous solid-state process has been monitored using XRD patterns collected at RT on a RIGAKU D-max/2500 X-ray diffractometer using Cu Kα radiation.

The difractograms of the precursor powders obtained at different stages of the continuous solid-state process are presented in Figure 9.4. The pattern at the top of the figure corresponds to the initial raw mixture of oxides and carbonates (powder CSS0), which shows the expected phases: Bi_2O_3, $SrCO_3$, $CaCO_3$ and CuO (see Table 9.1). Below is the pattern of the precursor powders after the first thermal treatment in the continuous furnace (powder CSS1). The strongest peaks associated with Bi_2O_3 (see for instance the peaks between $2\theta = 26°$ and $28°$) are no longer present, and also the $CaCO_3$ phase cannot be detected. The presence of the characteristic peak at 7.2° indicates that the Bi-2201 phase has started to be formed in this fist stage. Another Bi-containing compounds seem also to be present, identified by Naumov *et al.* [39] by the general formula $Bi_4(Ca_{2\text{-}x}Sr_{1.5\text{-}x})O_{9.5}$, but they have a wide range of compositions, making them difficult to identify by XRD. Some traces of $SrCO_3$ and CuO are also present. An important point is that the Bi-2212 phase is not detected in these powders.

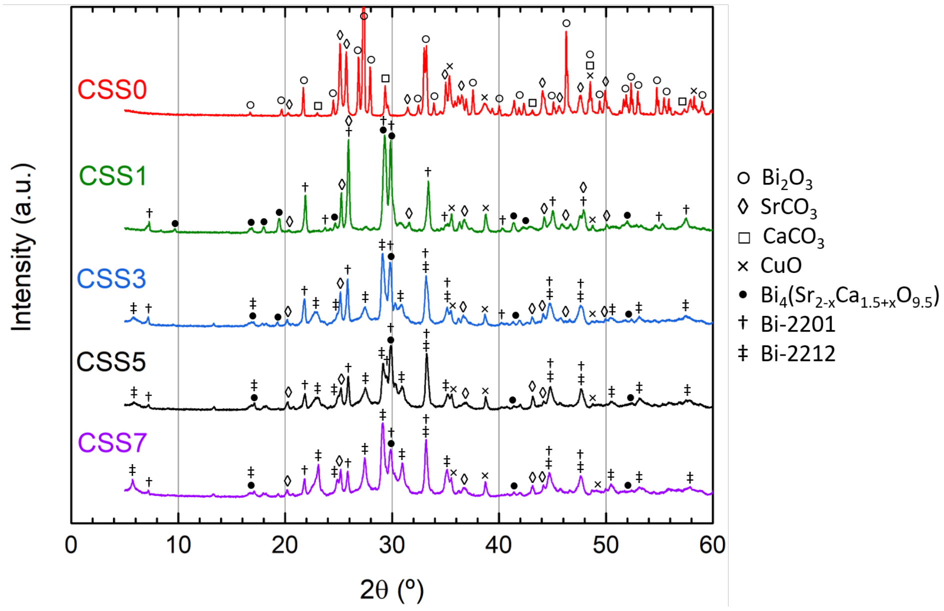

Figure 9.4: XRD patterns of the CSS0, CSS1, CSS3, CSS5 and CSS7 powders

The pattern corresponding to the precursor powders after the third thermal treatment (CSS3) shows that the Bi-2212 phase has started to form, which is remarkable considering the low number of heat treatments. Note that, in addition to the Bi-2201 phase, there are some low intensity peaks of $SrCO_3$, CuO and Bi-containing compounds, indicating that some small amounts of these phases are still present in these powders.

The XRD pattern after the fifth heat treatment in the continuous furnace (CSS5) shows the Bi-2212 and Bi-2201 as the main phases. The relative evolution of these two phases have been analyzed by the ratio of the intensities of the $2\theta = 23.1°$ (Bi-2212) and the $2\theta = 21.8°$ (Bi-2201) peaks. This ratio was 0 in the case of the sample CSS1, 0.51 in CSS3 and 0.76 in CSS5. The peak intensities of the $SrCO_3$ and CuO phases are very similar in these three powders, which could indicate that the changes in the amount of these two phases are very small during the different continuous stages.

It is worth noting that the pattern of the final precursor powders subjected to seven heat treatments (CSS7) does not show any significant differences with the corresponding one after five heat treatments (CSS5), except for the fact that the intensity of the Bi-2212 peaks of CSS7 is slightly enhanced ($i_{23.1}/i_{21.8} = 1.85$), meaning this transformation has been evolving during this step. Table 9.2 collects the main phases and the composition (wt.%) of the CSS7 and the SSS precursor powders. This composition analysis was performed using the RIR of each phase. It is important to take into account that these Bi-based superconductors form by intercalation of the different phase layers. In consequence, the Bi-2212 phase, for instance, shows a broad range of compositions. This is reflected in the broadening of the XRD peaks. For this reason, the values presented in Table 9.2 can be considered only as semi-quantitative estimations to analyze the trends induced by the thermal treatments.

Precursor Powders	*Phase*			
	Bi-2201	Bi-2212	$SrCO_3$	CuO
CSS7	41.2	33.6	14.1	11.1
SSS	19.9	42.0	21.0	17.1

Table 9.2: Phase composition (wt.%) of the CSS7 and SSS precursor powders obtained with a semi-quantitative analysis using the RIR of each phase.

As mentioned above, Bi-2212 phase begins to form in the continuous solid-state process during the second or third heat treatment, reaching ~ 34 wt.% in the CSS7 sample. It must be noted that the sum of Bi-2201 and Bi-2212 phases reaches ~ 75 wt.%. The other 25 wt.% corresponds mainly to $SrCO_3$ and CuO. In the standard solid-state powders, the Bi-2212 phase is present in about 42 wt.%, but the sum of Bi-2201 and Bi-2212 phases is slightly lower than in the case of the continuous process (∼ 62 wt.%).

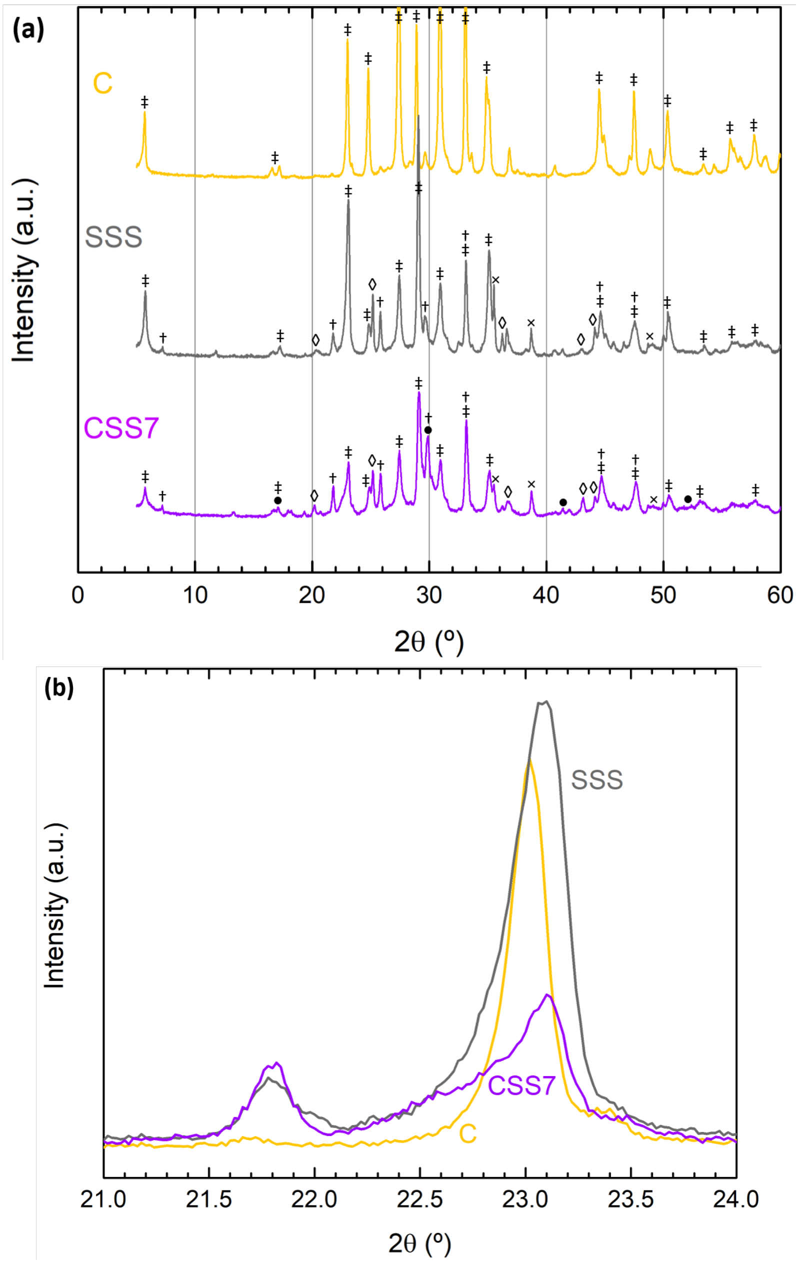

Figure 9.5: (a) XRD patterns of the C, SSS and CSS7 precursor powders. The different phases are identified by the same symbols as in Fig. 9.4. (b) Detail of the peak (008) of the Bi-2212 phase ($2\theta = 23.1°$) showing the broadening and the small shift.

In Figure 9.5 (a) the XRD patterns of the C, SSS and CSS7 precursor powders are compared. Sharper peaks of the Bi-2212 phase than in the SSS and CSS7 powders are clearly observed in the C powder pattern. If SSS and CSS7 powders are compared, Bi-2212 peaks are sharper and more prominent than those of the Bi-2201 phase ($i_{23.1}/i_{21.8} = 6.44$) in the SSS precursor, in good agreement with the results shown in Table 9.2. Figure 9.5 (b) shows a detail of these XRD patterns around the (008) peak of the Bi-2212 ($2\theta = 23.1°$). Besides a small shift in the position ($2\theta = 23.0°$ in C and $2\theta = 23.1°$ in SSS and CSS7 powders), it is clearly observed that the peaks of both solid-state powders are broader than that of C powder. This can be explained by the presence of intergrowths of Bi-2201 in the Bi-2212 grains [9] during the solid-state reaction process, which also complicates the phase quantification by XRD, as previously mentioned.

9.2.2 Particle size distribution

The particle size distribution of the SSS and the CSS precursor powders was analysed using a Beckman Coulter LS 13 320 laser diffraction particle size analyser.

Figure 9.6 shows a comparison of the measured particle size distribution of the SSS, CSS5 and CSS7 powders. The parameters d_{10}, d_{50} and d_{90}, characterising the powder particle size distribution are collected in Table 9.3 for these powders, together with those corresponding to the C powder, which were provided by the manufacturer.

Precursor Powders	d_{10} (µm)	d_{50} (µm)	d_{90} (µm)
C	0.10	1.18	2.18
SSS	4.74	22.95	55.59
CSS5	4.19	15.81	41.70
CSS7	4.05	16.84	42.45

Table 9.3: The particle size distribution parameters d_{10}, d_{50} and d_{90} for different precursor powders are collected.

The curves of both CSSX powders are very similar, as it would be expected since after every heat treatment in the continuous furnace the powders are

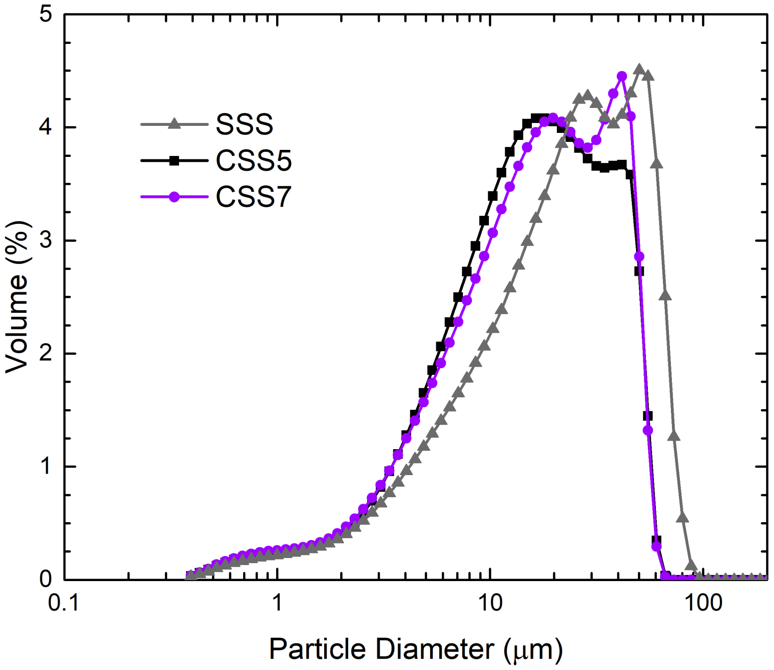

Figure 9.6: Particle size distribution of the SSS, CSS5 and CSS7 precursor powders.

ball milled, thus homogenizing the phases and the particle size. The main differences between both powders are observed in the region between 30 µm to 50 µm, where the number of particles is significantly higher in the powders that have been processed seven times. When we compare these distributions with that of the SSS powders, we observe that the grain size distribution is similar but slightly shifted in this case to higher sizes. This difference is probably due to the different duration of the milling used in each procedure. Note that the volume percentage of particles with sizes between 0.4 µm and 2 µm is very similar in these three powders. The C powders present the smaller grain size by more than an order of magnitude.

These results have also been confirmed by FESEM observations of the different precursor powders, as presented in Figure 9.7. Clearly, the differences in size of one order of magnitude can be observed if the image of powder C (Fig. 9.7 (a)) is compared with the images taken in the other three powders.

Figure 9.8 shows C and CSS7 powders using higher magnification for more detail. Note that these images were taken using the in-lens detector, which is a high-efficiency annular SE detector used to map the surface structure of a sample. These images clearly show that the grains are agglomerates of stacked planar grains.

In conclusion, the three powders fabricated using solid-state routes present very similar values of grain size, as discussed above, with no significant difference in the obtained values among the CSS5 and CSS7 precursor powders.

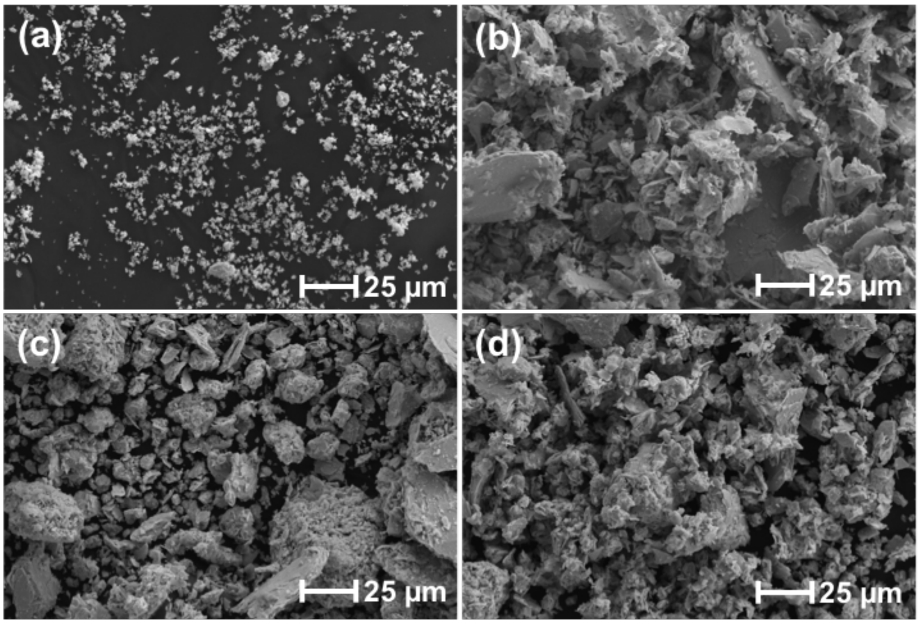

Figure 9.7: FESEM images using the SE detector of the different analyzed precursor powders: (a) C, (b) SSS, (c) CSS5, and (d) CSS7.

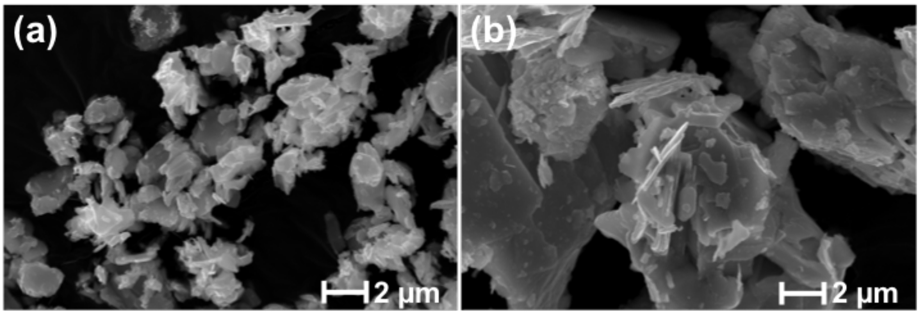

Figure 9.8: FESEM images using the InLens detector at a higher magnification of the (a) C and (b) CSS7 precursor powders.

9.2.3 Melting behaviour of the analysed powder

As these powders are intended for use as precursor for a melt-texture process, it is important to study if the above mentioned differences have any influence on their melting behaviour. This has been analysed using DSC and TGA techniques. The measurements were carried out in a SDT Q600 system which allows a simultaneous registry of weight loss (TGA) and heat flow changes (DSC) along programmed temperature scans. DSC was calibrated with sapphire standard and samples of about 15 mg were laid onto the tarred alumina pans and air was used as the purge gas at a flow of $100\,\mathrm{ml\,min^{-1}}$. The heat treatment applied to the precursor was a heating ramp of $10\,^{\circ}\mathrm{C\,min^{-1}}$ from RT up to $\sim 1000\,^{\circ}\mathrm{C}$.

The percentage of weight loss as a function of the temperature is displayed in Figure 9.9 for different precursor powders. The C powders present a weight loss of about a 2 % between 100 and 250 °C, which can be due to elimination of some hydroxide compounds that can be fixed in the surface of these small powders. This was expected since these powders have been stored for more than two years, they are very fine and, consequently, they are more reactive with the ambient in comparison with the other powders.

Concerning the continuous solid-state precursors, the CSS0 presents the greater weight loss as expected: up to a 14 % at 1000 °C. This is because the oxides and carbonates react to form the Bi-2212 phase loosing all the C in form of CO and CO_2. In fact, as detailed in Table 9.1, 114.8 g of oxides and carbonates are required to obtain 100 g of Bi-2212, which is in good agreement with the TGA measurement. CSS5, CSS7 and SSS precursor powders present very similar curves, so that the formation of the Bi-2212 would be similar in all three cases. The slight difference between the curves of CSS5 and CSS7 (5 % and 5.5 % respectively) indicates that additional heat treatments would not change essentially the precursor powder behaviour. Comparing the curves of the SSS, CSS5 and CSS7 with the curve of sample C, it is observed that the small mass loss at high temperatures in samples C starts at approximately 650 °C while in the other three samples starts near 750 °C.

The heat flow required to keep constant the heating ramp as a function of the temperature is displayed in Figure 9.10 for the same precursor powders

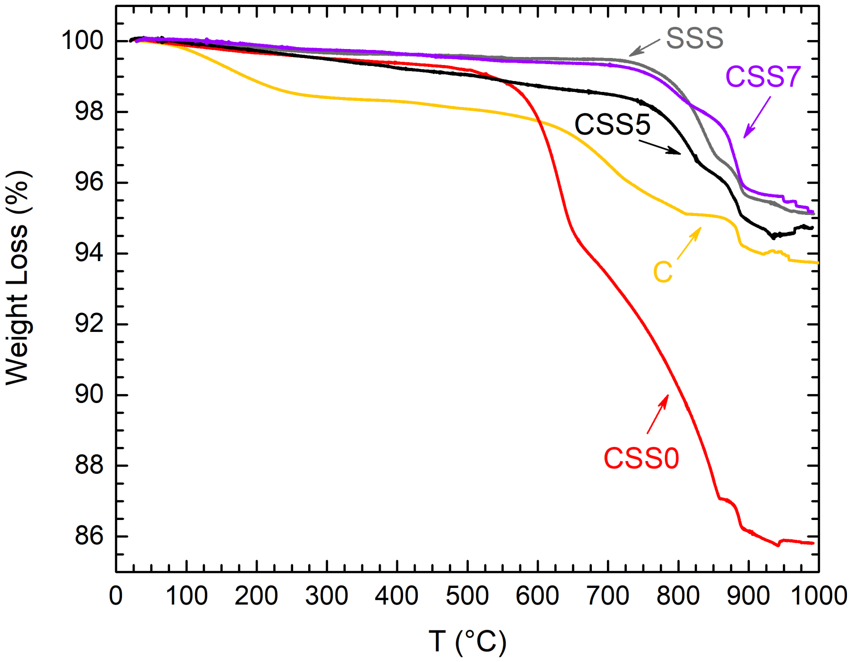

Figure 9.9: TGA of the C, SSS, CSS0, CSS5 and CSS7 precursor powders.

as in Fig. 9.9. The temperature region at which the Bi-2212 phase melts is shown in more detail in the inset. The values at which the main melting peak occurs are collected in Table 9.4.

Mayoral *et al.* showed that when low heating rates are used it is possible to distinguish the melting of different phases [40]. They found that a small part of the sample melts at temperatures between 865 and 870 °C, another fraction, associated with the Bi-2201 phase melts between 875 and 885 °C, and the greater portion melts between 885 and 895 °C. Data presented in the inset of Figure 9.10 shows that a similar behavior is observed in the SSS, CSS5 and CSS7 precursors, with different melting phenomena above 870 °C. The melting peaks of these powders are broader towards lower temperatures, which is expected due to the variations in the stoichiometry and in the presence of the lower melting temperature Bi-2201 phase [41] in these powders. The values at which the main melting peak occurs and the values of the energy involved in this endothermic peak are collected in Table 9.4. In the case of sample C, as the Bi-2212 phase is the main one, only a peak is observed. By contrast, the CSS0 sample shows a different behaviour showing a peak at 650 °C, and

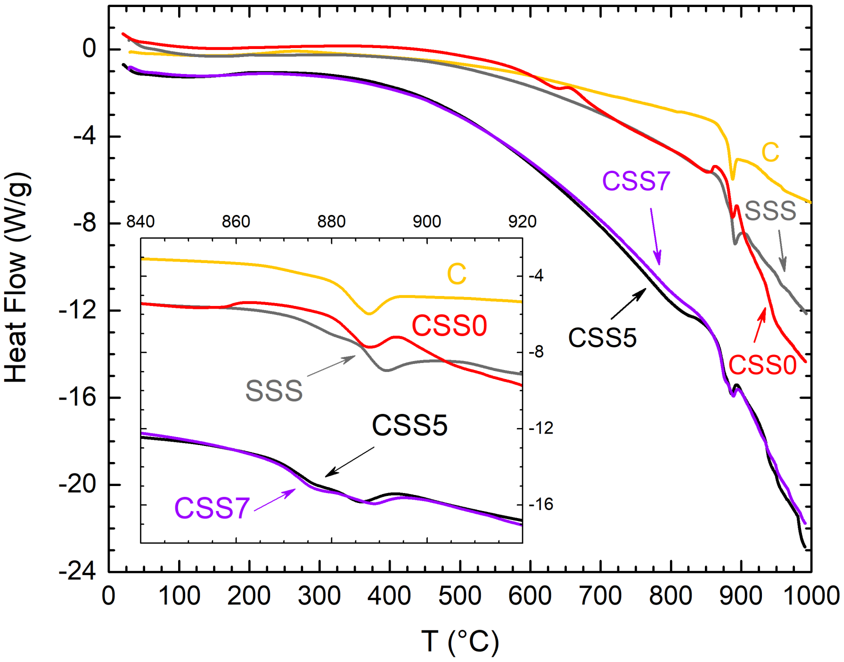

Figure 9.10: DSC as a function of the temperature of the C, SSS, CSS0, CSS5 and CSS7 precursor powders.

a small step in the heat flow at 857 °C showing that the Bi-2201 phase is forming. At temperatures above 890 °C it is possible to detect the formation of the Bi-2212 phase.

Precursor Powders	T (°C)	ΔH ($J\,g^{-1}$)
C	887.88	82.6
SSS	891.11	102.9
CSS0	887.18	35.8
CSS5	885.27	87.9
CSS7	888.53	113.0

Table 9.4: Melting temperatures and enthalpy changes of the Bi-2212 phase for the different precursor powders.

Mayoral *et al.* also showed that the Bi/(Sr+Ca) ratio can modify the melting temperature up to 7 °C, but without a clear trend when this ratio is changed [40]. In addition, depending on this ratio the mechanism that controls the solid-state reactions that are involved are different. In this work, the used stoichiometries give a value of Bi/(Sr+Ca) of 0.76 for the C powder and 0.7 for the other powders that are considered as Bi-rich precursor powders. In the case of the solid-state precursor powders, where a multiphase is obtained, the mobility of reactants is accelerated by the formation of a liquid phase.

These results show a similar melting behavior of SSS, CSS5 and CSS7 powders. Thus taking into account powder properties and processing method requirements, we can conclude that CSS5 present good characteristics to be used as precursor for melt-processed Bi-2212 materials. Additional heat treatments do not introduce substantial differences in the melting process of these powders.

9.2.4 AC magnetic susceptibility analysis

The AC magnetic susceptibility as a function of the temperature, $\chi_{ac}(T)$, of the precursor powders was measured using a SQUID-based Quantum Design MPMS-5T system. The measurements were performed in zero DC field and with AC magnetic fields of frequency of 120 Hz and amplitude of 0.1 mT.

Figure 9.11 (a) displays the in-phase component of χ_{ac}, χ', divided by the sample mass as a function of the temperature for C, SSS, CSS5 and CSS7 precursor powders. The same data together with the out-of-phase component, χ'', both scaled by $|\chi'(5\,\mathrm{K})|$, are also shown in 9.11 (b) and (c).

It is observed that all the samples show superconducting behaviour, but with remarkably smaller χ' values in the case of C precursor powders, by approximately one order of magnitude at low temperatures. This behaviour can be qualitatively explained by the differences in the grain sizes between these powders (see Table 9.3 and Figure 9.7) and taking into account the value of the in-plane London penetration depth in this material, $\lambda_{Lab}(0)$, which is $\sim 0.25\,\mu\mathrm{m}$ [42], the same order of magnitude than the grain size.

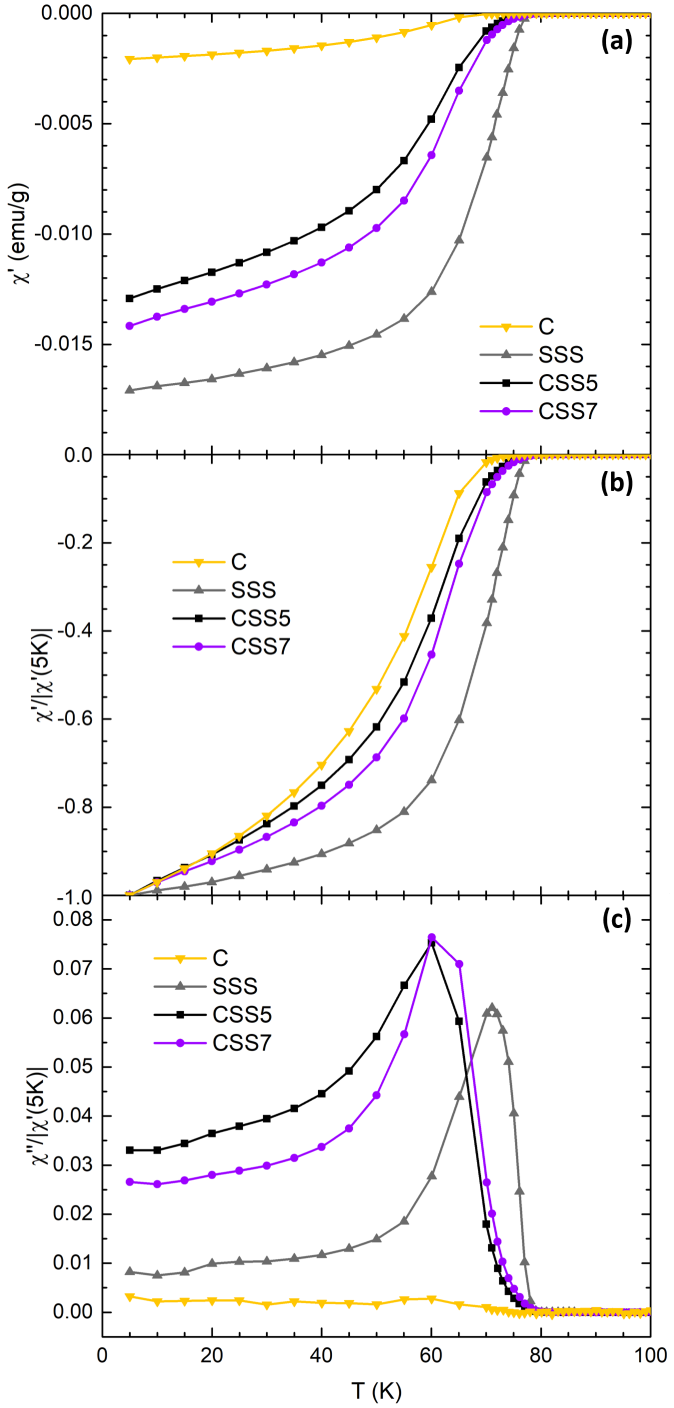

Figure 9.11: (a) Temperature dependence of the in-phase and out-of-phase components of the AC susceptibility, $\chi'(T)$ and $\chi''(T)$, divided (a) by the sample mass, (b) and (c) by $|\chi'(5\,\mathrm{K})|$ for C, SSS, CSS5 and CSS7 precursor powders.

As discussed by Campbell *et al.* [43], this is an important point to consider when χ_{ac} measurements are analysed. Clem and Kogan [44] presented the calculation of the magnetic moment, μ, of a superconducting spherical particle (radius r) as a function of the ratio $x = r/\lambda_L$ when a weak magnetic field, H, is applied:

$$\mu = -\frac{Hr^3}{2}P(x) \tag{9.1}$$

where $P(x) = 1 - (3/x)\coth(x) + 3/x^2$.

Although the Bi-2212 grains have a platelet-like shape, they are arranged in the form of agglomerates with rather spherical configuration, as can be seen in Figure 9.8. $P(x)$ is proportional to the percentage of the sample volume that would contribute to the diamagnetic signal. Table 9.5 shows the values of $P(x)$ at low temperatures if d_{50} and d_{90} values of each powder are considered. Taking into account that the contribution of smaller grains in powder C has a negligible contribution to the diamagnetic signal and that even with the grains associated to d_{90} the diamagnetic signal is only a 22 % of the volume, it is clear that the differences presented in Figure 9.11 (a), in which the C powder has a signal of approximately the 12 % of the diamagnetism of the SSS powder, could be explained taking into account the grain size distribution of each powder.

Precursor Powders	d_{50} (μm)	$P(r/\lambda_L(0))$	d_{90} (μm)	$P(r/\lambda_L(0))$
C	1.18	0.08	2.18	0.22
SSS	22.95	0.87	55.59	0.95
CSS5	15.81	0.82	41.70	0.93
CSS7	16.84	0.83	42.45	0.93

Table 9.5: Evolution of $P(x)$ for some characteristic grain sizes in the different powders.

The differences in the temperature dependence presented in Figure 9.11 (b) and (c) also can be explained considering the temperature dependence of the λ_L [44]. Transitions becomes broader as the particle size is reduced [43] following the trends presented in Figure 9.11 (b).

The results presented in this chapter show that it is possible to obtain

Bi-2212 precursor powders using a continuous solid-state fabrication process. Taking into account the characteristics of the continuous furnace that has been used, the Bi-2212 appears after three repetitions of the heat treatment (CSS3) and the main changes takes place after five repetitions (CSS5). Additional treatments facilitate the evolution to the transformation of the Bi-2212 phase but induce small changes in the overall properties of the powders.

In consequence, with these results, it is considered that after five repetitions of the heat treatment in a continuous furnace, the quality of the precursor powders obtained, CSS5, is sufficient to fabricate satisfactory high critical temperature Bi-2212 superconductor ceramic monoliths by Laser Zone Melting (LZM). In order to confirm these ideas, these powders are used as precursors to fabricate LZM textured samples in the following chapters. A comparison with the C precursor powders has been performed for selected cases in order to confirm this hypothesis.

Chapter 10

Influence of the precursor and the thermal heat treatment in laser textured materials

In this chapter we describe the developed technique for processing large and planar Bi-2212 bulk materials textured by LZM using industrial scale methods. We analyse and discuss the properties of the resulting superconducting materials and their microstructural characteristics at the different processing stages.

A new laser line scanning configuration for LZM processing has been used with this aim, which is described in 10.2. In order to validate the proposed method, it was firstly used to texture Bi-2212 materials made from commercial powders (10.3), and subsequently to texture materials made from the continuous solid-state precursors that were described in Chapter 9 (10.4). Finally, we have analysed the effect of texturing both sides of the planar samples instead of just one side with commercial powders (10.5). For those samples, we have studied the possibility of using a continuous heat treatment to obtain the superconducting phase after laser processing, instead of the “traditional” one (10.6).

10.1 Pellet preparation

Two different kinds of pellets were prepared prior to the LZM process:

- **Disks** - 14 g of Bi-2212 were uniaxially pressed into disk at 140 MPa. The disks have a diameter of 40 mm and a thickness of 2.1 mm. Besides, 3 wt.% of polymethyl methacrylate (PMMA, $(C_5H_2O_8)_n$) was used as binder in combination with 0.5 ml of acetone (C_3H_6O) as a dispersant. After the preparation, the dispersant was evaporated from the disks with an infrared bulb. An example of this kind of samples is shown in Figure 10.1.

- **Rectangular bars** - between ∼ 6 and 8 g of precursor powders were isostatically pressed at a equivalent pressure of 60 MPa without dispersant nor binder, to form rectangular bars of approximate dimensions 2 × 8 × 80 mm. A photograph of one of these rods is also displayed in Figure 10.1.

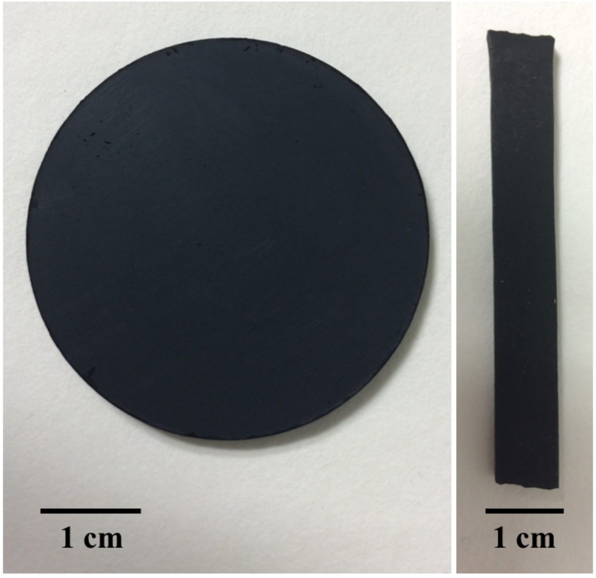

Figure 10.1: Pictures of the two pellet geometries used for LZM process: disks and rectangular bars.

10.2 New laser line scanning configuration for LZM processing

The prepared pellets were processed using a new laser line scanning configuration, consisting in a CO_2 pulsed laser coupled to a galvanometric mirror system. The aim is to demonstrate the feasibility of texturing pieces of width up to 40 mm and processing several samples in parallel, thus overcoming the limitations of traditionally used laser configurations [36], which impose restrictions in the sample width due to intrinsic features. Preliminary tests using this new set-up, carried out by Lennikov et al [32] for smaller samples, revealed that superconducting properties of the textured material strongly deteriorate when the texturing speed increases. The work developed in this thesis aims to scale-up this procedure to larger samples, to overcome some of the problems presented in [32] and to optimize the processing method. A novel two-step LZM procedure is proposed to gain better control of the processed material microstructure.

The LZM process was performed in air, inside a furnace, at a temperature of 450 °C. An Easy-Laser 350 W SLAB-type pulsed CO_2 laser, emitting at a wavelength $\lambda = 10.6\,\mu\mathrm{m}$, was used (see Figure 10.2). The laser is a pulsed system emitting with frequencies up to 20 kHz and pulse widths of 50 µs. One important parameter of the laser process is the duty cycle, which is the fraction of one period (the time that a pulsed laser needs to complete an on-and-off cycle) in which the laser is active. For the laser used in this work, the maximum duty cycle was 50 %.

The laser output beam is steered with a galvanometer mirror system, with a diameter of 0.8 mm at a distance of 1050 mm, and the laser beam is displaced along the y-direction with a steering speed of $12\,\mathrm{m\,s^{-1}}$. As it can be observed in Figure 10.3, this allows obtaining from a circular laser beam a line over the sample surface, which in this case is 250 mm long. The length of this line must be larger than the sample width, otherwise the laser will change the sense inside the sample and will create a localized region where the laser treatment is stronger.

The beam line was directed to the sample surface at an angle of 15° with respect to the sample surface normal. By modifying the laser power, the

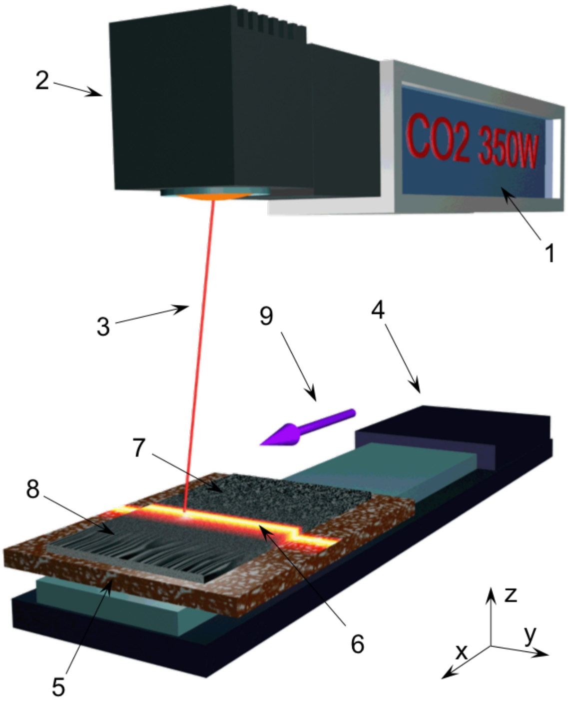

Figure 10.2: A scheme of the laser used for LZM processing of the samples [32]. 1. CO_2 laser. 2. Beam steering system. 3. Laser beam. 4. Sample movement stage. 5. Protection plate with metal power dissipaters (not shown in 3D simulation). 6. Melt line in the sample. 7. Non-processed zone of the sample. 8. Textured zone of the sample. 9. Sample movement direction.

laser steering speed and the line width is it possible to control the amount of energy deposited on the surface. In order to obtain a flat solidification front, it is essential to control all these parameters to maintain a constant molten volume, even when the laser beam is out of the sample. It is also possible to process several samples in parallel, as shown in Figure 10.3.

The sample is displaced in the x-direction, with a traverse rate determining the speed at which the molten zone travels along the sample. One of the limitations of the equipment used in this work is that the minimum sample displacement speed is $25\,\mathrm{mm\,h^{-1}}$.

Samples were textured at 450 °C using a two-step processing protocol. In the first one, the sample travelling velocity was $100\,\mathrm{mm\,h^{-1}}$ and the duty

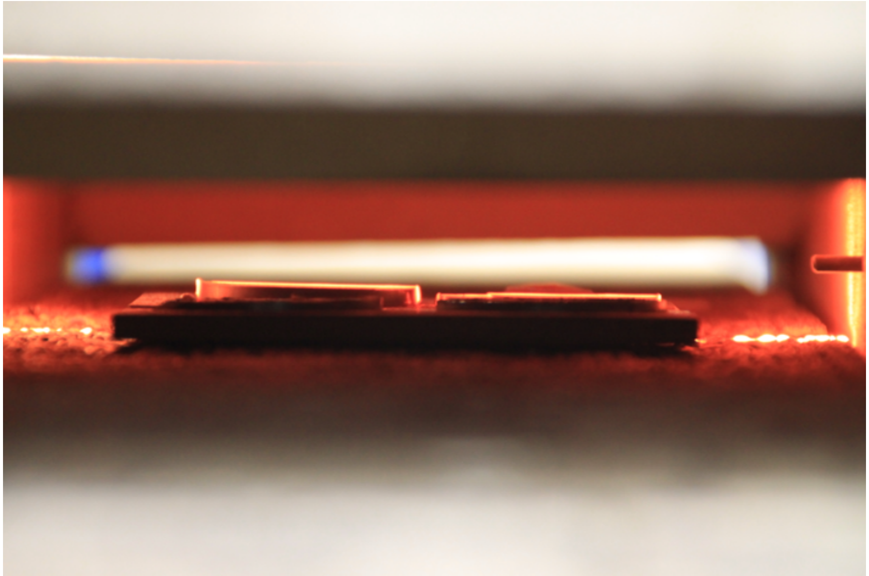

Figure 10.3: Picture of two Bi-2212 disks (4 cm in diameter) placed over a Cu piece inside the furnace during laser treatment. The image clearly shows that the width of the scaned laser line is longer than the sample width and that several samples can be processed in parallel.

cycle was 45 %. For the second step, the sample velocity was decreased to 30 mm h^{-1} and the duty cycle was increased to 50 %. The objective of the first texturing treatment is to quickly melt, densify and consolidate the sample surface, while in the second one, the objective is to induce an adequate texture to the previously treated surface of the sample. An example of a textured Bi-2212 disk and rectangular bar samples are displayed in Figure 10.4. In the case of the disk, the laser treatment was stopped 1 cm before the final of the sample to analyse the solidification front. The image clearly shows that it is horizontal and that a high degree of texture has been induced after the laser texturing process.

All samples are processed over a bulk Cu piece of 10 cm × 10 cm × 5 mm that acts as a sample holder and contributes to homogenize the temperature at the base. Thermal insulators, such as alumina plates, were initially used as substrates but discarded because, unlike copper, they absorb the laser radiation inducing additional local heating and cause bending of the sample.

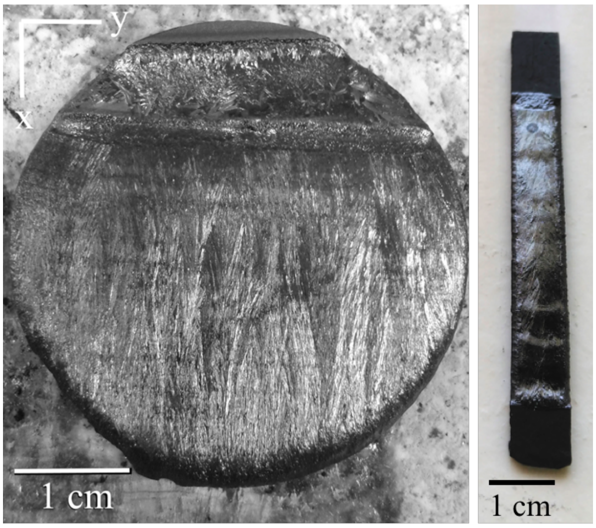

Figure 10.4: Left-hand side picture shows a textured Bi-2212 disk of 40 mm of diameter. Laser texturing process was started in the bottom part of the sample and was stopped 1 cm before finishing it in order to record the shape of the solidification front. Right-hand side picture shows a textured Bi-2212 rectangular bar 73 mm long. Not the full length of the rectangular bar is processed.

10.3 Validation of the new LZM processing method

General rectangular bar samples were prepared from commercial precursor powders using the processing method described in 10.2 and the results are presented in this section.

10.3.1 Microstructure after the first step of the LZM texturing process

Figure 10.5 shows the longitudinal cross-section of the textured monolith, named TC1 (Textured monolith fabricated with Commercial precursor), after the first processing step, performed at $100\,\mathrm{mm\,h^{-1}}$ to quickly melt and densify the sample surface. This microstructural analysis was performed on a less-than-usual wide rectangular bar (~ 3.2 mm-width) and before any heat treatment in order to better investigate the phase composition and texture induced by laser.

The FESEM images show the typical three regions frequently observed

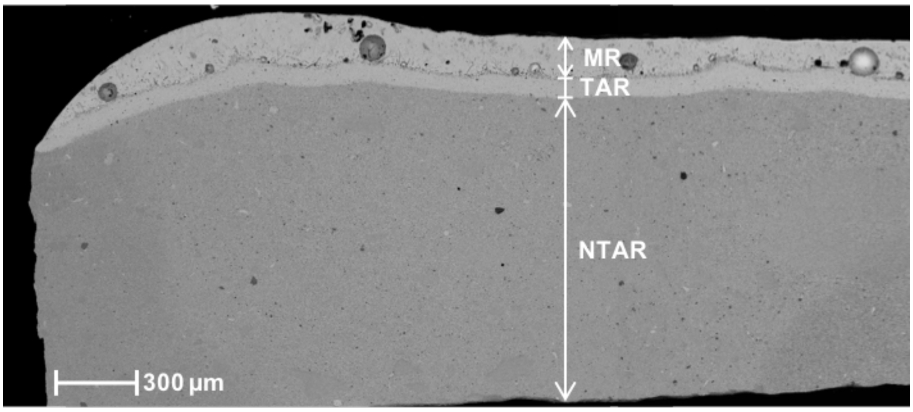

Figure 10.5: FESEM image using AsB detector of the longitudinal cross-section of sample TC1 subjected to the first step of the LZM texturing process at 100 mm h^{-1}.

in any laser process: the molten region (indicated as MR) near the treated surface, the original one (indicated as NTAR) at the bottom and a thermally affected region (indicated as TAR) in between.

In the lower part of the sample the initial raw commercial precursors can be seen. From the EDX analysis, adjusting the Bi to 2.18, the composition is 2.18:1.90:0.83:1.92, which is similar to the given nominal composition of 2.18:1.98:0.87:1.97.

The other two regions affected by the laser can be seen with higher magnification in Figure 10.6. The densification reached by the laser treatment creates bubbles in the lower part of the molten region.

In the thermally affected zone, the grain size ranges from less than 1 µm to more than 60 µm. The microstructure shows that the solidification rate was too high to produce texture and it produces a structure of grains that mainly nucleates from the interface between the melt and the thermally affected region, inside a matrix of amorphous material.

Several phases can be distinguished. The composition of the three major phases, deduced from FESEM images and EDX analysis, is collected in Table 10.1. The main component is a matrix with a regular grey contrast, that corresponds to a fast solidified liquid phase and whose composition is very close to the Bi-2212 phase of the precursor powders. The amount of Bi increases, most probably due to the formation of Bi-free oxides as well as Ca and Cu

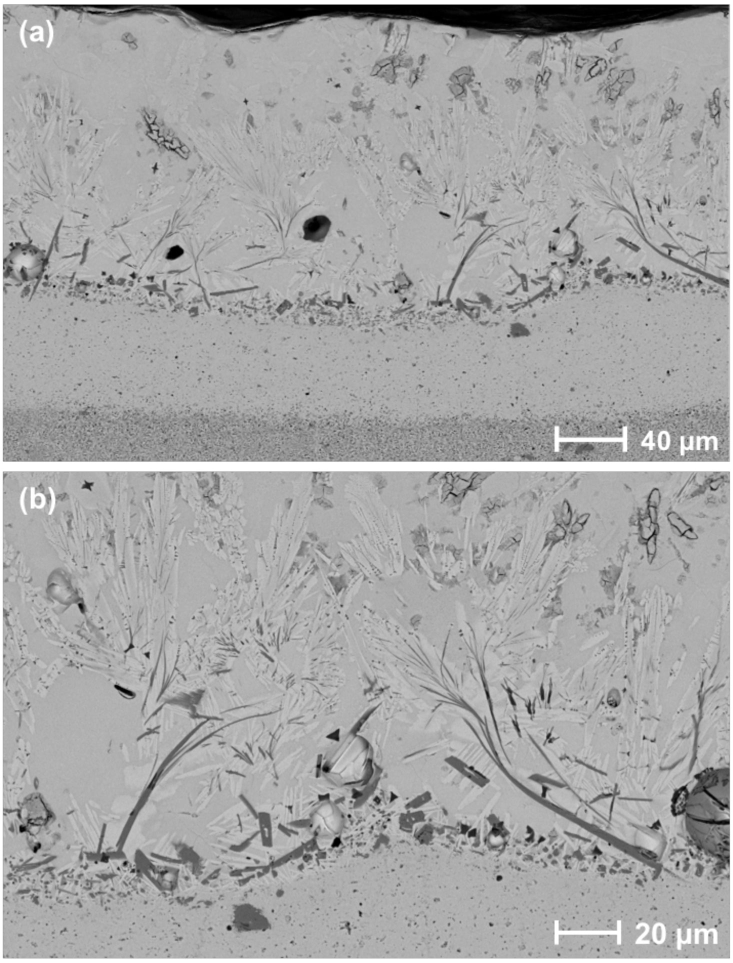

Figure 10.6: FESEM images using AsB detector of the longitudinal cross-section of the thermally affected zone by the first step of the laser processing at 100 mm h^{-1} in sample TC1. (a) General view of the microstructure. (b) Detail of the interfase between the melted and the thermally affected regions.

oxides. Inside this matrix, a random structure of Bi-2201 grains (lighter grey contrast) can be observed. From the analysis of the composition, also the amount of Bi is too high and some traces of Ca are also detected by EDX as a signal of the intergrowths between Bi-2201 and Bi-2212 phases and the possible contribution of the surrounding phases. Some Bi-free grains (dark grey contrast) nucleate in the interface of this region. This Bi-free phase is the so called 1:1, with a composition $(\mathrm{Sr_{1\text{-}x}Ca_x})\mathrm{CuO_2}$, $x = 0.6$. The presence of this Bi-free phase was previously reported in Bi-2212 laser textured samples by other authors [7,14,45]. Also small grains of Cu and Ca oxides can be found in the lower part of the laser melted region (black contrast).

Phase	*Composition* (at.%)				
	Bi	Sr	Ca	Cu	O
Matrix (Bi-2212)	16 (1)	13 (1)	5 (1)	12 (1)	54 (3)
Bi-2201	20 (1)	14 (1)	3 (1)	9 (1)	54 (2)
1:1	-	16 (1)	11 (1)	25 (1)	48 (2)

Table 10.1: Chemical composition values and standard deviations of the three major phases deduced from FESEM images and EDX analysis after the first step of the LZM processing of sample TC1.

10.3.2 Microstructure after the second step of the LZM texturing process

The second step of the laser processing is performed at $30\,\mathrm{mm\,h^{-1}}$ and affects more deeply the microstructure and phase composition, as can be seen in Figure 10.7. The thermally affected region (indicated as TAR) is approximately 240 µm, three times thicker than when the first laser treatment at $100\,\mathrm{mm\,h^{-1}}$ was performed. The melted region (indicated as MR) also grows in thickness. The lower part of the melted region is characterized by the accumulation of 1:1 phase grains whose growth direction is different across the melted area. This reflects the change in the thermal gradients in this region during the texturing process. Besides, grains of Cu and Ca oxides can also be seen, which are mainly at the bottom of the melted region.

In the upper part, the sample TC1 exhibits a region with long and oriented grains almost parallel to the surface. Figure 10.8 shows this region, where the three main phases previously mentioned, i.e. Bi-2201 (light grey contrast), matrix with a composition close to Bi-2212 (regular grey contrast) and Bi-free 1:1 (dark grey contrast), are clearly distinguishable. Furthermore, Ca oxide grains can also be seen in black.

Another example of this upper well-textured region from other part of the sample TC1 with a higher magnification is displayed in Figure 10.9, where even grains of the 1:1 phase aligned parallel to the surface can be observed.

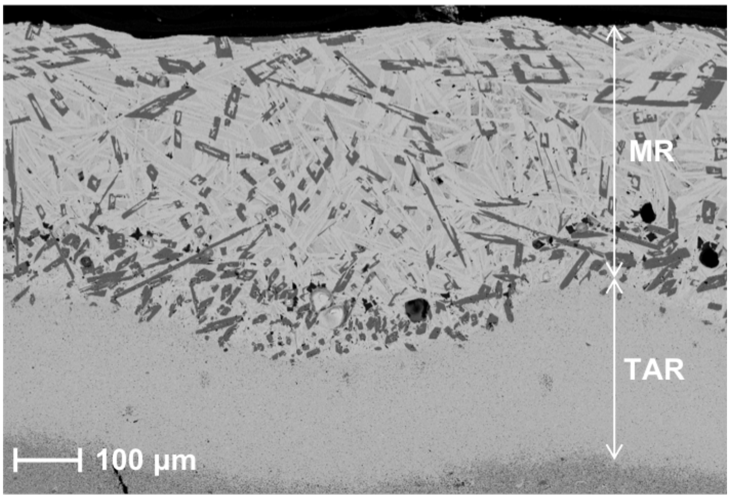

Figure 10.7: FESEM image using AsB detector of sample TC1 longitudinal cross-section after the second and final step of the laser processing at $30\,\mathrm{mm\,h^{-1}}$.

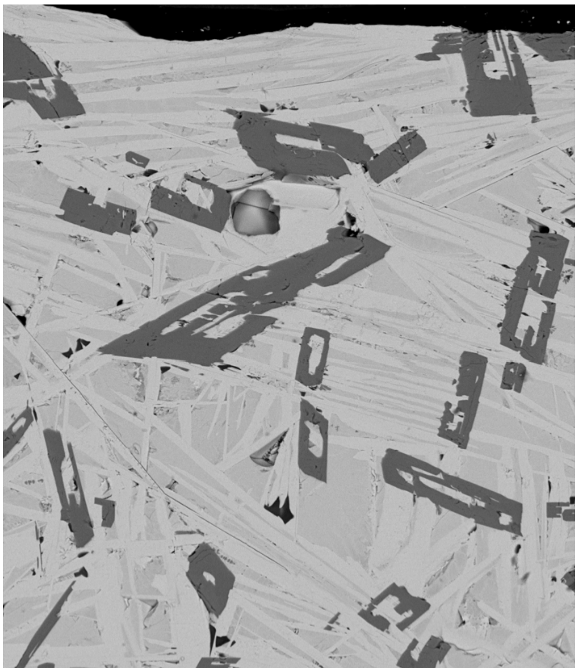

Figure 10.8: FESEM image using AsB detector of the well-textured region of sample TC1 longitudinal cross-section after the second and final step of the laser processing at $30\,\mathrm{mm\,h^{-1}}$.

Moreover, Cu oxide particles are observed inside the Bi-2212 matrix, showing an eutectic-like structure. These Cu oxide grains have a darker grey contrasts than that of the Bi-2212 matrix.

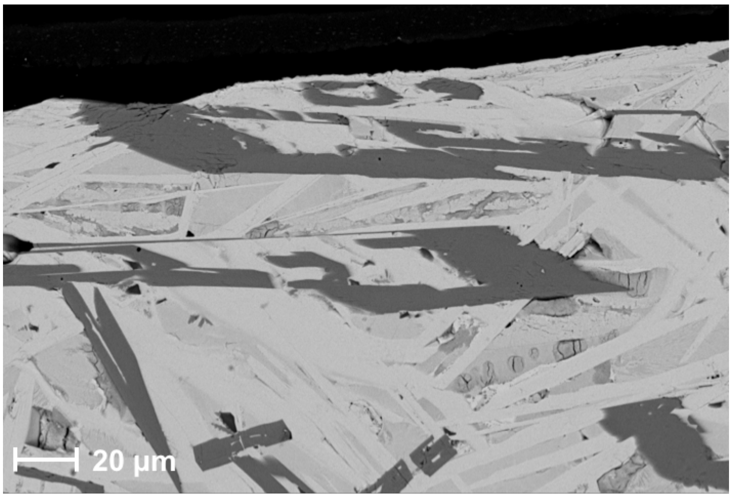

Figure 10.9: FESEM image using AsB detector at a higher magnification of the well-textured upper region of sample TC1 longitudinal cross-section after the second and final step of the laser processing at $30\,\mathrm{mm\,h^{-1}}$.

The compositions of these three phases (Table 10.2) are practically identical to those obtained when analysing the phase composition after the first step of the LZM texturing procedure (see Table 10.1).

Phase	*Composition* (at.%)				
	Bi	Sr	Ca	Cu	O
Matrix (Bi-2212)	16 (1)	13 (2)	5 (1)	13 (2)	53 (3)
Bi-2201	20 (1)	14 (1)	2 (1)	9 (1)	55 (3)
1:1	-	16 (1)	10 (1)	24 (1)	52 (2)

Table 10.2: Chemical composition values and standard deviations of the three major phases were deduced from FESEM images and EDX analysis after the two-step LZM processing of sample TC1, before the final heat treatment.

Typically, bar pellets are fabricated with a thickness of $\sim 2\,\mathrm{mm}$ (see section 10.1). After the texturing process the transverse cross-section of the laser affected region is not uniform due to the differences in the heat evacuation rates in the center and in the border of the sample. Figure 10.10 shows the typical transversal cross-section. From these measurements it can be deduced that the cross-section has been reduced a 40 % due to densification during the laser process. The final thickness at the center of the sample is approximately $\sim 1.2\,\mathrm{mm}$.

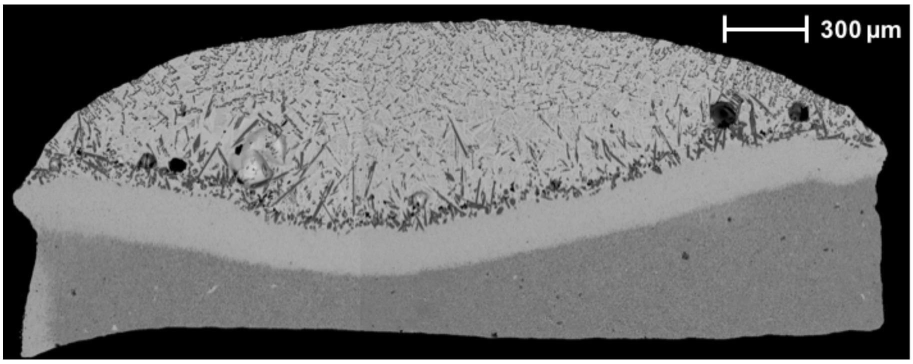

Figure 10.10: FESEM images using AsB detector of the transverse cross-section of sample TC1 after the second texturing step.

In fact, the thermally affected cross-section can be determined from these images to be $\sim 0.02\,\mathrm{cm}^2$, by subtracting the total area minus the dark grey lower part area which corresponds to the original non-processed ceramic.

10.3.3 Microstructure after heat treatment

Bi-2212 materials show an incongruent melting that leads to multiphase materials [38]. Thus, after the texturing process, a thermal treatment is required to recover the superconducting phase. Bi-2212 phase grows from the Bi-2201 phase due to diffusion phenomena of the $(\mathrm{Sr}_{1\text{-x}}\mathrm{Ca}_{\mathrm{x}})\mathrm{CuO}_2$.

Heat treatment

Mora *et al.* [46] obtained that as-grown LFZ Bi-2212 rods have to be maintained at 845 °C for at least 60 h to form the superconducting phase. Natividad *et al.* [47] used Simplex Methods to optimize the heat treatment of LFZ textured Bi-2212 rods, concluding that the heat treatment requires two steps, one at 870 °C to form the Bi-2212 phase and a second one at 800 °C to adjust the oxygen content.

Later works optimised this heat treatment for textured LZM monoliths [48–50], which is shown in Figure 10.11 and that we will denominate "traditional" treatment from now on in this thesis. It is performed in air and consists in a first heating from RT to 800 °C at 1.33 °C min^{-1} which slows down to 0.42 °C min^{-1} from 800 °C to 850 °C. Then, samples are kept at 850 °C for 60 h. Thus, the different phases present in the sample react to form the Bi-2212 superconducting phase [47]. After that, a quick cooling down to 800 °C is performed at 4.20 °C min^{-1} and the sample is maintained at this temperature for another 12 h to adjust the oxygen content. Finally, a decrease from 800 °C to RT is performed at a rate of 1.33 °C min^{-1}. When the temperature reaches values of the order of 600 °C, it is quenched in order to avoid the expulsion of the captured O-atoms at lower temperatures.

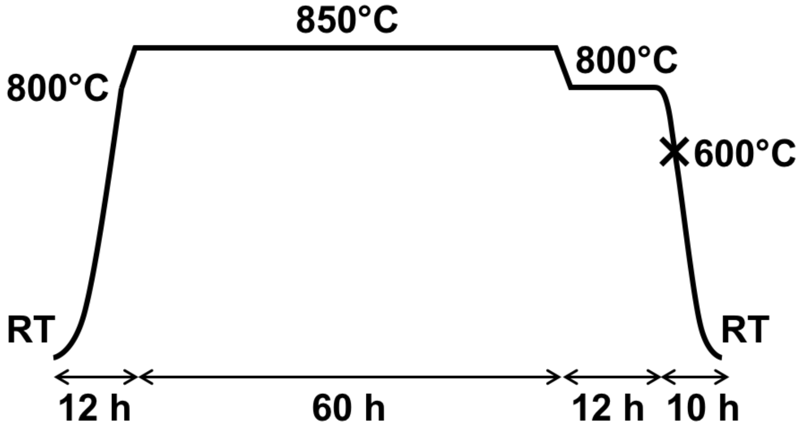

Figure 10.11: "Traditional" heat treatment comprised of an initial heating from RT to 850 °C in 12 h, followed by a two-step heat treatment at 850 °C for 60 h and 800 °C at 12 h respectively. Finally, a controlled cooling from 800 °C to RT in 10 h with a quench at 600 °C is performed. The complete treatment is carried out in air atmosphere.

Phase composition after heat treatment

Another rectangular bar also made with C precursor powders and named TC2 (8.6 mm-width) was prepared following the same process than sample TC1. As it can be observed in Fig. 10.12, the microstructure of the textured region of sample TC2 has homogenized considerably in terms of phase composition in comparison with the as-grown samples, i.e. just after the laser processing (sample TC1). From the images, it can be observed that the main phase is the Bi-2212, but some grains of the 1:1 and Bi-2201 phases still remain as minority phases. This indicates that the phase segregation occurred during the texturing process is not uniform and in some regions there are Bi-2201 deficiency and 1:1 excess to complete the reaction, while in others it is the opposite. The 1:1 grains are mainly concentrated in the upper well-textured region and in the inner part of the melted region.

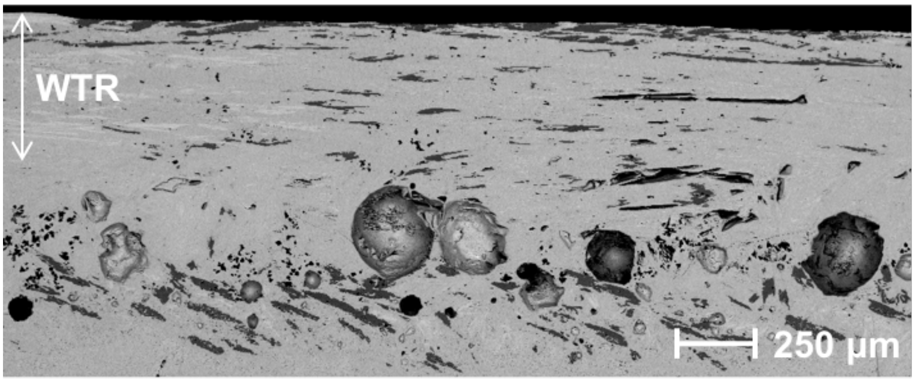

Figure 10.12: FESEM image using AsB detector of the longitudinal cross-section of LZM processed sample TC2. The image was taken after subjecting the sample to the "traditional" heat treatment.

Table 10.3 presents the chemical composition of the three major identified phases as measured by EDX analysis using the FESEM images. These compositions are similar to those measured in the as-grown samples (see Tables 10.1 and 10.2). This means that the recovery of the superconducting Bi-2212 phase achieved through the "traditional" heat treatment does not show chemical deviations from its original stoichiometry.

The upper well-textured region, indicated in Fig. 10.12 as WTR, is presented in Fig. 10.13, with higher magnification. With the exception of the 1:1 phase grains (dark grey) and some small and disperse holes, a highly homogeneous Bi-2212 phase (regular grey) is obtained. Some traces of Bi-2201 grains (light grey) are still present among the Bi-2212 matrix, as previously mentioned. Besides, some oblique scratches, consequence of the polishing used during the sample preparation, can be also observed. It is important to remark that the desired orientation of the superconducting grains, aligned parallel to the surface, it is successfully achieved.

Phase	*Composition* (at.%)				
	Bi	Sr	Ca	Cu	O
Bi-2212	15 (1)	13 (1)	5 (1)	13 (2)	54 (2)
Bi-2201	20 (1)	14 (1)	2 (1)	9 (1)	55 (2)
1:1	-	17 (1)	9 (1)	24 (1)	50 (2)

Table 10.3: Chemical composition values and standard deviations of the three major phases deduced from FESEM images and EDX analysis after subjecting the LZM textured sample TC2 to the "traditional" heat treatment.

Figure 10.13: FESEM image using AsB detector of the upper well-textured part of sample TC2 displayed in Fig. 10.12 at a higher magnification.

10.3.4 Superconducting properties

After performing the “traditional” heat treatment required to obtain again the superconducting Bi-2212 phase, the need to evaluate the superconducting performance of the rectangular bar shaped sample, TC2, arises. In order to do that, both the T_c and I_c (77 K) are measured for sample TC2 with the following dimensions: width $w = 8.6\,\mathrm{mm}$ and distance between voltage contacts $l = 10.5\,\mathrm{mm}$.

Taking into account that the cross-section of sample TC2 is not fully textured, instead of using quantities that require a precise determination of that transport cross-section, such as the resistivity (ρ) or the J_c, the resistance, $R(T)$, re-scaled by a geometrical factor w/l (being w and l the samples's width and distance between voltage contacts respectively), and the transport applied current also re-scaled (I/w) are used to compare the behaviour of different samples with different widths.

$R(T)$ measurements were performed using a four-point configuration, immersing the superconducting sample TC2 in liquid nitrogen and letting it warm up slowly as the nitrogen evaporates until reaching room temperature. A current bias of 1 mm was used. A T_c of 86.4 K was deduced from the $R(T)$ measurement presented in Figure 10.14.

Besides, the transport critical current value was measured at 77 K with the sample immersed in liquid nitrogen and the electrical current applied in the perpendicular direction to the solidification front. Figure 10.15 shows the obtained data from which the I_c value was determined using the $1\,\mu\mathrm{V\,cm^{-1}}$ criterion.

As can be seen in Fig. 10.15, the plotted data are not the measured $I - V$ curve but the measured electric field, E, versus the I/w. From the data at high E values, considering the potential dependence of the $I - V$ curve in the dissipative regimen:

$$E \propto \left(\frac{I/w}{I_c/w}\right)^n \tag{10.1}$$

an adjustment to an potential function $y = a \cdot x^b$ is performed as can be observed in Figure 10.16. From the constants of the fitting, we can deduce

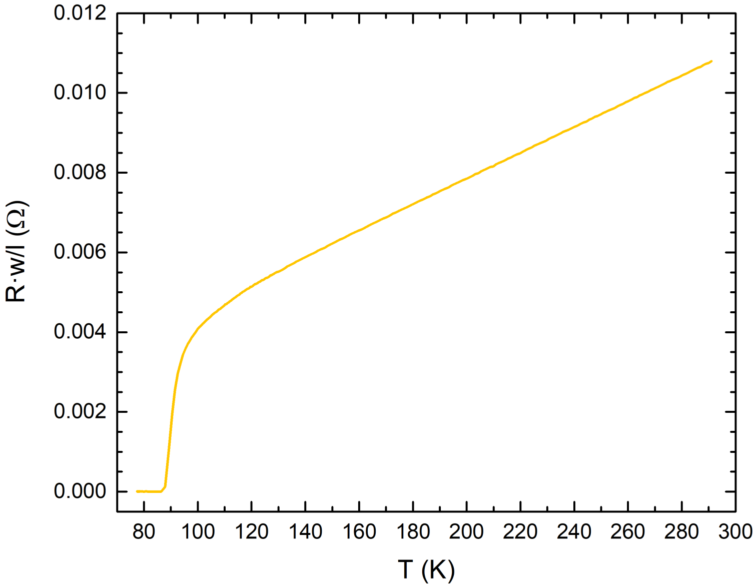

Figure 10.14: Measurement of the electrical resistance, R, as a function of the temperature from 77 K up to RT of sample TC2. R is re-scaled by a geometrical factor (w/l) for comparison purposes.

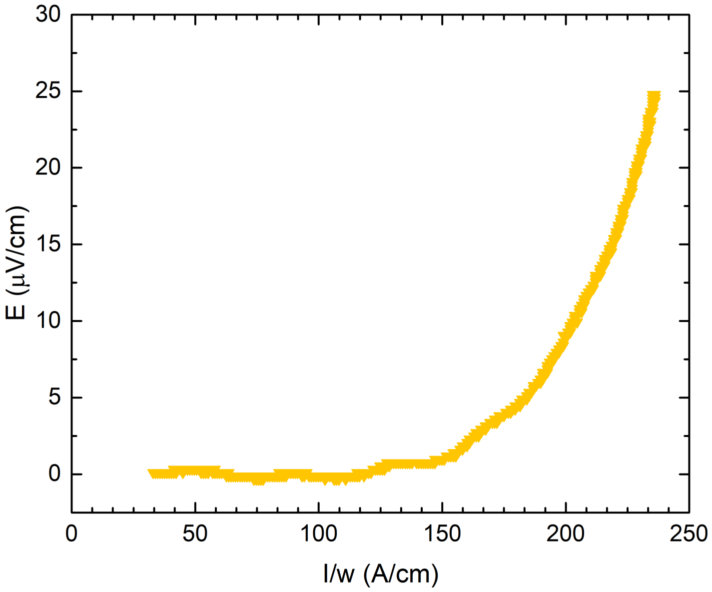

Figure 10.15: Transport critical current measurement of LZM textured sample TC2 on a linear plot. The x-axis is re-scaled dividing it by the width of the sample, w, for comparison purposes.

that $I_c/w = 141.2\,\mathrm{A\,cm^{-1}}$ and $n = 6.23$. The value of I_c/w is a 40 % higher than the maximum value published in the previous work of Lennikov *et al.* ($101.4\,\mathrm{A\,cm^{-1}}$) [32], even if the texturing speed was twice in the present work.

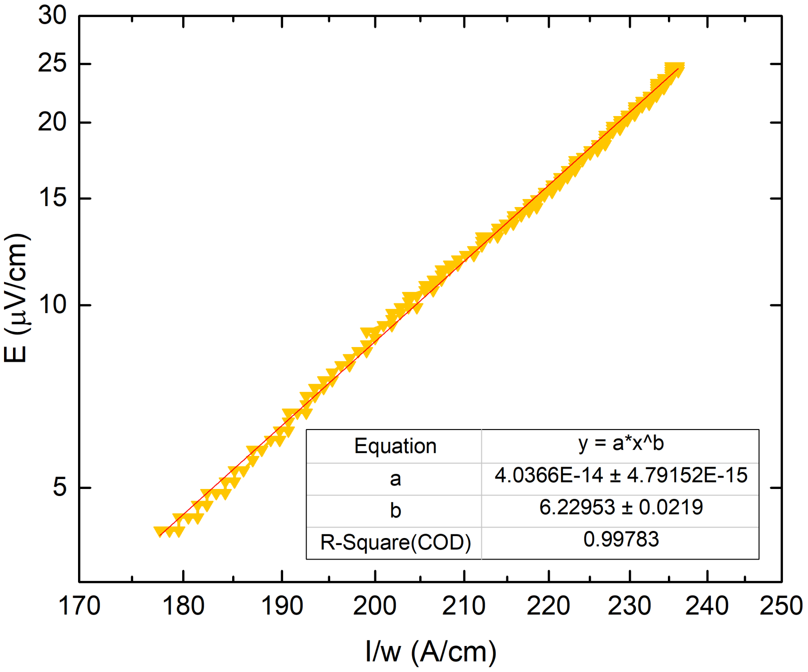

Figure 10.16: Fit of the $E-(I/w)$ curve of sample TC2 in the dissipative regimen to a potential dependence.

Therefore, considering the width of the sample TC2 (8.6 mm) and estimating the thickness of its well-textured region ($\sim$ 480 µm, see Fig. 10.12), the area of an ellipse, with these dimensions as axes, gives an approximate value of the textured transport region of $\sim 3.24\,\mathrm{mm^2}$. Thus, a J_c value of the order of $3.7\,\mathrm{kA\,cm^{-2}}$ can be obtained. This J_c value is in the range of typical values for Bi-2212 LFZ processed thin rods [15, 51] and slightly higher but in the order of magnitude of the best results obtained to date for LZM processed planar Bi-2212 bulks [27]. Despite the high sensitive to the transport region chosen for the definition of the J_c values, these results validate the two-step LZM process used to texture the samples.

10.4 Properties of LZM textured materials using CSS precursors

In order to study the microstructural and superconducting properties of the LZM Bi-2212 samples manufactured from the continuous solid-state precursor powders, three rectangular bar-shaped pellets were prepared using the CSS0, CSS1 and CSS5 powders described in section 9.1. CSS5 has been selected because the results obtained in Chapter 9 show that this is the minimum number of processing steps to reach a certain quality. CSS0 and CSS1 powders have also been studied to determine if textured materials obtained with these low reacted powders are similar. These pellets were processed by the two-step LZM method (detailed in 10.2) and subsequently subjected to the “traditional” heat treatment (shown in Fig. 10.11). The microstructure of the samples before and after this final heat treatment has been analysed.

10.4.1 Microstructure of the as-grown LZM samples

The microstructure of the longitudinal cross-sections of three Bi-2212 rectangular bars after the two-step LZM process is displayed in Figure 10.17. The textured sample processed with the CSSO precursor, TCSS0, presents a very disordered microstructure (Figure 10.17 (a)), with the presence of bubbles much larger than in the other analysed samples (Figs. (b) and (c)). This would be due to CO and CO_2 formation during the LZM process that get trapped inside the sample.

It is remarkable that not only the order in the microstructure, but also the depth of the molten region (indicated as MR), grows with the number of heat treatments of the precursor powders. In particular, it almost doubles from sample TCSS0 to sample TCSS5. Besides, the well-textured region (indicated as WTR) grows notably in depth when increasing the number of the precursor heat treatments. Note that the thickness of the well-textured region of the sample TCSS5 is very similar to that of sample TC2.

The three main observed phases are the same as those identified in sample TC1 (see Table 10.2), i.e. matrix close to Bi-2212 in regular grey, Bi-2201 in light grey and the Bi-free phase (1:1) in dark grey. Table 10.4 collects the

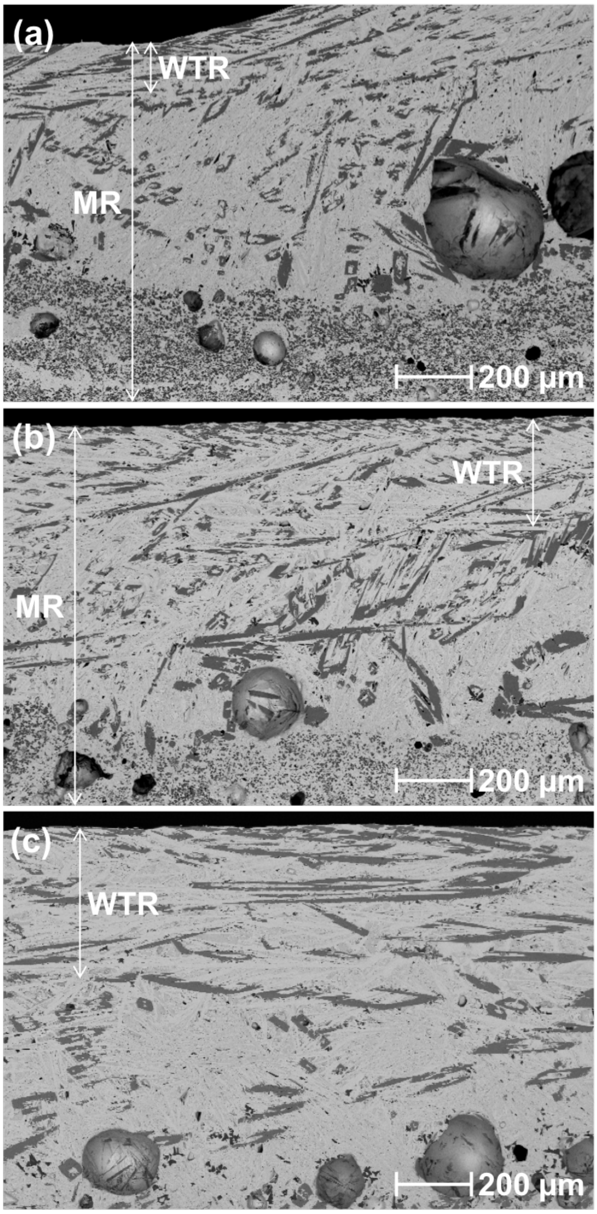

Figure 10.17: FESEM images using AsB detector of the longitudinal cross-sections after the LZM texturing process of samples (a) TCSS0, (b) TCSS1 and (c) TCSS5.

chemical composition of the three phases estimated from EDX analysis.

The composition of these phases in the as-grown samples does not depend on the powders used as precursor, CSS0, CSS1 or CSS5. Note that for the matrix with a composition close to the Bi-2212 phase, this would correspond

Sample	*Phase*	*Composition* (at.%)				
		Bi	Sr	Ca	Cu	O
TCSS0	Matrix (Bi-2212)	14 (1)	13 (2)	5 (1)	12 (2)	56 (2)
	Bi-2201	19 (2)	13 (1)	2 (1)	9 (1)	57 (3)
	1:1	-	12 (1)	11 (1)	22 (2)	55 (3)
TCSS1	Matrix (Bi-2212)	14 (1)	12 (1)	4 (1)	11 (1)	59 (2)
	Bi-2201	18 (1)	12 (1)	2 (1)	8 (1)	60 (2)
	1:1	-	13 (1)	10 (1)	21 (1)	56 (2)
TCSS5	Matrix (Bi-2212)	14 (1)	12 (2)	4 (1)	12 (2)	58 (3)
	Bi-2201	17 (1)	12 (1)	2 (1)	8 (1)	61 (3)
	1:1	-	12 (1)	10 (1)	21 (1)	57 (2)

Table 10.4: Chemical composition (in at.%) and (standard deviations) of the three major phases deduced from FESEM images and EDX analysis after the LZM processing of the samples fabricated using the continuous solid-state precursor powders CSS0, CSS1 and CSS5, before the final heat treatments.

approximately to a phase composition 2.33:2:0.67:2, i.e. laser processing produces Bi-enrichment and Ca-impoverishment with regard to the initial precursor stoichiometry (2.1:2:1:2). It is also remarkable that the composition of the different phases present in these samples is very similar to sample TC1 at this stage (Table 10.2).

The size of the 1:1 phase grains keeps approximately constant for the three samples and very long grains parallel to the sample's surface can be seen in Fig. 10.17. Those grains and the microstructure that surrounds them can be seen in Figure 10.18, where the upper well-textured region of the three samples is displayed at a higher magnification.

In addition to the previously mentioned phases, grains of Ca oxide (black contrast, red arrows) are more abundant in samples TCSS0 and TCSS1, as can be seen in Figure 10.19, where images of the well-textured region at a higher magnification are displayed. This is probably due to the fact that the oxides and carbonates are more abundant in the early stages of the heat treatment of the precursor powders, such as CSS0 and CSS1. Besides, traces of Cu oxide (blue arrows) are found inside the matrix regions between Bi-phase grains.

In conclusion, when comparing the microstructure and phase composition

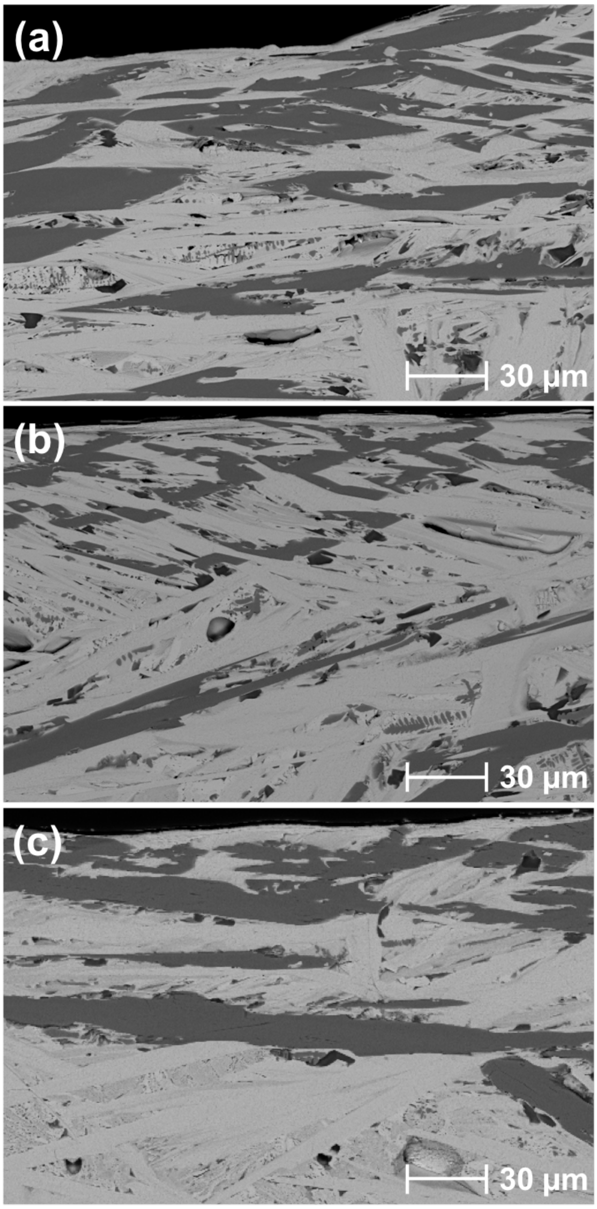

Figure 10.18: FESEM images using AsB detector of the well-textured upper region of the longitudinal cross-sections after the LZM texturing process of samples (a) TCSS0, (b) TCSS1 and (c) TCSS5.

of the as-grown LZM textured samples (prior to the final heat treatment) made with C and CSS5 precursor powders, it is observed that the chemical composition of the phases found is very similar. This is a positive result since this is achieved with precursors obtained using the novel continuous procedure

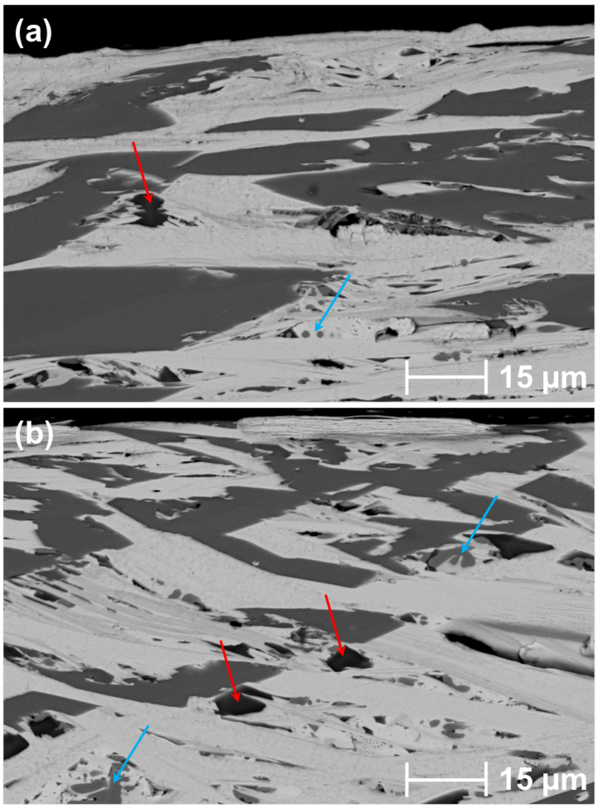

Figure 10.19: FESEM images using AsB detector of the closer to the surface of the sample region of the longitudinal cross-sections at a higher magnification of the LZM textured samples (a) TCSS0 and (b) TCSS1. Red arrows indicate Ca oxides and blue arrows indicate Cu oxides.

proposed in this work. Also, these results show that a minimum quantity of heat treatment cycles is required, because a better microstructure has been obtained in the sample TCSS5 than in the other two samples.

10.4.2 Microstructure of LZM samples after the final heat treatment

The same thermal treatment that was described in 10.3.3 has been used to form the Bi-2212 phase. Figure 10.20 shows a general image of the longitudinal cross-section of the three samples. As it can be seen, their microstructure tend to homogenize as the precursor powders are subjected to more heat treatments.

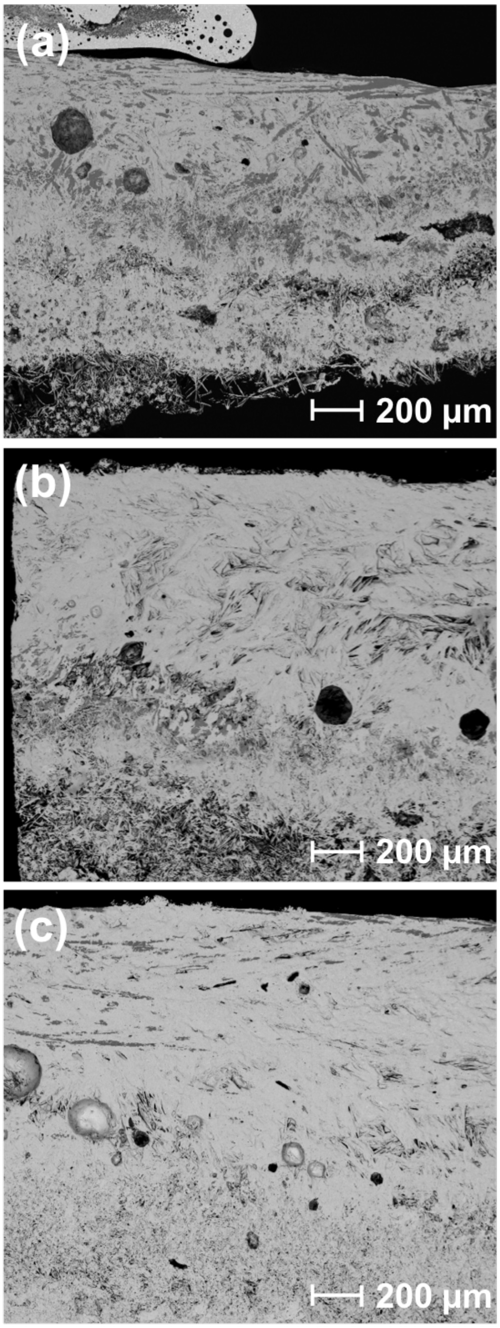

Figure 10.20: FESEM images using AsB detector of the longitudinal cross-sections after subjecting to the "traditional" heat treatment of LZM textured samples (a) TCSS0, (b) TCSS1 and (c) TCSS5 precursor powders. An Ag voltage contact can be seen on the surface of the sample TCSS0.

Thus, sample TCSS0 (Figure 10.20 (a)), presents the most heterogeneous microstructure in terms of phase composition. The elongated grains of the Bi-free phase (1:1) have not completely reacted with the Bi-2201 grains to form the superconducting Bi-2212 phase. Ca oxide grains are also distinguishable.

In agreement with the microstructural characteristics observed in the as -grown samples, after the final heat treatment the sample TCSS5 (Figure 10.20 (c)) shows much better phase homogeneity and texture (with grains aligned almost parallel to the sample surface), than samples TCSS1 (Figure 10.20 (b)) and TCSS0 (Figure 10.20 (a)), although some remaining secondary phases are still observed.

The upper well-textured region of the three samples is displayed in Figure 10.21. In these images, it is observed the presence of elongated 1:1 grains that are parallel to the sample surface. The edges of these grains are not straight due to their reaction with the surrounding Bi-2201 grains to form the Bi-2212 phase.

The phase analysis in these samples after the heat treatment (not shown) reveals very similar compositions to those observed in the as-grown samples (see Table 10.4). In particular, the composition of the Bi-2212 phase is exactly the same for the three samples (2.18:2:0.91:2), and very similar to the values obtained for the as-grown LZM samples.

In general, the obtained results indicate that the LZM process induces a similar phase composition in all samples regardless of the precursor powders used, either commercial or continuously processed. Main differences have been obtained in the distribution of the different phases, obtaining a better orientation in the border of the sample when more reacted or commercial powders are used.

In consequence, it should be expected that a better performance of the superconducting properties will be attained when the samples have been processed with these powders.

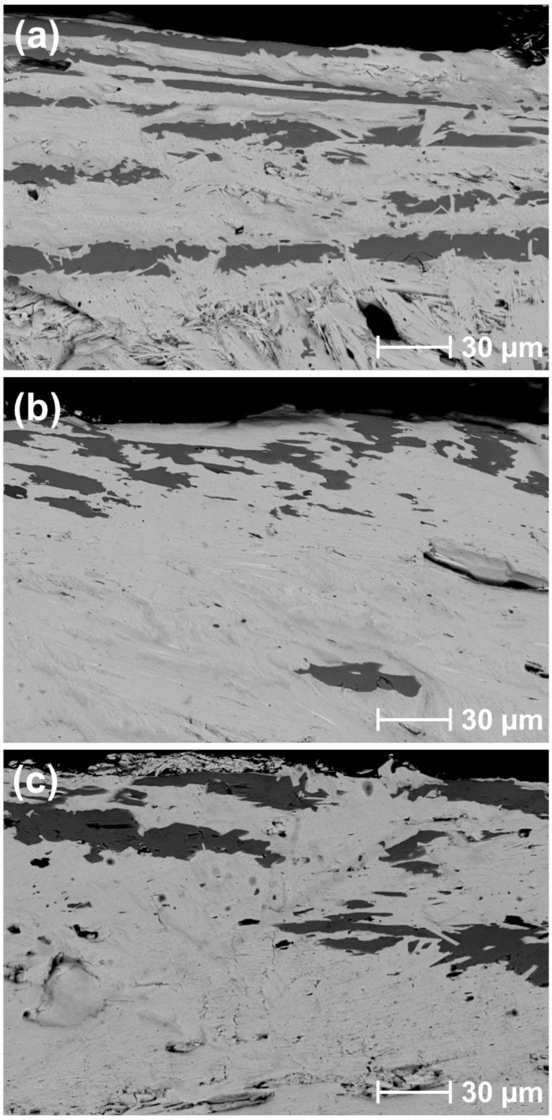

Figure 10.21: FESEM images at a higher mangification using AsB detector of the well-textured upper region of the longitudinal cross-sections after subjecting to the "traditional" heat treatment of LZM textured samples (a) TCSS0, (b) TCSS1 and (c) TCSS5.

10.4.3 Superconducting properties

In order to evaluate the superconducting performance of the rectangular bar shaped samples made with the continuous solid-state precursor powders, T_c and I_c (77 K) in self-field were measured using the same procedure and experimental conditions indicated in 10.3.4.

Figure 10.22 shows the $R(T)$ measurements (re-scaled by the w/l geometrical factor) of samples TCSS0, TCSS1 and TCSS5. T_c values of 85.0 K, 85.9 K and 85.7 K, respectively, were obtained from these measurements. Note that they are all remarkably similar, with differences within 1 K, and just slightly lower than the T_c value of sample TC2, which was 86.4 K.

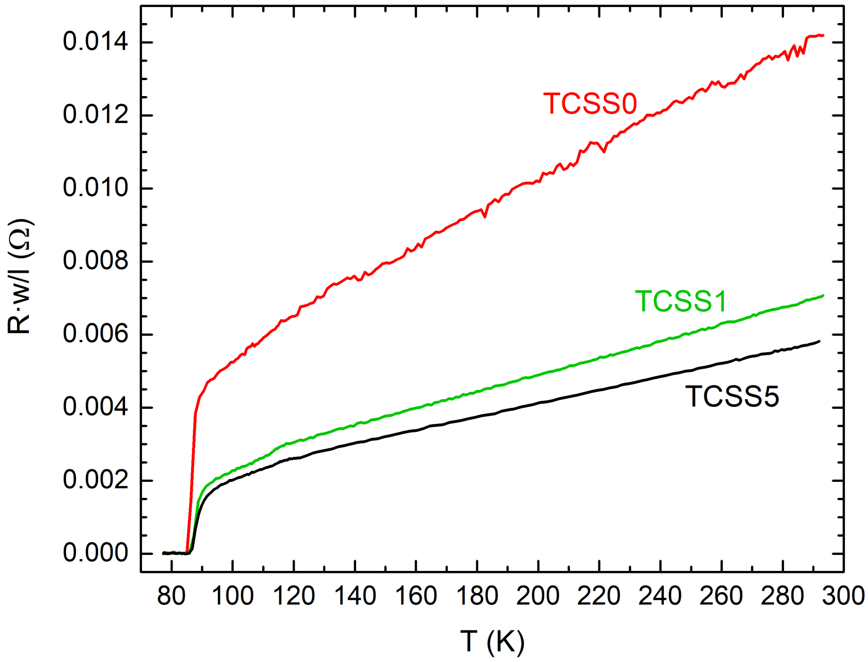

Figure 10.22: The electrical resistance, R, measured as a function of the temperature from 77 K up to RT for samples TCSS0, TCSS1 and TCSS5. R is re-scaled by a geometrical factor (w/l) for comparison purposes.

The important feature of this measurement is that the value of $R \cdot w/l$ at RT decreases as the number of heat treatments at which the precursor powders are subjected increases. The difference between samples TCSS0 and TCSS1 is high. Additional continuous treatments induce much lower differences.

The I_c/w values at 77 K in self-field were determined from the transport critical current measurements presented in Figure 10.23 of samples TCSS1 and TCSS5. The obtained values were $I_c/w = 64.3\,\mathrm{A\,cm^{-1}}$ and $n = 5.56$ for sample TCSS1, and $I_c/w = 104.6\,\mathrm{A\,cm^{-1}}$ and $n = 5.01$ for TCSS5. These I_c/w values are a 45 % and a 74 %, respectively, of the value obtained for sample TC2, and their n values are just slightly lower.

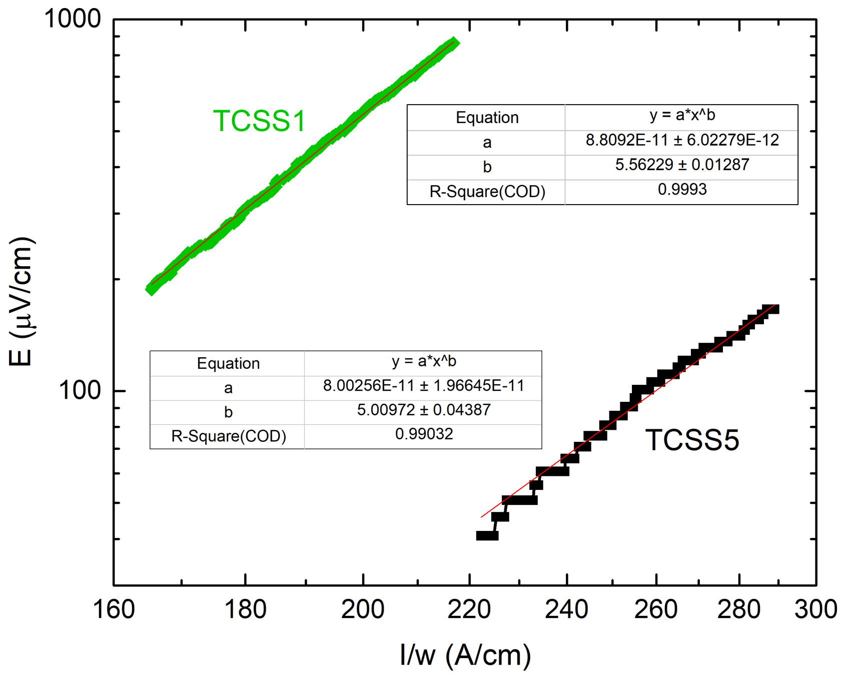

Figure 10.23: Measurement of the transport critical current at 77 K of a samples TCSS1 and TCSS5. The x-axis is re-scaled dividing it by the width of the sample, w, for comparison purposes.

In summary, the differences in the superconducting performance found between the samples made with commercial (C) and continuously processed (CSS5) precursor powders are not significant, provided that in the latter case the precursor is subjected to several heat treatments. This result constitutes not only a validation of the new proposed precursor synthesis route but also of the industrial scale-up method for processing, which uses a laser-line-scanning configuration and a two-step texturing procedure. Nevertheless, it is remarked that further optimization of the complete procedure would be still required, for example, by the optimization of the maximum temperature during the formation of the CSS5 precursor or by tuning the composition of the initial raw precursor.

10.5 Two-face LZM texturing process

During the LZM texturing process of the Bi-2212 monoliths, certain problems with the reproducibility of the results have appeared. We believe that this is related with two aspects of the sample microstructure that were observed in the characterization of these materials. The first one is that the depth of the textured region is not uniform in all the length of the sample, leaving some regions with a smaller transport cross-section which could limit the I_c performance.

The second problem is the presence of cracks on the lower part of the sample. These cracks just appear occasionally and are a consequence of the high thermal stresses induced in the sample during the laser treatment. The presence of these cracks can be reduced processing the samples over a metallic substrate that helps with the heat removal. In this case, as previously mentioned, a bulk Cu piece was used. But in some cases, samples bend during the laser processing, reducing the thermal contact with the metallic support substrate.

These two issues can be observed in Figure 10.24, which shows the longitudinal cross-section of sample TC1, a rectangular bar fabricated using commercial precursor powders after the LZM texturing process. The cracks, as the one displayed in the figure, can reach lengths up to several hundreds of microns, even reaching the laser textured region, affecting the transport I_c performance.

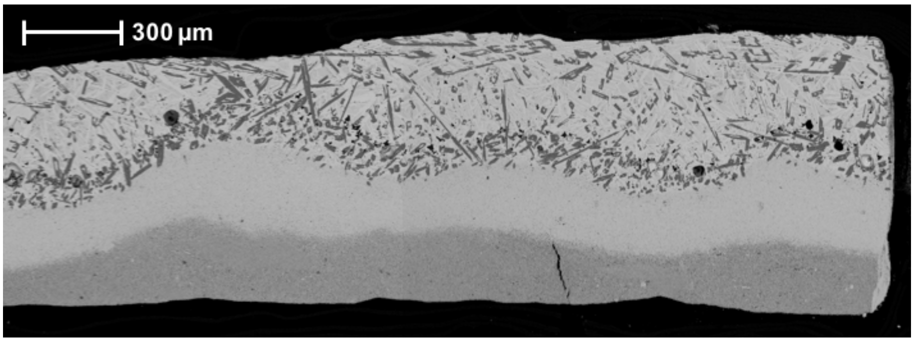

Figure 10.24: FESEM image using AsB detector of a longitudinal cross-section of sample TC1, subjected to the first and second step of the LZM texturing process at $100\,\mathrm{mm\,h^{-1}}$ and $30\,\mathrm{mm\,h^{-1}}$, respectively, and before the final heat treatment.

We have tried to reduce these problems by texturing both sides of the sample. This approach was developed by Mora *et al.* [31] with the objective of increasing the transport capability of these materials, which was reached in some experimental circumstances. In our case, we want to increase the density of the back side of the sample, with the objective of reducing the possibility of crack generation during the laser processing of the opposite side.

In order to investigate this possibility and as proof of concept, two disks were prepared with commercial silver doped precursor powders from Nexans SuperConductors GmbH. Their stoichiometry is $\mathrm{Bi_{2.02}Sr_{2.02}Ca_{0.98}Cu_{1.99}O_x}$ and a 2.9 wt.% of Ag, and present a grain size distribution characterized by $d_{10} = 0.10\,\mu\mathrm{m}$, $d_{50} = 1.18\,\mu\mathrm{m}$ and $d_{90} = 2.18\,\mu\mathrm{m}$.

These samples were LZM processed with the previously described setup (see 10.2) using a variation of the two-step method. This variation consisted in performing an initial laser process in both sides of the samples at high speed, $500\,\mathrm{mm\,h^{-1}}$. The second step is applied at $30\,\mathrm{mm\,h^{-1}}$ in only one of the faces to obtain a well-aligned textured microstructure.

Some other processing differences compared with the description in section 10.2 were used: the distance between the laser and the sample surface was reduced 100 mm, with the objective of increasing the laser beam diameter and the molten region length, and the steering speed was increased up to $18.75\,\mathrm{m\,s^{-1}}$ reducing the time the laser is out of the sample and, in consequence, reaching a more stable temperature of the melt volume. The line scan width and the furnace temperature used were the same, that is 250 mm and 450 °C respectively.

Figure 10.25: FESEM image using AsB detector of the longitudinal cross-section of a Bi-2212 disk made with C precursor powders processed with the two-face LZM texturing procedure.

The longitudinal cross-section of one of these samples is displayed in Figure 10.25, where the effects of the LZM process on both faces can be seen. Using the previously mentioned variation of the two-step method results in a complete absence of cracks on the lower part of the sample. Furthermore, the cross-section thickness homogeneity could be enhanced by this method.

10.6 Exploring the use of a continuous heat treatment in textured samples

The samples manufactured with the two-face LZM process have been used to explore the use of a continuous heat treatment. The objective of this study is to explore this possibility that can be an alternative to the heat treatments in standard furnaces when the dimensions of the samples increase above certain values.

From one of the textured disks, two samples ~ 3 cm-long were extracted. In one of the samples, 0.8 cm-wide and named TTA, the "traditional" heat treatment, described in section 10.3.3, has been performed. In the second one, 1.4 cm-wide and named TCAX, we have performed a continuous heat treatment in air using in the continuous furnace shown in Fig. 9.1. The temperature evolution followed by the sample is schemed in Figure 10.26.

The temperatures in the three regions of the continuous furnace were set

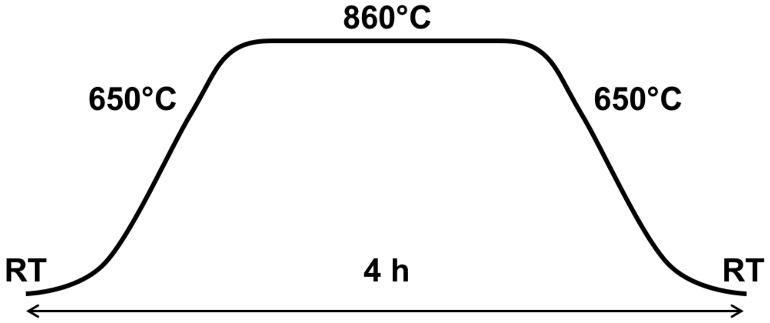

Figure 10.26: Scheme of the temperature evolution of the sample during a step of the continuous heat treatment in air in order to obtain the superconducting Bi-2212 phase. The temperatures shown are those of the three regions of the furnace.

to 650, 860 and 650 °C. With this temperature profile, the thermal treatment consists on an initial heating in ~ 1 h from RT to 860 °C, temperature at which the sample is maintained for about 2 h and finally cooled down again to RT in ~ 1 h. Considering that the total time of this continuous heat treatment is just ~ 4 h, which is not enough to allow a complete formation of the Bi-2212 phase, it is expected that several repetitions of this treatment would be needed. In particular, 10 repetitions were used and the sample is called TCA10.

Figure 10.27 shows the microstructure of both samples. Obviously the main trends are similar. The face subjected to the second step of the LZM processing at 30 mm h^{-1}, shown in the top side of Fig. 10.27, presents a good texture with a high degree of grain alignment in the two samples. The contrary occurs to the face subjected only to the first step of the LZM process at 500 mm h^{-1}, shown in the opposite lower side, which lacks of texture.

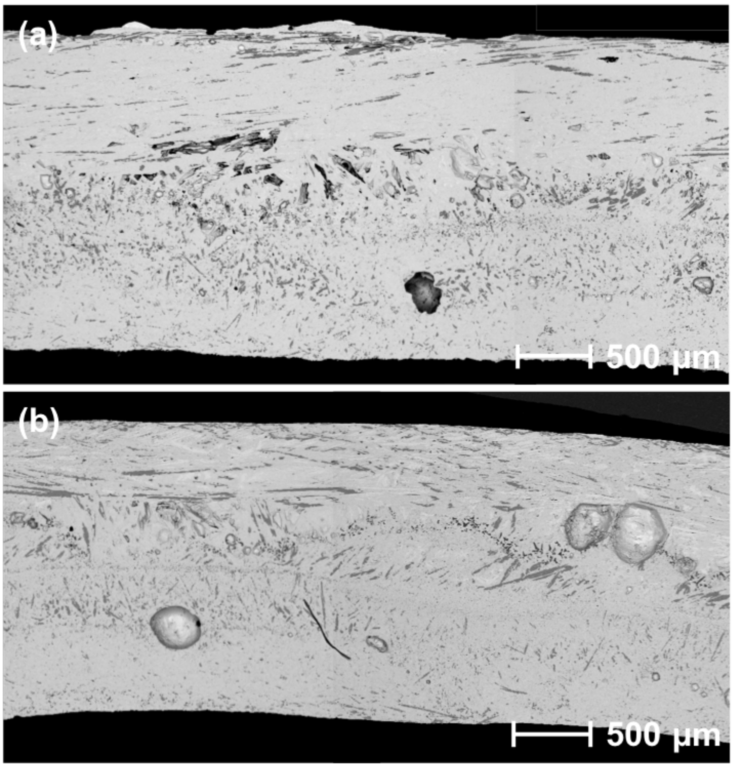

Figure 10.27: FESEM image using AsB detector of the longitudinal cross-section of the Bi-2212 two-face LZM textured samples. Sample TTA, displayed in (a), was subjected to the "traditional" heat treatment, while sample TCA10, shown in (b), was subjected to the continuous heat treatment.

The main difference between both treatments is better observed in Figure 10.28 which shows the upper well-textured region with higher magnification.

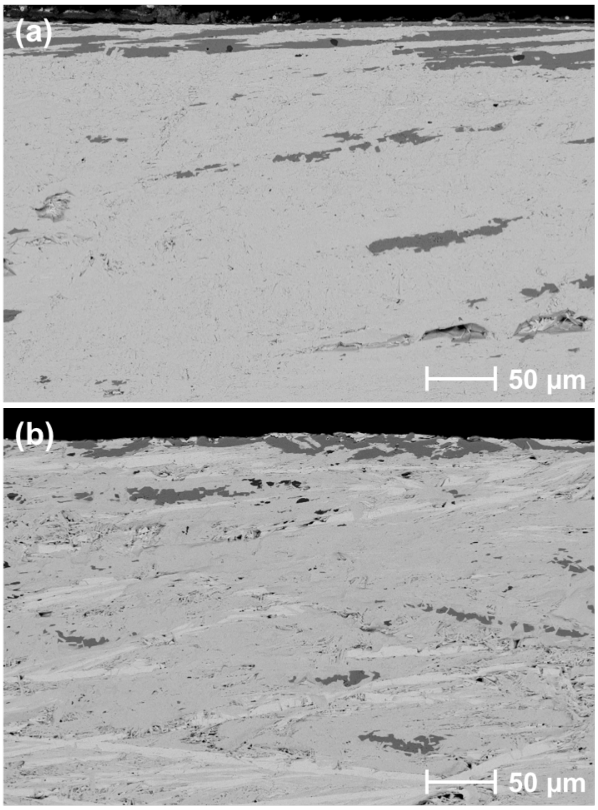

Figure 10.28: FESEM image using AsB detector of the longitudinal cross-section of the upper well-textured region of the Bi-2212 two-faces LZM textured samples. Sample TTA is displayed in (a), while TCA10 is shown in (b).

Table 10.5 collects the chemical composition of the three major phases identified in the samples after the heat treatments. The values obtained are very similar for both heat treatments, specially for the Bi-2212 phase. This is a remarkable feature because it means that the continuous heat treatment is comparable in terms of phase composition to the "traditional" heat treatment.

In sample TTA, the amount of the Bi-2201 phase is very low indicating that the transformation in the Bi-2212 phase is almost completed. By contrast, we observe that in the case of sample TCA10 this is not finished and the amount of Bi-2201 phase is still important.

Sample	*Phase*	*Composition* (at.%)				
		Bi	Sr	Ca	Cu	O
TTA	Bi-2212	15 (1)	13 (1)	6 (1)	13 (1)	53 (3)
	Bi-2201	21 (2)	15 (1)	2 (1)	9 (1)	53 (2)
	1:1	-	19 (2)	8 (1)	27 (2)	46 (3)
TCA10	Bi-2212	15 (1)	13 (1)	6 (1)	13 (1)	53 (3)
	Bi-2201	20 (1)	14 (2)	2 (1)	10 (1)	53 (3)
	1:1	-	17 (1)	9 (1)	25 (2)	49 (2)

Table 10.5: Chemical composition values and standard deviations of the three major phases deduced from FESEM images and EDX analysis of the samples made with C precursor powders after subjecting them to the "traditional" heat treatment, TTA, and to the continuous heat treatment repeated 10 times, TCA10.

10.6.1 Superconducting properties

Figure 10.29 shows the $R(T)$ curves measured in sample TTA and in two samples with the continuous heat treatment after 6 and 10 iterations, i.e. TCA6 and TCA10, respectively. The first remarkable difference is that the resistance in the normal state is approximately 2.5 times lower when the "traditional" heat treatment is performed.

The second point is the differences in T_c. In the case of sample TTA, the obtained value is 87.9 K, very similar to the values measured for the samples in the previous sections, just slightly higher. The T_c value obtained for the sample with the continuous heat treatment is 4 K lower (83.4 K). This can be explained taking into account that in the "traditional" heat treatment, two steps were required, one at high temperature to form the Bi-2212 phase and a second one, at 800 °C, to adjust the oxygen content.

This second step is not present in our case, because the speed of the sample is the same in each part of the furnace and the length is very short. But it could be done in longer furnaces with the possibility of controlling the temperature and the speed in different sections of the furnace. Another possibility would be to combine iterations of the continuous heat treatments at different temperatures, at 860-870 °C for the formation of the Bi-2212 phase and at 800 °C to adjust the oxygen.

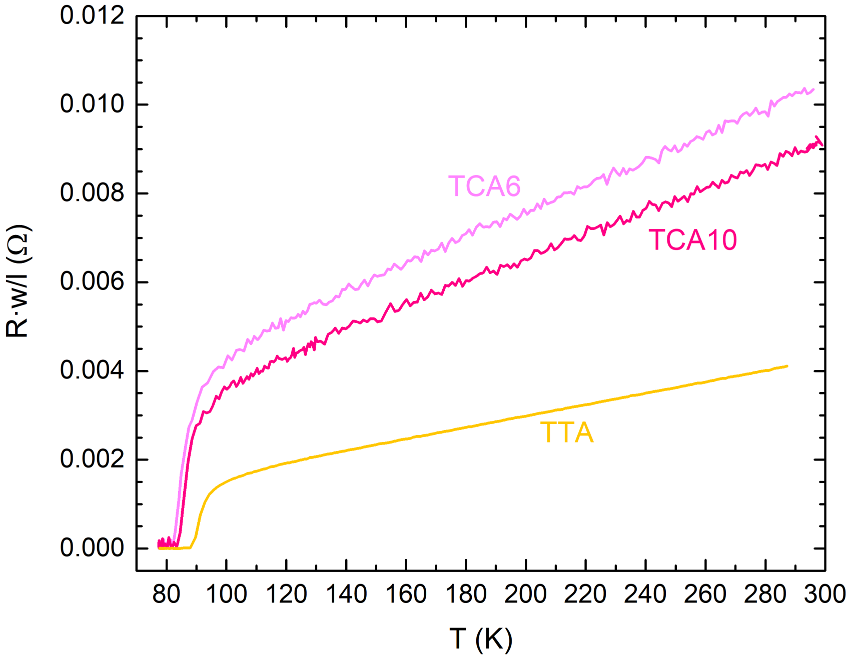

Figure 10.29: The electrical resistance, R, measured as a function of the temperature from 77 K up to RT for samples TTA, TCA6 and TCA10. R is re-scaled by a geometrical factor (w/l) for comparison purposes.

The transport critical current measurements at 77 K of both samples are displayed in Figure 10.30 with their respective fittings.

The obtained I_c/w value of sample TTA is 32.8 A cm^{-1} with $n = 4.80$, while sample sample TCA10 presented a slightly lower value of 31.2 A cm^{-1} with $n = 5.13$. This is probably due to the above mentioned lack of optimization of the continuous heat treatment. However, both I_c/w and n values are very similar, despite the difference with the values obtained for the other samples, TC2 and TCSSX. This is due to the different precursor powders used, which for samples TTA and TCA10 were the Ag-doped commercial precursors. An optimization of the "traditional" heat treatment for samples fabricated with these powders would be required to obtain the same I_c/w values.

Nevertheless, this proof of concept with Ag-doped commercial precursor powders opens a new scenario in which samples could be processed in a continuous process, from the raw mixture of carbonates and oxides, to the final heat treatment required to obtain the superconducting Bi-2212 phase. Thus,

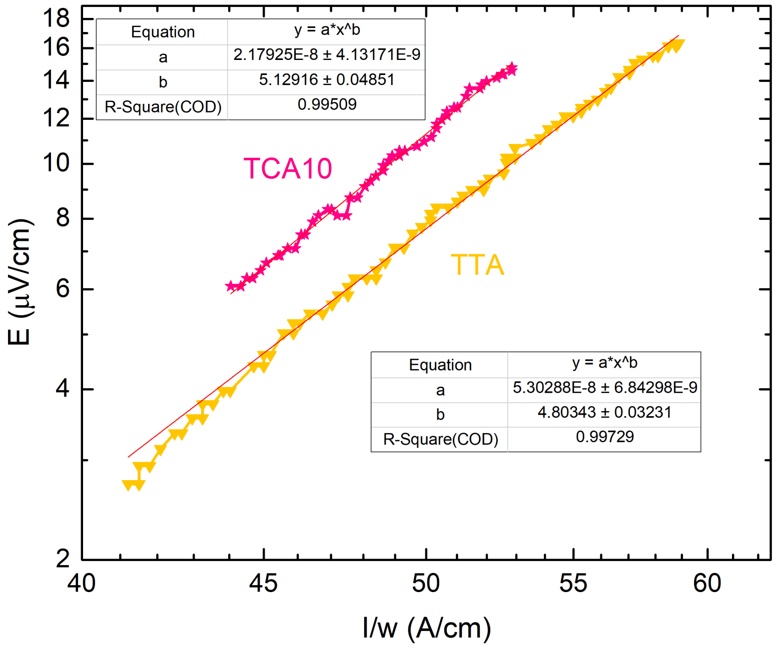

Figure 10.30: Transport critical current measurement of the samples TTA (gold inverted triangles) and TCA10 (pink stars). The x-axis is re-scaled by I_c/w of sample TTA for comparing purposes.

samples of almost any given size could be processed. The temperature profile of this furnace, as well as the sample speed inside the furnace, must be tuned in order to optimize this continuous heat treatment.

Chapter 11

Progress in electrically assisted laser processing of Bi-2212 monoliths

In this chapter we have analysed the effect of applying an electrical current to the Bi-2212 monoliths during the LZM process. This procedure will be called electrically assisted laser zone melting (EALZM), in a similar way to the EALFZ [21–25]. In particular, we analyse the influence of the polarity of the applied current during the texturing process and the modifications induced by the laser power in the microstructural and superconducting properties.

11.1 Reported benefits of the EALFZ technique

The EALFZ modification has been proven to be a very interesting tecnique to improve the LFZ sample processing, as previously introduced in Chapter 8. In particular, Costa *et al.* [25] observed that the polarity of the applied current is an important factor and summarized the changes induced by the electrical current in the microstructure in the EALFZ process in comparison with the LFZ technique: (i) the grain alignment is improved by current application; (ii) the primary Bi-free 1:1 phase characteristic of the LFZ technique is substituted by the equilibrium cuprate $(Sr,Ca)_{14}Cu_{24}O_{41}$ (known as 14:24 phase); (iii) the Bi-rich remaining liquid (last solidified fraction) is decreased with the applied current; and (iv) a higher amount of Bi-2212 phase compared to Bi-2201 phase is found when the electrical current is applied.

This is due to the modifications introduced by the applied electrical current in the electromigration phenomenon during the texturing process, which also changes the thermal gradients and modifies the freezing rate conditions, leading to solidification conditions closer to the equilibrium. The electromigration phenomenon is altered by promoting a cationic drift perpendicular to the solidification front, more significantly in the case of Cu ions. A scheme of this phenomenon can be seen in Figure 11.1.

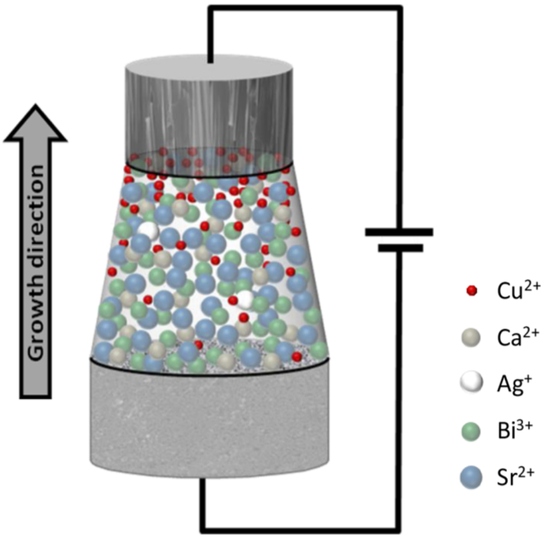

Figure 11.1: Scheme of the molten zone during the EALFZ growth of bulk Bi-2212/Ag rods as shown by Costa *et al.* [25]. This scheme evidences the Cu ionic drift toward the solidifaction interface.

The Cu ions increase their ionic mobility toward the solidification interface, thus favouring the developement of richer Cu phases. This explains the appearance of the Cu-rich equilibrium cuprate 14:24 phase instead of the metastable 1:1 phase. Also, the increase of Bi-2212 phase on behalf of Bi-2201 phase can be explained by this phenomenom. Besides, the ionic drift has also been proven to intensify the grain alignment and refinement, which favours the superconducting transport properties [20].

Furthermore, Carrasco *et al.* [23] showed that the benefits of the applied electrical current can be erased by reversing the current flow polarity. This induces a disordered microstructure where no preferential grain alignment is observed. Besides, multiple stoichiometric deviations occur. Consequently, the superconducting performance deteriorates.

11.2 Description of the electrically assited laser texturing process

Bi-2212 rectangular bar shaped monoliths of approximate dimensions 2 × 8 × 80 mm were prepared as in section 10.1 using commercial silver doped precursor powders from Nexans SuperConductors GmbH. Their stoichiometry is $\mathrm{Bi_{2.02}Sr_{2.02}Ca_{0.98}Cu_{1.99}O_x}$ and a 2.9 wt.% of Ag, and present a grain size distribution characterized by $\mathrm{d_{10}} = 0.10\,\mu\mathrm{m}$, $\mathrm{d_{50}} = 1.18\,\mu\mathrm{m}$ and $\mathrm{d_{90}} = 2.18\,\mu\mathrm{m}$.

These monoliths were textured using the experimental setup detailed below.

11.2.1 Diode laser

The laser is a diode model, Monocrom LBS-80300W, emitting in a continuous wave at $\lambda = 810\,\mathrm{nm}$. It emits 10 divergent lines that can be transformed in a line of 50 mm length and 0.5 mm width using a set of cylindrical focusing lenses. A scheme of the apparatus is shown in Figure 11.2.

The high power laser line induces a molten zone in the sample when inciding in its surface. This molten zone is moved along the sample using a movement control stage. In order to reduce the thermal shock, the sample is placed inside a small portable open air furnace at 500 °C.

This apparatus, with different configurations, has been previously used to process Bi-2212 monoliths [27, 31], thick films [48] and cylinders [51]. In these works, it was found that the minimum energy needed to texture these materials is 1 W/(mm-width).

One of the limitations of this laser configuration is that the energy distribution along the laser beam is not uniform. Figure 11.3 shows the typical energy profile of this line and shows that the working region is limited to sam-

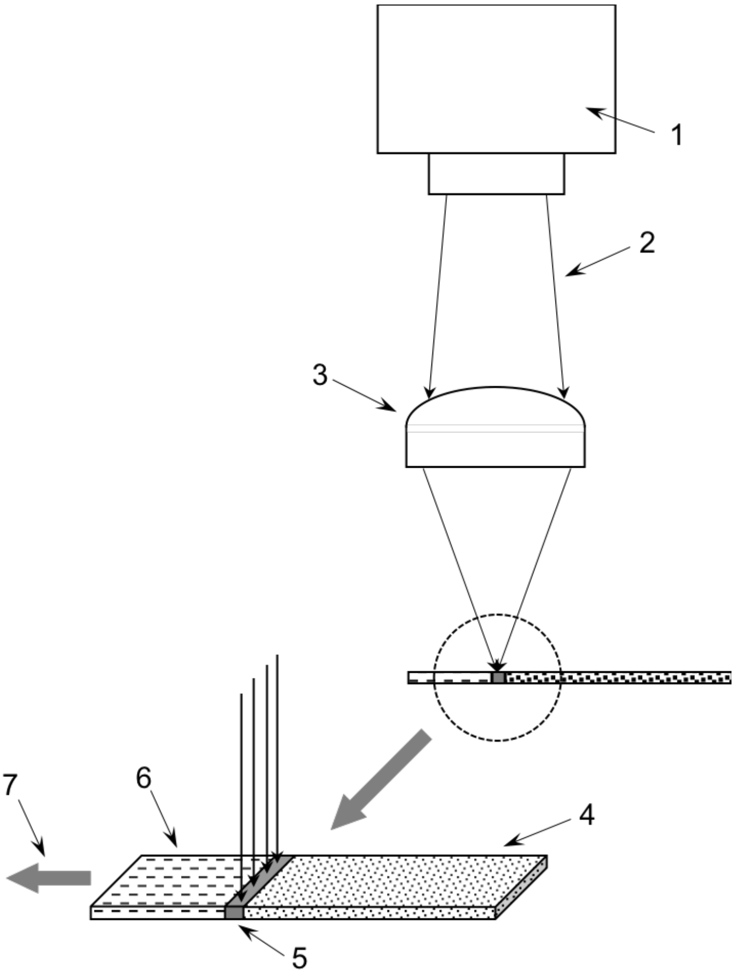

Figure 11.2: Scheme of the diode laser used for the EALZM processing of the samples as published in [48]. 1. Diode laser module. 2. Laser beam. 3. Cylindrical lens. 4. Non-processed zone of the sample. 5. Molten volume formed in the sample. 6. Textured zone of the sample. 7. Sample movement direction.

ples with widths lower than 15 mm, where the energy density differences are lower than a 10 %.

11.2.2 Sample holder

This is the first time that this apparatus is used for EALZM processing, and therefore a sample holder was developed to introduce the current during the texturing process. Figure 11.4 shows a scheme of the sample holder and

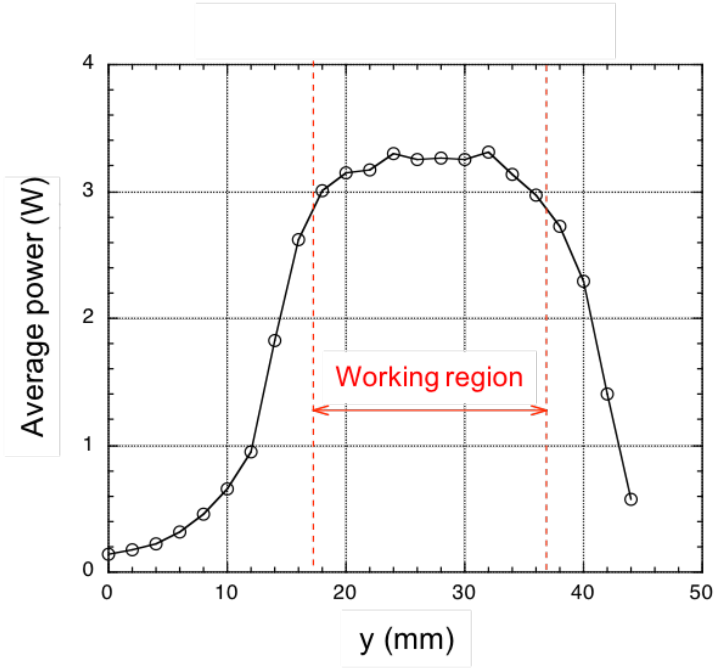

Figure 11.3: Power distribution profile along the laser beam length for a source current of 19 A.

the experimental configurations used during the experiments.

The sample is placed over a ceramic substrate and it is held on each extreme by a pair of copper pieces where two silver tapes were soldered. Typical current values of 1 A were used during the texturing process. This sample holder is

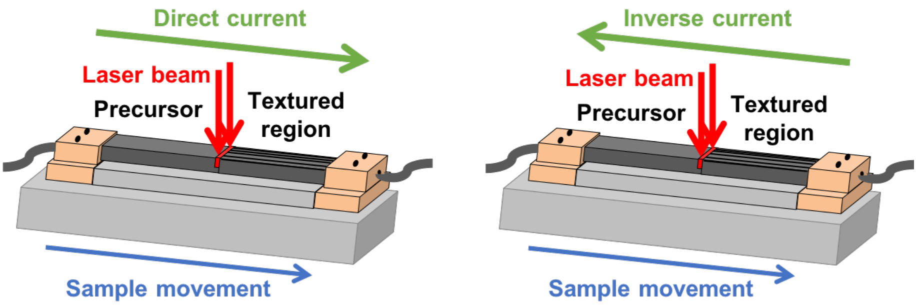

Figure 11.4: Scheme of the sample holder used for applying the electrical current during the EALZM processing of the samples. Two configurations were possible: direct and inverse current.

placed inside the open air furnace at 500 °C which is displaced at the processing velocity of 20 mm h^{-1}.

Three different configurations can be studied. The first one is the traditional configuration without applying an electrical current. When applying a current, two additional configurations are possible: the direct and the inverse one. In the direct configuration, the applied current polarity and the sample movement sense are the same, and the applied current flows from the non-textured to the textured regions through the molten region. In the inverse configuration, the current flows from the textured region to the non-textured one.

11.3 Influence of the electric current polarity

In order to study the influence of the applied current polarity, three Bi-2212 rectangular bar shaped samples (one for each configuration) were EALZM processed with the experimental setup described above using a source current for the diode laser of 19.5 A. This source current produced a laser power of 1.7 W mm^{-1}. An applied current of 1 A was used during the texturing process. The samples are named DC19.5 (direct), ZC19.5 (zero current) and IC19.5 (inverse).

11.3.1 Microstructure of the samples

Figure 11.5 shows the microstructure of the longitudinal cross-section close to the interface between the frozen molten pool and the textured region of the three samples, after the laser processing. Analysing the texture of the Bi-free grains, it can be observed that the thickness of the region with a good texture in sample CD19.5 is higher than for sample ZC19.5. When the inverse configuration is used, as in sample IC19.5, the degree of alignment of the well textured region is lower than in the other two samples. Another difference is the length of these well-oriented grains in these regions that reaches up to 1300 µm for sample DC19.5 and 650 µm for sample ZC19.5. These results are in good agreement with similar results reported in the literature [20, 25].

The difference in the thickness of the textured region is related with the

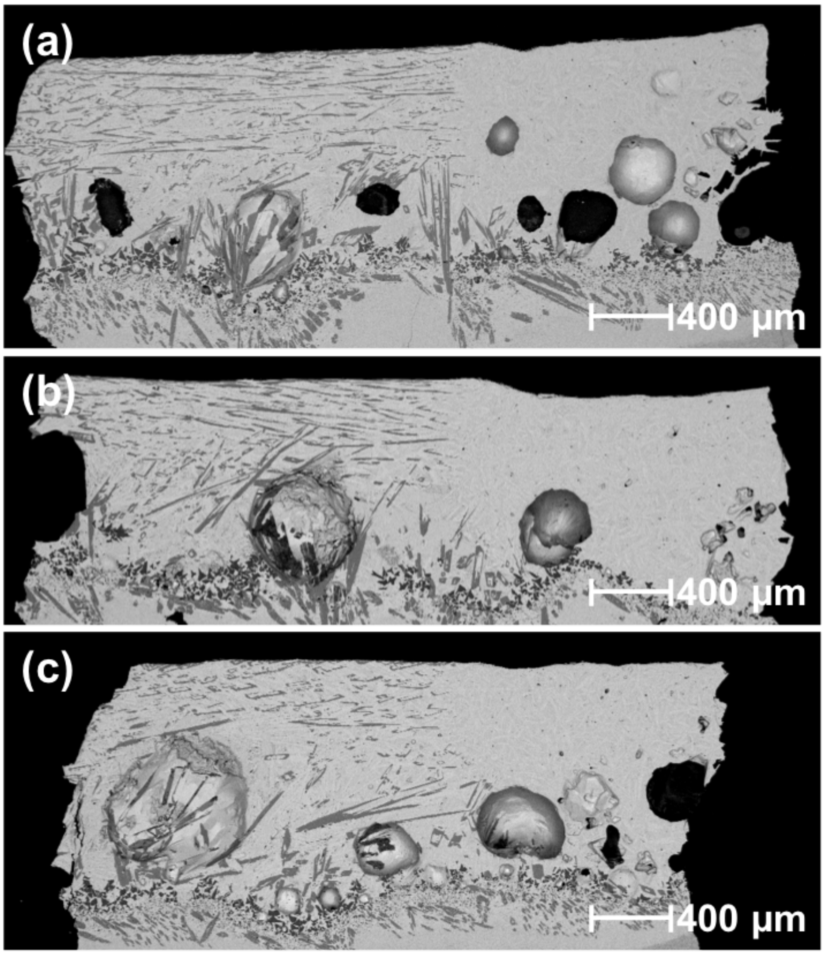

Figure 11.5: FESEM images using AsB detector of the longitudinal cross-section at the interface between the molten frozen pool and the textured region of the as-grown Bi-2212 EALZM processed samples with a diode laser source current of 19.5 A: (a) DC19.5, (b) ZC19.5 and (c) IC19.5.

shape of the solidification front. Close to the surface it is perpendicular to the sample surface and the region with this shape is bigger in sample DC19.5. In the case of sample IC19.5, this perpendicular section is very small. Also it is important to mention the presence of large bubbles in the lower part of the laser molten region. Due to the change in the direction of the thermal gradient in this lower part, the grains change their growth direction, reaching in some cases the perpendicular direction to the movement. The accumulation of Bi-free and Ca oxide (black grains) particles in the lower border of the molten region is also relevant.

Figure 11.6 shows a detail of the upper part of the textured regions in these three samples. As usual, all the samples exhibit the three main phases usually observed after laser treatment. The dark grey grains in the FESEM micrographs correspond to the 1:1 phase. We have not observed any difference in the composition of this phase due to the electric current application during processing as was observed for EALFZ Bi-2212 rods, where the presence of the phase 14:24 instead of the 1:1 was reported [25]. Around these Bi-free grains we observe some grains (in light grey) with a composition close to the Bi-2201 but with a ratio Bi/Sr = 1.4 and Bi/Cu = 2.25. The amorphous matrix between these grains has a composition close to the Bi-2212 with a ratio Bi/Sr = 1.25 and Bi/Cu = 1.2. There are not significant changes in the composition and the main differences between the samples can be found in the grains orientation of each phase. In the case of sample DC19.5, Fig. 11.6 (a), the Bi-2201 grains follow in most cases the orientation of the Bi-free grains. This orientation is lower in the sample ZC19.5, Fig. 11.6 (b), and it is mainly lost in sample IC19.5, Fig. 11.6 (c).

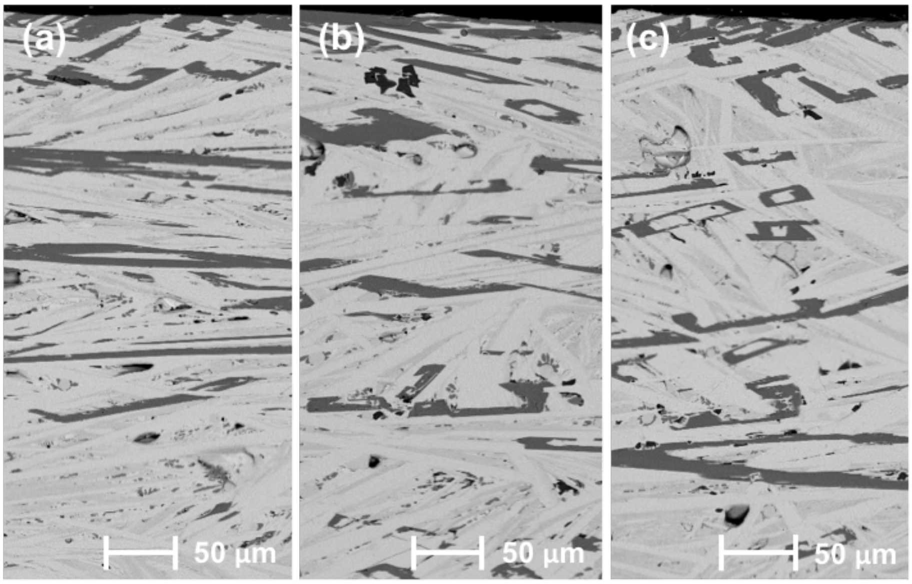

Figure 11.6: FESEM images using AsB detector of the longitudinal cross-section of the upper well-textured region of the as-grown Bi-2212 EALZM textured samples (a) DC19.5, (b) ZC19.5 and (c) IC19.5.

Figure 11.7 shows with more detail the microstructure of sample DC19.5, in order to point out the main relevant microstructural characteristics of these samples. Ag is segregated from the other phases. In most cases, Ag spheres can be observed between the Bi grains. In the photograph, some of these spheres are enclosed in circles. Also, between these Bi-grains we observe a second phase (round darker phases in Figure 11.7) that corresponds to Cu oxide and that forms an eutectic structure with the Bi-2212 matrix in some regions.

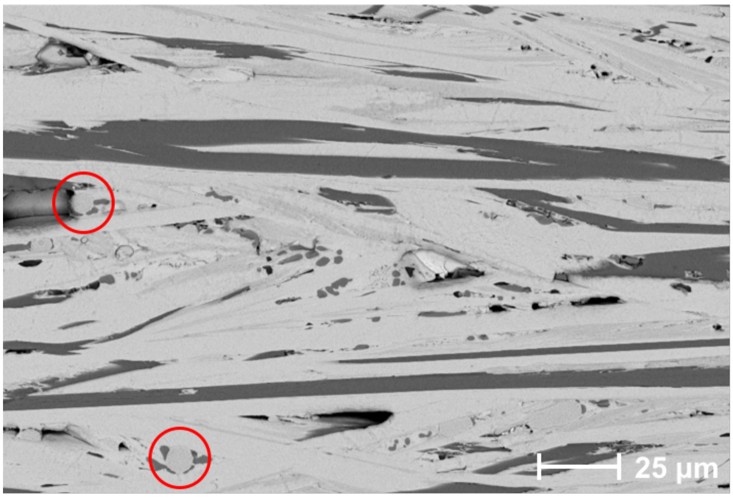

Figure 11.7: FESEM image using AsB detector of the same area shown in Figure 11.6 (a) taken at a higher mangnification, corresponding to a longitudinal cross-section of the well-textured region of the as-grown Bi-2212 EALZM processed sample DC19.5. Ag spheres are marked in circles.

The three EALZM textured samples were subjected to the “traditional” heat treatment described in 10.3.3. Figure 11.8 shows a detail of the microstructure of the transverse cross-section of sample DC19.5. This section does not show the alignment of the grains observed in the longitudinal direction but it has been used to identify the different phases that are present in the sample.

The main effect of the heat treatment is that the Bi-free phase transforms to the equilibrium 14:24 phase, probably due to the addition of Ag in the precursors. Besides, the main phase is Bi-2212, which shows Ca deficiency: Ca/Bi = 0.3, indicating that this phase corresponds to Bi-2212/Bi-2201 in-

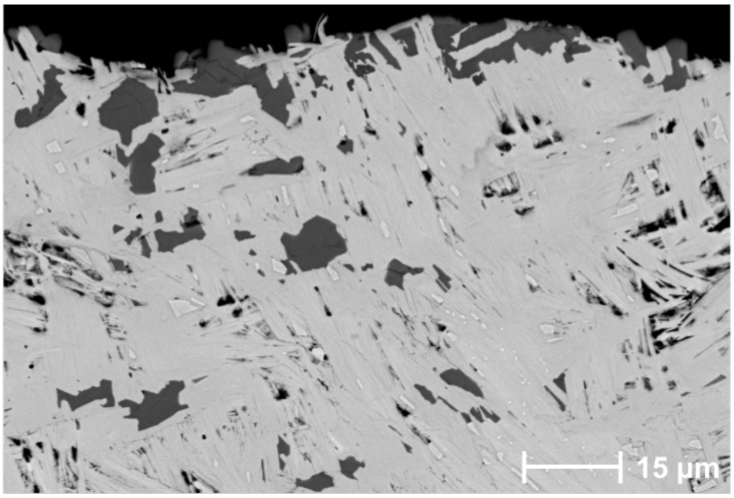

Figure 11.8: FESEM image using AsB detector of the upper well-textured region of the transversal cross-section of sample DC19.5 after subjecting it to the “traditional” heat treatment.

tergrowths. The small grains, with a lighter grey contrast in the micrograph, correspond to Ag grains that fulfil the pores between the superconducting grains, and obviously do not have the spherical shape that was observed just after the heat treatment.

In consequence, we have observed that the application of an electrical current during the texturing process of these monoliths can modify the orientation of the grains and the distribution of the different phases, but the chemical compositions are the same in all three cases, indicating that the effect is lower than in other geometries as in the EALFZ.

Figure 11.9 shows the total transverse cross-sections of the three samples. In accordance with the images presented in Figure 11.5, three regions can be observed: the textured region in the upper part of the sample; a second region that comprises the lower part of the molten material, which has large number of bubbles and is non-textured, and a thermally affected region; and finally, at the bottom, a third region that has not been affected by the laser.

From the analysis of the images, the percentage of each region is recorded in Table 11.1 and the transport cross-section (i.e. the textured area) can be estimated to be 3.6 mm^2 for sample DC19.5, 3.2 mm^2 for sample ZC19.5 and 2.5 mm^2 for sample IC19.5.

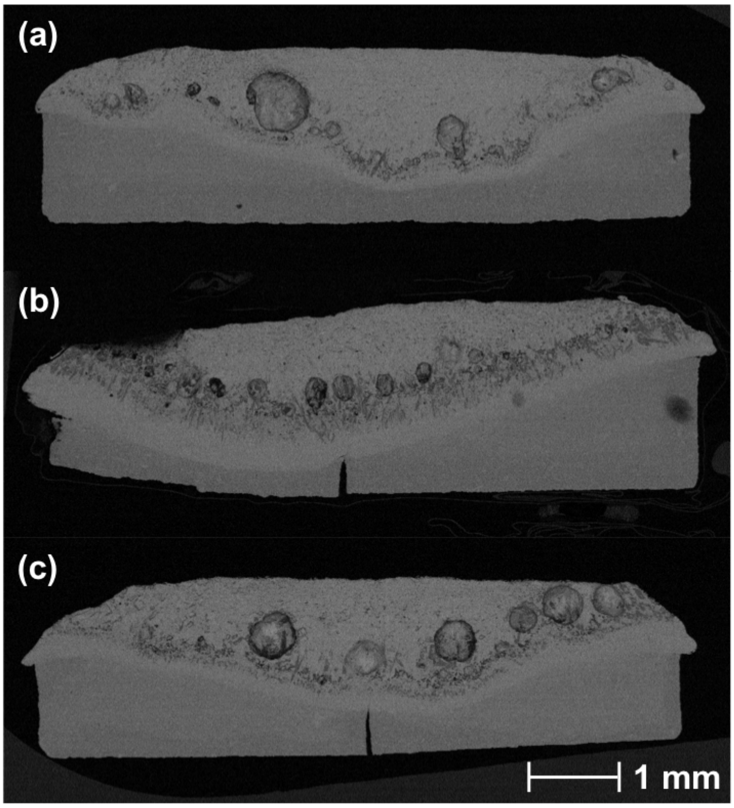

Figure 11.9: FESEM images using AsB detector of the transversal cross-sections of the EALZM processed samples (a) DC19.5, (b) ZC19.5 and (c) IC19.5.

Region	*Sample*		
	DC19.5	ZC19.5	IC19.5
Textured	26 %	22 %	18 %
Lower part of the molten	31 %	43 %	40 %
Non-affected by the laser	43 %	35 %	42 %

Table 11.1: Area percentage of each region of Bi-2212 EALZM textured samples with a diode laser source current of 19.5 A.

11.3.2 Superconducting properties

The superconducting properties of the three EALZM textured samples were investigated measuring their $R(T)$ (re-scaled by the geometrical factor w/l) from 77 K to RT. The measurement is shown in Figure 11.10. The distance between the voltage contacts was 7.2 mm for sample DC19.5, 13.5 mm for sample ZC19.5 and 9.7 mm for sample IC19.5.

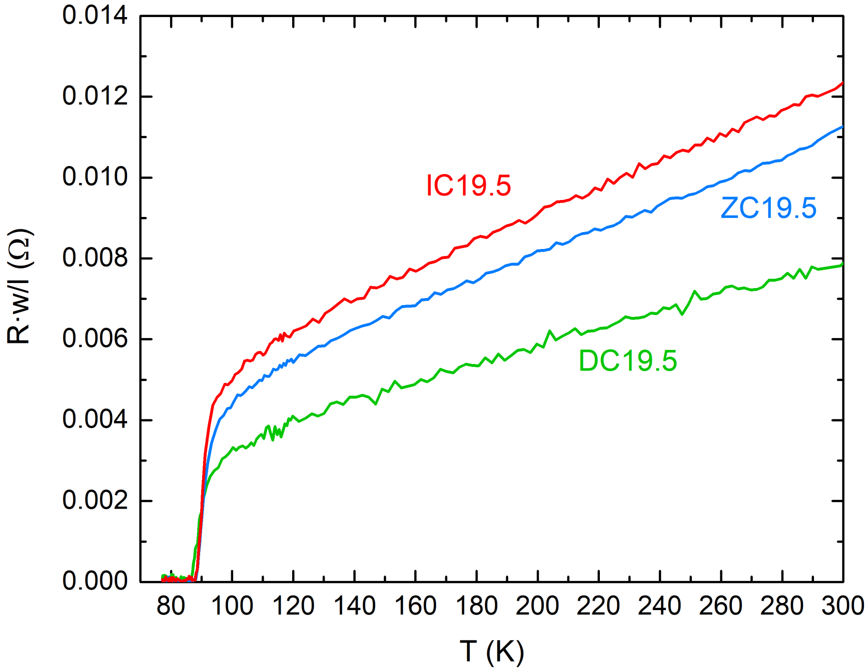

Figure 11.10: Measurement of $R(T)$ from 77 K up to RT for the EALZM textured samples DC19.5 (green), ZC19.5 (blue) and IC19.5 (red). R is re-scaled by a geometrical factor (w/l) for comparison purposes.

These measurements allow to determine their T_c, which were 86.6 K for sample DC19.5, 88.1 K for sample ZC19.5, and 87.9 K for sample IC19.5. These values are very similar among them and are also similar to other T_c values previously measured in this work.

It is remarkable that $R \cdot w/l$ at RT is lower for sample DC19.5 than for the other two samples. In particular, the data of the samples ZC19.5 and IC19.5 run rather parallel, being the latter the one with the highest $R \cdot w/l(300\,\mathrm{K})$. This is in good agreement with the degree of grain alignment seen in their microstructures displayed in Figure 11.6.

In addition to the $R(T)$ measurements, I_c measurements at 77 K were also carried out, and the results are displayed in Figure 11.11. From these measurements, the I_c/w and n values of each sample can be determined to be 41.2 A cm^{-1} and 4.92 for sample DC19.5; 28.2 A cm^{-1} and 4.56 for sample

ZC19.5; and 22.4 A cm^{-1} and 4.44 for sample IC19.5.

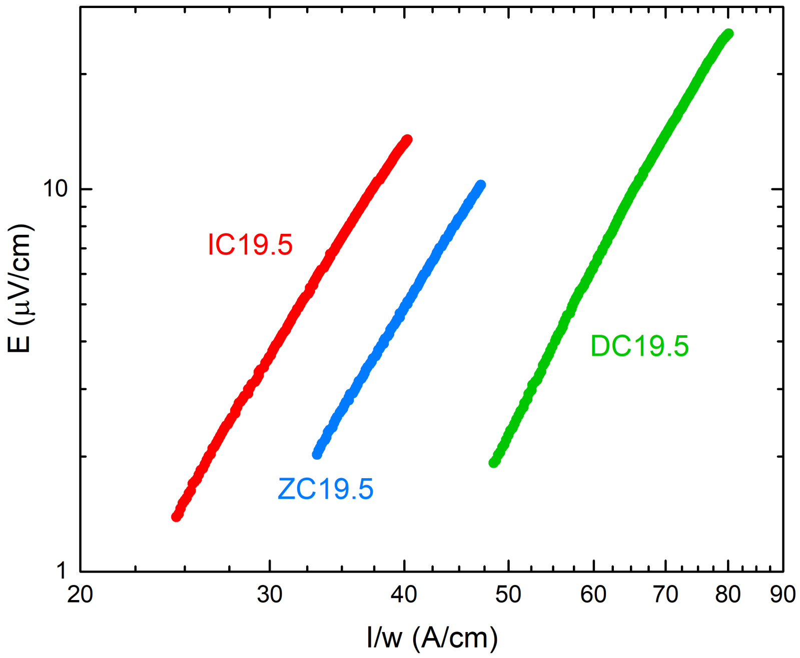

Figure 11.11: Transport critical current measurements of the EALZM processed samples DC19.5 (green circles), ZC19.5 (blue circles) and IC19.5 (red circles) are shown. Only the less noisy part of the curve is shown to obtain a better fitting.

These I_c/w values are in good agreement with both the $R(T)$ measurements and the microstructure of the samples, where the sample DC19.5 presents the best superconducting performance due to the influence of the electric current introduced during the texturing process to enhance the grain alignment.

Furthermore, a very similar I_c/w and n values were obtained for both samples ZC19.5 and TTA/TCA10 (see section 10.6), textured with rather similar conditions but with different lasers. This similitude is due to the fact that those samples were prepared using the same Ag-doped commercial precursor powders.

11.4 Modifications when increasing the textured area

After having established the benefits of EALZM processing samples with the direct configuration, where the applied electrical current flows from melt to the textured region, the next logical step is to analyse if this effect is maintained or even enhanced, when increasing the textured cross-section.

In order to study that, two more samples were EALZM textured with the direct configuration using again an applied current of 1 A and a source current for the diode laser of 19 A, named DC19, and 20 A, named DC20 (the sample processed at 19.5 A is characterized in the previous section). These two source currents correspond to a laser power of $1.6\,\mathrm{W\,mm^{-1}}$ and $1.8\,\mathrm{W\,mm^{-1}}$ respectively.

A test was performed for a diode laser source current of 21 A with the direct configuration but the melt reached completely the cross-section of the bar. Although this would be in principle the ideal case, the surface tension of the melt was not enough to maintain the shape of the sample, that ended up breaking the sample and interrupting the current flow through it. To use these levels of power, other geometries are required, as for instance, superconducting coatings, where the substrate will maintain the mechanical integrity of the total sample.

11.4.1 Microstructure of the samples

The FESEM images of the upper well-textured region of the longitudinal cross-sections of the samples DC19 and DC20 after subjecting them to the "traditional" heat treatment are displayed in Figure 11.12.

The phase homogeneity is similar in all the samples, i.e. DC19, DC19.5 and DC20, as expected due to the use of the direct configuration to texture them. In the three of them, the predominant phase is the Bi-2212, and some traces of unreacted grains of the 14:24 phase still remain, which is usual. However, the size of the well-aligned grains in the sample DC20 is greater compared to the other samples. This could be due to the fact that more cross-section of the sample is textured.

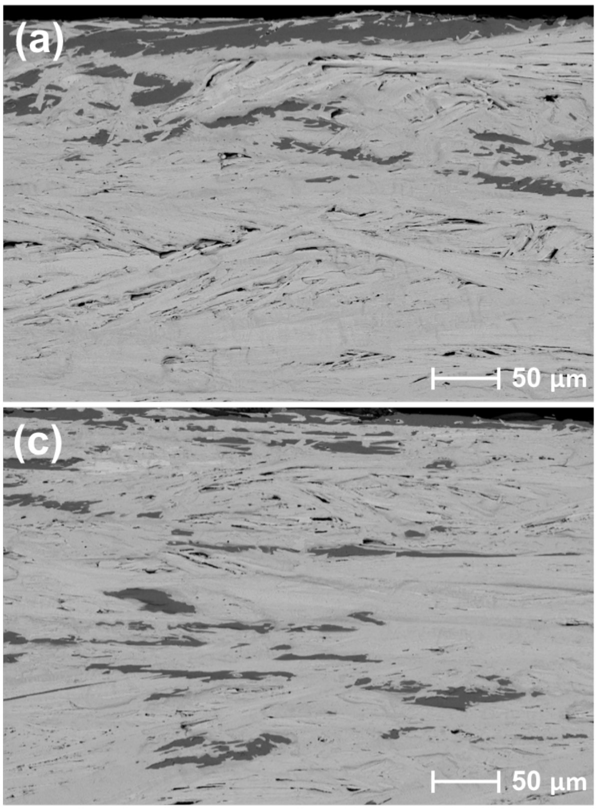

Figure 11.12: FESEM images using AsB detector of the longitudinal cross-section of the upper well-textured region of the annealed Bi-2212 EALZM textured samples (a) DC19 and (b) DC20.

Region	*Sample*		
	DC19	DC19.5	DC20
Textured	15 %	26 %	35 %
Lower part of the molten	20 %	31 %	37 %
Non-affected by the laser	65 %	43 %	28 %

Table 11.2: Area percentage of each region of Bi-2212 EALZM textured samples DC19, DC19.5 and DC20.

Figure 11.13 shows the total cross-sections of samples DC19 and DC20. The same three regions that were found in the samples processed at a diode source current of 19.5 A can be observed. From the analysis of the images, the percentage of each region is collected in Table 11.2 and the transport cross-sections are estimated to be 2.5 mm^2 for the sample DC19 and 4.8 mm^2 for the sample DC20.

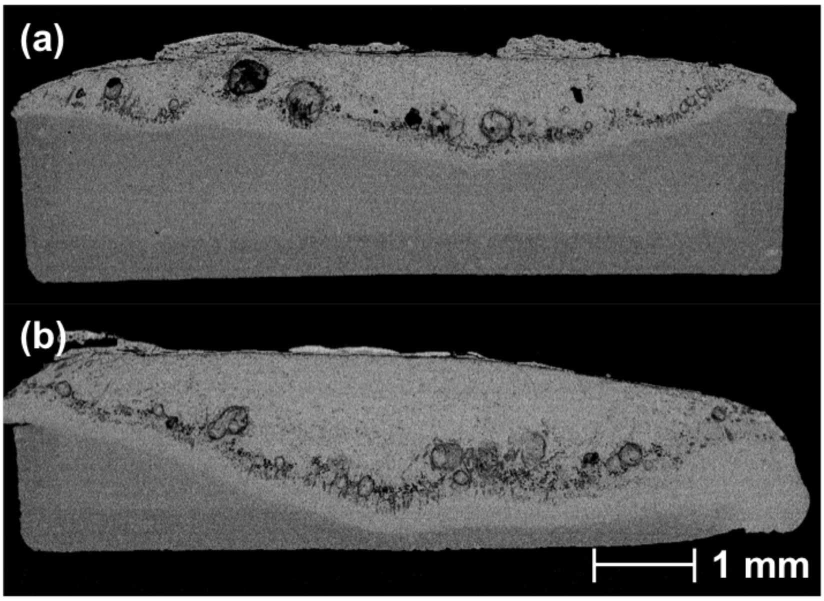

Figure 11.13: FESEM images using AsB detector of the transversal cross-sections of samples (a) DC19 and (b) DC20.

11.4.2 Superconducting properties

Figure 11.14 shows the $R(T)$ measurement (re-scaled by the geometrical factor w/l) from 77 K to 300 K for these samples. In this Figure, the measurement of a non-textured sample, named NT, subjected to the "traditional" heat treatment is also displayed for a comparison purpose. The distance between the voltage contacts was 13.3 mm for sample DC19A, 14.2 mm for sample DC20 and 14.3 mm for sample NT.

The T_c values derived from the $R(T)$ measurement were 87.8 K and 88.2 K for samples DC19 and DC20, which are very similar to the value obtained for the sample DC19.5 (88.1 K).

The value of $R \cdot w/l(300\,\mathrm{K})$ is rather similar for the three textured samples, which is in good agreement with the phase homogeneity observed in their microstructures.

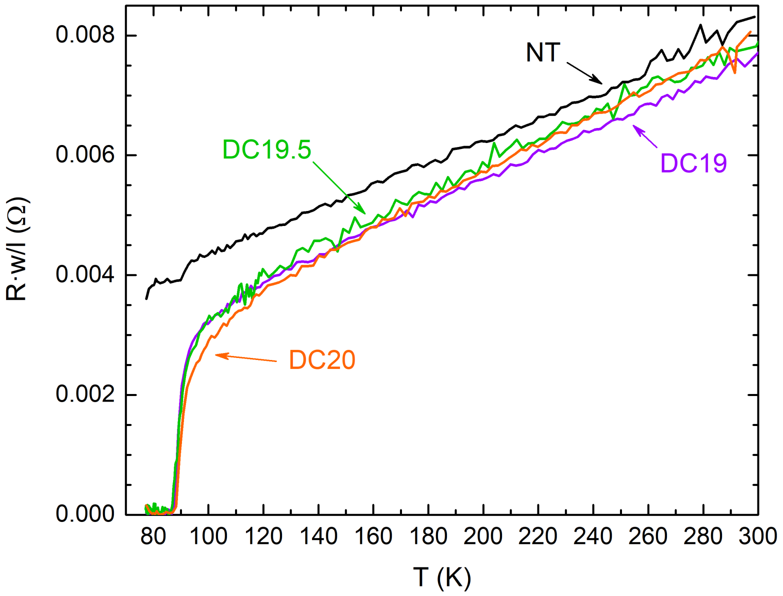

Figure 11.14: Measurement of $R(T)$ of the EALZM textured samples DC19, DC19.5 and DC20. The resistivity measurement of the non-textured sample NT is shown in black. R is re-scaled by a geometrical factor (w/l) for comparison purposes.

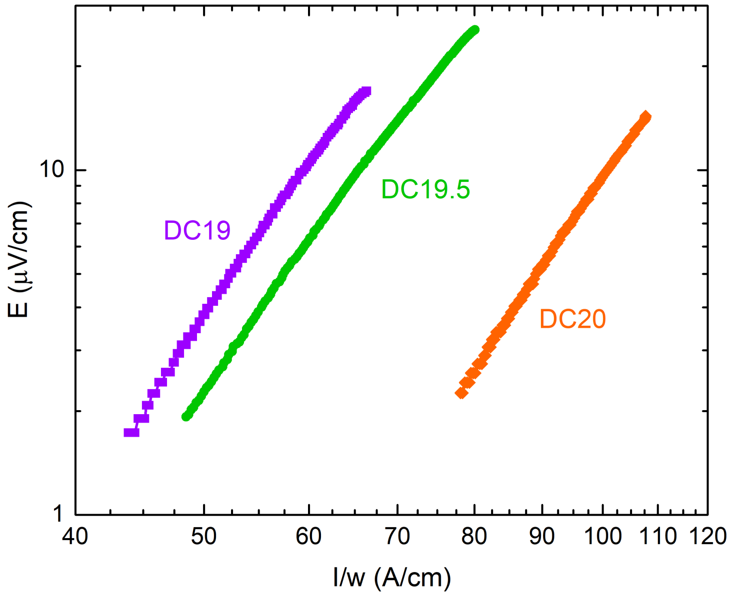

Figure 11.15: Transport critical current measurements of the EALZM processed samples DC19 (purple diamonds), DC19.5 (green circles) and DC20 (orange squares). Only the less noisy part of the curves are shown to obtain a better fitting.

Furthermore, I_c measurements at 77 K were performed and are displayed in Figure 11.15. Consequently, the I_c/w and n values were obtained for each sample, being 38.7 A cm^{-1} and 5.34 for sample DC19, and 66.4 A cm^{-1} and 5.59 for sample DC20. Sample DC19.5 presents intermediate I_c/w values as expected, specifically 41.2 A cm^{-1}. In order to understand these differences, it must be taken into account that transport current mainly flows in the region close to the surface where a well-textured microstructure is reached and that this region was much thicker in sample DC20.

11.5 Analysis of the current distribution during the EALZM process

Previous results show that the modifications induced in the microstructure during the EALZM are lower than in the case of the EALFZ process. A possible explanation can be found taking into account that only a fraction of the applied current can flow through the textured region.

In order to obtain some data for these calculations, the resistivity as a function of the temperature, $\rho(T)$ have been measured on the sample NT (i.e a pellet subjected to the final heat treatment, but without laser processing) and is presented in Figure 11.16.

From the evolution of $\rho(T)$ in the NT sample and taking into account its dimensions, the temperature dependence ($T > 200$ K) of the resistivity, ρ_{nt}, is:

$$\rho_{nt} = 11 + 0.06 \cdot T(\mu\Omega\,\mathrm{m})\ (T \text{ in K}) \tag{11.1}$$

During the EALZM process, the evolution of the sample resistance was recorded by measuring the voltage at the 1 A current supply. Taking into account that the resistance of the contacts also affects this measurement, the evolution of the sample resistance has been evaluated considering the variations of the total resistance and comparing with the extrapolated values deduced from the temperature dependence of the resistivity. Considering the texturing experiment of sample DC19, it was observed that after having turn

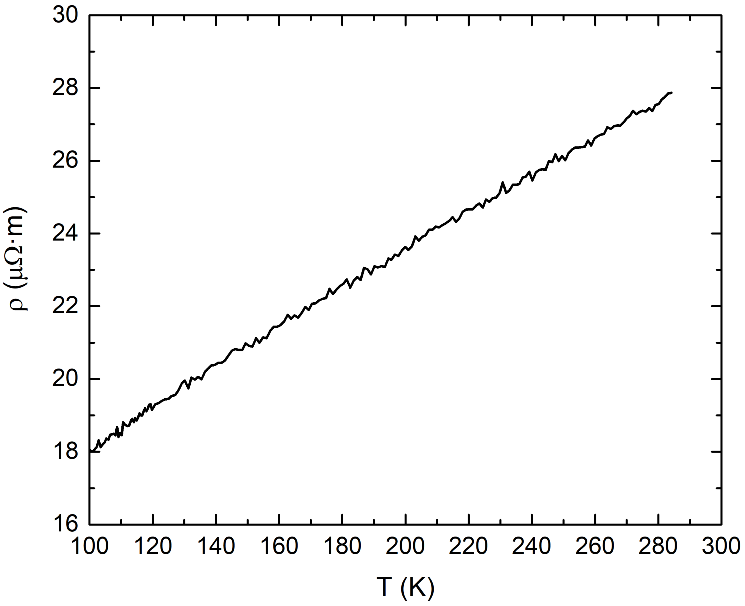

Figure 11.16: Resistivity of the sample NT. The whole cross-section of the sample was used in the calculation of ρ.

on the laser, the resistance of the sample increases 16 mΩ. In this increase, two contributions are important, the increase of the temperature in the region where the laser is acting from 500 °C to values close to 900 °C and the change in the resistance in the region that was melted. During the laser processing and additional increase of 29 mΩ was measured. After having textured a length of 31 mm the laser was turn off again and once the sample was cooled again to 500 °C, the sample resistance showed an increase of 19 mΩ in comparison with the resistance of the sample at the same temperature at the beginning of the experiment.

Taking into account the extrapolated value $\rho_{nt}(500\,°\mathrm{C}) = 57.4\,\mu\Omega\,\mathrm{m}$, the resistance at 500 °C of this 31 mm long sample before texturing, $R_{orig1}(500\,°\mathrm{C})$, was:

$$R_{orig1}(500\,°\mathrm{C}) = 57.4 \cdot 10^{-6} \cdot \frac{0.031}{16.8 \cdot 10^{-6}} = 0.106\,\Omega \tag{11.2}$$

where $16.8 \times 10^{-6}\,\mathrm{m}^2$ is the total cross-section of this sample. In consequence, the resistance after the texturing process increases up to $R_{19}(500\,°\mathrm{C}) = 0.019 + 0.106 = 0.125\,\Omega$.

In this model, at this moment the sample can be considered as two resistances in parallel, one associated with the 65 % of the total area that has not been affected by the laser (Table 11.2) and the second associated to the region that has been melted or affected with the laser process. The resistance of the non-affected region can be estimated to be $R_{nt19}(500\,°\mathrm{C}) = R_{orig1}(500\,°\mathrm{C})/0.65 = 0.163\,\Omega$ and, in consequence, the second resistance associated with the section that has been affected with the laser is $R_{t19}(500\,°\mathrm{C}) = 0.536\,\Omega$.

With these values, the percentage of the applied current that has been used to modify the texturing process is a 23.3 % of the applied current, 233 mA.

When the texturing process is performed with a diode source current of 19.5 A on a sample with a cross-section area of 13.9 mm^2, the resistance increase after having textured 34 mm is 77 mΩ.

$$R_{orig2}(500\,°\mathrm{C}) = 57.4 \cdot 10^{-6} \cdot \frac{0.034}{13.9 \cdot 10^{-6}} = 0.140\,\Omega \qquad (11.3)$$

$$R_{19.5}(500\,°\mathrm{C}) = 0.077 + 0.140 = 0.217\,\Omega \qquad (11.4)$$

In this sample the non-textured region covers a 43 % of the total section and, in consequence, $R_{nt19.5}(500\,°\mathrm{C}) = 0.326\,\Omega$ and $R_{t19.5}(500\,°\mathrm{C}) = 0.649\,\Omega$, using only a 33.4 % of the applied current.

When the texturing process is performed with a diode source current of 20 A (cross-section area, 14.5 mm^2) the resistance increase after having textured 33 mm is 115 mΩ:

$$R_{orig3}(500\,°\mathrm{C}) = 57.4 \cdot 10^{-6} \cdot \frac{0.033}{14.5 \cdot 10^{-6}} = 0.131\,\Omega \qquad (11.5)$$

$$R_{20}(500\,°\mathrm{C}) = 0.115 + 0.131 = 0.246\,\Omega \qquad (11.6)$$

In this sample the region that has not been affected by the laser covers a 28 % of the total section, and in consequence, $R_{nt20}(500\,°\mathrm{C}) = 0.468\,\Omega$ and $R_{t20}(500\,°\mathrm{C}) = 0.519\,\Omega$. With this distribution of resistances, the expected percentage of the applied current that flows through the region affected by the laser is 47.4 %.

This simplified model does not consider the heating and melting of a fraction of the sample that occurs when the laser is applied. The measured increase in the sample resistance when the laser is turned on is higher than expected, considering the local temperature increment and the size of the molten region. In consequence, it is expected that the resistance of the molten region would be higher than the values calculated with this simplified model in the textured regions. Thus, the obtained results only mark an upper limit for the fraction of the applied current that flows through the molten region. However, they clearly show that EALZM requires reducing as much as possible the region that is not affected by the laser and that the total applied current will be only used if the full cross-section is melted by the laser.

In conclusion, the EALZM is a technique that will be more adequate for superconducting coatings over non-conductive substrates where the laser can melt completely the cross-section of the coating and the current can only flow through the molten material.

Chapter 12

Conclusions

We have developed an industrially scalable process of texturing Bi-2212 monoliths regardless of their size that comprises several stages. In the first stage, the feasibility of producing precursor powders in a continuous process from a mixture of raw oxides and carbonates has been developed and demonstrated. This procedure has been called continuous solid-state route. A complete characterization (particle size distribution, phase composition, thermal stability and temperature dependence of the AC magnetic susceptibility analysis) of the precursor powders obtained with this process has been carried out and the obtained results compared with those of commercial and standard solid-state precursor powders. The advantages and disadvantages of this method in comparison with the standard solid-state process have also been reviewed. We concluded that the powders obtained with the continuous solid-state procedure after five heat treatments in the continuous furnace meet the requirements to be used as precursor in subsequent laser texturing processes.

Regarding the laser texturing process, the possibility of using a CO_2 pulsed laser apparatus with galvanometric mirrors to texture Bi-2212 monoliths has been investigated and demonstrated by developing a two-step laser zone melting (LZM) texturing process. This process is performed in air inside a furnace at $450\,^{\circ}\mathrm{C}$ and the samples are textured at $100\,\mathrm{mm\,h^{-1}}$ (first step) and $30\,\mathrm{mm\,h^{-1}}$ (second step) over a bulk Cu piece. This configuration allows texturing pieces up to $20\,\mathrm{cm}$ width or several samples in parallel. The microstructure and phase composition of samples made either with commercial or with the continuous solid-state precursor powders and subjected to an optimised two-step ("traditional") heat treatment were analysed after each step of the process. It has been observed that when continuous solid-state precursors are used, the superconducting properties are similar to the textured samples fabricated with commercial precursors. Moreover, the possibility of using a continuous heat treatment, which could eventually substitute the "traditional" one in a normal furnace, has also been analysed. It has been demonstrated that after a suitable optimisation process, this continuous heat treatment could be adequate.

Obviously, the best superconducting performance has been obtained in samples fabricated with commercial precursor powders subjected to the "traditional" heat treatment, with J_c values of the order of $\sim 3.7\,\mathrm{kA\,cm^{-2}}$ at 77 K and self-field. These results are among the best reported to date for planar Bi-2212 monoliths. However, a rather remarkable performance has also been obtained for samples made with continuous solid-state precursor powders subjected to the "traditional" heat treatment, obtaining I_c/w values up to a 74 % of the I_c/w of the sample made with commercial precursor powders.

All these results show that continuous processes can be used to fabricate the precursor, to texture the sample and to perform the heat treatment. These processes allow to overcome the main limitations associated with the sample dimensions when using typical furnaces.

The influence of the polarity of the applied current during the electrically assisted laser zone melting (EALZM) texturing of Bi-2212 monoliths has also been analysed. In the case of the EALZM process, a diode laser in continuous wave mode was used to texture the samples at $20\,\mathrm{mm\,h^{-1}}$ inside an open sky furnace at 500 °C. Three possible configurations (direct, zero current and inverse) were investigated. We concluded that the one in which the current flows from the melt to the textured region (direct configuration) favours the grain alignment and consequently the superconducting performance. Furthermore, it was demonstrated that the I_c/w value of EALZM processed samples in the direct configuration could be enhanced by increasing the textured cross-sectional area. How the applied current is distributed through the melt and the non-textured region during the processing of the samples has also been studied. The results indicate that only a fraction of the current flows through the molten volume, which leaves room for improving this technique. This could be done by texturing superconducting coatings over an insulating substrate where the full cross-section can be melted with the laser, so the total applied current will be forced to flow through the molten material.

Bibliography

[1] Mikheenko, P. N., Uprety, K. K., Dou, S. X.; Cardwell, D. A., Ginley, D. S. (Eds.), "BSCCO", Chapter C2 of *Handbook of Superconducting Materials* (IOP publishing Ltd, 2003), pp. 947-992.

[2] Farrell, D. E., Bonham, S., Foster, J., Chang, Y. C., Jiang, P. Z., Vandervoort, K. G., Lam, D. J., Kogan, V. G., "Giant superconducting anisotropy in $\mathrm{Bi_2Sr_2CaCu_2O_{8+x}}$", *Phys. Rev. Lett.* **63**, 782 (1989).

[3] Sunshine, S. A., Siegrist, T., Scheenmeyer, L. F., Murphy, D. W., Cava, R. J., Batlogg, B., van Dover, R. B., Fleming, R. M., Glarum, S. H., Nakahara, S., Farrow, R., Krajewski, J. J., Zahura, S. M., Waszczak, J. V., Marshal, J. H., Marsh, P., Rupp Jr., L. W., Peck, W. F., "Structure and physical properties of single crystals of the 84-K superconductor $\mathrm{Bi_{2.2}Sr_2Ca_{0.8}Cu_2O_{8+\delta}}$", *Phys. Rev. B* **38**, 893 (1988).

[4] Larbalestier, D. C., Gurevich, A., Feldmann, D. M., Polyanskii, A., "High-T_c superconducting materials for electric power applications", *Nature* **414**, 368 (2001).

[5] Larbalestier, D. C., Jiang, J., Trociewitz, U. P., Kametani, K., Scheuerlein, C., Dalban-Canassy, M., Matras, M., Chen, P., Craig, N. C., Lee, P. J., Hellstrom, E. E., "Isotropic round-wire multifilament cuprate superconductor for generation of magnetic fields above 30 T", *Nature Mater.* **13**, 375 (2014).

[6] de la Fuente, G. F., Díez, J. C., Angurel, L. A., Peña, J. I., Sotelo, A., Navarro, R., "Wavelength dependance in laser floating

zone processing. A case study with Bi-Sr-Ca-Cu-O superconductors", *Adv. Mater.* **7**, 853 (1995).

[7] Díez, J. C., Angurel, L. A., Peña, J. I., Martínez, E., de la Fuente, G. F., Navarro, R., "Fabricación de superconductores texturados con altas corrientes críticas por métodos de fusión zonal inducida con láser", *Bol. Soc. Esp. Ceram. Vidrio* **36**, 159 (1997).

[8] Fiegelson, R. S., Gazit, D., Fork, D. K., Geballe, T. H., "Superconducting Bi-Ca-Sr-Cu-O fibers grown by the laser-heated pedestal growth method", *Science* **240**, 1642 (1988).

[9] Gazit, D., Fiegelson, R. S., "Laser-heated pedestal growth of high T_c Bi-Sr-Ca-Cu-O superconducting fibers", *J. Crystal Growth* **91**, 318 (1988).

[10] Takekawa, S., Nozaki, H., Umezono, A., Kosuda, K., Kobayashi, M., "Single crystal growth of the superconductor $\mathrm{Bi_{2.0}(Bi_{0.2}Sr_{1.8}Ca_{1.0})Cu_{2.0}O_8}$", *J. Crystal Growth* **92**, 687 (1988).

[11] Brody, H. D., Haggerty, J. S., Cima, M. J., Flemings, M. C., Barns, R. L., Gyorgy, E. M., Johnson, D. W., Rhodes, W. W., Sunder, W. A., Laudise, R. A., "Highly textured and single crystal $\mathrm{Bi_2CaSr_2Cu_2O_x}$ prepared by laser heated float zone crystallization", *J. Crystal Growth* **96**, 225 (1989).

[12] Cima, M. J., Jiang, X. P., Chow, H. M., Haggerty, J. S., Flemings, M. C., Brody, H. D., Laudise, R. A., Johnson, D. W., "Influence of growth parameters on the microstructure of directionally solidified $\mathrm{Bi_2Sr_2CaCu_2O_y}$", *J. Mater. Res.* **5**, 9 1834 (1990).

[13] Costa, F. M., Gonçalves, A. P., Abílio, C., Godinho, M. M., Almeida, M., Vieira, J. M., "Crystallization process, phase chemistry and transport properties of superconducting fibers prepared by the LFZ method followed by isothermal annealing", *Physica C* **235**, 513 (1994).

[14] Angurel, L. A., Díez, J. C., Martínez, E., Peña, J. I., de la Fuente, G. F., Navarro, R., "Growth rate effects on thin $\mathrm{Bi_2Sr_2CaCu_2O_{8+x}}$ textured rods", *Physica C* **302**, 39 (1998).

[15] Díez, J. C., Angurel, L. A., Miao, H., Fernández, J. M., de la Fuente, G. F., "Processing of textured BSCCO superconductors

by laser-induced directional solidification", *Supercond. Sci. Technol.* **11**, 101 (1998).

[16] Miao, H., Dí, J. C., Angurel, L. A., de la Fuente, G. F., "Precursor powder influence on melt processing of high critical current BSCCO rods", *Supercond. Sci. Technol.* **13**, 1135 (2000).

[17] Angurel, L. A., Bona, M., Andrés, J. M., Muñoz-Rojas, D., Casañ-Pastor, N., "High quality silver contacts on ceramic superconductors obtained by electrodeposition from non-aqueous solvents", *Supercond. Sci. Technol.* **18**, 135 (2005).

[18] Costa, F. M., Carrasco, M. F., Ferreira, N., Silva, R. F., Vieira, J. M., "LFZ fibre texture modification induced by electrical polarization", *Physica C* **408**, 915 (2004).

[19] Carrasco, M. F., Siva, R. F., Vieira, J. M., Costa, F. M., "Electrical field freezing effect on laser floating zone (LFZ)-grown $Bi_2Sr_2Ca_2Cu_4O_{11}$ superconducting fibers", *Supercond. Sci. Technol.* **17**, 612 (2004).

[20] Carrasco, M. F., Amaral, V. S., Silva, R. F., Costa, F. M., "Electrical assisted laser floating zone (EALFZ) growth of 2212-BSCCO superconducting fibres", *Appl. Surf. Sci.* **257**, 5283 (2011).

[21] Carrasco, M. F., Silva, R. F., Vieira, J. M., Costa, F. M., "Pulling rate and current intensity competition in an electrically assisted laser floating zone", *Supercond. Sci. Technol.* **22**, 065016 (2009).

[22] Ferreira, N. M., Rasekh, S., Costa, F. M., Madre, M. A., Sotelo, A., Díez, J. C., Torres, M. A., "New method to improve the grain alignment and performance of thermoelectric ceramics", *Mater. Lett.* **83**, 144 (2012).

[23] Carrasco, M. F., Amaral, V. S., Vieira, J. M., Silva, R. F., Costa, F. M., "The effect of current direction on superconducting properties of BSCCO fibres grown by an electrically assisted laser floating zone process", *Supercond. Sci. Technol.* **19**, 15 (2006).

[24] Costa, F. M., Rasekh, S., Ferreira, N. M., Sotelo, A., Díez, J. C., Madre, M. A., "Effect of current polarity on BSCCO/Ag ceramics

textured by Electrically Assisted Laser Floating Zone", *J. Supercond. Nov. Magn.* **26**, 943 (2013).

[25] Costa, F. M., Ferreira, N. M., Rasekh, S., Fernandes, A. J. S., Torres, M. A., Madre, M. A., Díez, J. C., Sotelo, A., "Very large superconducting currents induced by growth tailoring", *Cryst. Growth Des.* **15**, 2094 (2015).

[26] Larrea, A., de la Fuente, G. F., Merino, R. I., Orera, V. M., "ZrO_2–Al_2O_3 eutectic plates produced by laser zone melting", *J. Eur. Ceram. Soc.* **22**, 191 (2002).

[27] Mora, M., Díez, J. C., López-Gascón, C. I., Martínez, E., de la Fuente, G. F., "Laser textured Bi-2212 in planar geometries", *IEEE Trans. Appl. Supercond.* **13**, 3188 (2003).

[28] Oka, Y., Yamamoto, N., Kitaguchi, H., Oda, K., Takada, J., "Crystallization behavior and partially melted states in Bi-Sr-Ca-Cu-O", *Jpn. Appl. Phys.* **28**, L213 (1989).

[29] Oka, Y., Yamamoto, N., Tomii, Y., Kitaguchi, H., Oda, K., Takada, J., "Crystalline phases formed in the partially melted states of Bi-Sr-Ca-Cu-O", *Jpn. Appl. Phys.* **28**, L801 (1989).

[30] Roth, R. S., Rawn, C. J., Ritter, J. J., Burton, B. P., "Phase equilibria of the system SrO-CaO-CuO", *J. Am. Ceram. Soc.* **72**, 1545 (1989).

[31] Mora, M., López-Gascón, C. I., Angurel, L. A., de la Fuente, G. F., "The influence of support temperature on Bi-2212 monoliths textured by diode laser zone melting", *Supercond. Sci. Technol.* **17**, 1329 (2004).

[32] Lennikov, V., Özkurt, B., Angurel, L. A., Sotelo, A., Özçelik, B., de la Fuente, G. F., "Microstructure and transport properties of Bi-2212 prepared by CO_2 laser line scanning", *J. Supercond. Nov. Magn.* **26**, 947 (2013).

[33] Estepa, L. C., de la Fuente, G. F., "Continuous furnace with coupled laser for the surface treatment of materials", EU Patent 1 992 445, Nov. 19 (2008), China Patent 200780011481, Apr. 15 (2009), U.S. Patent 2009/0230105A1 Sept. 17, (2009).

[34] de Francisco, I., Lennikov, V., Bea, J. A., Vegas, A., Carda, J. B., de la Fuente, G. F., “In-situ laser synthesis of rare earth aluminate coatings in the system *Ln*-Al-O (*Ln* = Y, Gd)”, *Solid State Sci.* **13**, 1813 (2011).

[35] Gurauskis, J., Lennikov, V., de la Fuente, G. F., Merino, R. I., “Laser-assisted, crack-free surface melting of large eutectic ceramic bodies”, *J. Eur. Ceram. Soc.* **31**, 1251 (2011).

[36] Rey-García, F., “Planar waveguides obtained on commercial glass substrates by sol-gel and laser irradiation methods”, PhD Thesis - Universidade de Santiago de Compostela (2012).

[37] Rey-García, F., Lennikov, V., Amaveda, H., Laliena, C., Mora, M., Martínez, E., Bao-Varela, C., Angurel, L. A., de la Fuente, G. F., “Effect of laser treatments in the microstructure and physical properties of Bi-2212 and Gd-123 bulk samples”, *IEEE Trans. Appl. Supercond.* **25**, 6800604 (2015).

[38] Sotelo, A., Rasekh, Sh., Madre, M. A., Díez, J. C., “Precursor influence on the electrical properties of textured Bi-2212 superconductors”, *J. Supercond. Nov. Magn.* **24**, 19 (2011).

[39] Naumov, D. Yu., Kozeeva, L. P., Kameneva, M. Yu., Kuratieva, N. V., Podberezskaya, N. V., “Structure and refinement of the composition of Bi-Sr-Ca-Cu oxide crystals”, *Crystallogr. Rep+* **53**, 216 (2008).

[40] Mayoral, M. C., Andrés, J. M., Bona, M. T., Angurel, L. A., Natividad, E., “Approximation to the laser floating zone preparation of high temperature BSCCO superconductors by DSC”, *Thermochim. Acta* **409**, 157 (2004).

[41] Maljuk, A., Li, C.; Chen, D., Lin, C., Maljuk, A., Zhou, F. (Eds.), “Bi-Based High-T_c Superconductors”, in *Growth and Characterization of Bulk Superconductor Material* (Springer International Publishing, 2016), pp. 47-114.

[42] Shibauchi, T., Maeda, A., Kitano, H., Honda, T., Uchinokura, K., “Microwave complex conductivity in single crystals of $YBa_2Cu_3O_7$ and $Bi_2Sr_2CaCu_2O_y$”, *Physica C* **203**, 315 (1992).

[43] Campbell, A. M., Blunt, F. J., Johnson, J. D., Freeman, P. A., "Quantitative determination of percentage superconductor in a new compound", *Cryogenics* **31**, 732 (1991).

[44] Clem, J. R., Kogan, V. G., "Theory of the magnetization of granular superconductors: application to high-T_c superconductors", *Jpn. J. Appl. Phys.* **26**, 1161 (1987).

[45] Natividad, E., Díez, J. C., Angurel, L. A., Andrés, J. M., Ferrando, A. C., Mayoral, M. C., "Radial changes in the microstructure of LFZ-textured Bi-2212 thin rods induced by stoichiometry modifications", *Physica C* **383**, 379 (2003).

[46] Mora, M., Martínez, E., Díez, J. C., Angurel, L. A., de la Fuente, G. F., "Phase growth and microstructure modifications induced by annealing in highly textured superconducting Bi-2212 thin rods", *J. Mater. Res.* **15**, 614 (2000).

[47] Natividad, E., Díez, J. C., Angurel, L. A., Andrés, J. M., "Successful application of Simplex Methods to the optimization of textured superconducting ceramics", *J. Am. Ceram. Soc.* **87**, 1216 (2004).

[48] Mora, M., Gimeno, F., Angurel, L. A., de la Fuente, G. F., "Laser zone melted $\mathrm{Bi_2Sr_2CaCu_2O_{8+x}}$ thick films on (100) MgO substrate", *Supercond. Sci. Technol.* **17**, 1133 (2004).

[49] Mora, M., López-Gascón, C., Angurel, L. A., de la Fuente, G. F., "The influence of support temperature on Bi-2212 monoliths textured by diode laser zone melting", *Supercond. Sci. Technol.* **17**, 1329 (2004).

[50] Sotelo, A., Mora, M., Madre, M. A., Díez, J. C., Angurel, L. A., de la Fuente, G. F., "Ag distribution in thick Bi-2212 floating zone textured rods", *J. Eur. Ceram. Soc.* **25**, 2947 (2005).

[51] Angurel, L. A., Díez, J. C., de la Fuente, G. F., "Laser induced cylindrical zone melting of $\mathrm{Bi_2Sr_2CaCu_2O_{8+x}}$ superconductors", *Anorg. Allg. Chem.* **635**, 1767 (2009).

Conclusiones

A continuación se detallan las principales conclusiones obtenidas en esta tesis. En primer lugar, se describen las relativas al estudio de las propiedades superconductoras de hilos de MgB_2 a partir de los procesos de optimización de los parámetros de molienda y de dopaje de los precursores.

Se ha analizado cómo se modifican las propiedades de los hilos y cintas monofilamento de MgB_2 con forro de hierro fabricados con la técnica de *polvo en tubo* (PIT, de sus siglas en inglés) y reacción *in situ* al modificar los parámetros utilizados en la molienda de los precursores. En particular, se ha estudiado el efecto de la energía por unidad de masa de las moliendas en el rango 1.2×10^6 y $1 \times 10^8 \mathrm{J\,kg^{-1}}$ (siendo este último valor mayor al límite de aleación mecánica) en las propiedades superconductoras de estos hilos y cintas.

La molienda de los precursores modifica considerablemente la microestructura de los conductores mejorando el anclaje de los vórtices para campos magnéticos altos. El hilo fabricado con los precursores molidos con la energía más alta es el que presenta el valor de J_c más alto a $5\,\mathrm{K}$ y $\mu_0 H > 5\,\mathrm{T}$. Sin embargo, a partir de un valor determinado de energía de molienda se observan defectos en la microestructura de los hilos, como es la presencia de grietas transversales de gran tamaño. Este hecho muestra que cuando se utilizan estos precursores, los hilos no se pueden fabricar únicamente por trefilado. Es conveniente utilizar otros métodos, como por ejemplo técnicas de laminado con surcos o de estampación con martillo rotatorio, en los que se produce una mayor compresión sobre el núcleo en la dirección radial durante la deformación del hilo.

El hilo y la cinta fabricados con precursores molidos con menor energía presentan una buena homogeneidad y valores de J_c muy reproducibles. Esta alternativa resuelve los problemas de inhomogeneidad observados en los hilos dopados con carbono y sin molienda. Además, combinando una adecuada energía de molienda con dopaje con carbono se obtienen valores de J_c más elevados en presencia de altos campos magnéticos y permite obtener microestructuras homogéneas.

Una de las formas de mejorar las propiedades de los hilos y cintas (dopados y sin dopar) sería realizar el traspaso de los polvos desde el molino al tubo de hierro en una atmósfera inerte, minimizando la cantidad de oxígeno presente en los precursores.

Para visualizar la penetración de flujo magnético en estos conductores y por tanto poder estudiar las propiedades superconductoras locales, hemos utilizado técnicas magneto-ópticas (MO). Se han observado variaciones locales de J_c en algunos de los hilos superconductores, lo que ha permitido entender las razones del deterioro de J_c a bajos campos magnéticos en alguno de los hilos fabricados. Utilizando la técnica MO en distintas condiciones de enfriamiento, con y sin campo magnético, se ha podido comprobar que las características de la microestructura afectan de manera significativa al frente de propagación del flujo magnético. Las medidas realizadas durante el enfriamiento con campo magnético muestran las distorsiones en el patrón magnético, muy útil a la hora de desvelar inhomogeneidades en el superconductor. Las imágenes MO han confirmado las características microestructurales observadas con microscopía electrónica de barrido de emisión de campo (FESEM) como, por ejemplo, la presencia de pequeñas grietas, poros en el forro de hierro o agregados de granos de MgB_2 con uniones débiles que se han encontrado en algunas de las cintas estudiadas.

A continuación, se detallan las conclusiones relativas al estudio del escalado industrial de un proceso de texturado láser en monolitos de $Bi_2Sr_2CaCu_2O_{8+x}$.

Se ha desarrollado un método escalable a nivel industrial para texturar monolitos de Bi-2212 independientemente de su tamaño. Para ello, se ha estudiado la viabilidad de producir polvos precursores en un proceso continuo con una mezcla de óxidos y carbonatos al que se ha llamado ruta de estado sólido en continuo. Se han caracterizado de manera completa los precursores así obtenidos (denominados polvos en continuo) y se han comparado con los polvos Bi-2212 comerciales y con los obtenidos mediante síntesis de estado sólido estándar (polvos estándar). Esta caracterización abarca el ánalisis de la distribución del tamaño de partícula, composición de fases, estabilidad térmica y la dependencia de la susceptibilidad magnética AC con la temperatura. Tras 5 tratamientos térmicos en el horno de rodillos, los polvos en continuo son adecuados para utilizarlos como polvos precursores en los procesos de texturado láser que se realizan a continuación.

En lo relativo al texturado láser de monolitos de Bi-2212, se ha desarrollado un proceso de texturado en dos pasos por fusión zonal láser (LZM) que utiliza un láser pulsado de CO_2 acoplado a espejos galvanométricos. Esta configuración permite texturar muestras con una anchura de hasta 20 cm o varias muestras en paralelo. Las muestras se texturan en aire en un horno de rodillos a 450 °C, moviéndose sobre una pieza de cobre a una velocidad de $100\,\mathrm{mm\,h^{-1}}$ durante el primer tratamiento y $30\,\mathrm{mm\,h^{-1}}$ el segundo. Después de cada etapa, se ha analizado la microestructura y la composición de las muestras fabricadas tanto con polvos precursores comerciales como con polvos estándar, una vez que han sido sometidas al tratamiento térmico habitual. Las propiedades superconductoras obtenidas utilizando los precursores estándar son parecidas a las de las muestras texturadas fabricadas con polvos comerciales. Además, se ha analizado la posibilidad de realizar un tratamiento térmico en continuo en el interior de un horno de rodillos que, después de una optimización adecuada, podría llegar a sustituir al habitual y ser utilizado en muestras de gran tamaño.

Las mejores propiedades superconductoras se han obtenido en las muestras texturadas fabricadas con polvos comerciales sometidos al tratamiento térmico habitual, alcanzando valores de $J_c \sim 3.7\,\mathrm{kA\,cm^{-2}}$ a 77 K y campo propio. Estos resultados están entre los mejores que se han publicado hasta la fecha para monolitos de Bi-2212. No obstante, también se han obtenido resultados del mismo orden de magnitud en las muestras fabricadas con los polvos precursores en continuo sometidos al tratamiento térmico habitual, con valores de I_c/w hasta un 74 % de los obtenidos para las muestras fabricadas con precursores comerciales.

Estos resultados muestran que los procesos en continuo son válidos para fabricar precusores, texturar muestras y realizar tratamientos térmicos. De esta manera, se pueden superan las principales limitaciones relativas al tamaño de las muestras que están asociadas con los tratamientos realizados en hornos convencionales.

También se ha estudiado la posibilidad de aplicar una corriente eléctrica durante el proceso de texturado de los monolitos de Bi-2212 por fusión zonal láser asistida con corriente (EALZM). En este caso, se ha empleado un láser continuo de diodos para texturar las muestras a $20\,\mathrm{mm\,h^{-1}}$ dentro de un horno abierto a 500 °C. Se han estudiado tres posibles configuraciones: directa, sin corriente e inversa. Se ha observado que la configuración directa (en la que la corriente fluye de la zona fundida a la zona texturada) favorece el alineamiento de los granos del material y por tanto permite obtener mejores propiedades supercondutoras. Además, se ha demostrado que en las muestras procesadas por EALZM en configuración directa, el valor de I_c/w mejora al aumentar la sección transversal que ocupa la zona texturada, ya que conlleva que un mayor porcentaje de la corriente eléctrica aplicada se utiliza para favorecer el texturado de la muestra. Asimismo, se ha investigado cómo se distribuye la corriente a través de la zona fundida y de la zona no texturada durante el procesado. Los resultados muestran que solo una parte de la corriente fluye por la zona fundida. Esto supone que para poder utilizar esta técnica en todo su potencial es mejor trabajar con recubrimientos superconductores sobre sustratos aislantes en donde la zona fundida puede cubrir todo el espesor de la muestra y por tanto toda la corriente aplicada deberá atravesar el fundido.

List of publications

- Laliena, C., Martínez, E., Angurel, L. A., Navarro, R., "Effect of ball milling and fatty acid addition on the properties of MgB_2 wires", *IEEE Trans. Appl. Supercond.* **25**, 6200204 (2015).
- Rey-García, F., Lennikov, V., Amaveda, H., Laliena, C., Mora, M., Martínez, E., Bao-Varela, C., Angurel, L. A., de la Fuente, G. F., "Effect of laser treatments in the microstructure and physical properties of Bi-2212 and Gd-123 bulk samples", *IEEE Trans. Appl. Supercond.* **25**, 6800604 (2015).
- Laliena, C., Qureishy, T., Martínez, E., Navarro, R., Mikheenko, P., Johansen, T. H., Kováč, P., "Effect of ball milling on the local magnetic flux distribution and microstructure of *in situ* Fe/MgB_2 conductors", *J. Alloys Compd.* **717**, 164 (2017).
- Qureishy, T., Laliena, C., Martínez, E., Qviller, A. J., Vestgården, J. I., Johansen, T. H., Navarro, R., Mikheenko, P., "Dendritic avalanches in a superconducting MgB_2 tape", *Supercond. Sci. Technol.* **30**, 125005 (2017).
- Laliena, C., Amaveda, H., Özçelik, B., Martínez, E., de la Fuente, G. F., Angurel, L. A., "Continuous processing of $Bi_2Sr_2CaCu_2O_{8+x}$ precursor powders", submitted.

List of symbols and abbreviations

$\boldsymbol{\beta}$ - ball-to-powder mass ratio

γ - superconducting anisotropy

$\boldsymbol{\Delta H}$ - enthalpy change

$\boldsymbol{\Delta M}$ - width of magnetic hysteresis loop

$\boldsymbol{\Delta T_w}$ - superconducting transition width

$\boldsymbol{\theta}$ - angle of the diffracted wave

$\boldsymbol{\lambda}$ - wavelength

$\boldsymbol{\lambda_L}$ - London penetration depth

$\boldsymbol{\lambda_{Lab}}$ - in-plane London penetration depth

$\boldsymbol{\mu}$ - magnetic moment

$\boldsymbol{\mu_0}$ - magnetic permeability of free space

$\boldsymbol{\mu_0 H}$ - magnetic field

$\boldsymbol{\mu_0 H_p}$ - magnetic field of full penetration

$\boldsymbol{\xi}$ - superconducting coherence length

$\boldsymbol{\xi_{ab}}$ - superconducting in-plane coherence length

$\boldsymbol{\xi_c}$ - superconducting coherence length in the c-axis

$\boldsymbol{\rho}$ - resistivity

$\boldsymbol{\rho_c}$ - contact resistivity

$\boldsymbol{\rho_{nt}}$ - resistivity of non-textured region

$\boldsymbol{\rho_t}$ - resistivity of textured region

$\boldsymbol{\chi_{ac}}$ - magnetic susceptibility

$\boldsymbol{\chi'}$ - in-phase component of χ_{ac}

$\boldsymbol{\chi''}$ - out-of-phase component of χ_{ac}

$\boldsymbol{\omega_p}$ - angular frequency

a - tapes width

b - tapes thickness

c - tapes length

d - diameter

$\mathbf{d_{10}}$, $\mathbf{d_{50}}$, $\mathbf{d_{90}}$ - intercepts for 10 %, 50 % and 90 % of the cumulative mass

E - electric field

E_t/m - energy transferred per unit mass

H - magnetic field strength

H_c - critical magnetic field

H_{c1} - lower critical field

H_{c2} - upper critical field

H_{irr} - irreversibility field

i - intensity of the strongest line of the pattern

I - transport current

I_c - superconducting critical current

i_{cor} - intensity of the strongest peak at a reference phase (taken by convention to be α-Al_2O_3, corondum, in a 50/50 weight mixture)

J_c - superconducting critical current density

J_{cL} - superconducting critical current density along wire axis

J_{cT} - superconducting critical current density along wire radial direction

J_e - superconducting engineering critical current density

l - distance between voltage contacts

L - length

M - magnetization

M_W - molecular weight

n - number of moles

R - electrical resistance

r - radius

r_b - ball radius

R_c - contact resistance

R_{nt} - resistance of non-textured region

r_p - sun disk radius

R_t - resistance of textured region

r_v - jar inner radius

S - surface

$\boldsymbol{t}$ - time

$\boldsymbol{T}$ - temperature

$\boldsymbol{T_c}$ - superconducting critical temperature

$\boldsymbol{V}$ - voltage

$\boldsymbol{w}$ - width of the sample

AC - alternate current

AsB - angle-selective backscattered electrons

Bi-2201 - $\mathrm{Bi_2Sr_2CuO_{6+x}}$

Bi-2212 - $\mathrm{Bi_2Sr_2CaCu_2O_{8+x}}$

Bi-2223 - $\mathrm{Bi_2Sr_2Ca_2Cu_3O_{10+x}}$

BSCCO - family of superconductors $\mathrm{Bi_2Sr_2Ca_{n\text{-}1}Cu_nO_{2n+4+x}}$, $n = 1, 2, 3$

C - commercial

CCD - charge coupled device

CERN - Conseil Européen pour la Reserche Nucléaire

CHPD - cold high pressure densification technique

CIP - cold isostatic press

CSS - continuous solid-state

CVD - chemical vapour deposition

DC - direct current

DSC - differential scanning calorimetry

EALFZ - electrically assisted laser floating zone

EALZM - electrically assisted laser zone melting

EDX - energy-dispersive X-ray spectroscopy

FC - field cooling

FESEM - field-emission scanning electron microscopy

HIP - hot isostatic press

HTS - high temperature superconductor

IBAD - ion beam-assisted deposition

IMD - internal magnesium diffusion process

in-lens - high-efficiency annular secondary electron detector

LFZ - laser floating zone

LTS - low temperature superconductor

LZM - laser zone melting

MR - molten region

MRI - magnetic resonance imaging system

MO - magneto-optical

NTAR - non-thermally affected region

O-cont. - oxygen content

PIT - powder-in-tube technique

PPMS - physical property measurement system

RIR - reference intensity ratio

RT - room temperature

SE - secondary electrons

SMES - magnetic energy storage device

SQUID - superconducting quantum interference device

SSS - standard solid-state

TAR - thermally affected region

TGA - thermogravimetric analysis

VSM - vibrating sample magnetometer

WTR - well-textured region

XRD - X-ray diffraction

YBCO - $YBa_2Cu_3O_{7-x}$

ZFC - zero-field cooling

Agradecimientos

Quiero comenzar dando las gracias a todas las instituciones y organismos que han hecho posible este trabajo: al Ministerio de Economía y Competitividad por la beca FPI enmarcada en el proyecto MAT2011-22719, a la Universidad de Zaragoza y al Instituto de Ciencia de Materiales de Aragón.

Me gustaría también agradecer a mis directores Luis Alberto y Elena, sin los que este trabajo no tendría sentido, por su ayuda y apoyo durante estos años de tesis. Ha sido un placer teneros como directores y aprender tantas cosas de vosotros.

También me gustaría acordarme de todos los compañeros del área de Ciencia y Tecnología de Materiales, en especial de Vassili, Hippolyte, Mario, Rafa, Germán, José Antonio, Israel, Ruth, Isabel, Carlos, Miguel, Eva, Michel, Marisol y Macarena por su ayuda y el cariño que me han mostrado durante esta etapa.

Quisiera aprovechar para agradecer al Servicio General de Apoyo a la Investigación-SAI de la Universidad de Zaragoza por toda la asistencia recibida. A Rosa Bueno, Rosa Lou y Mª Ángeles del Servicio de Microscopía Electrónica de Materiales y, en especial, a Cristina por los buenos ratos que pasamos y las conversaciones que tuvimos durante las observaciones con el FESEM. También quiero agradecerle a Ana Arauzo del Servicio de Medidas Físicas que siempre ha estado ahí para echarme una mano con las medidas en el SQUID y el PPMS.

I would also like to thank Pavlo and Thomas at University of Oslo, not only for the stimulating scientific colaboration but also, for making me feel welcome and comfortable during my stay in Norway.

Quiero también agradecer a Elías Palacios y Ramón Burriel por confiar en mí y darme mi primera oportunidad en esto de la investigación durante mi último año de carrera.

Pasando a un nivel más personal, quiero dar las gracias muy fuerte (si es que eso es posible) a todos y todas los que pasasteis por la sala de colaboradores: María, Irene, Gabriel, Hernán, José Antonio, Cristian, Álvaro, Laura, Jorge, Javi, Patricio, David y Guillermo, por los buenos ratos que pasamos y las cosas que compartimos. Habéis sido mucho más que compañeros.

Fuera del ámbito académico, me gustaría dar las gracias a mis nuevos compañeros en Asturias: Vero, Laura, Álvaro, Cris y Juan, que me han escuchado y ayudado cuando han podido y que han hecho el tiempo que llevo aquí mucho más agradable.

Además, me gustaría dar las gracias a todos los miembros de mi familia y a los de la de Cris, especialmente a mis primas Clara, Ana y Rosa por compartir conmigo ratos tan divertidos y por sus particulares locuras. Por supuesto, quiero dar las gracias también a mis padres, Carlos y Maite, y a mi hermano Jorge, por vuestro cariño, apoyo y por creer siempre en mí.

No quisiera terminar sin acordarme de algunas de las personas que han sido especialmente importantes para mí, con las que he compartido momentos muy felices a lo largo de este tiempo y que considero mis amigos: Belén, Pau, Rai, Moni, Richi, Lalo, Javi, Garri y Pablo. Muchas gracias por estar ahí.

Por último, a Cris, sin la que nada de todo esto habría sido posible.